Control of Coexisting Attractors in Nonsmooth Dynamical Systems

Zhi Zhang

Department of Engineering
University of Exeter

Submitted by Zhi Zhang to the University of Exeter for the degree of
Doctor of Philosophy in Engineering.

This thesis is available for Library use on the understanding that it is copyright material and that no quotation from the thesis may be published without proper acknowledgement.

I certify that all material in this thesis which is not my own work has been identified and that any material that has previously been submitted and approved for the award of a degree by this or any other University has been acknowledged.

Signature:..

College of Engineering, Mathematics
and Physical Sciences

December 2021

Declaration

I hereby declare that except where specific reference is made to the work of others, the contents of this dissertation are original and have not been submitted in whole or in part for consideration for any other degree or qualification in this, or any other university. This dissertation is my own work and contains nothing which is the outcome of work done in collaboration with others, except as specified in the text and Acknowledgements.

Zhi Zhang
December 2021

Acknowledgements

My deepest gratitude goes first and foremost to my academic supervisor, Dr Yang Liu, who has been carefully guiding and meticulously helping me in my PhD research and live. He has led me to a promising research field with his solid background and foundation, creative mind and extensive experience in academic research.

I am very thankful to my second supervisor, Prof. Jan Sieber, for his guidance, timely support and useful suggestions during my PhD research. I would like to show my special thanks to Prof. Joseph Páez Chávez who shares many experiences and had many useful discussion with me.

I also would like to thank all my colleagues of Applied Dynamics and Control Lab in the Department of Engineering at the University of Exeter, Dr Bingyong Guo, Dr Wei Lin, Mr Kenneth Omokhagbo Afebu, Miss Jiajia Zhang, Mr Kingsley Amadi, Mr Ahmed Al Shekaili and Mr Jiyuan Tian, who have helped me with many useful discussions and provided many supports on my life.

I gratefully acknowledge the financial support from the University of Exeter for the Exeter International Excellence Scholarship.

Finally, a special acknowledgement owes to my family for their understanding, support and encouragement during all these years.

Abstract

Nonsmooth dynamical systems are widely used in many engineering applications. Because of its nonsmooth property, it is very common to observe coexisting attractors in this type of dynamical systems. These coexisting attractors are extremely sensitive to noise due to their fractal basin boundaries. For some certain requirements and application scenarios, some of them are not desireable, which should be avoided. Obviously, achieving the switching among these attractors could offer the dynamical systems more flexibilities. Hence, studying the control of coexisting attractors in nonsmooth dynamical systems is vital. In this thesis, the study focuses on developing new control strategies and computational methods for evaluating the controlling process, and in particular, the near-grazing dynamics of the nonsmooth dynamical systems with and without delay. To be more specific, the key contents of this thesis are summarised as follows:

- Due to the infinite-dimensional nature of dynamical systems with delay, analytical studies of such models are difficult and can provide in general only limited results, in particular when some kind of nonsmooth phenomenon is involved, such as impacts, switches, impulses, etc. Also, there exists so far no dedicated software package to carry out numerical continuation for such type of models. In order to overcome this problem, an approximation scheme for nonsmooth dynamical systems with delay was proposed so that a numerical bifurcation analysis can be allowed via continuation (path-following) methods, using existing numerical packages, such as COCO.

- Lyapunov exponent is a widely used tool for studying dynamical systems. When calculating Lyapunov exponents for piecewise-smooth systems with time-delayed arguments one faces a lack of continuity in the variational problem. In this thesis, the part of our works studies how to build a variational equation for the efficient construction of Jacobians along trajectories of a delay nonsmooth system. Trajectories of a piecewise-smooth system may encounter the so-called grazing event where the trajectory approaches a discontinuity surface in the state space in a non-transversal manner. For this event a grazing point estimation algorithm was developed to ensure the accuracy of trajectories for the nonlinear and the variational equations. Through

adopting this algorithm, the eigenvalues of the Jacobian matrix computed by the algorithm converge with an order consistent with the order of the numerical integration method, therefore guaranteeing the reliability of the proposed numerical method.

- For the nonsmooth dynamical systems, the coexisting attractors are widely existing. But this property increases the complexity of the system's dynamics. For example, the dynamical system with this property can have many different motions under some different initial conditions. It is easy for the system to present some undesired attractors, which should be avoided. In order to suppress the complex dynamics, a delay feedback control was considered for the nonsmooth dynamical systems to achieve the switch from the undesired attractors to the desired one. The efficiency and dynamical property of this control were demonstrated numerically for nonsmooth dynamical systems.
- In order to control coexisting attractors a control strategy for switching stable coexisting attractors of a class of non-autonomous dynamical systems was developed. The central idea is to introduce a continuous path for the system's trajectory to transition from its original undesired stable attractor to a desired one by varying one of the system parameters according to the information of the desired attractor. The behavior of the control strategy was demonstrated numerically for both nonsmooth and smooth dynamical systems. It was shown that the proposed control concept can be implemented through either using an external control input or by varying a system parameter.

Table of contents

List of figures

List of abbreviations and nomenclatures

Abbreviation

COCO	Continuation Core and Toolboxes
DDEs	Delay Differential Equations
LEs	Lyapunov Exponents
ODEs	Ordinary Differential Equations
OGY	Ott-Grebogi-Yorke
RFDE	Retarded Functional Differential Equation

Nomenclature

b	nondimensional static forcing of impact system with a drift
d	nondimensional dry friction force of impact system with a drift
α	nondimensional forcing amplitude of vibro-impact system capsule system
ϕ	phase shift of external force containing a harmonic component
τ	nondimensional time
τ_d	nondimensional delay time
ξ	nondimensional damping ratio of impact system with a drift and vibro-impact capsule system
ζ	nondimensional damping ratio of soft impact system
A	dimensional forcing amplitude of soft impact system

a	nondimensional forcing amplitude of soft impact system and impact system with a drift
c	dimensional damping
e	nondimensional gap of soft impact system
G	dimensional gap
g	nondimensional gap of impact system with a drift
K	control gain of delay feedback control
k	dimensional stiffness of linear spring of impact system with a drift
k_1	dimensional primary stiffness
k_2	dimensional secondary stiffness
m	mass of soft impact system and impact system with a drift
m_1	internal mass of vibro-impact capsule system
m_2	rigid capsule of vibro-impact capsule system
P_d	dimensional forcing amplitude of impact system with a drift and vibro-impact capsule system
P_f	dimensional dry friction force
P_s	dimensional static forcing of impact system with a drift
T	one period of the external excitation
X_1	dimensional absolute displacement of the internal mass of vibro-impact capsule system
X_2	dimensional absolute displacement of the capsule of vibro-impact capsule system
X_b	dimensional displacement of slider top of impact system with a drift
X_m	dimensional displacement of impact system with a drift
X_t	dimensional displacement of slider top of impact system with a drift
$\bar{v}$	nondimensional displacement of the slider bottom of impact system with a drift

Ω	dimensional forcing/base excitation frequency
ω	frequency ratio
v	nondimensional velocity of the mass of soft impact system and duffing system
x	nondimensional displacement of the mass of soft impact system and impact system with a drift
x_1	nondimensional displacement of the internal mass of vibro-impact capsule system
x_2	nondimensional displacement of the rigid capsule of vibro-impact capsule system
y	nondimensional velocity of the mass of impact system with a drift
y_1	nondimensional velocity of the internal mass of vibro-impact capsule system
y_2	nondimensional velocity of the rigid capsule of vibro-impact capsule system
z	nondimensional displacement of the slider top of impact system with a drift
β	nondimensional stiffness ratio
Γ	nondimensional forcing amplitude

Chapter 1

Introduction

1.1 Motivation

Nonsmooth system is widely existed in physics and engineering, such as self-propelled capsule systems [5, 6], rotor systems [7, 8], energy harvesting [9], mechanical bearings [10], manufacturing cutting [11], and oil and gas drilling [12–14]. Due to the nonsmooth property, this class of dynamical systems presents many complex nonlinear phenomena, such as chaotic motion, coexisting attractors, and grazing and sliding events. The coexisting attractors mean a dynamical system is able to present many dynamical responses under different initial conditions. Apparently, among the coexisting dynamical responses, some of them can present good dynamics, which are desired, and the others should be avoided, due to the undesired properties. For example, in [15], for the vibro-impact systems, the chaotic attractor is undesirable, due to random and unpredictable property. Furthermore, choosing among the coexisting attractors can improve and optimize the dynamical performance of the dynamical system. For instance, Liu *et al.* [16] and Liao *et al.* [17] showed that through choosing the most efficient operational mode among possible coexisting attractors, the efficiency of the vibro-impact drilling can be improved. However, introducing some methods to achieve the control of coexisting attractors undoubtedly can change the basic dynamical properties of dynamical systems. For example, in [18], the delay feedback controller developed by Pyragas [19] can reduce the numbers of coexisting attractors and increase the dimensions of the system. In [20], a feedback controller including the information of the desired attractor can drive the system to the desired attractor, and the system with this controlled becomes monostable. There are many control methods [21–24] that also change the basic dynamical properties during the control of coexisting attractors. Therefore, studying these changes appearing in the control of coexisting attractors is necessary to understand how the control impact the dynamical performances.

1.2 Aims and scope of the thesis

In this thesis, the main aim is to develop mathematical tools for controlling coexisting attractors in nonsmooth dynamical systems, and analyse the dynamical characteristcs of the controlled nonsmooth dynamical systems. To this end, this work will employ the delay feedback control method based on the velocity of the systems, and develop a number of new control strategies for the switching between coexisting attractors. In addition, some new numerical methods will be developed in order to analyse the complex dynamics for the controlled nonsmooth dynamical systems.

In this chapter, the general motivation of the research has been illustrated. From the next chapter (Chapter 2), detailed related works and state-of-the-art analysis and control methods related to the control of coexisting attractors will be thoroughly surveyed.

In Chapter 3, three different types of piecewise continuous dynamical systems will be introduced, which widely exist in many engineering applications. In addition, it gives a brief preliminary discussion about some important properties of these systems.

In Chapter 4, an approximation method for nonsmooth DDEs will be introduced to enable the numerical bifurcation analysis of the system dynamics via existing and well-established numerical continuation packages, such as COCO [25]. Specifically, the method is based on the *chain method* outlined above, in combination with a second-order approximation scheme of the original DDE by considering a finite sequence of Taylor expansions as proposed in [26]. In this way, a piecewise-smooth dynamical system with (constant) delay can be approximated by a piecewise-smooth system of ODEs of large dimension, which then allows the study of the resulting model in the framework of hybrid dynamical systems. following the ideas of [27] and [28].

In Chapter 5, the contribution is the development of a novel method for precisely calculating the LEs of piecewise-smooth differential equations with a delay argument, which can promote the accuracy for stability analysis of periodic orbits. In detail, if an algorithm cannot estimate the point of discontinuity along trajectory with an accuracy of the same order as its integration method, especially in the grazing event, the expected discontinuous coefficients of the variational problem will have unexpectedly low accuracy leading to an accumulation of errors. In order to improve the accuracy, it is necessary to consider the accurate information about the time of crossing or grazing of a discontinuity (when impact occurs), which can be estimated by a grazing estimation algorithm. The novelty of this method is that it can estimate the point of discontinuity locally along trajectories of piecewise-smooth DDEs, improving the accuracy of computations of the system trajectory and of the LEs. The proposed method can also be extended to other nonsmooth dynamical systems, such as the hard impact oscillator with a time-delayed controller or stick-slip vibrations with a delay term.

In Chapter 6, it attempts to investigate the dynamical performance of three different impact systems with a.periodically forced impacting system by delay feedback controller and present how time-delayed feedback control suppresses multistability, through a non-invasive approach, without affecting its original dynamics. Specifically, coexisting attractors, caused by nonsmooth property, can be reduced to one of attractors, through the delay feedback controller, and without introducing any external attractors, or changing any existing attractors.

In Chapter 7, the primary focus is to address the continuous switching between two of coexisting stable attractors by varying a system parameter without affecting their original dynamics. In order to achieve this, a continuous control method is proposed, and can adjust a system parameter based on the information of trajectory of the desired attractor. This control method is applied to the controlled system continuously until its trajectory is sufficiently close to the desired one. Based on this control concept, two control strategies, the so-call linear and nonlinear control strategies, were developed. The former one can be treated as an external control input and the latter one can be treated as the variation of a system parameter. The advantage of the latter one is that it depends only on the original properties of system parameter and does not rely on any external input.

Finally, Chapter 8 summarises the thesis contributions and comments on the achievements made during the PhD study. Also, future work is outlined in Chapter 8.

1.3 Contribution of the thesis

The main topic of this thesis is to study the control of coexisting attractors in nonsmooth dynamical systems. The main contributions of this thesis mainly includes two parts. First of all, some new numerical tools were developed to study the dynamical performances and properties of nonsmooth dynamical systems. Specifically, an approximation scheme for nonsmooth dynamical systems with delay was proposed to allow a numerical bifurcation analysis for nonsmooth DDEs, via continuation (path-following) methods, using existing numerical packages, such as COCO. Also, a novel method was developed for precisely calculating the LEs of piecewise-smooth differential equations with a delay argument, so that the stability of this type of nonsmooth differential equations can be studied. Secondly, the problem related to the control of coexisting attractors in nonsmooth dynamical systems was considered. Specifically, a delay feedback controller was introduced to a type of nonsmooth dynamical systems to achieve the control of coexisting attractors. In addition, a feedback control strategy was developed to achieve the switch from the undesired attractors to the desired coexisting attractors for the nonsmooth and smooth dynamical systems.

During the PhD study, three journal papers were published, one journal paper is under review and two abstracts were submitted and presented at two international conferences, which are summarised as below.

- Z. Zhang, J. Páez Chávez, J. Sieber, Y. Liu, Controlling coexisting attractors of a class of non-autonomous dynamical systems. (Submitted to *Physica D*).
- Z. Zhang, J. Páez Chávez, J. Sieber, Y. Liu, Controlling grazing-induced multistability in a piecewise-smooth impacting system via the time-delayed feedback control. *Nonlinear Dynamics*, 2021. https://doi.org/10.1007/s11071-021-06511-2.
- Z. Zhang, J. Sieber, Y. Liu, Calculating the Lyapunov exponents of a piecewise-smooth soft impacting system with a time-delayed feedback controller. *Communications in Nonlinear Science and Numerical Simulation*, vol. 91, pp. 10545, 2020.
- J. Páez Chávez, Z. Zhang, Y. Liu, A numerical approach for the bifurcation analysis of nonsmooth delay equations. *Communications in Nonlinear Science and Numerical Simulation*, vol. 83, pp. 105095, 2020.
- Z. Zhang, Y. Liu, J. Sieber, Lyapunov exponents of an impact oscillator with delayed feedback control, the Fourth International Conference on Recent Advances in Nonlinear Mechanics, Lodz, Poland, 2019.
- Z. Zhang, Y. Liu, J. Páez Chávez, J. Sieber, Delayed feedback control of grazing-induced multistability in an impacting system, the First International Nonlinear Dynamics Conference, Rome, Italy, 2019.

Chapter 2

Previous works

2.1 Nonsmooth dynamical systems

Nonsmooth dynamical systems are very common in many engineering applications, such as the occurrence of impacting motion in mechanical systems [29–31, 2, 3, 32], stick-slip motion in oscillators with friction [33], switchings in electronic circuits [34, 35], and hybrid dynamics in control systems [36, 37]. Studying these dynamical systems is able to observe many complex new phenomena, which are hard to be discovered in the smooth dynamical systems. For example, grazing bifurcation [38] cannot be observed in smooth dynamical systems, and is bifurcation presenting that systems witness a varying from a nonimpacting to an impacting state (or vice versa) with the smooth varying of system parameter. In addition, the flow of the nonsmooth system can witness the discontinuity due to the discontinuous conditions, which cannot discovered from smooth dynamical systems [39]. Thus, studying the nonsmooth dynamical systems enables us to have a better understanding of the dynamical charateristics of these systems, so their performance in practical applications can be optimised.

Among nonsmooth dynamical systems, impacting systems play important role and are widely existed in many physical and engineering systems, such as self-propelled capsule systems [5, 6], rotor systems [7, 8], energy harvesting [9], mechanical bearings [10], manufacturing cutting [11], and oil and gas drilling [12–14]. Impacting systems show many complex nonlinear phenomena, e.g. chaotic motion, multistability, and grazing and sliding events [39], which can be exploited during design. For example, Liu *et al.* [16] and Liao *et al.* [17] suggested that the efficiency of the vibro-impact drilling can be improved by choosing the most efficient operational mode among possible coexisting attractors. For the self-propelled capsule system in [5], Guo *et al.* validated the mathematical model by comparing it with experimental results. Then the numerical results obtained from the model were used to optimise the progression speed and energy efficiency of the capsule prototype. In [40], Páez Chávez *et al.* studied the mathematical model of a Jeffcott rotor within a snubber ring with anisotropic supports, and the model was used to predict the onset of impacts between the rotor and the snubber ring. The present work will study a periodically excited system with soft impacts, which can represent a wide range of mechanical collisions. Here, soft impact, in contrast to hard impact [41], refers to a collision that has a finite nonzero contact time and the colliding body hits the obstacle modelled by a spring This type of soft impact is a representative model for mechanical collisions. Its nonlinearity brings complex phenomena into system's dynamics. For example, in [32], the motion of the impact oscillator with one-sided elastic constraint may experience a significant change due to a slight variation on its parameter when a grazing bifurcation is encountered. In addition, this thesis will study some impacting systems, such as the impact system with a drift and the piecewise-smooth capsule system with bidirectional drifts, which also have many complex phenomena induced by their nonlinearity.

2.2 Near-grazing dynamics

Analysing grazing events for nonsmooth systems is a challenging task [39]. In general, vibro-impact systems, such as ship mooring interactions [42], bearing looseness [43] and multi-degree-of-freedom impact oscillators [44], may have abundant coexisting attractors when grazing occurs. Here, “Grazing” refers to the scenario when the colliding body encounters the impact with zero transversal velocity. Near-by trajectories experience qualitatively different forces: some will not impact, others will have an impact with non-zero transversal velocity. When an attractor encounters a grazing event, it may change qualitatively (see e.g. [44–46]), which is called a *discontinuity-induced* (or, short, discontinuous or non-smooth) bifurcation. For insttance, Budd and Dux [47] studied grazing-induced intermittent chaotic behaviour for a impact oscillator, which shows that grazing bifurcations can result in intermittent chaotic behaviour with low velocity impacts followed by an irregular sequence of high velocity impacts. In [48], Normark presented that some periodic orbits can be found due to appearing of grazing bifurcations and gave the sufficient conditions for the existence of a periodic orbit for a type of impact systems. Nordmark [49] and Pavlovskaia *et al.* [50] analyse what dynamics occurs near grazing events. The textbook [39] classifies grazing bifurcations also for other piecewise-smooth systems. Their analysis find coexistence of multistable attractors, chaotic motions and vulnerable attractors, which can be easily perturbed by any variations of system parameters or any external disturbances. Detection of grazing events helps predicting the performance behavior of the impacting systems. For example, Lamba and Budd [51] studied the grazing bifurcation of an impacting system through calculating its Lyapunov exponents (LEs), and the bifurcation was observed as a jump in LEs. In [49], Normark investigated the grazing bifurcation of a single-degree-of-freedom oscillator subjected to a rigid amplitude constraint and the singularities caused by grazing impacts by controlling a system parameter. Normark showed that the grazing impact resulted in the apparence of a square root singularity. In [52] , Foale and Bishop studied grazing bifurcations for two different models of the impact oscillator, which cannot be classified by the usual bifurcation theory of smooth dynamical systems. In [38], Chin *et al.* showed that a simple impact oscillator with periodic excitation can present different types of grazing bifurcations. They presented numerical evidence that the observed discontinuous bifurcations were limits of standard bifurcations of smooth dynamical systems as the impact was hardened. In [53], Dankowicz and Zhao studied three different bifurcation scenarios associated with grazing conditions for a periodic response of an impact microactuator, a discontinuous jump to an impacting periodic response, a continuous transition to an impacting chaotic attractor and a discontinuous jump to an impacting chaotic attractor, by using the concept of discontinuity mappings. Furthermore, Ing *et al.* [32, 54] carried out experimental investigations on different bifurcation scenarios of an impact oscillator with a one-sided elastic constraint, leading to smooth (that is, classical) and non-smooth bifurcations. Previous works have presented the detailed complexities induced by near-grazing events. However, the above works did not mention how to avoid these complexities. Thus, introducing control methods to suppress them will be a focus of this thesis.

2.3 Control of coexisting attractors

Coexisting attractors or multistability widely exist in all areas of science and nature. For example, in engineering applications, such as an impact rig with two-sided constraint [55], electronic circuits [56, 57], gas laser [58] and drilling system [12], these systems are all present the multistability. From the biological aspect, multistability is also a fundamental property in many biological systems, such as spiking neurons[59], cancer progression [60], cell fate transitions [61, 62] and cell cycle control [63, 64]. A common feature of coexisting attractors is that the final state of the system crucially depends on the relevant initial conditions, which means that the initial conditions can decide the long-term dynamical behaviours related to one of the coexisting attractors. Since coexisting many attractors is a phenomenon describing that a dynamical system can present many long-term motions, studying the switching among these coexisting attractors can offer more flexibility and convenience on analysis for dynamical properties of a system with multistability. Therefore, developing a reliable method for achieving the control from one of the coexisting attractors to others can be necessary to achieve the above target.

As the mentioned above, many nonsmooth dynamical systems have the property of coexisting attractors or multistability. Due to this property, the dynamical reponses of nonsmooth dynamical systems can behave differently under different initial conditions. For example, in [1], Liu *et al.* presented that an impact oscillator with a one-sided elastic constraint near grazing is able to coexist different 4 attractors, which their dynamical properties have significant differences. While, since this system's basin has fractal basin boundary, any tiny differences in initial condition may result in the different motions. In [65], a vibro-impact capsule system can coexist forward and backward motion, which means that the capsule is able to move forward or backward direction under some initial conditions,.

Switching between coexisting attractors by control methods plays an essential role in studying the multistability of dynamical systems [22]. There are many methods to achieve the above targets. For example, it is well known that the OGY method [66] was initially developed for stabilising the chaotic attractor to an unstable periodic orbit embedded in a chaotic motion via adjusting the system parameter in a small area. After that, besides the OGY method, Pyragas [19] designed a delay feedback control to achieve the stabilisation of unstable periodic orbits of a chaotic system. Pyragas type delay feedback control has input $u(\tau)$ of the form

$$u(\tau) = K(y(\tau - \tau_d) - y(\tau)),$$

where $y(\tau)$ is some output of the system, τ is the time and τ_d is a time delay. The control's aim is to achieve the switching from one of its coexisting attractors to a target attractor. If τ_d is equal to the forcing period and the system with delay feedback control shows periodic motion with period τ_d, the control effort $u(\tau)$ is zero (hence, called *non-invasive*). This type of control has many important applications on controlling chaos. For example, in [67], Pyragas and Tamaševičius used the proposed delay feedback control method to stabilise the chaotic attractor to the unstable attractor on an analogue circuit. In [67], Pyragas *et al.* controlled a chaotic electronic oscillator successfully by using the time-delayed feedback controller. In [68], a modified delay feedback control using the act-and-wait concept was proposed to reduce the dimension of phase space of the time-delayed feedback systems. Yamasue *et al.* [69] used time-delayed feedback control to stabilise irregular and non-periodic cantilever oscillations in amplitude modulation atomic force microscopy experiments.

The above methods focus on stabilising the system with chaotic motions to the coexisting unstable periodic attractors, which are embedded into the chaotic attractor. For the control of coexisting stable attractors, these methods and their concepts also can be useful. For example, Lai [21] constructed a hierarchy of paths to the desired attractor by introducing a feedback perturbation which is generated by the similar idea with the OGY method, for the system with fractal basin boundaries in the phase space. However, Lai's method might not be successful since the initial condition is far away from the basin boundary. In [18], Martínez-Zérega *et al.* presented that the delay feedback control can achieve the control of coexisting attractors of the logistic map. Besides that, there are many other methods for controlling multistability. In [23], Pisarchik and Goswami studied that one of the coexisting states can be annihilated by applying a slow external periodic perturbation to a system parameter. Arecchi *et al.* [70] discovered that external noise could bridge two states of Duffing oscillator. In [20], Jiang adopted a feedback-type drivings to achieve the switch among different stable trajectories of the dynamical systems with multistability. Through modifying the above control method, an intermittent control was designed to give an impulsive force to control the one attractor to others by introducing the information of the desired attractor as the target, and does not change the structure of the system's basins of attraction [71]. In [72], Wang *et al.* presented that the control principle based on bifurcation can be used for controlling the multistability of complex networks. In details, through adjusting the parameters, the controlled system can move to the basin of the desired attractor and then converge to the desired attractor after returning the parameters to the original value. However, this method needs large amount of computations on controlling coexisting attractors of relatively large dynamical networks by multiple parameter perturbation. For the similar system, Cornelius *et al.* [73] proposed a realistic control method, which introduces a perturbation based on the information from the desired attractor, to the system's states.

Multistable impact motions may have negative effects [74], such as degrading efficiency or reducing service life for the system, which should be avoided. Control of multistable impact motions, especially the near-grazing dynamics, has been studied extensively by many researchers in the past decade. For example, the linear augmentation feedback control law was adopted to control switching between coexisting attractors in a soft impacting system [1]. De Souza *et al.* used both, a perturbation method [75] and a feedback damping controller [76], to control chaotic attractors in an impacting system. The intermittent control method proposed by Liu *et al.* [71] can switch between coexisting attractors of the soft impact oscillator. A class of control strategies was developed by Dankowicz *et al.* [77–79] to ensure the persistence of desired attractors near the grazing bifurcation of an impact oscillator. Veldman *et al.* [80] introduced an impulsive control method to bring a single-degree-of-freedom system from an undesired to a desired attractor.

2.4 Dynamical systems with delay

In many applications [81–84, 11, 85] arise differential equations in which the derivative of the unknown functions at a certain time depends on the value of the function at previous time. These are so-called delay differential equations (DDEs). Delay differential equations (DDEs) are widely used in physical, mechanical, and biological systems to simulate the time delay phenomena caused by human observer [86], feedback control [87], actuation [88], and communication [89]. With the introduction of time delay in differential equations, the model can be more accurate for predicting the real system. For example, Zhang *et al.* [83] studied a delay pest control model which was a high-dimensional differential equation with impulsive effects at different fixed impulse times. In [84], Carvalho and Pinto used a mathematical model with delay to describe the dynamics of AIDS- related cancers with the treatment of HIV and chemotherapy. In [11], Yan *et al.* used the basin of a time-delayed system modelling cutting process to determine the unsafe cutting zone. On the other hand, time delay is sometimes artificially introduced to the system for control purposes. For example, constant maturation time delay, pulse pesticide input, and pulse harvesting prey may have obvious effects on the predator-prey model with stage-structure for pests [83]. Pyragas [19] proposed to use the famous delay self-controlling feedback for chaos control, which does not require a priori analytical knowledge of the system dynamics and are applicable to experiment. The above studies are concerned with smooth DDEs. The analysis of nonsmooth DDEs is more challenging due to infinite-dimensional nature and nonsmooth property. In principle, in order to analyse the basic property of DDEs, a DDE could be approximated by a high-dimensional ODE, which can be linearised along trajectories obtained by numerical integration [90]. For example, Repin [91] proposed a system of ODEs to approximate a DDE through a first-order approximation of the original solution, currently referred to as the *chain method*. Later on, Gyori and Turi [92] proved the uniform convergence of this method for a DDE in an infinite interval. In [93], Westdal and Lehn proposed the time optimal control by approximating the linear time invariant differential-difference system. Hess [94] used this method to approximate the linear differential equation with a large time delay. Further improvements of the numerical approach proposed in [91] were introduced in the work by Banks [95]. This numerical framework was later employed by Lipták *et al.* [96] to study delay chemical reaction networks.

Until now, there are very few systematic studies regarding to nonsmooth DDEs. While, the available general-purpose computational tools for the numerical treatment of smooth DDEs are rather limited, and almost nonexistent for piecewise-smooth DDEs, specially for numerical bifurcation analysis. Therefore, while a number of software packages have been developed for numerical continuation in smooth DDEs (e.g. DDE-BIFTOOL [97, 98], PDDE-

CONT [99] and Knut [100]), no software package of this kind exists for the path-following analysis of piecewise-smooth DDEs. In addition, as mentioned above, piecewise-smooth dynamical systems have received considerable attention in the past, mainly due to their crucial role played in understanding complex nonsmooth phenomena. For instance, in the study of piecewise linear suspension bridge model [101], the model of a DC-DC buck converter [102], and the recurrent dynamics of human gait system [103]. For the bifurcation analysis of this type of systems, a number of continuation tools have been developed in the past, for instance, TC-HAT [28], SlideCont [104] and the multi-segment continuation capability included in COCO [25]. However, when time delay is introduced, there is no continuation software available to carry out bifurcation studies via path-following routines. In the past, however, a solid numerical framework has been proposed for this task (see e.g. [105, 106, 27]), but the related codes are not yet available in a user friendly and general-purpose form.

2.5 Calculation of Lyapunov exponents

The LE of a trajectory is a quantity that characterises the rate of separation of infinitesimally near-by trajectories [107]. It determines a notion of sensitivity of this trajectory to perturbations in initial conditions. If the largest LE, which is referred to the maximal LE, is greater than zero, any small perturbation of the initial condition will result in an exponential divergence of the resulting perturbed trajectory until the distance between the perturbed and unperturbed trajectories is no longer small. This sensitivity with respect to initial condition is one of the defining features of chaos. If the LEs are identical for typical trajectories of an attractor in a dynamical system, one speaks of the LE for this attractor (or this dynamical system). The LE indicates predictability (or lack of it) for dynamical systems, such that it is considered as an important tool for studying the stability of dynamical systems. Therefore, the development of an efficient method for calculating the LEs of dynamical system is an active area of research, see e.g. [108–115]. For finite-dimensional dynamical systems Benettin *et al.* [109] introduced a systematic method for estimating the LEs of smooth dynamical systems. Wolf *et al.* [110] developed a method for extracting the largest LE from an experimental time series. For nonsmooth systems, Müller [113] developed a model-based algorithm to calculate the LEs of nonlinear dynamical systems with discontinuities. They found that the required linearised equations must be supplemented by certain transition conditions when crossing the discontinuities. In [114], Dellago *et al.* generalised Benettin's classical algorithm and applied it to the case of dynamical systems where smooth streaming was interrupted by a differentiable map at discrete times. Lamba and Budd [51] have shown that the largest LE has a discontinuous jump at grazing bifurcations in Filippov systems and scales like $1/|\ln \varepsilon|$, where ε is the bifurcation parameter. These works focused on computing LEs for finite dimensional systems. However, the methods for the finite dimensional systems are hard to be implemented directly to DDEs that have infinite dimensions. Obviously, in contrast to ordinary differential equations (ODEs), the computation of LEs for nonsmooth DDEs is more complex due to the discontinuities and high dimensionality. In principle, a DDE could be approximated by a high-dimensional ODE, which can be linearised along trajectories obtained by numerical integration [90], such that the LEs can be constructed for the Poincaré map. Studies by Repin [116] and Györi and Turi [92] have shown that DDEs can be analysed using approximating high-dimensional ODEs. However, if the delay time is large, calculating the LEs of nonsmooth DDEs needs to store excessive history data points during delay period compared to smooth DDEs [117–119], e.g. the data at past encounters of the discontinuity. In this case the global convergence of the system cannot be guaranteed. Therefore, it may cause inaccuracy in calculating the eigenvalues of Jacobian matrix which is used for estimating the LEs of nonsmooth DDEs.

2.6 Conclusion

In this chapter, an organised overview of the techniques for the control of coexisting attractors and the investigation of characteristics of nonsmooth dynamical systems was presented. It is clear that the control of coexisting attractors in nonsmooth dynamical systems is a challenging and complex task due to the complex dynamics and the lack of a systematic study on the dynamical characteristics during the control process. Meanwhile, many methods on controlling coexisting attractors have been presented showing good performance. However, with the consideration of different application scenarios of nonsmooth dynamical systems, control of coexisting attractors has many new requirements, which were rarely studied in the previous works. For example, one may have limited information of the desired attractor, or sometimes may require using the properties of the original system rather than the external inputs to achieve the switching between the two coexisting attractors in the presence of a large distance on their basins of attraction. Thus, based on those of different requirements, new control methods are needed. In order to address this issue, the delay feedback control and a new control method based on adjusting system parameter will be introduced into the piecewise-smooth dynamical systems. Besides that, the dynamics of the controlled nonsmooth dynamical systems under the delay feedback control is complex, and there exists so far no dedicated numerical methods to carry out numerical analysis for such type of systems. Without the numerical methods, it is hard to analyse the dynamical responses of nonsmooth dynamical systems during the control process. Thus, developing new numerical methods to carry out above analyses will also be considered in this thesis.

Section 2.1 gives the detailed review of the dynamical properties and applications of nonsmooth dynmaiclal systems. Since the grazing events is widely existing in many nonsmooth dynamical systems, the relevant phenomena and dynamical properties are outlined in Section 2.2. Following that, in Section 2.3, the background of coexisting attractors and its control problems are introduced. Since at the following chapters the delay feedback control and analysis tools for DDEs will be studied, the review of DDEs is discussed in Section 2.4. Finally, Section 2.5 reviews the calculating methods of LEs.

Chapter 3

Mathematical models of nonsmooth dynamical systems

3.1 Introduction

The aim of this chapter is to introduce some piecewise impact mathematical models corresponding to the different applications, which will be detailed at the following. It is well-known that impacting systems are very common and important components in many engineering applications, such as self-propelled capsule systems [5, 6], rotor systems [7], mechanical bearings [10], manufacturing cutting [11], and oil and gas drilling [12–14]. For Impacting systems, there are many complex nonlinear phenomena, e.g. chaotic motion, multistability, and grazing and sliding events [39], which can have significant effects on the performance of engineering systems.

In this chapter, it includes three impact models: a soft impact system, an impact system with a drift and a vibro-impact capsule system.

3.2 Soft impact system

The soft impact system shown in Fig. 3.2.1 represents a mechanical system encountering intermittent so-called soft impacts, which will be studied in the present work. Soft impacts occur in mechanical systems when an object hits an obstacle of negligible mass but non-negligible stiffness. In Fig. 3.2.1 the object is modelled by the block of mass m and the obstacle is modelled by the spring with stiffness k_2 (a *backlash* spring). The collision occurs when the distance G between block and spring reaches 0. Since at impact the spring is relaxed, the forces in the system depend continuously on G (and, hence, on the position y of the block), but the spring constants exerted by the backlash spring are discontinuous: 0 for $g > 0$, k_2 for $g \leq 0$. Hence, the operation of mass can be divided into 2 phases.

- There is no contact between the mass and the right spring. The dynamics of system can be described as a differential equation

$$m\ddot{y} = mA\omega^2 \sin \omega t - c\dot{y} - k_1 y, \tag{3.2.1}$$

- When the mass and the right spring are in contact, the dynamics of system can be described as a differential equation

$$m\ddot{y} = mA\omega^2 \sin \omega t - c\dot{y} - k_1 y - k_2(y - G), \tag{3.2.2}$$

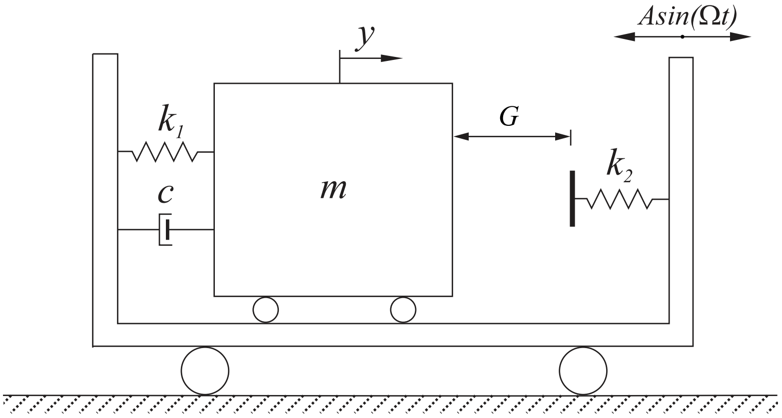

Fig. 3.2.1 Physical model of the soft impact system [1].

Based on the following nondimensional variables and system parameters:

$$\omega_n = \sqrt{\frac{k_1}{m}}, \qquad \tau = \omega_n t, \qquad \omega = \frac{\Omega}{\omega_n}, \qquad \zeta = \frac{c}{2m\omega_n},$$
$$x = \frac{y}{y_0}, \qquad e = \frac{G}{y_0}, \qquad a = \frac{A}{y_0}, \qquad \beta = \frac{k_2}{k_1},$$

where $y_0 > 0$ is an arbitrary reference distance, ω_n is the natural angular frequency of the mass-spring system (m, k_1 in Fig. 3.2.1), ω is the ratio between forcing and natural frequency, β is the stiffness ratio, ζ is the damping ratio, and a is the nondimensionalised forcing amplitude, the nondimensional equations of motion of the soft impact system can be written in a compact form as below [32],

$$\begin{cases} x'(\tau) = & v(\tau), \\ v'(\tau) = & a\omega^2 \sin(\omega\tau) - 2\zeta v(\tau) - x(\tau) - \beta(x(\tau) - e)H(x(\tau) - e), \end{cases} \tag{3.2.3}$$

where $H(\cdot)$ stands for the Heaviside step function and x', v' denote differentiation with respect to the nondimensional time τ. The discontinuity boundary is fixed at $x = e$, with $e > 0$ being the nondimensional gap to the rest point of the linear spring.

3.3 Impact system with a drift

A simple two degree-of-freedom system introduced by Pavlovskaia *et al.* [2, 4, 120], as shown in Fig. 3.3.1, presents that mass M driven by an external force progresses when the threshold of the dry friction P_f is smaller than the force acting on the slider exceeds. The external force acting on mass M consists of amplitude P_d, frequency Ω and phase shift ϕ, and a static component P_s. In Fig. 3.3.1, the absolute displacements of the slider bottom, slider top and mass are denoted by X_b, X_t, X_m respectively. G represents the gap between the mass and the slider top, and its value may be positive, negative, or equal to zero. When $G > 0$, the mass moves freely without any interaction with the slider. When $G = 0$, the mass just touches the slider top, but there is not any compression in the slider spring. Finally, when $G < 0$, the slider is compressed. Hence, the operation of mass can be divided into 3 phases.

- There is no contact between the mass and the slider. The dynamics of the system can be described as a differential equation

$$\begin{aligned} &m\ddot{X}_m = P_s + P_d \cos(\Omega t + \phi), \\ &c(\dot{X}_t - \dot{X}_b) + k(X_t - X_b) = 0, \\ &\dot{X}_b = 0. \end{aligned} \tag{3.3.1}$$

- When the mass and the slider are in contact and moving oscillatory without progression, the dynamics of the system can be described as a differential equation

$$\begin{aligned} &m\ddot{X}_m + c(\dot{X}_t - \dot{X}_b) + k(X_t - X_b) = P_s + P_d \cos(\Omega t + \phi), \\ &\dot{X}_b = 0. \end{aligned} \tag{3.3.2}$$

- When the mass and the slider are progressing, the dynamics of system can be described as a differential equation

$$\begin{aligned} m\ddot{X}_m &= -P_f + P_s + P_d\cos(\Omega t + \phi), \\ c(\dot{X}_t - \dot{X}_b) + k(X_t - X_b) &= P_f. \end{aligned} \tag{3.3.3}$$

In addition, for Eq. (3.3.2) and (3.3.3), X_t and X_m satisfy that

$$X_t = X_m - G.$$

In order to discuss conveniently, the above three phases can be denoted as: (i) **No contact**, (ii) **Contact without progression** and (iii) **Contact with progression**.

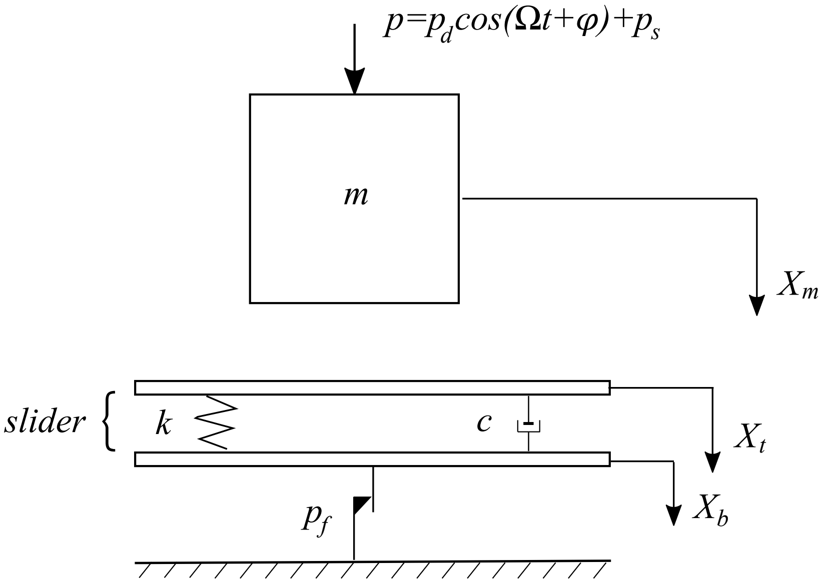

Fig. 3.3.1 Physical model of the impact system with a drift [2].

Based on the following nondimensional variables:

$$\tau = \Omega_0 t,\ x = \frac{k}{P_{max}} X_m,\ y = \frac{dx}{d\tau} = \frac{k}{\Omega_0 P_{max}} \dot{X}_m,\ z = \frac{k}{P_{max}} X_t,\ \bar{v} = \frac{k}{P_{max}} X_b,$$

and parameters:

$$\omega = \frac{\Omega}{\Omega_0},\ \Omega_0 = \sqrt{\frac{k}{m}},\ a = \frac{P_d}{P_{max}},\ b = \frac{P_s}{P_{max}},\ d = \frac{P_f}{P_{max}},\ \xi = \frac{c}{2m\Omega_0},\ g = \frac{k}{P_{max}} G,$$

where P_{max} is a normalization constant force, the relevant nondimensional system can be described as the following:

- **No contact**, i.e. $x < z + g$. This phase means that the mass and the slider top move separately, since the mass does not contact the slider top. Then, the motions of the mass, the top and bottom of slider are:

$$\begin{aligned}
x' &= y,\\
y' &= a\cos(\omega\tau + \phi) + b,\\
z' &= -\frac{1}{2\xi}(z - \bar{v}),\\
\bar{v}' &= 0,
\end{aligned} \tag{3.3.4}$$

- **Contact without progression**, i.e. $x \geq z + g$ and $0 < 2\xi z' + (z - \bar{v}) < 1$. This phase means that the mass has a contact with the top of slider, but the force acting on mass is larger than zero. Meanwhile, the threshold of the dry friction force is greater than the force on mass. Hence, the mass and the top of slider are moving together without any progression, and the bottom of the slider remains stationary. Then, the motions of the mass, the top and bottom of slider are:

$$\begin{aligned}
x' &= y,\\
y' &= -2\xi z' - (z - \bar{v}) + a\cos(\omega\tau + \phi) + b,\\
z' &= x',\\
x &= z + g,\\
\bar{v}' &= 0,
\end{aligned} \tag{3.3.5}$$

- **Contact with progression**, i.e. $x \geq z + g$ and $2\xi z' + (z - \bar{v}) \geq 1$. This means that the mass has a contact with the top of slider and the force acting on mass is greater than the threshold of dry friction force. Then, the motions of the mass, the top and bottom of slider are:

$$\begin{aligned}
x' &= y,\\
y' &= a\cos(\omega\tau + \phi) + b - 1,\\
z' &= x',\\
x &= z + g,\\
\bar{v}' &= z' + \frac{1}{2\xi}(z - \bar{v} - 1),
\end{aligned} \tag{3.3.6}$$

The impact system with a drift can presented many different periodic and chaotic motions. It is difficult to study some dynamical properties of this system in a standard way, due to the problem of the motion unboundeness. To overcome this difficulty, in [4], Pavlovskaia and Wiercigroch adopted a simple co-ordinates transformation to ensure the boundedness of this system, which offers a possibility to analyse the dynamical properties in a standard way. At the following discussion, this transformation, i.e. $p := x - \bar{v}$ and $q := z - \bar{v}$, also will be adopt to rewrite system as following:

- **No contact**, i.e. $p < q + g$.

$$\begin{aligned} p' &= y, \\ y' &= a\cos(\omega\tau + \phi) + b, \\ q' &= -\frac{1}{2\xi}(q), \end{aligned} \tag{3.3.7}$$

- **Contact without progression**, i.e. $p \geq q + g$ and $0 < 2\xi y + q < 1$.

$$\begin{aligned} p' &= y, \\ y' &= -2\xi y - q + a\cos(\omega\tau + \phi) + b, \\ q' &= y, \end{aligned} \tag{3.3.8}$$

- **Contact with progression**, i.e. $p \geq q + g$ and $2\xi y' + q \geq 1$.

$$\begin{aligned} p' &= -\frac{1}{2\xi}(q - 1), \\ y' &= a\cos(\omega\tau + \phi) + b - 1, \\ q' &= -\frac{1}{2\xi}(q - 1), \end{aligned} \tag{3.3.9}$$

According to the above transformation, the stability, chaotic property and multistability can be observed clearly from the above new system. At the following chapters, the system described by Eq. (3.3.7), (3.3.8) and (3.3.9) will be used to study the stability and control of coexisting attractors of the impact system with a drift.

3.4 Vibro-impact capsule system

In this section, a two degree-of-freedom system introduced by Liu *et al.* [3] in Fig. 3.4.1 is considered. In details, there is a movable internal mass m_1, which is driven by an external harmonic force with amplitude P_d and frequency Ω. The internal mass m_1 interacts with a rigid capsule m_2 by a linear spring with stiffness k_1 and a viscous damper with damping coefficient c. The absolute displacements of the internal mass and the capsule separately denote by X_1 and X_2. At the right hand side of the rigid capsule, there is a weightless plate connecting to the capsule by a secondary linear spring with stiffness k_2. When the relative displacement $X_1 - X_2$ is larger than or equal to the gap G, the weightless plate can be hit by the internal mass m_1. The capsule starts to moving forward or backward until the force acting on the capsule exceeds the threshold of the dry friction force P_f between the capsule and supporting surface.

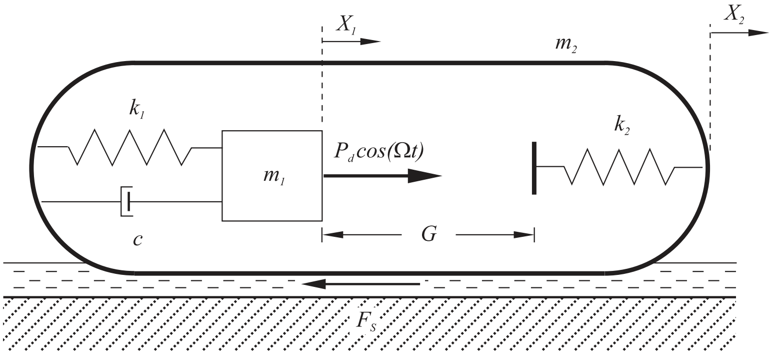

Fig. 3.4.1 Physical model of the vibro-impact capsule system [3].

At the following discussion, Coulomb friction model is considered to calculate the frictional force between the capsule and the sliding surface

$$f = \begin{cases} 0, \ \dot{X}_2 = 0 \\ -sign(\dot{X}_2) \cdot P_f, \ \dot{X}_2 \neq 0, \end{cases} \tag{3.4.1}$$

where $P_f = \mu(m_1 + m_2)g$, μ is the friction coefficient between the capsule and the supporting surface, and g is the acceleration resulted by gravity. The operation of the system can be divided into 4 phases.

- If there is no contact between the mass m_1 and the plate, i.e. $X_1 - X_2 < G$, and the threshold of the dry friction force is larger than the force acting on the capsule from the internal mass, i.e, $|k_1(X_2 - X_1) + c(\dot{X}_2 - \dot{X}_1)| < P_f$, which means that the capsule is stationary, the dynamics of the internal mass and capsule can be described as

$$m_1\ddot{X}_1 = P_d\cos(\Omega t) + k_1(X_2 - X_1) + c(\dot{X}_2 - \dot{X}_1), \tag{3.4.2}$$

$$\dot{X}_2 = 0. \tag{3.4.3}$$

- If there is no contact between the mass m_1 and the plate, i.e. $X_1 - X_2 < G$, and the capsule is moving, the dynamics of the internal mass can be described as Eq. (3.4.2) and the capsule can be described as

  $$m_1\ddot{X}_2 = -\operatorname{sign}(\dot{X}_2)\cdot P_f - k_1(X_2 - X_1) - c(\dot{X}_2 - \dot{X}_1). \tag{3.4.4}$$

  It is necessary to point out that the dry friction force acting on the capsule has an opposite direction with the force acting on the capsule, when the dry friction force is just equal to the threshold of the dry friction force, i.e. $|k_1(X_2 - X_1) + c(\dot{X}_2 - \dot{X}_1)| = P_f$ and the capsule begins to move. At this moment, the dry friction force can be described as

  $$f = -\operatorname{sign}(k_1(X_2 - X_1) + c(\dot{X}_2 - \dot{X}_1))\cdot P_f. \tag{3.4.5}$$

- If there is a contact between the mass m_1 and the plate, i.e. $X_1 - X_2 \geq G$, and the threshold of the dry friction force is larger than the force acting on the capsule from the internal mass, i.e, $|k_1(X_2 - X_1) + c(\dot{X}_2 - \dot{X}_1) - k_2(X_1 - X_2 - G)| < P_f$, which means that the capsule is stationary, the dynamics of the internal mass and capsule can be described as

  $$m_1\ddot{X}_1 = P_d\cos(\Omega t) + k_1(X_2 - X_1) + c(\dot{X}_2 - \dot{X}_1) - k_2(X_1 - X_2 - G), \tag{3.4.6}$$

  $$\dot{X}_2 = 0. \tag{3.4.7}$$

- If there is a contact between the mass m_1 and the plate, i.e. $X_1 - X_2 \geq G$, and the capsule is moving, the dynamics of the internal mass can be described as Eq. (3.4.6) and the capsule can be described as

  $$m_1\ddot{X}_2 = -\operatorname{sign}(\dot{X}_2)\cdot P_f - k_1(X_2 - X_1) - c(\dot{X}_2 - \dot{X}_1) + k_2(X_1 - X_2 - G). \tag{3.4.8}$$

  Also, it should point out that the dry friction force acting on the capsule has an opposite direction with the force acting on the capsule, when the dry friction force is just equal to the threshold of the dry friction force, i.e. $|k_1(X_2 - X_1) + c(\dot{X}_2 - \dot{X}_1) - k_2(X_1 - X_2 -$

$G)| = P_f$ and the capsule begins to move. In this moment, the dry friction force can be described as

$$f = -\operatorname{sign}(k_1(X_2 - X_1) + c(\dot{X}_2 - \dot{X}_1) - k_2(X_1 - X_2 - G)) \cdot P_f. \tag{3.4.9}$$

In order to discuss conveniently, the above four phases can be denoted as: (i) **No contact with stationary capsule**, (ii) **Contact with moving capsule**, (iii) **Contact with stationary capsule** and (iv) **Contact with moving capsule** .

Based on the following nondimensional variables:

$$\tau = \Omega_0 t,\ x_i = \frac{k_1}{P_f} X_i,\ y_i = \frac{dx_i}{d\tau} = \frac{k_1}{\Omega_0 P_f} \dot{X}_i,\ \dot{y}_i = \frac{dy_i}{d\tau} = \frac{k_1}{\Omega_0^2 P_f} \ddot{X}_i,$$

and parameters:

$$\Omega_0 = \sqrt{\frac{k_1}{m_1}},\ \omega = \frac{\Omega}{\Omega_0},\ \alpha = \frac{P_d}{P_f},\ \delta = \frac{k_1}{P_f} G,\ \beta = \frac{k_2}{k_1},\ \xi = \frac{c}{2m\Omega_0},\ \gamma = \frac{m_2}{m_1}.$$

where $i = 1, 2$, the relevant nondimensional system can be described as the following:

- **No contact with stationary capsule**, i.e. $x_1 - x_2 < \delta$, and $|(x_2 - x_1) + 2\xi(y_2 - y_1)| \leq 1$. This phase means that the mass does not contact with the plate and the force acting on the capsule is smaller or equal to threshold of the dry friction force. Then, the motions of the mass and capsule are:

  $$\begin{aligned} \dot{x}_1 &= y_1, \\ \dot{y}_1 &= \alpha\cos(\omega\tau) + (x_2 - x_1) + 2\xi(y_2 - y_1), \\ \dot{x}_2 &= 0, \\ \dot{y}_2 &= 0, \end{aligned} \tag{3.4.10}$$

  When the capsule begins to move and the force acting on the capsule just equals to the threshold $|(x_2 - x_1) + 2\xi(y_2 - y_1)| = 1$, the direction of the dry friction force is opposite to the elastic force acting on the capsule, which can be illustrated as $-\operatorname{sign}((x_2 - x_1) + 2\xi(y_2 - y_1))$.

- **No contact with moving capsule**, i.e. $x_1 - x_2 < \delta$, and $|(x_2 - x_1) + 2\xi(y_2 - y_1)| > 1$. This phase means that the mass does not contact with the plate and the force acting on the capsule is larger than the threshold of the dry friction force. Then, the motions of the mass and capsule are:

$$\begin{aligned}
\dot{x}_1 &= y_1, \\
\dot{y}_1 &= \alpha\cos(\omega\tau) + (x_2 - x_1) + 2\xi(y_2 - y_1), \\
\dot{x}_2 &= y_2, \\
\dot{y}_2 &= [-\operatorname{sign}(y_2) - (x_2 - x_1) - 2\xi(y_2 - y_1)]/(\gamma),
\end{aligned} \tag{3.4.11}$$

- **Contact with stationary capsule**, i.e. $x_1 - x_2 \geq \delta$, and $|(x_2 - x_1) + 2\xi(y_2 - y_1) - \beta(x_1 - x_2 - \delta)| \leq 1$. This phase means that the mass is contacting with the plate and the force acting on the capsule is smaller or equal to the threshold of the dry friction force. Then, the motions of the mass and capsule are:

$$\begin{aligned}
\dot{x}_1 &= y_1, \\
\dot{y}_1 &= \alpha\cos(\omega\tau) + (x_2 - x_1) + 2\xi(y_2 - y_1) - \beta(x_1 - x_2 - \delta), \\
\dot{x}_2 &= 0, \\
\dot{y}_2 &= 0,
\end{aligned} \tag{3.4.12}$$

  It is necessary to point out that when the capsule begins to move and the force on the capsule is just equal to the threshold of dry friction (i.e. $|(x_2 - x_1) + 2\xi(y_2 - y_1) - \beta(x_1 - x_2 - \delta)| = 1$), the relation between the direction of the dry friction force and the force acting on the capsule from the springs and damper can be represented as $-\operatorname{sign}((x_2 - x_1) + 2\xi(y_2 - y_1) - \beta(x_1 - x_2 - \delta))$.

- **Contact with moving capsule**, i.e. $x_1 - x_2 \geq \delta$, and $|(x_2 - x_1) + 2\xi(y_2 - y_1) - \beta(x_1 - x_2 - \delta)| > 1$. This phase means that the mass is contacting with the plate and the force acting on the capsule is larger than the threshold of the dry friction force. Then, the motions of the mass and capsule are:

$$\begin{aligned}
\dot{x}_1 &= y_1, \\
\dot{y}_1 &= \alpha\cos(\omega\tau) + (x_2 - x_1) + 2\xi(y_2 - y_1) - \beta(x_1 - x_2 - \delta), \\
\dot{x}_2 &= y_2, \\
\dot{y}_2 &= [-\operatorname{sign}(y_2) - (x_2 - x_1) - 2\xi(y_2 - y_1) + \beta(x_1 - x_2 - \delta)]/\gamma.
\end{aligned} \tag{3.4.13}$$

Similarly to the impact system with a drift, the above capsule system also has a problem of the motion unboundedness. It is necessary to adopt the similar idea from the impact system with a drift to change the above capsule system. Assuming that $\upsilon := x_1 - x_2$ and $\kappa := y_1 - y_2$, the above capsule system can be written as:

- **No contact with stationary capsule**, i.e. $\upsilon < \delta$, and $|\upsilon + 2\xi\kappa| \leq 1$,

$$\begin{aligned}
\dot{\upsilon} &= y_1, \\
\dot{\kappa} &= \alpha\cos(\omega\tau) - \upsilon - 2\xi\kappa, \\
\dot{y}_1 &= \alpha\cos(\omega\tau) - \upsilon - 2\xi\kappa, \\
\dot{y}_2 &= 0.
\end{aligned} \tag{3.4.14}$$

- **No contact with moving capsule**, i.e. $\upsilon < \delta$, and $|\upsilon + 2\xi\kappa| > 1$,

$$\begin{aligned}
\dot{\upsilon} &= \kappa, \\
\dot{\kappa} &= \alpha\cos(\omega\tau) - \upsilon - 2\xi\kappa - (-\operatorname{sign}(y_2) + \upsilon + 2\xi\kappa)/(\gamma), \\
\dot{y}_1 &= \alpha\cos(\omega\tau) - \upsilon - 2\xi\kappa, \\
\dot{y}_2 &= [-\operatorname{sign}(y_2) + \upsilon + 2\xi\kappa]/(\gamma).
\end{aligned} \tag{3.4.15}$$

- **Contact with stationary capsule**, i.e. $\upsilon \geq \delta$, and $|\upsilon + 2\xi\kappa - \beta(\upsilon - \delta)| \leq 1$,

$$\begin{aligned}
\dot{\upsilon} &= y_1, \\
\dot{\kappa} &= \alpha\cos(\omega\tau) - \upsilon - 2\xi\kappa - \beta(\upsilon - \delta), \\
\dot{y}_1 &= \alpha\cos(\omega\tau) - \upsilon - 2\xi\kappa - \beta(\upsilon - \delta), \\
\dot{y}_2 &= 0.
\end{aligned} \tag{3.4.16}$$

- **Contact with moving capsule**, i.e. $\upsilon \geq \delta$, and $|\upsilon + 2\xi\kappa - \beta(\upsilon - \delta)| > 1$,

$$\begin{aligned}
\dot{\upsilon} &= \kappa, \\
\dot{\kappa} &= \alpha\cos(\omega\tau) - \upsilon - 2\xi\kappa - \beta(\upsilon - \delta) - [-\operatorname{sign}(y_2) + \upsilon + 2\xi\kappa + \beta(\upsilon - \delta)]/\gamma, \\
\dot{y}_1 &= \alpha\cos(\omega\tau) - \upsilon - 2\xi\kappa - \beta(\upsilon - \delta), \\
\dot{y}_2 &= [-\operatorname{sign}(y_2) + \upsilon + 2\xi\kappa + \beta(\upsilon - \delta)]/\gamma.
\end{aligned} \tag{3.4.17}$$

According to the above transformation, the stability, chaotic property and multistability can be observed clearly from the above new system. At the following chapters, the system described by Eq. (3.4.14), (3.4.15), (3.4.16) and (3.4.17) will be used to study the stability and control of coexisting attractors of the vibro-impact capsule system.

3.5 Conclusion

In this section, three different nonsmooth dynamical systems were introduced. Their nonsmooth properties can introduce many complex phenomena, such as coexisting attractors (multistability), grazing bifurcations, and chaotic motions. Among these phenomena, the coexisting attractors and grazing bifurcation are the main concerns of this work. In order to suppress the complexity, in the following sections, the delay feedback control will be considered to control the above three nonsmooth dynamical systems, and a new control method also will be studied. In addition, it is important to analyse how the control methods can affect the dynamics of the above three systems. In order to address this problem, a new numerical method and an algorithm will be developed to study the dynamical characteristics of the controlled nonsmooth dynamical systems.

Chapter 4

A numerical approach for bifurcation analysis of nonsmooth delay differential equations

4.1 Introduction

In fact, for the Piecewise-smooth dynamical systems with delay terms, there is no continuation software available to carry out bifurcation studies via path-following routines. In order to study the dynamical properties of these systems, a new numerical scheme has to be considered. It is well-known that many engineering applications experiencing repeated collisions at their mechanical parts can be represented using a soft-impact model as the one considered here, where the discontinuity boundary is neither motion- nor time-dependent but fixed at a constant. One of the main questions in such mechanical scenarios is to identify parameter values that allows the user to drive the system from impacting to non-impacting system responses and viceversa, in a controllable and reliable manner. In order to answer the above question, an approximation method for nonsmooth DDEs will be proposed to carry out the numerical bifurcation analysis of the system dynamics via numerical continuation.

The chapter is organised as follows. Section 4.2 presents the basic mathematical framework for the study of dynamical systems with delay, as well as a detailed development of the numerical approach to approximate their solutions via systems of ODEs of large dimension. In Section 4.3, the physical and mathematical description of the soft impact system is presented, together with its formulation as a hybrid dynamical system and numerical approximation considering the delay feedback controller. After that the system is analysed numerically via the continuation software COCO in Section 4.4. This part also includes some preliminary numerical tests regarding the approximation properties of the proposed numerical scheme. Finally, the main conclusions of the present work are given in Section 4.5.

4.2 Approximation of delay differential equations

As mentioned before, the main goal of the present work is to develop a numerical approach in order to analyse nonsmooth DDEs via path-following (continuation) methods. Numerical continuation is a well-established technique that permits an in-depth analysis of a system dynamics, under parameter variations. In particular, it allows tracing certain invariant sets (such as equilibria, periodic orbits, homoclinic orbits, etc.) as selected system parameters vary, usually via a predictor-corrector approach [121]. For ODEs there is a variety of software packages that are widely used for numerical continuation in such class of models, for example AUTO [122], CONTENT [123] and MATCONT [99], among many others. On the other hand, software tools for piecewise-smooth systems are much less abundant, being SLIDECONT [104], TC-HAT [28] and COCO [25] essentially the only available in the field. Similarly, path-following software for (smooth) DDEs have received relatively little attention in the literature, with the packages DDE-BIFTOOL [97] and PDDE-CONT [99] being the most widely used tools for such type of models.

Right now, there is no software package able to perform numerical continuation for DDEs considering nonsmooth phenomena, such as impacts, switches, impulses, etc. Numerical continuation of periodic solutions in piecewise-smooth DDEs has been carried out by Barton [124], where the author combines the mathematical framework designed for hybrid dynamical systems [28] with a multi-point boundary-value problem that is then embedded in a numerical continuation setting, whose applicability is illustrated in four different examples. From this work, however, no software packages or codes have been made available for general applications. Another approach for dealing with nonsmooth DDEs consists in substituting Heaviside and sign functions by a tanh function with certain calibrating parameters to adjust the desired degree of approximation to the original functions [105, 99, 106]. After the replacements have been made, the original system is turned into a smooth DDE for which any of the continuation tools mentioned in the previous paragraph can be applied. This approach, however, presents some limitations, especially when the considered orbit possesses a nontrivial *solution signature* [28, 124]. In addition, this technique cannot be applied when the DDE considers impulsive perturbations, and also it does not allow the study of dynamical phenomena inherent to nonsmooth systems, such as grazing and sliding events. Therefore, the subsection studies a different approach, consisting in approximating a DDE via large systems of ODEs, in combination with the mathematical formulation for hybrid dynamical systems, which then allows the application of any of the software tools mentioned above, designed for nonsmooth dynamical systems.

4.2.1 Basic mathematical setup

Delay differential equations can be considered as dynamical systems of infinite dimension, where the present state depends also on values in the past [125–127]. Such systems are usually defined over the Banach space of continuous functions $C([-\tau_{\max}, 0], \mathbb{R}^n)$, equipped with the supremum norm, where $\tau_{\max} > 0$ represents the largest delay, $n \geq 1$. For some $t_0 \in \mathbb{R}$ and $\sigma > 0$, suppose that $x : [t_0 - \tau_{\max}, t_0 + \sigma] \to \mathbb{R}^n$ is a continuous mapping. Then, for any $t \in [t_0, t_0 + \sigma]$, $x_t(\theta) := \bar{x}(t + \theta)$ should be defined, $\theta \in [-\tau_{\max}, 0]$. Under this setting,

$$\dot{\bar{x}} = F(t, x_t), \tag{4.2.1}$$

is a retarded functional differential equation (RFDE), where $F : \Omega \to \mathbb{R}^n$ is a given function, with Ω being an open subset of $\mathbb{R} \times C([-\tau_{\max}, 0], \mathbb{R}^n)$. A function $x \in C([t_0 - \tau_{\max}, t_0 + \sigma], \mathbb{R}^n)$ is called a solution to (4.2.1) if $(t, x_t) \in \Omega$ and x satisfies (4.2.1) for all $t \in [t_0, t_0 + \sigma]$. The solution to (4.2.1) can be made unique [125] if F is continuous and locally Lipschitz with respect to its second argument and impose the initial condition $x_{t_0} = \bar{\phi}$, for some fixed $\bar{\phi} \in C([-\tau_{\max}, 0], \mathbb{R}^n)$.

An important feature of the RFDE (4.2.1) is that of *smoothing* [128], i.e., an increase in the regularity of the solution x as the time t grows. Specifically, it can be shown [129] that if F is of class C^k, $k \geq 1$, and $I := [t_0, \sigma_{\max})$ stands for the maximum interval of existence for the solution x, then x is of class C^q on $[t_0 + q\tau_{\max}, \sigma_{\max})$ for $q = 0, 1, \ldots, k$, provided $t_0 + q\tau_{\max}$ does not exceed $\sigma_{\max}$. In particular, one has that periodic solutions are as smooth as the operator F [130], a property that can be exploited for the numerical approximation of the solution of the RFDE (4.2.1) that will be introduced in the next section.

4.2.2 Numerical approach

In this work, it is interesting to analysing a particular type of retarded functional differential equation (see (4.2.1)), namely

$$\dot{\bar{x}}(t) = f(t, \bar{x}(t), \bar{x}(t - \tau_d)), \tag{4.2.2}$$

which represents a system of delay differential equations (DDEs) with constant delay $\tau_d > 0$, where $f : \mathbb{R} \times \mathbb{R}^n \times \mathbb{R}^n \to \mathbb{R}^n$ is a sufficiently smooth function. This type of equations considered here can be seen as dynamical systems with an infinite-dimensional phase space, due to which analytical studies of such systems are generally difficult and require careful mathematical treatment. The situation becomes even more complicated when some kind of nonsmooth phenomenon is involved, such as impacts, switches, impulses, etc., as can be seen later. Consequently, numerical approximations are fundamental to gain both a quantitative and qualitative insight into the model dynamics.

A preliminary approach to reduce the infinite-dimensional problem to one of finite dimension is via a Taylor expansion [131]:

$$\bar{x}(t-\tau_d)=\sum_{k=0}^{M}\bar{x}^{(k)}(t)\frac{(-\tau_d)^k}{k!}+\mathscr{O}\left(\tau_d^{M+1}\right), \tag{4.2.3}$$

which can then be inserted into (4.2.2) (neglecting the $\mathscr{O}$-terms), hence obtaining a system of ordinary differential equations of high order, see for example [132, 133] for practical applications of this technique. This is by all means an analytically valid approach, however, it suffers from certain limitations. For instance, the power series expansion (4.2.3) provides good approximations depending on the size of the delay τ_d and how many terms are used in the expansion (which depends on M). Therefore, this approach restricts the size of the delay and also may require the solution to be many times differentiable, which is not always the case. The main idea, however, can be slightly modified in order to overcome the aforementioned limitations, by considering a finite sequence of Taylor expansions as follows [26].

For the sake of simplicity, it is necessary to assume that the solution $\bar{x}$ of (4.2.2) is as smooth as required for our discussion, which can be achieved via the smoothing property outlined in the previous section. Take $N\in\mathbb{N}$ sufficiently large and define the grid points $t_i := i\frac{\tau_d}{N}$, $i=0,\dots,N$. Furthermore, define $u_i(t):=\bar{x}(t-t_i)$ for all $t\geq 0$, $i=0,\dots,N$. In this setting, via Taylor expansion, the following can be obtained

$$u_{i-1}(t)=\bar{x}\left(t-\left(t_i-\frac{\tau_d}{N}\right)\right)=u_i\left(t+\frac{\tau_d}{N}\right)=\sum_{k=0}^{M}\frac{1}{k!}u_i^{(k)}(t)\left(\frac{\tau_d}{N}\right)^k+\mathscr{O}\left(\left(\frac{\tau_d}{N}\right)^{M+1}\right), \tag{4.2.4}$$

and

$$\dot{u}_0(t)=f(t,u_0(t),u_N(t)), \tag{4.2.5}$$

for all $t\geq 0$, $i=1,\dots,N$, $M\geq 1$. After neglecting the $\mathscr{O}$-terms, from (4.2.4), a system of dN differential equations of order M can be obtained. As is well known, the resulting set of equations can then be written as a first-order system of ODEs, in such a way that the ordinary differential equations (from (4.2.4) and (4.2.5)) with $n(NM+1)$ can be obtained to approximate the solution of the DDE (4.2.2). If $M=1$ is chosen, the approach outlined above reduces itself to the well-known *chain method*, which results in the following system of $n(N+1)$ ODEs:

$$\begin{cases} \dot{u}_0(t) = f(t, u_0(t), u_N(t)), & t \geq 0, \\ \dot{u}_i(t) = \dfrac{N}{\tau_d}(u_{i-1}(t) - u_i(t)), & t \geq 0, \quad i = 1, \dots, N, \\ u_i(0) = \bar{\phi}\left(-i\dfrac{\tau_d}{N}\right), & i = 0, \dots, N, \end{cases} \tag{4.2.6}$$

where $\bar{\phi} \in C([-\tau_{\max}, 0], \mathbb{R}^n)$ is a suitably chosen initial function at $t_0 = 0$ (i.e. $x_{t_0} = \bar{x}_0 = \bar{\phi}$). This approximating system was developed and studied since mid 1960s, see for example the works by Krasovskii [134], Repin [91] and Westdal [93]. In particular, it has been shown that the solution of (4.2.6) converges uniformly to the solution of the original DDE (4.2.2) as $N \to \infty$, provided the initial function ϕ is suitably chosen [91]. Further results regarding convergence have been derived in the past, see for instance the studies by Gyori et al. [92, 135], Banks [95] and Demidenko [136], as well as recent applications in practical problems [96, 137]. Here, the present work will apply a second-order approximation of the DDE (4.2.2) based on the general scheme shown in (4.2.4) and (4.2.5), which takes the following form

$$\begin{cases} \dot{u}_0(t) = f(t, u_0(t), u_N(t)), & t \geq 0, \\ \dot{u}_i(t) = w_i(t), & t \geq 0, \quad i = 1, \dots, N, \\ \dot{w}_i(t) = \dfrac{2N^2}{\tau_d^2}\left(u_{i-1}(t) - u_i(t) - \dfrac{\tau_d}{N}w_i(t)\right), & t \geq 0, \quad i = 1, \dots, N, \end{cases} \tag{4.2.7}$$

where w_i, $i = 1, \dots, N$, represent auxiliary functions introduced to write the approximating system as a set of $n(2N+1)$ first-order scalar ODEs.

4.2.3 Mathematical framework for nonsmooth DDEs

A simple example of a nonsmooth DDE, considering two vector fields and an impulsive perturbation [138], is given by

$$\begin{cases} \dot{\bar{x}}(t) = f_1(t, \bar{x}(t), \bar{x}(t-\tau_d)), & h(\bar{x}(t), \bar{x}(t-\tau_d)) > 0, \\ \dot{\bar{x}}(t) = f_2(t, \bar{x}(t), \bar{x}(t-\tau_d)), & h(\bar{x}(t), \bar{x}(t-\tau_d)) < 0, \\ \bar{x}(t^+) = g(\bar{x}(t^-)), & h(\bar{x}(t), \bar{x}(t-\tau_d)) = 0, \end{cases} \tag{4.2.8}$$

where $f_{1,2} : \mathbb{R} \times \mathbb{R}^n \times \mathbb{R}^n \to \mathbb{R}^n$, $h : \mathbb{R}^n \times \mathbb{R}^n \to \mathbb{R}$ and $g : \mathbb{R}^n \to \mathbb{R}^n$ are sufficiently smooth functions. Model (4.2.8) belongs to the class of *hybrid dynamical systems* [39], which are characterized by a continuous evolution interrupted by discrete events, hence producing a piecewise-continuous flow. This type of systems appears typically in applications dealing with switches, impacts, stick-slip phenomena, etc. A classical example is that of an elastic ball bouncing on a rigid surface. A continuous evolution of the ball position is produced under action of the gravity. However, a discontinuous transition occurs every time the ball touches the rigid surface. At this moment, the ball experiences an "instantaneous" reversal of its direction of motion, and the magnitude of the outgoing velocity is usually assumed to be smaller than that of the velocity right before the impact (Newton's restitution law). The general framework to model this type of dynamical systems consists in dividing the state space into disjoint subregions associated to a particular operation mode of the system, described by a certain smooth vector field (f_1 and f_2 in system (4.2.8)). A transition to a different mode of operation takes place whenever a system trajectory reaches the boundary of the corresponding subregion. The boundaries are often defined as the zero-set of smooth scalar functions (referred to as *event functions*, given by the function h in system (4.2.8)), which normally describe physical instantaneous events, such as impacts, switches, transitions from stick to slip motion, etc., as mentioned earlier. Once a transition has been detected, the vector field describing the system behavior is changed according to the governing laws of the system, and the initial point of the next system trajectory is defined by a certain *reset function*, represented by the mapping g in (4.2.8). In the example of the bouncing ball, the reset function would be given in terms of the described restitution law that reverses and reduces the magnitude of the ball velocity after an impact occurs.

In general, a hybrid dynamical system can be characterized by a collection of (smooth) vector fields, event and reset functions

$$\left\{f_{\mathrm{M}_i} : \mathbb{R} \times \mathbb{R}^n \times \mathbb{R}^n \to \mathbb{R}^n\right\}_{i=1}^{K_{\mathrm{M}}}, \quad \left\{h_{\mathrm{E}_j} : \mathbb{R}^n \times \mathbb{R}^n \to \mathbb{R}\right\}_{j=1}^{K_{\mathrm{E}}} \ \text{ and } \ \left\{g_{\mathrm{R}_m} : \mathbb{R}^n \to \mathbb{R}^n\right\}_{m=1}^{K_{\mathrm{R}}},$$

respectively, with $n, K_{\mathrm{M}}, K_{\mathrm{E}}, K_{\mathrm{R}} \in \mathbb{N}$. Here, the subindex M_i, $i = 1, \ldots, K_{\mathrm{M}}$, represents a mode of operation of the system, for which the system dynamics is described by the smooth vector field f_{M_i}. Each mode of operation is defined within a subregion of the state space $\mathbb{R}^n$. The boundaries of these subregions are determined by the zero-set of the smooth scalar functions h_{E_j}, $j = 1, \ldots, K_{\mathrm{E}}$. The subindex E_j represents in this case an event related to e.g. collisions, switches, etc., as outlined at the beginning of this section. Whenever a system trajectory reaches one of these boundaries, the final state of the system is mapped to the initial state of the next solution branch via a predefined reset function g_{R_m}, for some fixed $m = 1, \ldots, K_{\mathrm{R}}$. A periodic solution of a hybrid dynamical system can then be represented by a sequence of *segments* $\left\{I_{s_{\tilde{n}}}\right\}_{\tilde{n}=1}^{K_{\rm S}}$, $1 \leq s_{\tilde{n}} \leq K_{\rm I}$, also referred to as *solution signature*. Here, $K_{\rm S} \in \mathbb{N}$ represents the length of the signature, while $K_{\rm I} \in \mathbb{N}$ stands for the total number of available segments. Each segment is associated with a vector field, an event function and a reset function, i.e. $I_\ell := \left\{\mathrm{M}_{i_\ell}, \mathrm{E}_{j_\ell}, \mathrm{R}_{m_\ell}\right\}$ for all $\ell = 1, \ldots, K_{\rm I}$, $1 \leq i_\ell \leq K_{\rm M}$, $1 \leq j_\ell \leq K_{\rm E}$, $1 \leq m_\ell \leq K_{\rm R}$. More details about this formulation can be found in [28, 25].

4.3 Soft impact system with the delay feedback controller

4.3.1 Mathematical model

The present work will consider a control signal $u(\tau)$, $\tau \geq 0$, which will be applied to the system's external excitation as follows

$$\begin{cases} x'(\tau) = v(\tau), \\ v'(\tau) = \Big(a\omega^2 \sin(\omega\tau) + u(\tau)\Big) - 2\zeta v(\tau) - x(\tau) - \beta(x(\tau) - e)H(x(\tau) - e), \end{cases} \tag{4.3.1}$$

where

$$u(\tau) = K\left(v(\tau - \tau_d) - v(\tau)\right), \quad \tau \geq 0, \tag{4.3.2}$$

defines the delay feedback controller. In the expression above, $K \geq 0$ represents a control gain used to calibrate the coupling strength between the soft impact system and the controller, while $\tau_d > 0$ stands for a predefined time delay.

4.3.2 Preliminary transformations

Since most of the continuation packages are written for autonomous systems, it will consider the following standard nonlinear oscillator [139] that will be appended to the equations of motion:

$$\begin{cases} r'(\tau) = r(\tau) + \omega s(\tau) - r(\tau)\left(r(\tau)^2 + s(\tau)^2\right), \\ s'(\tau) = s(\tau) - \omega r(\tau) - s(\tau)\left(r(\tau)^2 + s(\tau)^2\right), \end{cases} \tag{4.3.3}$$

which has the asymptotically stable solution, $r(\tau) = \sin(\omega\tau)$ and $s(\tau) = \cos(\omega\tau)$, $\tau \geq 0$. In this way, the periodically forced model can be written as an autonomous system. Furthermore, to allow the time delay $\tau_d > 0$ vary as a control parameter, it is convenient to perform a re-scaling of the model according to

$$\widetilde{t} = \frac{\tau}{\tau_d}, \quad \widetilde{x}(\widetilde{t}) = x(\tau_d\widetilde{t}), \quad \widetilde{v}(\widetilde{t}) = v(\tau_d\widetilde{t}), \tag{4.3.4}$$

and hence it follows that

$$u(\tau) = u(\tau_d \widetilde{t}) = K\left(v(\tau_d \widetilde{t} - \tau_d) - v(\tau_d \widetilde{t})\right) = K\left(\widetilde{v}(\widetilde{t} - 1) - \widetilde{v}(\widetilde{t})\right) =: \widetilde{u}(\widetilde{t}).$$

In this way, the numerical approximation of the resulting DDE will be carried out for a fixed delay (equal to 1), which will facilitate the time discretization, while the effective control delay τ_d can be now embedded into the system as follows (cf. (4.3.1), (4.3.3) and (4.3.4))

$$\begin{cases} \widetilde{x}'(\widetilde{t}) = \tau_d \widetilde{v}(\widetilde{t}), \\ \widetilde{v}'(\widetilde{t}) = \tau_d \left(\left(a\omega^2 r(\widetilde{t}) + \widetilde{u}(\widetilde{t}) \right) - 2\zeta \widetilde{v}(\widetilde{t}) - \widetilde{x}(\widetilde{t}) - \beta(\widetilde{x}(\widetilde{t}) - e) H(\widetilde{x}(\widetilde{t}) - e) \right), \\ r'(\widetilde{t}) = r(\widetilde{t}) + \omega \tau_d s(\widetilde{t}) - r(\widetilde{t}) \left(r(\widetilde{t})^2 + s(\widetilde{t})^2 \right), \\ s'(\widetilde{t}) = s(\widetilde{t}) - \omega \tau_d r(\widetilde{t}) - s(\widetilde{t}) \left(r(\widetilde{t})^2 + s(\widetilde{t})^2 \right), \end{cases} \tag{4.3.5}$$

where now the derivatives are given with respect to the re-scaled time $\widetilde{t}$. In what follows, all tildes will be dropped for the sake of simplicity.

4.3.3 Formulation of the model as a hybrid dynamical system

Let us define $\alpha := (\omega, a, \beta, \zeta, e, K, \tau_d) \in \left(\mathbb{R}_0^+\right)^7$ and $\bar{z} := (x, v, r, s)^T \in \mathbb{R}^4$ as the parameters and state variables of the system, respectively, where $\mathbb{R}_0^+$ represents the set of nonnegative numbers. As explained in Section 4.2.3, the trajectories of the soft impact system (4.3.5) can be divided into segments, as detailed below:

No contact (NC). This segment occurs when the mass m is not in contact with the secondary spring k_2 (see Fig. 3.2.1), i.e. $x - e < 0$. The dynamics of the system during this regime is governed by the (smooth) DDE (cf. (4.3.5))

$$\begin{aligned} \bar{z}'(t) &= f_{\text{NC}}(\bar{z}(t), \bar{z}(t-1), \alpha) \\ &:= \begin{pmatrix} \tau_d v(t) \\ \tau_d \left(a\omega^2 r(t) + K\left(v(t-1) - v(t)\right) - 2\zeta v(t) - x(t) \right) \\ r(t) + \omega \tau_d s(t) - r(t) \left(r(t)^2 + s(t)^2 \right) \\ s(t) - \omega \tau_d r(t) - s(t) \left(r(t)^2 + s(t)^2 \right) \end{pmatrix}. \end{aligned} \tag{4.3.6}$$

This segment terminates when the mass hits the secondary spring k_2, which can be detected via the condition $h_{\text{imp}}(\bar{z}(t), \bar{z}(t-1), \alpha) := x(t) - e = 0$. After the contact occurs, the initial point for the next segment is given by the jump function $g_{\text{id}}(\bar{z}) := \bar{z}$.

Contact (C). During this segment, the mass is in contact with the secondary spring (i.e. $x - e \geq 0$), and the behavior of the system is described by the equation (cf. (4.3.5))

$$\bar{z}'(t) = f_{\mathrm{C}}(\bar{z}(t), \bar{z}(t-1), \alpha)$$
$$:= \begin{pmatrix} \tau_d v(t) \\ \tau_d \left(a\omega^2 r(t) + K\left(v(t-1) - v(t)\right) - 2\zeta v(t) - x(t) - \beta(x(t) - e) \right) \\ r(t) + \omega\tau_d s(t) - r(t)\left(r(t)^2 + s(t)^2\right) \\ s(t) - \omega\tau_d r(t) - s(t)\left(r(t)^2 + s(t)^2\right) \end{pmatrix}, \quad (4.3.7)$$

The terminal point of this segment occurs when the mass loses contact with the secondary spring, which again can be detected via the condition $h_{\mathrm{imp}}(\bar{z}(t), \bar{z}(t-1), \alpha) = 0$, as before. In this case, the initial point for the next segment is given by the jump function g_{id} previously defined.

In the mathematical framework introduced in Section 4.2.3, the segments defined above can be expressed as follows: $I_1 := \{\mathrm{NC}, \mathrm{imp}, \mathrm{id}\}$ (*no contact*) and $I_2 := \{\mathrm{C}, \mathrm{imp}, \mathrm{id}\}$ (*contact*), where the labels stand for the corresponding vector field describing the dynamics of the operation mode, the event function that defines the terminal condition and the jump function, which is in both cases just the identity function, since no impulsive phenomena are considered. Consequently, every solution to system (4.3.5) can be characterized by a sequence $\left\{I_{s_{\tilde{n}}}\right\}_{\tilde{n}=1}^{K_{\mathrm{S}}}$, with $1 \leq s_{\tilde{n}} \leq 2$, which is referred to as the solution signature, as defined earlier. Under this setting, the mathematical model of the considered impact system can be written in compact form as follows

$$\begin{cases} \bar{z}'(t) = f_{\mathrm{NC}}(\bar{z}(t), \bar{z}(t-1), \alpha), & h_{\mathrm{imp}}(\bar{z}(t), \bar{z}(t-1), \alpha) < 0 \quad (\textit{no contact}), \\ \bar{z}'(t) = f_{\mathrm{C}}(\bar{z}(t), \bar{z}(t-1), \alpha), & h_{\mathrm{imp}}(\bar{z}(t), \bar{z}(t-1), \alpha) \geq 0 \quad (\textit{contact}). \end{cases} \quad (4.3.8)$$

4.3.4 Finite-dimensional approximation of the model

Note that the set of DDEs (4.3.8) introduced in the previous section to describe the behavior of the soft impact system can be interpreted as a piecewise-smooth dynamical system of infinite dimension. Therefore, in order to study numerically the dynamics of the system, it is necessary to obtain a finite-dimensional approximation of the model (4.3.8) firstly. For this purpose, the numerical approach described in Section 4.2.2 will be employed to obtain a piecewise-smooth system of ODEs of large dimension. Once the system of ODEs has been constructed, it can then be solved numerically by any standard integration technique [140], including path-following methods for piecewise-smooth systems, as will be done here.

Now, the state variable $\widetilde{z} := (x, r, s, u_0, \ldots, u_N, w_1, \ldots, w_N)^T \in \mathbb{R}^{2N+4}$ is considered. Hence, by applying the numerical approximation given by (4.2.7) to (4.3.6), it is convenient to obtain the system of ODEs

$$\widetilde{z}'(t) = \widetilde{f}_{\text{NC}}(\widetilde{z}(t), \alpha) := \begin{pmatrix} \tau_d u_0(t) \\ r(t) + \omega\tau_d s(t) - r(t)\left(r(t)^2 + s(t)^2\right) \\ s(t) - \omega\tau_d r(t) - s(t)\left(r(t)^2 + s(t)^2\right) \\ \tau_d\left(a\omega^2 r(t) + K\left(u_N(t) - u_0(t)\right) - 2\zeta u_0(t) - x(t)\right) \\ \left(w_i(t)\right)_{i=1,\ldots,N} \\ \left(2N^2\left(u_{i-1}(t) - u_i(t) - \frac{1}{N}w_i(t)\right)\right)_{i=1,\ldots,N} \end{pmatrix}, \tag{4.3.9}$$

which gives a finite-dimensional approximation of the DDE (4.3.6), corresponding to the *no contact* mode. Here, assume $u_0(t) = v(t)$ and

$$u_i(t) \approx v(t - t_i), \text{ for all } t \geq 0, \quad t_i = \frac{i}{N}, \quad i = 1, \ldots, N. \tag{4.3.10}$$

Note that owing to the transformation (4.3.4), the time discretization is carried out over the unit interval, regardless the value of the delay τ_d. Following the same procedure, another set of ODEs can be obtained for the *contact* regime

$$\widetilde{z}'(t) = \widetilde{f}_{\text{C}}(\widetilde{z}(t), \alpha) := \begin{pmatrix} \tau_d u_0(t) \\ r(t) + \omega\tau_d s(t) - r(t)\left(r(t)^2 + s(t)^2\right) \\ s(t) - \omega\tau_d r(t) - s(t)\left(r(t)^2 + s(t)^2\right) \\ \tau_d\left(a\omega^2 r(t) + K\left(u_N(t) - u_0(t)\right) - 2\zeta u_0(t) - x(t) - \beta\left(x(t) - e\right)\right) \\ \left(w_i(t)\right)_{i=1,\ldots,N} \\ \left(2N^2\left(u_{i-1}(t) - u_i(t) - \frac{1}{N}w_i(t)\right)\right)_{i=1,\ldots,N} \end{pmatrix}, \tag{4.3.11}$$

In this way, the original infinite-dimensional, piecewise-smooth system (4.3.8) can be approximated by the following system of finite dimension

$$\begin{cases} \tilde{z}'(t) = \widetilde{f}_{\mathrm{NC}}(\tilde{z}(t), \alpha), & x(t) - e < 0 \quad (\textit{no contact}), \\ \tilde{z}'(t) = \widetilde{f}_{\mathrm{C}}(\tilde{z}(t), \alpha), & x(t) - e \geq 0 \quad (\textit{contact}). \end{cases} \tag{4.3.12}$$

With this mathematical setup it is ready to test the proposed numerical approach to approximate the solution of piecewise-smooth DDEs.

4.4 Numerical investigation of dynamical response of the controlled impact system

4.4.1 Preliminary numerical studies

The preliminary analysis of the soft impact system (3.2.3) begins with the multistable scenario where two stable attractors coexist. Fig. 4.4.1 shows the bifurcation of the system without the delay feedback control when its stiffness ratio varies in the range $\beta \in [20, 100]$. As can be seen from the figure, blue dots represent a period-2 attractor with two impacts, and red dots denote a period-2 attractor with one impact. The soft impact system is monostable exhibiting the period-2 motion with one impact for $\beta \in [20, 27.081)$, and when $\beta \approx 27.081$, the period-2 motion with two impacts emerges. As can be seen from the right windows of Fig. 4.4.1, the period-2 motion with two impacts becomes more stable as the stiffness ratio increases, and the basin of the period-2 motion with one impact shrinks. Next, the dynamics of the soft impact system with the delay feedback control, under variation of the control parameter K, will be investigated.

Bifurcation diagram for the controlled soft impact system under variation of the control parameter K is presented in Fig. 4.4.2. As the control parameter increases up to $K \approx 0.0027$, the period-2 attractor with two impacts disappears and the system becomes monostable. A comparison of this bistability with and without the delay feedback controller is shown in the left windows of Fig. 4.4.2, where the basin for the period-2 attractor with two impacts shrinks as the control parameter K increases. Thereafter, only the period-2 attractor with one impact exists until a reverse period doubling encountered at $K = 0.177$, and the system bifurcates into a period-1 motion with one impact per period of excitation. Examples of the soft impact system controlled from bistable to monostable is given in Fig. 4.4.3, where time histories of the external excitation (including the delay feedback control) and the displacement of the soft impact system are presented. As can be seen from the figure, the controller was switched

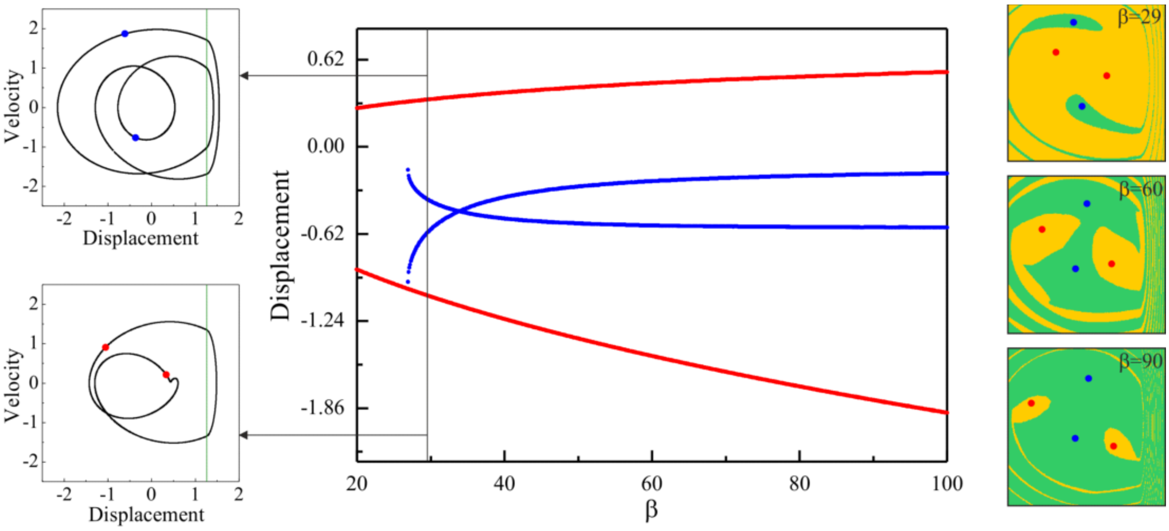

Fig. 4.4.1 Bifurcation diagram of the soft impact system without the delay feedback controller computed for $\omega = 0.8$, $a = 0.9$, $\zeta = 0.01$, $e = 1.26$ by varying the stiffness ratio β. Blue dots represent the period-2 attractor with two impacts per period of excitation, red dots denote the period-2 attractor with one impact per period of excitation. The location of the impact boundary is shown by the vertical green line. Right windows show the evolution of basins of attraction of the system as the stiffness ratio increases.

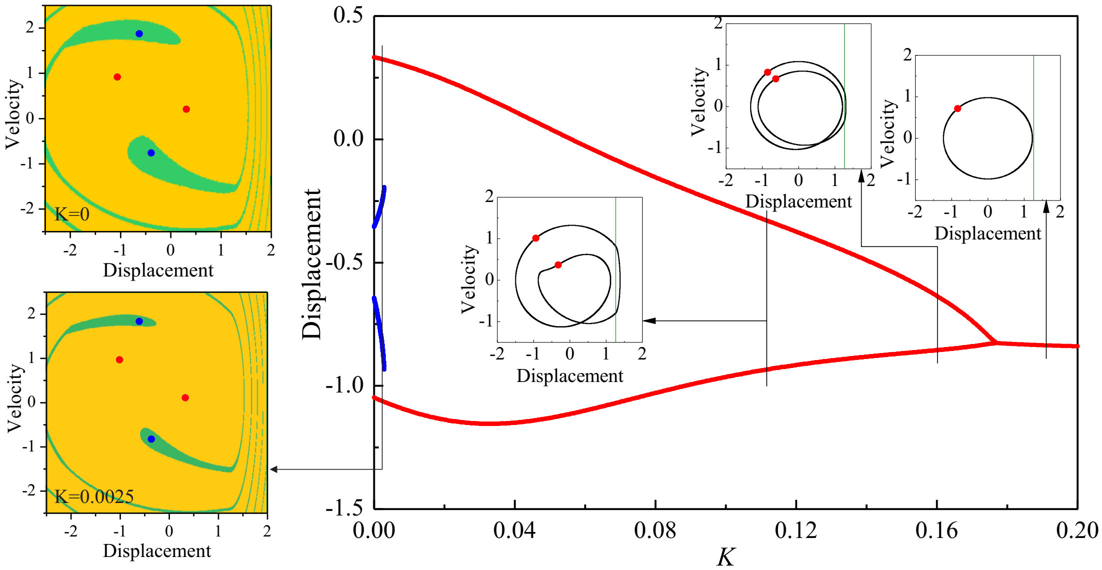

Fig. 4.4.2 Bifurcation diagram of the soft impact system with the delay feedback controller computed for $\omega = 0.8$, $a = 0.9$, $\zeta = 0.01$, $e = 1.26$, $\beta = 29$, $\tau_d = 3.8$ by varying the control parameter K. Red dots represent the period-2 attractor with one impact, and blue dots denote the period-2 attractor with two impacts per period of excitation. Left windows compare the basins of attraction of the system with ($K = 0.0025$) and without ($K = 0$) the time-delayed feedback controller.

on at $\tau = 4000$, and both the period-2 attractor with two impacts and the period-2 attractor with one impact were controlled to a new period-2 attractor with one impact per period of excitation.

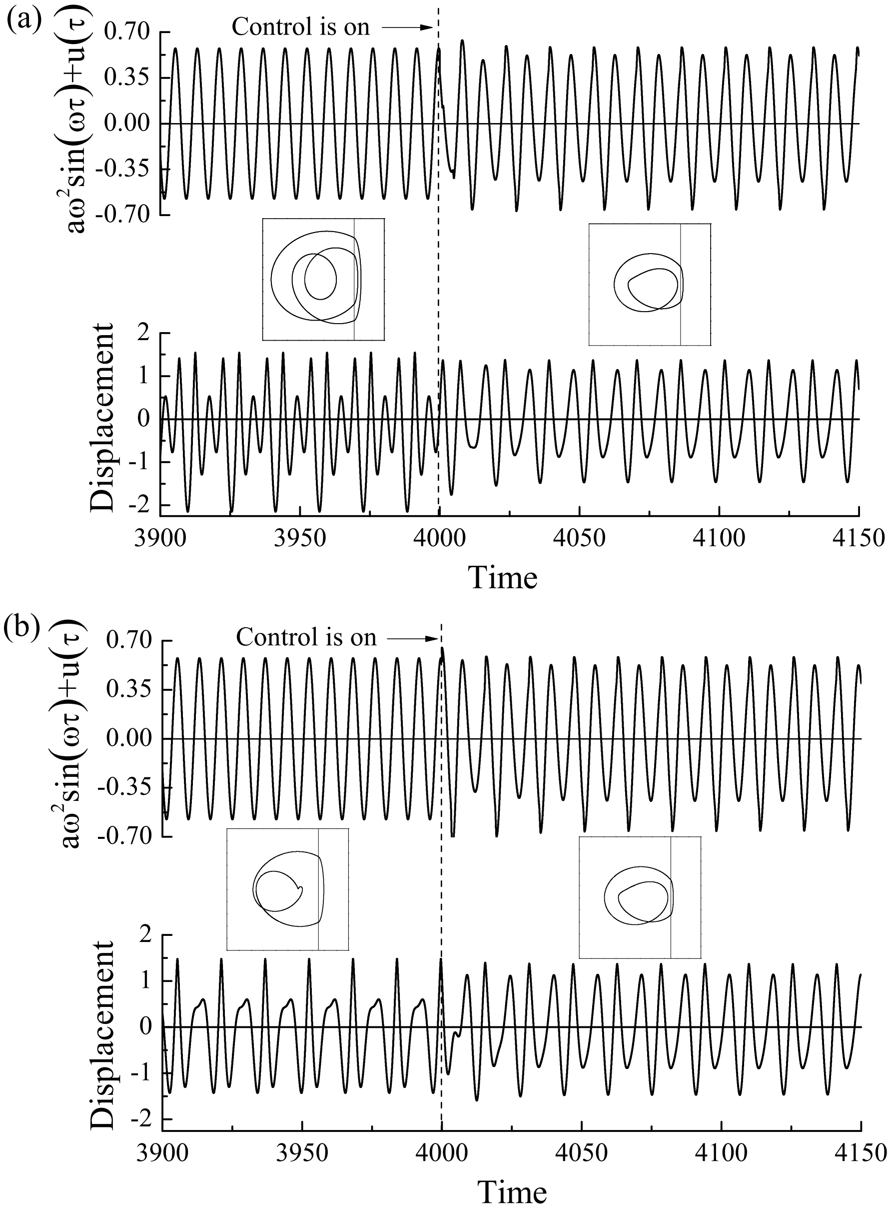

Fig. 4.4.3 Trajectories and external excitations of the soft impact system with the delay feedback controller, computed for $\omega = 0.8$, $a = 0.9$, $\zeta = 0.01$, $e = 1.26$, $\beta = 29$, $K = 0.12$ and $\tau_d = 3.8$. The soft impact system is controlled from (a) the period-2 attractor with two impacts and (b) the period-2 attractor with one impact to a new period-2 attractor with one impact per period of excitation.

4.4.2 Numerical test of the approximation scheme for nonsmooth DDEs

In Section 4.3.4 a nonsmooth ODE of large dimension approximating the original DDE model (4.3.8) was introduced. This approximation was based on the numerical scheme explained in detail in Section 4.2.2, where the main idea is to introduce auxiliary functions defined via suitable time shifts of the exact solution, which are then expanded through a Taylor series of a predefined order. The time shift is defined, after re-scaling (see (4.3.4)), over the unit interval, at the grid points $t_i = \frac{i}{N}$, $i = 0, \ldots, N$, with $N \in \mathbb{N}$ sufficiently large. It is convenient to obtain a finite-dimensional approximation of a DDE, which then can be solved numerically by any standard integration technique. In this section, a numerical investigation will be carried out to study the approximation properties of the nonsmooth ODE (4.3.12) introduced in Section 4.3.4, as the dimension of this system varies with the discretization parameter N.

In Fig. 4.4.4 a numerical comparison was made for the dynamical behavior of the original nonsmooth DDE (4.3.8) with the approximating system of ODEs (4.3.12), for different values of the delay parameter τ_d. In this diagram, and in the remainder of this work, all DDE and ODE models are integrated using the MATLAB solvers 'dde23' and 'ode15s', respectively, in combination with their built-in event location routines [141, 142] so as to detect accurately collisions with the impact boundary $x = e$. For the chosen discretization parameter $N = 50$ (which gives a step-size $\frac{1}{N} = 0.02$), the computed solutions of the original DDE (plotted in red, dashed lines) and the approximating ODE system (blue, solid lines) are very close to each other, for different values of τ_d. In addition, for each case the figure presents time plots showing trajectories for $u_0(t)$ $(= v(t)$, in blue) and $u_N(t)$ $(\approx v(t-1)$, in black), corresponding to the solutions of the approximating system (4.3.12) (see (4.3.10)). These plots can present that the proposed numerical scheme provides reasonable approximations of the original DDE, although the time plots present some perturbations of the solution observable in the lower peaks, produced by a well-known effect referred to as numerical distortion, which typically appears in semi-discretization schemes as the one proposed in the present work [143]. This numerical distortion, however, does not affect significantly the approximation of the orbits depicted in the phase plots shown in Fig. 4.4.4.

Next, some of the convergence properties of the proposed numerical scheme to approximate the solution of nonsmooth DDEs will be investigated numerically. Specifically, this investigate will focus on the experimental order of approximation for the specific case of the soft impact system driven by a delay feedback controller, considered in the present work. For this purpose, a suitable distance function will be defined to quantify how close a solution of the original DDE and its numerical approximation are, as the step-size $\frac{1}{N}$ varies. This study is also motivated by the fact that local truncation errors act as perturbations to the original

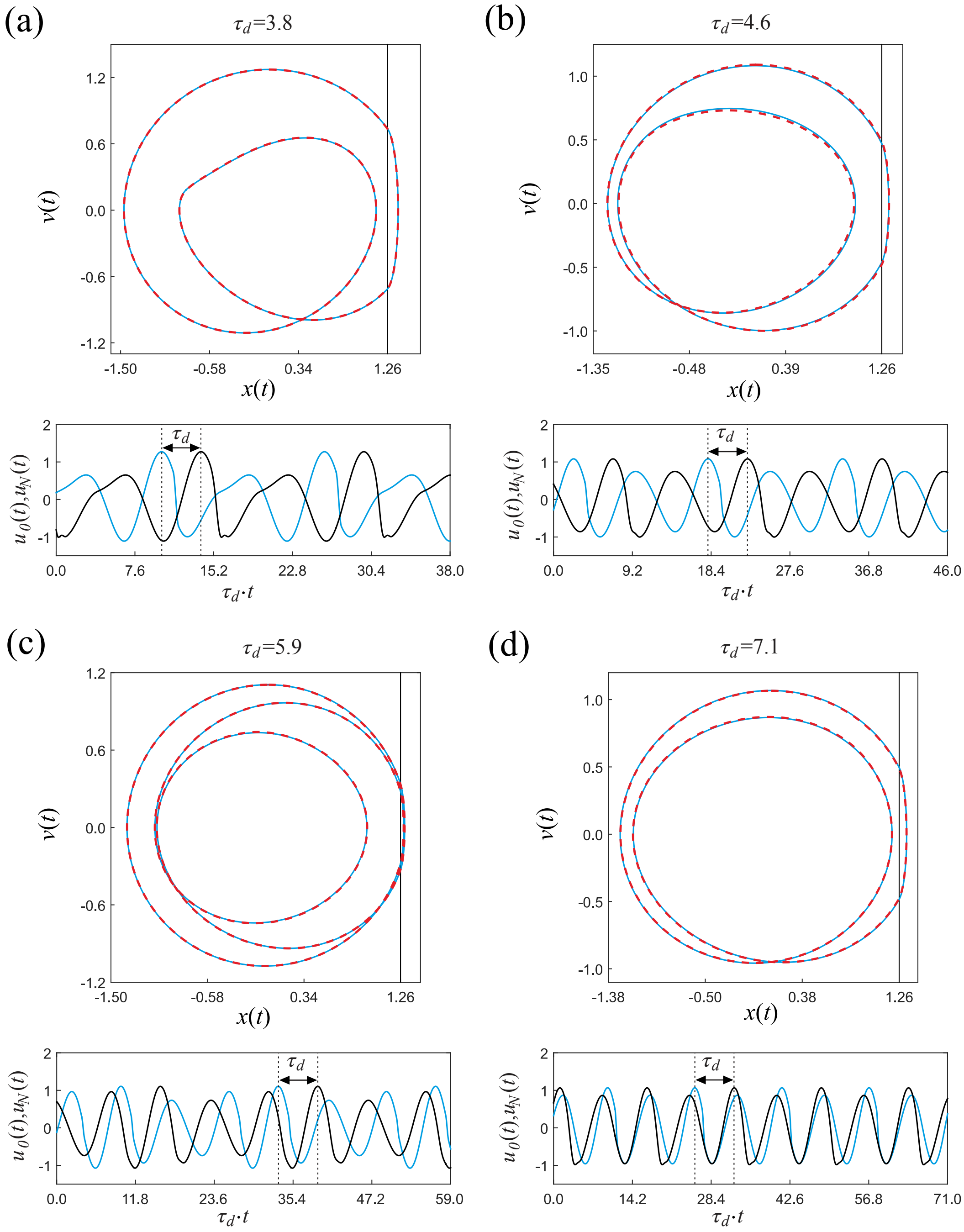

Fig. 4.4.4 Numerical comparison of the dynamical response of the nonsmooth DDE (4.3.8) with the approximating system of ODEs (4.3.12), for the parameter values $\omega = 0.8$, $a = 0.9$, $\zeta = 0.01$, $e = 1.26$, $\beta = 29$, $K = 0.12$ and $N = 50$. Panels (a) to (d) show phase plots for $\tau_d = 3.8$, $\tau_d = 4.6$, $\tau_d = 5.9$ and $\tau_d = 7.1$, respectively. The solutions to the original system (4.3.8) and their approximations are depicted in red (dashed line) and in blue (solid line), respectively. In all phase plots, the vertical black line stands for the impact boundary $x = e$. The time plots show the behavior of $u_0(t)$ $(= v(t)$, in blue) and $u_N(t)$ $(\approx v(t-1)$, in black), corresponding to the solutions of the approximating system (4.3.12) (see (4.3.10)). The time plots are given with respect to the original timescale $\tau_d \cdot t$, see (4.3.4).

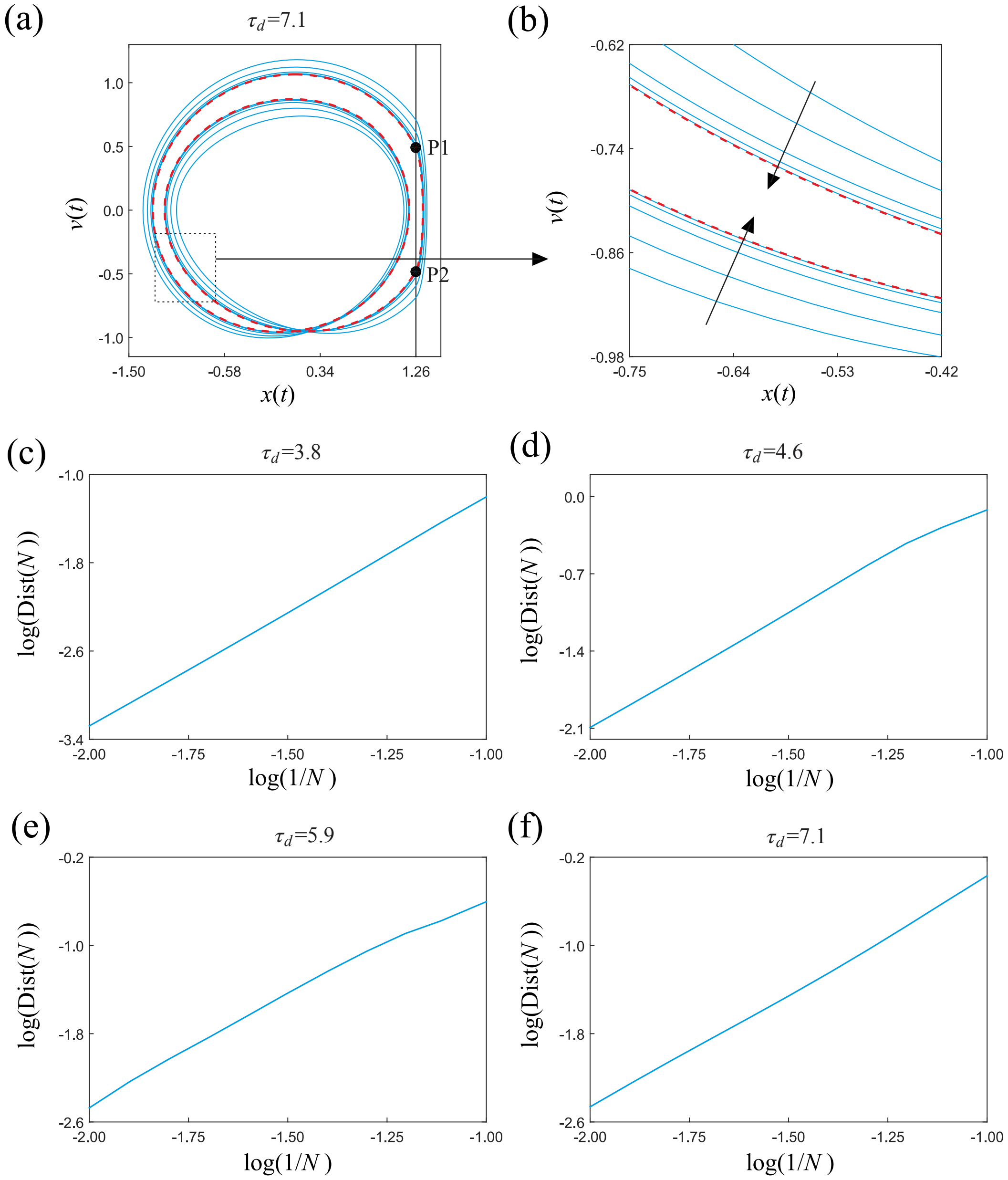

Fig. 4.4.5 (a) Family of approximating orbits (in blue) computed from the system of ODEs (4.3.12), for the parameter values used in Fig. 4.4.4 (with $\tau_d = 7.1$) and $10 \leq N \leq 100$. Here, the reference solution of the piecewise-smooth DDE (4.3.8) is plotted in red (dashed line), showing the intersections P1 and P2 with the discontinuity boundary $x = e$. An enlargement of the boxed region is depicted in panel (b), where the arrows indicate the direction of increasing N. Panels (c) to (f) show the behavior of the distance function (4.4.1) as N varies, computed for $\tau_d = 3.8$, $\tau_d = 4.6$, $\tau_d = 5.9$ and $\tau_d = 7.1$, respectively, using the reference solutions (in red, dashed lines) depicted in Fig. 4.4.4.

system whose solutions are approximated, and in some cases the computed solutions may exhibit high sensitivity when the mesh width is varied [144].

To investigate the approximation properties of the proposed numerical scheme, it is necessary to consider bounded periodic solutions of the nonsmooth DDE (4.3.8), and assume that the solutions intersect (transversally) the impact boundary ($x = e$) $m \geq 2$ times, at the points $(x_1, v_1), \ldots, (x_m, v_m)$, with $(x_i, v_i) \in \mathbb{R}^2$, for $i = 1, \ldots, m$. Let us pick one of such solutions and consider the corresponding numerical approximation computed from the nonsmooth system of ODEs (4.3.12). If N is sufficiently large, then the approximating solution will also intersect the impact boundary m times, at the points $(\widetilde{x}_1^{(N)}, \widetilde{v}_1^{(N)}), \ldots, (\widetilde{x}_m^{(N)}, \widetilde{v}_m^{(N)})$. Assuming a suitable ordering of the intersection points, the following distance function can be defined

$$\mathrm{Dist}(N) := \sum_{i=1}^{m} \left\| (x_i, v_i) - (\widetilde{x}_i^{(N)}, \widetilde{v}_i^{(N)}) \right\|, \tag{4.4.1}$$

where $\|\cdot\|$ stands for the Euclidean norm in $\mathbb{R}^2$. This function can be used as a quantitative indicator of how close a solution of the original DDE and its numerical approximation are, when the step-size $\frac{1}{N}$ is adjusted.

The main results are shown in Fig. 4.4.5. Panel (a) presents a periodic solution of the original nonsmooth DDE (4.3.8) (plotted in red, dashed lines) together with a family of approximating solutions computed from the system of ODEs (4.3.12) (in blue), with $10 \leq N \leq 100$ and $\tau_d = 7.1$. In this picture, it can be observed that the approximating solutions indeed become closer and closer to the reference solution as the mesh width $\frac{1}{N}$ decreases. This procedure was repeated also for $\tau_d = 3.8$, $\tau_d = 4.6$ and $\tau_d = 5.9$, and the convergence was verified as well. A closer look into the convergence is obtained from panels (c) to (f), where the behavior of the distance function defined in (4.4.1) is analysed with respect to variations of N, on a logarithmic scale, for the values of τ_d considered above. The panels reveal an almost linear response indicating that the distance function decreases according to $\mathscr{O}\left(N^{-p}\right)$, with $p \approx 2$. This observed order of accuracy is consistent with the second-order approximation given by (4.2.7) and applied in (4.3.12), which confirms the reliability of the proposed numerical scheme to approximate the solution of nonsmooth DDEs. In what follows and unless otherwise indicated, the numerical study will considers the approximation with $N = 15$, which was found to be a suitable value to keep a good balance between computational cost and accuracy of the results.

4.4.3 Numerical investigation of the delay soft impact system via continuation methods

In this section, the main purpose will be the application of the proposed numerical approach to study the dynamics of the considered soft impact system with delay feedback control, via continuation techniques. The starting point for this numerical investigation will be the periodic solution computed in Fig. 4.4.4(a) (the one in blue, computed from system (4.3.12)). To begin with, the control delay τ_d can be treated as the bifurcation parameter and investigate how the initial periodic solution behaves as this parameter is changed. The result is presented in Fig. 4.4.6. The figure includes a diagram showing the behavior of the test function

$$h_{\mathrm{GR}}(\bar{z}(t),\alpha) := x(t) - e, \tag{4.4.2}$$

which is evaluated at a suitably chosen point along a periodic solution where the mass velocity is zero (for example at the point Pt shown in one of the phase plots in Fig. 4.4.6). In this way, an accurate detection of grazing events is possible. As can be observed in the figure, the bifurcation diagram is limited by two grazing bifurcations, labeled GR1 and GR2, detected at $\tau_d \approx 3.1903$ and $\tau_d \approx 4.6563$, respectively, whose phase plots are depicted in the smaller external panels. A closer look to the system dynamics around the grazing point GR2 reveals a period-doubling effect produced when the grazing contact occurs, when GR2 is crossed from above, which is a classical phenomenon observed near grazing points, see e.g. [39, Section 6.3.3].

Next, with varying of the control gain K, the periodic response of the approximating system (4.3.12) will be investigated. The result of this study is presented in Fig. 4.4.7, where the plot shows the contact time, i.e., the time the mass is in contact with the secondary spring within one orbital period, as a function of K. As can be seen in this diagram, large values of K induce a periodic response with no impacts with the secondary spring, hence the contact time equals zero. As this parameter decreases, a periodic solution with a tangential intersection with the impact boundary $x = e$ is detected at the point labeled GR, found for $K \approx 0.1747$. Therefore, this value defines a boundary between impacting and non-impacting periodic behavior. In addition, further investigations reveal that this grazing bifurcation also produces a period-doubling effect, similarly to the case studied in the previous paragraph. The bifurcation diagram finishes at $K = 0$, corresponding to the situation when the delay feedback controller is switched off, due to which any delay effect disappears from the model. In this case the original DDE model (4.3.8) and its approximating system of ODEs (4.3.12) are equivalent.

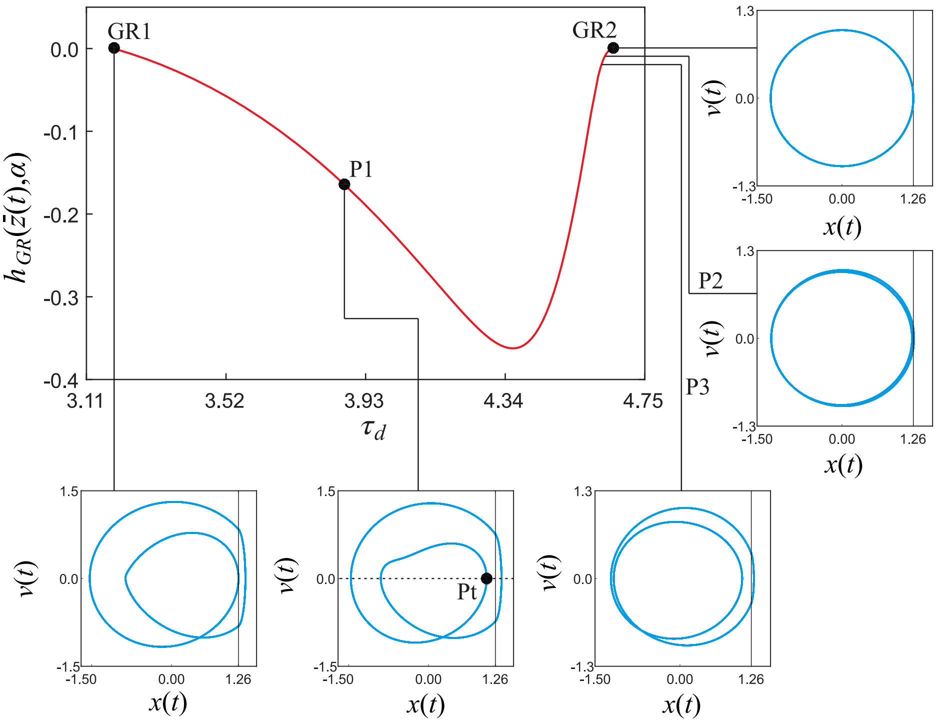

Fig. 4.4.6 Continuation of the periodic response of system (4.3.12) with respect to the control delay τ_d, for the parameter values given in Fig. 4.4.4. The diagram presents the behavior of the test function h_{GR} introduced in (4.4.2) to detect grazing events. The labels GR1 and GR2 stand for grazing bifurcations detected at $\tau_d \approx 3.1903$ and $\tau_d \approx 4.6563$, respectively. The phase plots show periodic solutions computed at GR1, GR2 and at the test points P1 ($\tau_d = 3.868$), P2 ($\tau_d = 4.620$) and P3 ($\tau_d = 4.558$).

As can be observed from the studies above, the dynamics of the controlled soft impact system is dominated by the presence of grazing phenomena. In particular, the investigation revealed that the delay feedback controller is able to drive the system from impacting to non-impacting responses and viceversa, where the boundary point is defined by a grazing bifurcation. Therefore, a two-parameter continuation of this critical point with respect to the main control parameters, i.e., the control delay τ_d and the control gain K, will be carried out at the next step. The result of this process is displayed in Fig. 4.4.8. Panel (a) shows a curve representing all combinations of τ_d and K producing periodic solutions making tangential contact with the impact boundary $x = e$. In this way, the parameter space is divided locally by this curve into two regions. The first one (above the curve) corresponds to all pairs (τ_d, K) for which the system presents non-impacting periodic solutions, as the one computed at the test point P2 (see panel (d)). On the contrary, below the grazing curve, the operation points (τ_d, K) producing impacting periodic solutions can be found, for instance at the test points P1 and P3, depicted in panels (c) and (e), respectively. In panels (c) to (e), the solutions

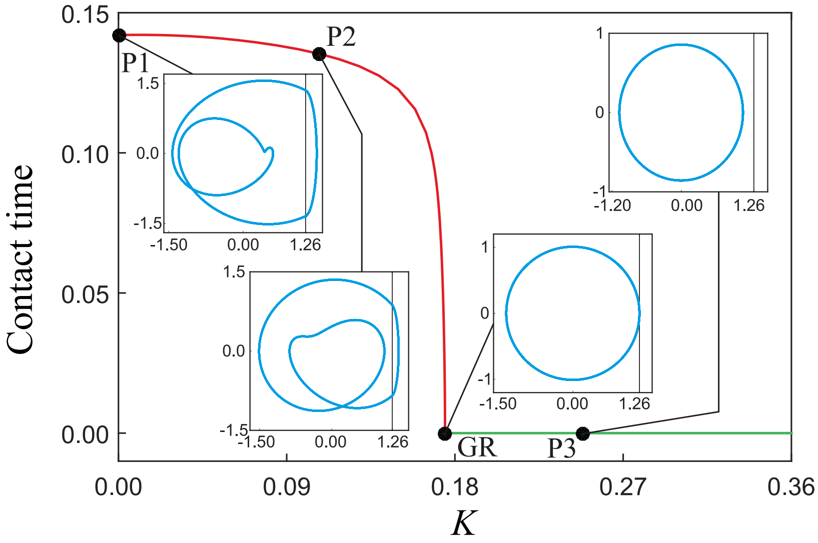

Fig. 4.4.7 Continuation of the periodic response of system (4.3.12) with respect to the control gain K, for the parameter values given in Fig. 4.4.4, with $\tau_d = 3.8$. The diagram presents the time spent during the *contact* mode (see Section 4.3.3) on the vertical axis. The label GR represents a grazing bifurcation found at $K \approx 0.1747$. The inner panels show phase plots on the x-v plane for the test points P1 ($K = 0$), P2 ($K = 0.1071$), P3 ($K = 0.2482$) and GR.

to the original system (4.3.8) and their approximations (computed from system (4.3.12)) are depicted in red (dashed line) and in blue (solid line), respectively. Furthermore, in Fig. 4.4.8(b) it presents the solution manifold computed along the grazing curve displayed in panel (a), showing the components $u_0(t)$ $(= v(t))$, $u_N(t)$ $(\approx v(t-1))$ and the delay parameter τ_d. In this graph, two particular values can be identified. The first one, when τ_d takes the value closest to zero, presents that the phase plot corresponding to this value resembles the identity function. This is because, since the delay is close to zero, both the signals $v(\tau)$ and $v(\tau - \tau_d)$ (in the original time scale) are almost in phase, and this is reflected on the phase plane u_0-u_N. A similar phenomenon can be observed for $\tau_d = 2\pi/\omega \approx 3.927$, where the signals are 180 degrees out phase, which can also be identified from the 3D plot.

4.5 Conclusion

Nonsmooth dynamical systems with delay have been widely used in the past to describe complex phenomena in a variety of research areas, for instance in biology, mechanics and control. Despite the popularity and importance of such type of models, the available computational tools for numerical study and simulation are rather limited, owing to the infinite-dimensional nature of dynamical systems with delay, in combination with the analytical and numerical difficulties arising when nonsmooth phenomena are considered. While a number of

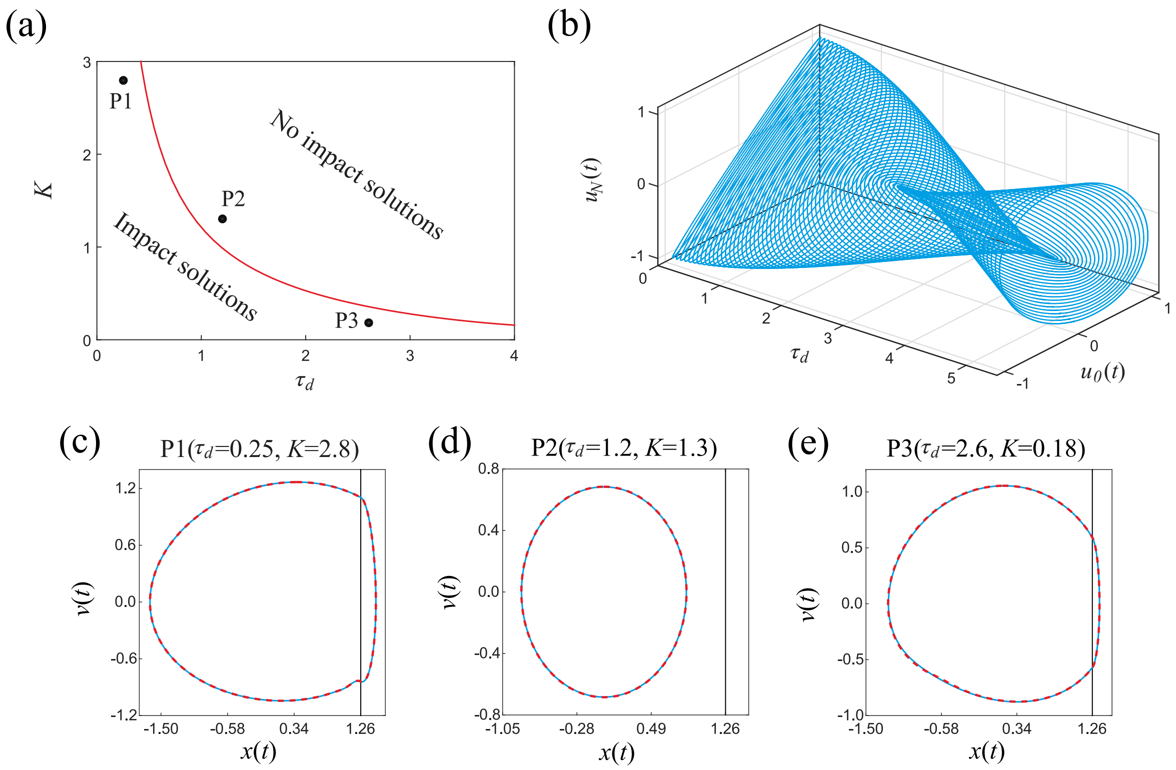

Fig. 4.4.8 (a) Continuation in two parameters of the grazing bifurcation (GR) encountered in Fig. 4.4.7, with respect to τ_d and K. The resulting curve defines the boundary between impacting and non-impacting responses. (b) Solution manifold computed along the grazing curve plotted in (a). The axes show the components $u_0(t)$ $(= v(t))$, $u_N(t)$ $(\approx v(t-1))$ and the delay parameter τ_d. Panels (c) to (e) show phase plots computed at the test points P1, P2 and P3, respectively, marked in panel (a). The solutions to the original system (4.3.8) and their approximations (computed from system (4.3.12)) are depicted in red (dashed line) and in blue (solid line), respectively.

software packages have been developed for numerical continuation in smooth DDEs (e.g. DDE-BIFTOOL [97], PDDE-CONT [99] and Knut [100]), no software package of this kind exists for the path-following analysis of nonsmooth DDEs. There is, however, a solid computational framework developed for this purpose (see for instance [124]), but the related codes are not yet available in a user friendly form.

The present work proposed a numerical approach for the numerical continuation of periodic solutions of nonsmooth dynamical systems with delay. The numerical approach is based on the well-known technique of approximating delay differential equations via large systems of ODEs. Such approximating systems were developed and studied since mid 1960s, see for example the works by Krasovskii [134], Repin [91] and Westdal [93]. In particular, it has been shown that the solution of the approximating systems of ODEs converges uniformly to the solution of the original DDE as the number of ODEs tends to infinity [91]. Further results regarding convergence have been derived thereafter, see for instance the studies by Gyori et al. [92, 135], Banks [95] and Demidenko [136], as well as recent applications in practical problems [96, 137]. Following these previous works, the present study applied a second-order approximation of the original DDE by considering a finite sequence of Taylor expansions as proposed in [26]. In this way, a nonsmooth dynamical system with (constant) delay can be approximated by a nonsmooth system of ODEs of large dimension, which then allows the study of the resulting model in the framework of hybrid dynamical systems, following the ideas of [124] and [28]. This enables the numerical bifurcation study of the system response via path-following methods, for instance via the general-purpose continuation platform COCO [25].

The effectiveness of the proposed scheme was tested on a well-known and widely studied impact system [32, 145], driven by a delay feedback controller. One of the advantages of the proposed numerical approach is that it allows the study of discontinuity-induced bifurcations, such as sliding and grazing, a task that is difficult to perform if discontinuity boundaries are not clearly identified in the numerical implementation, for instance when smoothing the original system via e.g. parameter-dependent families of tanh functions. Via the numerical software COCO, the numerical continuation was carried out for periodic solutions of the soft impact system, with special focus on detection of grazing phenomena when the main control parameters are varied, specifically, the control delay τ_d and the control gain K. This investigation revealed that the considered delay feedback controller is able to steer the system from impacting to non-impacting responses and viceversa, where the boundary point is defined by a grazing bifurcation. By using the COCO capability of tracing loci of special points in two parameters, the two-parameter continuation of the detected grazing bifurcation with respect to τ_d and K was carried out. In this way, it was convenient to obtain a curve in the τ_d-K plane defining the boundary between impacting and non-impacting periodic behavior.

Although the proposed the numerical approach provides a straightforward mean to study nonsmooth dynamical systems with delay via existing and well-established continuation packages, it suffers from a number of limitations. To begin with, a significant increase of computation time can be noticed when the mesh width $\frac{1}{N}$ decreases (see (4.2.7)), which is an unavoidable effect owing to the infinite-dimensional nature of dynamical systems with delay. Nevertheless, the numerical investigation showed that still a good balance between computational cost and accuracy of the results can be found. It is also important to mention that the above implementation has not consider to track secondary discontinuities that are known to be propagated as the time increases. Due to the well-known *smoothing* property of DDEs [128], this does not seem to affect the numerical accuracy in the considered continuation framework (since the study focused on periodic solutions), however, this is something that needs to be looked into when dealing with DDEs with nonsmooth phenomena. Therefore, in the long term future work should focus on the development of general-purpose, portable and user friendly computational tools for the numerical continuation and bifurcation analysis of nonsmooth dynamical systems with delay, combining the capabilities offered by e.g. DDE-BIFTOOL and the multi-segment continuation toolbox of COCO.

Chapter 5

Lyapunov exponents of soft impact system with the delay feedback control

5.1 Introduction

Grazing events for nonsmooth systems can introduce coexisting attractors (also called Multistability), which means that the nonsmooth system can has many different motions caused by grazing events. Controlling multistability offers a possibility to understand the relation among the relevant coexisting attractors. The delay feedback controller [19] can be used to stabilise the system to one of periodic coexisting attractors. But, under some conditions, the delay feedback controller can lose its effectiveness on stabilising at the desired attractors. Thus, Lyapunov Exponents (LEs) should be considered to analyse the nonsmooth dynamical system with a delay feedback controller. In addition, during the simulation of the nonsmooth dynamical system with a delay feedback control near grazing, the convergence of the numerical result always cannot be improved through adopting high numerical integration.

The chapter is organised as follows. Section 5.2 introduces the mathematical model of a periodically forced mechanical oscillator subjected to a one-sided soft impact, with the delay feedback controller. This is followed by some basic relevant definitions and preparations. Section 5.3 presents the method for constructing the Jacobian of Poincaré map of piecewise-smooth DDEs. However, such a construction is inaccurate due to the nonsmooth property of the considered system. Thus, Section 5.4 studies an estimation method for determining the points of discontinuity accurately. Here, two cases of grazing events are considered based on the geometry of the trajectory. Section 5.5 uses linear operator theory to carry out an error analysis for the eigenvalues of the Jacobian, which can validate the reliability of the proposed method. In Section 5.6, the steps for computing LEs are detailed. Examples and several control scenarios of the oscillator are presented in Section 5.7 to demonstrate the accuracy of the method. Finally, some concluding remarks are drawn in Section 5.8.

5.2 Mathematical preparation

The present work will consider a control signal $u(\tau)$, which will be superimposed on the system's external excitation as follows

$$\begin{cases} x'(\tau) = & v(\tau), \\ v'(\tau) = & \Big(a\omega^2 \sin(\omega\tau) + u(\tau)\Big) - 2\zeta v(\tau) - x(\tau) - \beta(x(\tau) - e)H(x(\tau) - e), \end{cases} \tag{5.2.1}$$

where

$$u(\tau) = K\left(v(\tau - \tau_d) - v(\tau)\right), \quad \tau \geq 0, \tag{5.2.2}$$

defines the proportional feedback control that feedbacks the difference between the current measurement of v and a measurement of v from some time τ_d ago [19]. In the expression above, $K \geq 0$ represents the feedback gain of the controller and $\tau_d > 0$ stands for a predefined time delay. The control objective here is to avoid undesired chaotic responses and to suppress the multistability of the soft impact system in the vicinity of the grazing events. This type of delay feedback control has many advantages. For instance, it may result in a zero control signal if $\tau_d = 2\pi/\omega$ and if (5.2.2) successfully stabilises a period-1 motion. This case does not need to know the precise time profile of this period-1 motion, which is in contrast to standard linear feedback control $u(\tau) = k(v_{\text{ref}}(\tau) - v(\tau))$. The asymptotically vanishing control signal is attractive in applications where energy consumption is a critical issue, e.g. [5].

Eq. (5.2.1) can be rewritten in the form of a general piecewise continuous DDE with a periodic external excitation as

$$\begin{cases} \dot{y}(t) = f_1(y(t), y(t-\tau_d)) + p(t), & \text{for } H(y(t), e) > 0, \\ \dot{y}(t) = f_2(y(t), y(t-\tau_d)) + p(t), & \text{for } H(y(t), e) < 0, \\ y(t^+) = y(t^-), & \text{for } H(y(t), e) = 0, \end{cases} \tag{5.2.3}$$

where $f_{1,2} : \mathbb{R}^n \times \mathbb{R}^n \to \mathbb{R}^n$, $H : \mathbb{R}^n \to \mathbb{R}$ are sufficiently smooth functions and $p : \mathbb{R}^+ \to \mathbb{R}^n$ is smooth and periodic with the period $T > 0$. The delay τ_d is assumed to be positive but may be different from the period in general. The present work only considers one single delay in the system for simplicity, and assumes that for any $y, \bar{y}, y_d, \bar{y}_d \in \mathbb{R}^n$, f_1, f_2 and H

satisfy the Lipschitz condition

$$\begin{aligned} |f_{1,2}(y,y_d) - f_{1,2}(\bar{y},\bar{y}_d)| &\leq l_1|y-\bar{y}| + l_2|y_d - \bar{y}_d|, \\ |H(y,e) - H(\bar{y},e)| &\leq l_3|y-\bar{y}|, \end{aligned}$$

where $l_1, l_2, l_3 \geq 0$ and $|\cdot|$ is a norm on $\mathbb{R}^n$. Also, a suitable initial function on $[t_0, t_0 - \tau_d]$ is chosen for the initial condition. The general form (5.2.3) belongs to the class of *hybrid dynamical systems* [39], which consists of a flow (in our case only forward in time), combined with discrete events.

Take $N \in \mathbb{Z}^+$ sufficiently large, and define the discretisation grid points $\tau_d^i := i\frac{\tau_d}{N}$, $i = 0, \ldots, N$, and $u_i(t) := y(t - \tau_d^i)$ for all $t \geq 0$, $i = 0, \ldots, N$. Eq. (5.2.3) can be approximated by a $n(N+1)$ dimensional piecewise-smooth discretised problem studied in [116], which will be presented in Section 5.3. This approximation method has also been studied by Krasovskii [146], finding that the solution of the approximating system uniformly converges to the solution of the original DDEs when $N \to \infty$. By using the same approach, Györi and Turi [92] and Banks [95] carried out convergence analyses for two DDEs. Breda *et al.* [118]. studied the characteristic roots of linear DDEs, and used a Runge-Kutta method to construct a high-dimensional approximating system. The nonzero eigenvalues of evolution operators were computed through a pseudospectral collection, which was used to analyse the asymptotic stability of DDEs. Since Eq. (5.2.3) is a nonsmooth DDE whose trajectories can encounter discontinuities, the methods used for smooth DDEs are not suitable, or, at least, converge with lower-than-expected order. Therefore, motivated by the periodic forcing of Eq. (5.2.3), the plan here is to derive a Poincaré map (also called stroboscopic map) for discretising the system and study linear stability of its orbits by considering the Jacobian matrix of the map in these orbits. After such a reduction to the Poincaré map, it is convenient to define LEs for this time-discrete map.

For the nonsmooth DDE (5.2.3), a constant phase surface as the Poincaré section can be defined as $P_s^T := \{(y,t) \in C([t_0 - \tau_d, t_0], \mathbb{R}^n) \times \mathbb{R}^+ |\, t = t_0 + kT,\ k \in \mathbb{Z}^+\}$. For the corresponding Poincaré map

$$P:\ P_s^T \to P_s^T \tag{5.2.4}$$

the LEs can be defined as follows.

Definition 5.2.1. [108] For any initial condition $x_0 \in P_s^T$, let $\{x_{m^*}\}_{m^*=0}^{\infty}$ be the corresponding orbit of the map P, and let $\lambda_0^{m^*}, \cdots, \lambda_{n^*}^{m^*}$ be the n^* largest in modulus eigenvalues of $DP^{m^*}(x_0)$, where is the Jacobian matrix of P^{m^*} with the relevant orbit, which is the Jacobian matrix of P^{m^*} with respect to the relevant orbit, sorted such that $|\lambda_0^{m^*}| \geq \ldots \geq |\lambda_{n^*}^{m^*}|$. The Lyapunov exponents of x_0 are

$$\vartheta_i := \lim_{m^*\to\infty} \ln|\lambda_i^{m^*}|^{\frac{1}{m^*}}, i = 1,\ldots,n^* \tag{5.2.5}$$

whenever the limit exists for x_0 and for all $i \leq n^*$.

The above definition is applicable to the map P acting on the infinite dimensional space P_s^T, since P is differentiable and its linearisation is bounded and has a spectrum only consisting of a sequence (finite or infinite) of eigenvalues of finite multiplicity converging to 0 and zero. The expression in the limit (5.2.5) is not a practical recipe for computation since $\lambda_i^{m^*}$ may be very large or very small.

5.3 Constructing the Jacobian matrix of the Poincaré map

For a nonsmooth system with a delay τ_d smaller than its forcing period T, i.e. $0 < \tau_d < T$, the period T can be written as $T = \hat{n}\tau_d + \Delta t$, for some $\hat{n} \in \mathbb{Z}^+$ and $\Delta t \in [0, \tau_d)$. For any time interval $[t_{\bar{m}}, t_{\bar{m}} + \tau_d]$, where $t_{\bar{m}} = t_1 + (\bar{m}-1)T$, $t_1 = t_0$ and $\bar{m} \in \mathbb{Z}^+$, the solution of system (5.2.3) can be approximated by N steps of size $h = \frac{\tau_d}{N}$ by using numerical integration. The expressions derived in this section initially ignore grazing of the discontinuity surface $\{H = 0\}$. Section 5.4 will explain how the expressions will be modified at the respective events. The modified Euler integration formula [147] gives for a single step of size $h = \tau_d/N$

$$\begin{aligned} u_0(t_{\bar{m}} + h) =& u_0(t_{\bar{m}}) + \tfrac{h}{2}\Big[f_j(u_0(t_{\bar{m}}), u_0(t_{\bar{m}} - hN)) \\ &+ f_j(u_E, u_0(t_{\bar{m}} - h(N-1)))\Big] + \tfrac{h}{2}\Big[p(t_{\bar{m}}) + p(t_{\bar{m}} + h)\Big], \end{aligned} \tag{5.3.1}$$

(here written only for the first step at $t_{\bar{m}}$) where $u_E = u_0(t_{\bar{m}}) + hf_j(u_0(t_{\bar{m}}), u_0(t_{\bar{m}} - hN)) + hp(t_{\bar{m}})$ and

$$\begin{cases} j = 1, & \text{if } H(u_0(t_{\bar{m}}), e) > 0, \\ j = 2, & \text{if } H(u_0(t_{\bar{m}}), e)) < 0, \\ u_0(t_{\bar{m}}^+) = u_0(t_{\bar{m}}^-), & \text{if } H(u_0(t_{\bar{m}}), e) = 0. \end{cases}$$

Iterating this map $N+1$ times gives a discretised map for the delay-time interval $[t_{\bar{m}}, t_{\bar{m}} + \tau_d]$, which it can be called $P_d : \mathbb{R}^{n(N+1)} \to \mathbb{R}^{n(N+1)}$. It satisfies

$$U_{\bar{m},1} = P_d(U_{\bar{m},0}), \tag{5.3.2}$$

where $U_{\bar{m},0} := (u_N^T(t_{\bar{m}}), \cdots, u_1^T(t_{\bar{m}}), u_0^T(t_{\bar{m}}))^T \in \mathbb{R}^{n(N+1)}$ and $U_{\bar{m},1} := (u_N^T(t_{\bar{m}} + \tau_d), \cdots, u_1^T(t_{\bar{m}} + \tau_d), u_0^T(t_{\bar{m}} + \tau_d))^T \in \mathbb{R}^{n(N+1)}$, and let $u_i(t) := u_0(t - (i/N)\tau_d)$ for arbitrary $i \in \{0, \ldots, N\}$

and t. Iterating the map P_d $\hat{n}$ times, it is convenient to obtain a map $P_d^{\hat{n}}$ from U at time $t_{\bar{m}}$ to U at time $t_{\bar{m}} + \hat{n}\tau_d$,

$$U_{\bar{m},\hat{n}} = P_d \circ \cdots \circ P_d(U_{\bar{m},0}) = P_d^{\hat{n}}(U_{\bar{m},0}), \tag{5.3.3}$$

where $U_{\bar{m},i} := (u_N^T(t_{\bar{m}} + ihN), \cdots, u_0^T(t_{\bar{m}} + ihN))^T \in \mathbb{R}^{n(N+1)}$. Finally the discretised map for the time Δt is defined as $P_{\Delta t} : \mathbb{R}^{n(N+1)} \to \mathbb{R}^{n(N+1)}$, which can be represented as

$$U_{\bar{m},\hat{n}+\Delta N} = P_{\Delta t}(U_{\bar{m},\hat{n}}), \tag{5.3.4}$$

where $U_{\bar{m},\hat{n}+\Delta N} := (u_N^T(t_{\bar{m}} + h(\hat{n}N + \Delta N))^T, \cdots, u_0^T(t_{\bar{m}} + h(\hat{n}N + \Delta N))^T \in \mathbb{R}^{n(N+1)}$ and $\Delta N := \frac{\Delta t}{h}$. Thus combining Eqs. (5.3.3) and (5.3.4) it is easy to construct the map P_{disc} as the discretised Poincaré map P advancing by time T

$$U_{\bar{m},\hat{n}+\Delta N} = P_{\text{disc}}(U_{\bar{m}+1,0}) = P_{\Delta t} \circ P_d^{\hat{n}}(U_{\bar{m},0}), \tag{5.3.5}$$

which can then be iterated further by setting $U_{\bar{m}+1,0} = U_{\bar{m},\hat{n}+\Delta N}$. When an arbitrary perturbation δU is applied, the variational equation for P_{disc} can be written as

$$\delta U_{\bar{m}+1,0} = \sum_{i=1}^{N+1} \frac{\partial P_{\text{disc}}(U_{\bar{m},0})}{\partial u_{i-1}(t_{\bar{m}})} \delta u_{i-1}(t_{\bar{m}}), \tag{5.3.6}$$

where $\delta U_{\bar{m},0} := (\delta u_N^T(t_{\bar{m}}), \cdots, \delta u_1^T(t_{\bar{m}}), \delta u_0^T(t_{\bar{m}}))^T \in \mathbb{R}^{n(N+1)}$, and again let $\delta u_i(t) := \delta u(t - \tau_d^i), i = 0, \cdots, N$. In fact, Eq. (5.3.6) can be obtained from discretising the continuous variational equation of system (5.2.3), and its form can be obtained as

$$\frac{\mathrm{d}}{\mathrm{d}t}\delta u_0(t) = \frac{\partial f_j(t, u_0(t), u_N(t))}{\partial u_0} \delta u_0(t) + \frac{\partial f_j(t, u_0(t), u_N(t))}{\partial u_N} \delta u_N(t), \tag{5.3.7}$$

where

$$\begin{cases} j = 1, & \text{if } H(u_0(t), e) > 0, \\ j = 2, & \text{if } H(u_0(t), e) < 0, \\ u_0(t^+) = u_0(t^-), & \text{if } H(u_0(t), e) = 0. \end{cases}$$

An example initial function ϕ_δ for Eq. (5.3.7) is of the form $\phi_\delta(t_1) = (\varepsilon, 0, \cdots, 0)^T \in \mathbb{R}^d$ and $\phi_\delta(t) = (0, \cdots, 0)^T \in \mathbb{R}^n$ for $t \in [t_1 - \tau_d, t_1)$, and sufficiently small ε. Discretising Eq. (5.3.7) in the interval $[t_{\bar{m}}, t_{\bar{m}} + \hat{n}\tau_d]$ by using the modified Euler integration gives

$$
\begin{aligned}
\delta u_0(t_{\bar{m}}+lh) = &\,\delta u_0(t_{\bar{m}}+(l-1)h) \\
&+\frac{h}{2}\Big[A_{\bar{m},l}\delta u_0(t_{\bar{m}}+(l-1)h+B_{\bar{m},l}\delta u_0(t_{\bar{m}}-(N-l+1)h)] \\
&+\frac{h}{2}[A_{\bar{m},l+1}\delta u_0(t_{\bar{m}}+lh)+B_{\bar{m},l+1}\delta u_0(t_{\bar{m}}-(N-l)h)\Big],
\end{aligned}
\tag{5.3.8}
$$

where $l=1,\cdots,N,\cdots,nN+\Delta N$, $A_{\bar{m},l}=\frac{\partial f_j(u_0(t),u_N(t))}{\partial u_0}|_{t=t_{\bar{m}}+h(l-1)}$, $B_{\bar{m},l}=\frac{\partial f_j(u_0(t),u_N(t))}{\partial u_N}|_{t=t_{\bar{m}}+h(l-1)}$ and $\bar{m}\in\mathbb{Z}^+$. Rewriting Eq. (5.3.8) in a matrix form gives

$$
\begin{bmatrix}
\delta u_N(t_{\bar{m}}+lh) \\
\vdots \\
\delta u_1(t_{\bar{m}}+lh) \\
\delta u_0(t_{\bar{m}}+lh)
\end{bmatrix}
= M_{\bar{m},l}
\begin{bmatrix}
\delta u_N(t_{\bar{m}}+(l-1)h) \\
\vdots \\
\delta u_1(t_{\bar{m}}+(l-1)h) \\
\delta u_0(t_{\bar{m}}+(l-1)h)
\end{bmatrix},
\tag{5.3.9}
$$

where

$$
M_{\bar{m},l}=\hat{M}_{\bar{m},l}\tilde{M}_{\bar{m},l},
$$

$$
\hat{M}_{\bar{m},l}=
\begin{bmatrix}
I & \cdots & 0 & 0 \\
\vdots & \ddots & \vdots & \vdots \\
0 & \cdots & I & 0 \\
-\frac{h}{2}B_{\bar{m},l+1} & \cdots & 0 & I-\frac{h}{2}A_{\bar{m},l+1}
\end{bmatrix}^{-1},
$$

and

$$
\tilde{M}_{\bar{m},l}=
\begin{bmatrix}
0 & I & \cdots & 0 \\
\vdots & \vdots & \ddots & \vdots \\
0 & 0 & \cdots & I \\
\frac{h}{2}B_{\bar{m},l} & 0 & \cdots & I+\frac{h}{2}A_{\bar{m},l}
\end{bmatrix}.
$$

By using the map (5.3.2), the matrix form of the variational equation (5.3.9) can be rewritten as

$$
\delta U_{\bar{m},N}=M_{\bar{m},N}\circ\cdots\circ M_{\bar{m},1}\delta U_{\bar{m},0}.
$$

Since there are $\hat{n}$ maps constructed, combining all the maps for the interval $[t_{\bar{m}}, t_{\bar{m}} + T]$ gives

$$\delta U_{\bar{m},\hat{n}} = M_{\bar{m},\hat{n}N} \circ \cdots \circ M_{\bar{m},2} \circ M_{\bar{m},1} \delta U_{\bar{m},0}.$$

In addition, the map $P_{\triangle t}$ for the interval $[t_{\bar{m}} + \hat{n}\tau_d, t_{\bar{m}} + T]$ can be written as

$$\delta U_{\bar{m}+1,0} = M_{\bar{m},\hat{n}N+\Delta N} \circ \cdots \circ M_{\bar{m},\hat{n}N} \delta U_{\bar{m},\hat{n}}. \tag{5.3.10}$$

Finally, the overall variational equation can be obtained as

$$\delta U_{\bar{m}+1,0} = M_{\bar{m}} \delta U_{\bar{m},0}, \tag{5.3.11}$$

where $M_{\bar{m}} = M_{\bar{m},\hat{n}N+\Delta N} \circ \cdots \circ M_{\bar{m},\hat{n}N} \circ \cdots \circ M_{\bar{m},1}$ is the approximation of Jacobian matrix of the Poincaré map P.

Similarly, for the system with a large delay time, e.g. $\tau_d \geq T$, the solution of system (5.2.3) can be approximated by N steps of size $h = \frac{\tau_d}{N}$ by using numerical integration, which can be considered as a special case of the nonsmooth system with a small delay time $(0 < \tau_d < T)$ when $\hat{n} = 0$. Let $N_T = \frac{T}{h}$ be the sample number for one period T, construct the map P_d, and combine all the linearised maps at the interval $[t_{\bar{m}}, t_{\bar{m}} + T]$. Finally, the same variational equation as Eq. (5.3.11) and the Jaocbian matrix of the Poincaré map P can be obtained .

5.4 Modifying the algorithm at the discontinuity

In this section, a special phenomenon of the soft impact system, the so-called crossing and grazing events will be discussed. Since the system has rich complex dynamics when it experiences grazing [54, 148], a careful consideration in calculating the time of reaching the discontinuity is required. In addition, the global error of the above proposed algorithm will depend on how accurately the algorithm captures the effect of switching, as the error made at the switching boundary could accumulate, leading to unexpected large global error. Therefore, during the grazing event, the two grazing cases illustrated in Fig. 5.4.1 will be introduced to modify the proposed algorithm from Section 5.3.

5.4.1 Case 1

In the Case 1, for time step $l^* \in \mathbb{Z}^+$ at time $t^* := t_{\bar{m}} + (l^* - 1)h$ the switching function H changes sign:$H_1 := H(u_0(t^*), e) < 0$ and $H_2 := H(u_0(t^* + h), e) > 0$, or $H_1 > 0$, $H_2 < 0$.

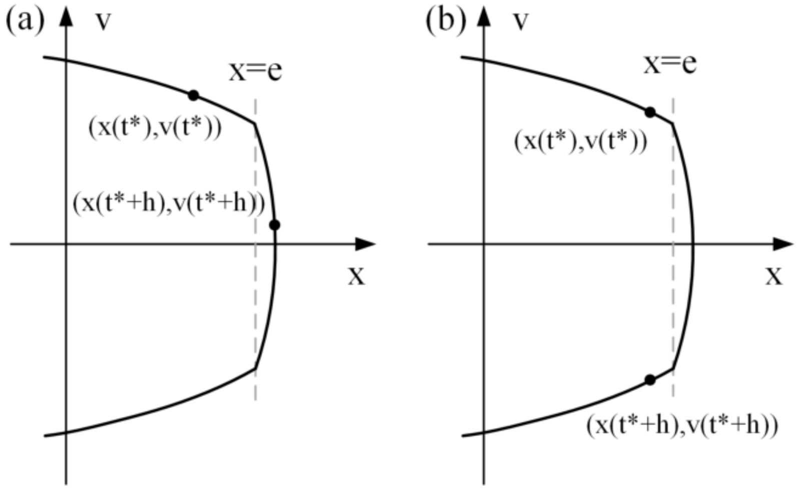

Fig. 5.4.1 (a) Case 1: for $t = t^* > 0$, such that $H_1 := H(u_0(t^*), e) < 0$ and $H_2 := H(u_0(t^* + h), e) > 0$ (or $H_1 > 0$ and $H_2 < 0$). (b) Case 2: for $t = t^* > 0$, and there exists $\delta t \in (0, h)$, such that $H_1 := H(u_0(t^*), e) < 0$, $H_2 := H(u_0(t^* + h)) < 0$ and $H_{cr,1} := H(u_0(t^* + \delta t), e) = 0$ (or $H_1 > 0$, $H_2 > 0$ and $H_{cr,1} = 0$).

Thus, for some time $\delta t \in (0, h)$, the switching fucntion is zero: $H_{cr,1} := H(u(t^* + \delta t), e) = 0$. In order to guarantee the order of convergence of the proposed algorithm to $O(h^2)$, the crossing time δt needs to be estimated first. Since $\delta t < h$, the condition $H_{cr,1} = 0$ can be linearised as

$$H_{cr,1} \approx H(u(t^*) + \dot{u}(t^*)\delta t, e) \approx H_1 + \tfrac{d}{du}H_1[\dot{u}(t^*)\delta t] = 0,$$

such that

$$\delta t = \frac{-H_1}{\frac{d}{du}H_1[\dot{u}(t^*)]}. \tag{5.4.1}$$

Once δt is calculated, the switching time $t^* + \delta t$ can be obtained, and the variational equation at the step crossing the switching can be written as

$$\begin{aligned}\delta u_0(t^* + \delta t) = \delta u_0(t^*) &+ \tfrac{\delta t}{2}[A_{\bar{m},l^*}\delta u_0(t^*) + B_{\bar{m},l^*}\delta u_N(t^*)] \\ &+ \tfrac{\delta t}{2}[A^{\delta t}_{\bar{m},l^*}\delta u_0(t^* + \delta t) + B^{\delta t}_{\bar{m},l^*}\delta u_N(t^* + \delta t)],\end{aligned} \tag{5.4.2}$$

where $A^{\delta t}_{\bar{m},l^*} = \frac{\partial f_j(u_0(t), u_N(t))}{\partial u_0}|_{t=t^-_{\bar{m}}+h(l^*-1)+\delta t}$, $B^{\delta t}_{\bar{m},l^*} = \frac{\partial f_j(u_0(t), u_N(t))}{\partial u_N}|_{t=t^-_{\bar{m}}+h(l^*-1)+\delta t}$ and $l^* = 1, \cdots, N, \cdots, \hat{n}N + \Delta N$. Thus the discretised map from t^* to $t^* + \delta t$ can be written as

$$\begin{bmatrix} \delta u_N(t^*+\delta t) \\ \vdots \\ \delta u_1(t^*+\delta t) \\ \delta u_0(t^*+\delta t) \end{bmatrix} = M^{\delta t}_{\bar{m},l^*} \begin{bmatrix} \delta u_N(t^*) \\ \vdots \\ \delta u_1(t^*) \\ \delta u_0(t^*) \end{bmatrix}, \tag{5.4.3}$$

where

$$M^{\delta t}_{\bar{m},l^*} = \hat{M}^{\delta t}_{\bar{m},l^*} \tilde{M}^{\delta t}_{\bar{m},l^*},$$

$$\hat{M}^{\delta t}_{\bar{m},l^*} := \begin{bmatrix} I & \cdots & 0 & 0 \\ \vdots & \ddots & \vdots & \vdots \\ 0 & \cdots & I & 0 \\ -\frac{\delta t}{2} B^{\delta t}_{\bar{m},l^*} & \cdots & 0 & I - \frac{\delta t}{2} A^{\delta t}_{\bar{m},l^*} \end{bmatrix}^{-1},$$

$$\tilde{M}^{\delta t}_{\bar{m},l^*} := \begin{bmatrix} 0 & I & \cdots & 0 \\ \vdots & \vdots & \ddots & \vdots \\ 0 & 0 & \cdots & I \\ \frac{\delta t}{2} B_{\bar{m},l^*} & 0 & \cdots & I + \frac{\delta t}{2} A_{\bar{m},l^*} \end{bmatrix},$$

$A_{\bar{m},l^*} = \frac{\partial f_j(u_0(t),u_N(t))}{\partial u_0}|_{t=t_{\bar{m}}+h(l^*-1)}$ and $B_{\bar{m},l^*} = \frac{\partial f_j(u_0(t),u_N(t))}{\partial u_N}|_{t=t_{\bar{m}}+h(l^*-1)}$. It is worth noting that $\delta u_i(t^*+\delta t)$ can be approximated through linear interpolation based on the historical data obtained from the delay time interval which also includes the grazing data.

Similarly, for the time interval $[t^*+\delta t, t^*+h]$, the relevant discretised map can be written as

$$\begin{bmatrix} \delta u_N(t^*+h) \\ \vdots \\ \delta u_1(t^*+h) \\ \delta u_0(t^*+h) \end{bmatrix} = \bar{M}^{h}_{\bar{m},l^*} \begin{bmatrix} \delta u_N(t^*+\delta t) \\ \vdots \\ \delta u_1(t^*+\delta t) \\ \delta u_0(t^*+\delta t) \end{bmatrix}, \tag{5.4.4}$$

where $\bar{M}^h_{\bar{m},l^*} := \hat{M}^h_{\bar{m},l^*}\tilde{M}^h_{\bar{m},l^*}$,

$$\tilde{M}^h_{\bar{m},l^*} := \begin{bmatrix} 0 & I & \cdots & 0 \\ \vdots & \vdots & \ddots & \vdots \\ 0 & 0 & \cdots & I \\ \frac{h-\delta t}{2}B^{\delta t}_{\bar{m},l^*} & 0 & \cdots & I+\frac{h-\delta t}{2}A^{\delta t}_{\bar{m},l^*} \end{bmatrix}$$

and

$$\hat{M}^h_{\bar{m},l^*} := \begin{bmatrix} I & \cdots & 0 & 0 \\ \vdots & \ddots & \vdots & \vdots \\ 0 & \cdots & I & 0 \\ -\frac{h-\delta t}{2}B_{\bar{m},l^*+1} & \cdots & 0 & I-\frac{h-\delta t}{2}A_{\bar{m},l^*+1} \end{bmatrix}^{-1}.$$

Finally, the discretised map for the time interval $[t^*, t^*+h]$can be written as

$$\begin{bmatrix} \delta u_N(t^*+h) \\ \vdots \\ \delta u_1(t^*+h) \\ \delta u_0(t^*+h) \end{bmatrix} = \bar{M}^h_{\bar{m},l^*} M^{\delta t}_{\bar{m},l^*} \begin{bmatrix} \delta u_N(t^*) \\ \vdots \\ \delta u_1(t^*) \\ \delta u_0(t^*) \end{bmatrix}. \tag{5.4.5}$$

Therefore, when Case 1 occurs, $\bar{M}^h_{\bar{m},l^*} M^{\delta t}_{\bar{m},l^*}$ should be inserted between $M_{\bar{m},l^*+1}$ and $M_{\bar{m},l^*}$ for the time interval $[t^*, t^*+h]$ in Eq. (5.3.10). The expressions for crossing events from $H > 0$ to $H < 0$ look identical, except that the subscripts 1 and 2 for f in Eq. (5.2.3) are reversed.

5.4.2 Case 2

Let δt be the first crossing time for Case 2, which can be calculated based on Eq. (5.4.1). δt^* can be defined as the time where H is maximal, such that $H_{\max} := H(u(t^* + \delta t + \delta t^*)) = \max_{t\in[t^*,t^*+h]} H(u(t), e)$, and $\delta \bar{t}$ as the time where H changes sign back, such that $H_{cr,2} := H(u(t^* + \delta t_{\text{graz}})) = 0$, where $\delta t_{\text{graz}} := \delta t + \delta t^* + \delta \bar{t}$. The estimate of δt follows Eq. (5.4.1). From a computational point of view, Case 2 can be triggered either by (i) $H_1 < 0$, $H_2 < 0$, $\frac{d}{dt}H_1 > 0$, $\frac{d}{dt}H_2 < 0$ and $0 < \delta t_{\text{graz}} < h$, or (ii) $H_1 > 0$, $H_2 > 0$, $\frac{d}{dt}H_1 < 0$, $\frac{d}{dt}H_2 > 0$ and $0 < \delta t_{\text{graz}} < h$.

Since

$$\tfrac{d}{dt}H(t^*+\delta t+t)|_{t=\delta t^*} \approx \tfrac{d}{du}H_{cr,1}[\dot{u}(t^*+\delta t)+\ddot{u}(t^*+\delta t)\delta t^*]+\tfrac{d^2}{du^2}H_{cr,1}[\dot{u}^2(t^*+\delta t)\delta t^*]=0,$$

δt^* can be obtained as

$$\delta t^* = \frac{-\frac{d}{du}H_{cr,1}[\dot{u}(t^*+\delta t)]}{\frac{d}{du}H_{cr,1}[\ddot{u}(t^*+\delta t)]+\frac{d^2}{du^2}H_{cr,1}[\dot{u}^2(t^*+\delta t)]}. \tag{5.4.6}$$

For $\delta\bar{t}$ it is convenient to have

$$\begin{aligned} H_{cr,2} &\approx H_{\max}+\tfrac{d}{du}H_{\max}[\dot{u}(t^*+\delta t+\delta t^*)]\delta\bar{t} \\ &\approx H_{\mathrm{cros},1}+\tfrac{d}{du}H_{\mathrm{cros},1}[\dot{u}(t^*+\delta t)]\delta t^* \\ &\quad+\left[\tfrac{d}{du}H_{\mathrm{cros},1}+\tfrac{d^2}{du^2}H_{\mathrm{cros},1}[\dot{u}(t^*+\delta t)\delta t^*]\right]\left[\dot{u}(t^*+\delta t)+\ddot{u}(t^*+\delta t)\delta t^*\right]\delta\bar{t}=0, \end{aligned}$$

which gives

$$\begin{aligned} \delta\bar{t} = -&\left[H_{cr,1}+\tfrac{d}{du}H_{cr,1}[\dot{u}(t^*+\delta t)]\delta t^*\right]\left[\tfrac{d^2}{du^2}H_{cr,1}\right. \\ &\left.+\tfrac{d^2}{du^2}H_{cr,1}[\dot{u}(t^*+\delta t)\delta t^*]\right]\left[\dot{u}(t^*+\delta t)+\ddot{u}(t^*+\delta t)\delta t^*\right]^{-1}. \end{aligned} \tag{5.4.7}$$

Therefore, for the step from t^* to $t^*+\delta t$, the variational equation can be written as

$$\begin{bmatrix} \delta u_N(t^*+\delta t) \\ \vdots \\ \delta u_1(t^*+\delta t) \\ \delta u_0(t^*+\delta t) \end{bmatrix} = M^{\delta t}_{\bar{m},l^*} \begin{bmatrix} \delta u_N(t^*) \\ \vdots \\ \delta u_1(t^*) \\ \delta u_0(t^*) \end{bmatrix}. \tag{5.4.8}$$

For the step from $t^*+\delta t$ to $t^*+\delta t_{\mathrm{graz}}$, the relevant map can be written as

$$\begin{bmatrix} \delta u_N(t^*+\delta t_{\mathrm{graz}}) \\ \vdots \\ \delta u_1(t^*+\delta t_{\mathrm{graz}}) \\ \delta u_0(t^*+\delta t_{\mathrm{graz}}) \end{bmatrix} = M^{\delta t_{\mathrm{graz}}}_{\bar{m},l^*} \begin{bmatrix} \delta u_N(t^*+\delta t) \\ \vdots \\ \delta u_1(t^*+\delta t) \\ \delta u_0(t^*+\delta t) \end{bmatrix}, \tag{5.4.9}$$

where

$$M^{\delta t_{\mathrm{graz}}}_{\bar{m},l^*} := \hat{M}^{\delta t_{\mathrm{graz}}}_{\bar{m},l^*}\tilde{M}^{\delta t_{\mathrm{graz}}}_{\bar{m},l^*},$$

$$\hat{M}^{\delta t_{\text{graz}}}_{\bar{m},l^*} := \begin{bmatrix} I & \cdots & 0 & 0 \\ \vdots & \ddots & \vdots & \vdots \\ 0 & \cdots & I & 0 \\ -\frac{\delta t^* + \delta \bar{t}}{2} B^{\delta t_{\text{graz}}}_{\bar{m},l^*} & \cdots & 0 & I - \frac{\delta t^* + \delta \bar{t}}{2} A^{\delta t_{\text{graz}}}_{\bar{m},l^*} \end{bmatrix}^{-1},$$

$$\tilde{M}^{\delta t_{\text{graz}}}_{\bar{m},l^*} := \begin{bmatrix} 0 & I & \cdots & 0 \\ \vdots & \vdots & \ddots & \vdots \\ 0 & 0 & \cdots & I \\ \frac{\delta t^* + \delta \bar{t}}{2} B^{\delta t}_{\bar{m},l^*} & 0 & \cdots & I + \frac{\delta t^* + \delta \bar{t}}{2} A^{\delta t}_{\bar{m},l^*} \end{bmatrix},$$

$A^{\delta t_{\text{graz}}}_{\bar{m},l^*} = \frac{\partial f_j(u_0(t), u_N(t))}{\partial u_0}\big|_{t = t^-_{\bar{m}} + h(l^*-1) + \delta t_{\text{graz}}}$ and $B^{\delta t_{\text{graz}}}_{\bar{m},l^*} = \frac{\partial f_j(u_0(t), u_N(t))}{\partial u_N}\big|_{t = t^-_{\bar{m}} + h(l^*-1) + \delta t_{\text{graz}}}$. For the period $[t^* + \delta t_{\text{graz}}, t^* + h]$,

$$\begin{bmatrix} \delta u_N(t^* + h) \\ \vdots \\ \delta u_1(t^* + h) \\ \delta u_0(t^* + h) \end{bmatrix} = \bar{M}^h_{\bar{m},l^*} \begin{bmatrix} \delta u_N(t^* + \delta t_{\text{graz}}) \\ \vdots \\ \delta u_1(t^* + \delta t_{\text{graz}}) \\ \delta u_0(t^* + \delta t_{\text{graz}}) \end{bmatrix}, \tag{5.4.10}$$

where

$$\bar{M}^h_{\bar{m},l^*} = \hat{M}^h_{\bar{m},l^*} \tilde{M}^h_{\bar{m},l^*},$$

$$\hat{M}^h_{\bar{m},l^*} := \begin{bmatrix} I & \cdots & 0 & 0 \\ \vdots & \ddots & \vdots & \vdots \\ 0 & \cdots & I & 0 \\ -\frac{h - \delta t_{\text{graz}}}{2} B_{\bar{m},l^*+1} & \cdots & 0 & I - \frac{h - \delta t_{\text{graz}}}{2} A_{\bar{m},l^*+1} \end{bmatrix}^{-1}$$

and

$$\tilde{M}^h_{\bar{m},l^*} := \begin{bmatrix} 0 & I & \cdots & 0 \\ \vdots & \vdots & \ddots & \vdots \\ 0 & 0 & \cdots & I \\ \frac{h-\delta t_{\mathrm{graz}}}{2} B^{\delta t_{\mathrm{graz}}}_{\bar{m},l^*} & 0 & \cdots & I + \frac{h-\delta t_{\mathrm{graz}}}{2} A^{\delta t_{\mathrm{graz}}}_{\bar{m},l^*} \end{bmatrix}.$$

Finally, the discretised map for the time interval $[t^*, t^*+h]$can be written as

$$\begin{bmatrix} \delta u_N(t^*+h) \\ \vdots \\ \delta u_1(t^*+h) \\ \delta u_0(t^*+h) \end{bmatrix} = \bar{M}^h_{\bar{m},l^*} M^{\delta t_{\mathrm{graz}}}_{\bar{m},l^*} M^{\delta t}_{\bar{m},l^*} \begin{bmatrix} \delta u_N(t^*) \\ \vdots \\ \delta u_1(t^*) \\ \delta u_0(t^*) \end{bmatrix}, \tag{5.4.11}$$

Thus, once Case 2 is encountered, $\bar{M}^h_{\bar{m},l^*} M^{\delta t_{\mathrm{graz}}}_{\bar{m},l^*} M^{\delta t}_{\bar{m},l^*}$ should be inserted between $M_{\bar{m},l^*+1}$ and $M_{\bar{m},l^*}$ in Eq. (5.3.10) for the step from t^* to t^*+h.

From the discussion above, an accurate Jacobian matrix for the Poincaré map (5.2.4) can be obtained. In the next section, in order to ensure the accuracy of the proposed method considering the two grazing cases, the convergence of eigenvalues of the Jacobian matrix will be discussed when a perturbation is introduced.

5.5 Convergence analysis

5.5.1 Properties of the evaluation operator

According to [149, 150], the spectrum of the Jacobian for the Poincaré map consists of eigenvalues and 0. So the Poincaré map of Eq. (5.3.7) and its relevant Jacobian will be studied.

For the space $\mathbb{C}^n$, assume $\mathbb{P} := [t_1, t_1 + \Delta T]$, which is a bounded interval in $\mathbb{R}$ and $\Delta T < +\infty$. $C(\mathbb{P}, \mathbb{C}^n)$ denotes the Banach space with all bounded continuous functions from $\mathbb{P}$ to $\mathbb{C}^n$ with the norm $||u||_C = \max_{t\in\mathbb{P}} |u(t)|$, where $u \in C(\mathbb{P}, \mathbb{C}^n)$ and $|\cdot|$ is a given norm on $\mathbb{C}^n$.

Now, Eq. (5.3.7) can be written as

$$\begin{cases} \frac{\mathrm{d}}{\mathrm{d}t}\delta u_0(t) = F(t, \delta u_0(t), \delta u_N(t)), \quad \text{where } t \in \mathbb{P} \text{ and } F : \mathbb{P}\times\mathbb{C}^n\times\mathbb{C}^n \to \mathbb{C}^n, \\ \delta u_0(t) = \phi_\delta(t), \quad \text{where } t \in [t_1 - \tau_d, t_1] \text{ and } \phi_\delta \in C([t_1 - \tau_d, t_1], \mathbb{C}^n), \end{cases} \tag{5.5.1}$$

where ϕ_δ is defined in Eq. (5.3.7). Here, let $\delta u_d(t) = \delta u_N(t)$, and F can be written as

$$F(t, \delta u_0(t), \delta u_d(t)) = F_{j,1}(t)\delta u_0(t) + F_{j,2}(t)\delta u_d(t), \tag{5.5.2}$$

where

$$\begin{cases} j = 1, \text{ if } H(u_0(t), e) > 0, \\ j = 2, \text{ if } H(u_0(t), e) < 0, \\ F(t^-, \delta u_0(t^-), \delta u_d(t^-)) = F(t^+, \delta u_0(t^+), \delta u_d(t^+)), \text{ if } H(u_0(t), e) = 0, \end{cases}$$

$F_{j,1}(t) := \frac{\partial f_j(t,u_0(t),u_d(t))}{\partial u_0}$, and $F_{j,2}(t) := \frac{\partial f_j(t,u_0(t),u_d(t))}{\partial u_d}$.

According to [119], a nonautonomous delay dynamical system can be represented as an evolution operator. So, for any $t_1 \in \mathbb{P}$ and sufficiently small $h > 0$,

$$U(t_1 + h, t_1)\phi_\delta = \delta u_0(t_1 + h), \tag{5.5.3}$$

where $\delta u_0(t_1 + h)$ is the solution of Eq. (5.5.1) at $t = t_1 + h$. For any time $t = t_1 + N_t h$, $\forall N_t \in \mathbb{Z}^+$, $\delta u_0(t)$ can be written as

$$\delta u_0(t) = U(t_1 + hN_t, t_1 + h(N_t - 1)) \cdots U(t_1 + 2h, t_1 + h)U(t_1 + h, t_1)\phi_\delta.$$

Next, the following will construct the approximation operator with finite dimension for the evolution operator $U(t_1 + h, t_1)$. In order to simplify the discussion, the following spaces can be defined

$$\mathscr{P} := C([t_1 - \tau_d, t_1], \mathbb{C}^n),$$

and

$$\mathscr{P}^+ := C([t_1, t_1 + h], \mathbb{C}^n),$$

their relevant norms

$$||\cdot|| := \max_{t \in [t_1 - \tau_d, t_1]} |\cdot|,$$

and

$$||\cdot||^+ := \max_{t \in [t_1, t_1 + h]} |\cdot|,$$

and the space

$$\mathscr{P}^* := C([t_1 - \tau_d, t_1 + h], \mathbb{C}^n),$$

with the map $L: \mathscr{P} \times \mathscr{P}^{+} \to \mathscr{P}^{*}$ satisfying

$$L(\phi_\delta, z)(\eta) = \begin{cases} \phi_\delta(t_0) + \int_{t_1}^{\eta} z(\theta) d\theta, & \text{if } \eta \in [t_1, t_1 + h], \\ \phi_\delta(\eta), & \text{if } \eta \in [t_1 - \tau_d, t_1]. \end{cases}$$

According to [119], the map L can be divided into two operators $L_1 : \mathscr{P} \to \mathscr{P}^{*}$ and $L_2 : \mathscr{P}^{+} \to \mathscr{P}^{*}$ with

$$L(\phi_\delta, \omega) = L_1 \phi_\delta + L_2 \omega, \tag{5.5.4}$$

where $(\phi_\delta, \omega) \in \mathscr{P} \times \mathscr{P}^{+}$, $L_1 \phi_\delta = L(\phi_\delta, 0)$ and $L_2 \omega = L(0, \omega)$.

In addition, a linear operator can be defined to satisfy $\Theta : \mathscr{P}^{*} \to \mathscr{P}^{+}$ and

$$[\Theta v](t) = F(t, v(t), v_d(t)), \tag{5.5.5}$$

where $v \in \mathscr{P}^{*}$, $t \in [t_1, t_1 + h]$ and $v_d(t) = v(t - \tau_d)$. The fixed point problem

$$\omega^{*} = \Theta L(\phi_\delta, \omega^{*}). \tag{5.5.6}$$

has a fixed point $\omega^{*} \in \mathscr{P}^{+}$ if the original problem (5.5.1) has a solution in $[t_1, t_1 + h]$. So ω^{*} satisfies

$$U(t_1 + h, t_1) \phi_\delta = L(\phi_\delta, \omega^{*}). \tag{5.5.7}$$

According to Eq. (5.5.4), Eq. (5.5.6) can be rewritten as

$$(I_{\mathscr{P}^{+}} - \Theta L_2) \omega^{*} = \Theta L_1 \phi_\delta \tag{5.5.8}$$

where $I_{\mathscr{P}^{+}}$ is the identity operator for the space $\mathscr{P}^{+}$. Therefore, the following properties for the operators ΘL_1 and ΘL_2 can be derived.

Proposition 1. If the operator Θ is defined by Eq. (5.5.5), it is a bounded linear operator acting on $v \in \mathscr{P}^{*}$.

Proof: Let $v_1, v_2 \in \mathscr{P}^{*}$, where

$$\Theta v_1(t) = F(t, v_1(t), v_1(t - \tau_d)),$$

and

$$\Theta v_2(t) = F(t, v_2(t), v_2(t - \tau_d)).$$

Then we can obtain

$$
\begin{aligned}
||\Theta(v_1+v_2)|| \leq & |F_{\bar{j},1}(t)v_1(t)+F_{\bar{j},2}(t)v_1(t-\tau_d)|+|F_{j,1}(t)v_2(t)+F_{j,2}(t)v_2(t-\tau_d)| \\
= & ||\Theta v_1||+||\Theta v_2||
\end{aligned}
$$

In addition, according to Eq. (5.5.2), there must exist a positive constant B_Θ satisfying that, for any $v \in \mathscr{P}^*$, $||\Theta v|| \leq B_\Theta ||v||$. Therefore, the operator Θ is bounded and linear in the space.

Proposition 2. If L_1 and L_2 are defined by Eq. (5.5.4), then $\Theta L_1 : \mathscr{P} \rightarrow \mathscr{P}^+$ and $\Theta L_2 : \mathscr{P}^+ \rightarrow \mathscr{P}^+$ are bounded linear operators with regard to $\omega \in \mathscr{P}^+$.

Proof: For all ϕ_δ, there exist $\omega_0, \omega_1, \omega_2 \in \mathscr{P}^+$ such that $\Theta L(\phi_\delta, \omega_0) = \omega_0$ and $\omega_0 = \omega_1 + \omega_2$. So, the following can be obtained

$$
\begin{aligned}
\Theta L(\phi_\delta, \omega_0) = & \Theta[L_1(\phi_\delta, \omega_1) + L_2\omega_2] \\
= & \Theta L_1(\phi_\delta) + \Theta L_2\omega_1 + \Theta L_2\omega_2 \\
= & \Theta L_1(\phi_\delta) + \Theta L_2(\omega_1 + \omega_2).
\end{aligned}
$$

According to the Eqs. (5.5.5)-(5.5.7), if $\Theta L(0, \omega) = \omega$ (where $\omega \in \mathscr{P}^+$) holds, $L(0, \omega)$ must be the solution of the following system

$$
\begin{cases}
\frac{\mathrm{d}}{\mathrm{d}t}\delta u_0(t) = F(t, \delta u_0(t), \delta u_d(t)), \\
\delta u_0(s) = 0,
\end{cases}
\tag{5.5.9}
$$

where $F \in C(\mathbb{P}, \mathbb{R}^n)$ and $s \in [t_1 - \tau_d, t_1]$. Then for any $\omega \in \mathscr{P}^+$, it gives $||\Theta L_2 \omega|| = ||\omega||$, so ΘL_2 is bounded.

Let $\phi_{\delta,1}, \phi_{\delta,2} \in \mathscr{P}$, and for $\phi_{\delta,1} + \phi_{\delta,2}$, there exists $\omega \in \mathscr{P}^+$ such that $\Theta L(\phi_{\delta,1} + \phi_{\delta,2}, \omega) = \omega$. Also, there exists ω_1, $\omega_2 \in \mathscr{P}^+$, such that $\omega = \omega_1 + \omega_2$. Then we have

$$
\begin{aligned}
L(\phi_{\delta,1} + \phi_{\delta,2}, \omega) = & L(\phi_{\delta,1}, \omega_1) + L(\phi_{\delta,2}, \omega_2) \\
= & L_1\phi_{\delta,1} + L_2\omega_1 + L_1\phi_{\delta,2} + L_2\omega_2 \\
= & L_1(\phi_{\delta,1} + \phi_{\delta,2}) + L_2\omega
\end{aligned}
$$

Since

$$
\Theta[L_1\phi_{\delta,1} + L_2\omega_1 + L_1\phi_{\delta,2} + L_2\omega_2] = \Theta L_1\phi_{\delta,1} + \Theta L_1\phi_{\delta,2} + \Theta L_2\omega
$$

and

$$\Theta[L_1(\phi_{\delta,1}+\phi_{\delta,2})+L_2\omega] = \Theta L_1(\phi_{\delta,1}+\phi_{\delta,2})+\Theta L_2\omega,$$

ΘL_1 is a bounded linear operator.

5.5.2 Approximation of the evaluation operator

Since system (5.5.1) can be approximated by large finite ODE systems, the approximated operators are constructed through discretisation by introducing the relevant discrete space for $\mathscr{P}$ and $\mathscr{P}^+$ along with the following operators. As large finite ODE systems can be obtained from the modified Euler integration, the linear interpolation will be adopt to discretise the space $\mathscr{P}$ and $\mathscr{P}^+$.

First of all, based on the time step h, consider the mesh $\Lambda_{N+1} := (t_1 - Nh, \cdots, t_1 - h, t_1)$ in $[t_1 - \tau_d, t_1]$. a restriction operator can be constructed to satisfy $r_h : \mathscr{P} \to \mathscr{P}_{N+1} := \mathbb{C}^{d(N+1)}$ on Λ_{N+1}, such that $r_h\phi_\delta \in \mathscr{P}_{N+1}$, where $[r_h\phi_\delta]_i = \phi_\delta(t_1 - (N+1-i)h) \in \mathbb{C}^n$. In addition, there exists a prolongation operator on the mesh Λ_{N+1} such that for any $\varpi_{N+1} := (\varpi^T(t_1 - Nh), \cdots, \varpi^T(t_1))^T \in \mathscr{P}_{N+1}$, where $\varpi \in \mathscr{P}$, $\bar{r}_h : t \in [t_1 - \tau_d, t_1] \to \bar{r}_h(t) \in \mathbb{C}^{1\times n(N+1)}$, $\bar{r}_h(t_1 - (N+1-i)h)\varpi_{N+1} = \varpi(t_1 - (N+1-i)h)$, $i \in \mathbb{Z}[1, N+1]$, and $\bar{r}_h(t)\varpi_{N+1}$ is a polynomial with a degree less than or equal to 2.

Similarly, consider the mesh $\Lambda_{\hat{K}+1} := (t_1, t_1 + h_s, \cdots, t_1 + \hat{K}h_s)$ in $[t_1, t_1 + h]$, where $0 < h_s < h$, $\hat{K} = h/h_s$, the space $\mathscr{P}^+$ can be discretised by the restriction operator $R_{h_s} : \mathscr{P}^+ \to \mathscr{P}^+_{\hat{K}+1} := \mathbb{C}^{n(\hat{K}+1)}$ on the mesh $\Lambda_{\hat{K}+1}$ such that $R_{h_s}\psi \in \mathscr{P}^+_{\hat{K}+1}$, where $R_{h_s}\psi^i = \psi(t_1 + (i-1)h_s) \in \mathbb{C}^n$. For mesh $\Lambda_{\hat{K}+1}$ a relevant prolongation operator can be constructed as follows. For any $\varpi_{\hat{K}+1} := (\varpi^T(t_1), \cdots, \varpi^T(t_1 + \hat{K}h_s)) \in \mathscr{P}^+_{\hat{K}+1}$, where $\varpi \in \mathscr{P}^+$, $\bar{R}_{h_s} : t \in [t_1, t_1 + h] \to \bar{R}_{h_s}(t) \in \mathbb{C}^{n(\hat{K}+1)}$, such that $\bar{R}_{h_s}(t_1 + (i-1)h_s)\varpi_{\hat{K}+1} = \varpi(t_1 + (i-1)h_s)$, $i \in \mathbb{Z}[1, \hat{K}+1]$, and $\bar{R}_{h_s}(t)\varpi_{\hat{K}+1}$ is a polynomial with degree less than or equal to $\hat{K}+1$. Here, the operator $\mathfrak{L} := \bar{R}_{h_s}(t)R_{h_s}$ is a Lagrange operator [151].

Let $\hat{K} = 1$ (i.e. $h_s = h$) and for any given N, the relevant approximated operator $U_{N+1,1}(t_1 + h, t_1) : \mathscr{P}_{N+1} \to \mathscr{P}_{N+1}$ satisfies

$$U_{N+1,2}(t_1 + h, t_1)\Phi = r_h L(\bar{r}_h(t - \tau_d)\Phi, \bar{R}_{h_s}(t)\Psi^*), \tag{5.5.10}$$

where $t \in [t_1, t_1 + h]$, $\Phi \in \mathscr{P}_{N+1}$ and $\Psi^* \in \mathscr{P}^+_{K+1}$, which is the solution of the following equation

$$\Psi^* = R_{h_s}\Theta L(\bar{r}_h(t - \tau_d)\Phi, \bar{R}_{h_s}(t)\Psi^*). \tag{5.5.11}$$

It is worth noting that the operator $\bar{R}_{h_s}$ at the time interval $[t_1, t_1 + h]$ can be more accurate if the time step h is reduced.

5.5.3 Convergence analysis for the nonzero eigenvalues of Jacobian matrix

In this section, the convergence analysis for $0 < \tau_d < T$ will be presented. The proof for $\tau_d \geq T$ is similar, so will be omitted here. In order to ensure a unique solution for the initial problem (5.5.1), a subspace $\mathscr{P}^+_{Lip}$ of $\mathscr{P}^+$ can be introduced and has the following the norm

$$||\psi||^+_{Lip} = l(\psi) + ||\psi||^+, \ \psi \in \mathscr{P}^+_{Lip},$$

where $l(\psi)$ is the Lipschitz constant of ψ, and the subspace $\mathscr{P}_{Lip}$ of $\mathscr{P}$ with the norm as

$$||\psi||_{Lip} = l(\psi) + ||\psi||, \ \psi \in \mathscr{P}_{Lip}.$$

To carry out convergence analysis for the eigenvalues of Jacobian of the Poincaré map (5.2.4), the following lemmas are given based on [119].

Lemma 5.5.1. For any $\sigma_1^*, \sigma_2^* \in \mathscr{P}^+$,

$$\sigma_1^* = \mathfrak{L}\Theta L(\phi_\delta, \sigma_1^*), \ \phi_\delta \in \mathscr{P}, \tag{5.5.12}$$

and

$$\sigma_2^* = \Theta L(\phi_\delta, \sigma_2^*), \ \phi_\delta \in \mathscr{P},$$

for sufficiently small h, then

$$||\sigma_1^* - \sigma_2^*||^+ \leq c_1 h^2, \tag{5.5.13}$$

where c_1 is a positive constant.

Proof: Based on Theorem 3.3 in [119] and let $\sigma_1^* = \sigma_2^* + \rho^*$, then

$$||\rho^*|| := ||\sigma_1^* - \sigma_2^*||^+ = ||(I_{\mathscr{P}^+} - \mathfrak{L}\Theta L_2)^{-1}|| \ ||(I_{\mathscr{P}^+} - \mathfrak{L})||^+ ||\sigma_2^*||^+_{Lip}, \tag{5.5.14}$$

For sufficiently small h, $||(I_{\mathscr{P}^+} - \mathfrak{L})||^+$ is the global error from the modified Euler integration, which satisfies

$$||(I_{\mathscr{P}^+} - \mathfrak{L})||^+ \leq c_2 h^2,$$

where c_2 is a positive constant. Since

$$I_{\mathscr{P}^+} - \mathfrak{L}\Theta L_2 = (I_{\mathscr{P}^+} - \Theta L_2) + (I_{\mathscr{P}^+} - \mathfrak{L})\Theta L_2,$$

and ΘL_2 is bounded, if $h \to 0$, $(I_{\mathscr{P}^+} - \mathfrak{L}\Theta L_2)^{-1} = (I_{\mathscr{P}^+} - \Theta L_2)$. In addition, as

$$\sigma_2^* = (I_{\mathscr{P}^+_{Lip}} - \Theta L_2)^{-1}\Theta L_1 \phi_\delta, \tag{5.5.15}$$

and

$$||\sigma_2^*||^+_{Lip} \leq ||(I_{\mathscr{P}^+_{Lip}} - \Theta L_2)^{-1}||\ ||\Theta L_1||\ ||\phi_\delta||_{Lip}, \tag{5.5.16}$$

$||\sigma_2^*||^+_{Lip}$ is bounded. Thus, there must exist a positive constant c_1 for Eq. (5.5.14) satisfying

$$||\rho^*|| \leq c_1 h^2.$$

Based on Eq. (5.5.10), a new operator in the interval $[t_1, t_1 + h]$ can be introduced as

$$\bar{U}_{N+1,2}(t_1 + h, t_1) = \bar{r}_h U_{N+1,2}(t_1 + h, t_1) r_h : \mathscr{P} \to \mathscr{P}, \tag{5.5.17}$$

which has the same geometric and partial multiplicities as the operator $U_{N+1,2}(t_1 + h, t_1)$ in Eq. (5.5.10). Therefore, there exists a map $\bar{U}_2(t_1 + h, t_1) : \mathscr{P} \to \mathscr{P}$ such that

$$\bar{U}_2(t_1 + h, t_1)\phi_\delta = L(\phi_\delta, \sigma^*),\ \phi_\delta \in \mathscr{P}, \tag{5.5.18}$$

where $\sigma^* \in \mathscr{P}^+$ is the solution of Eq. (5.5.12), and $\bar{U}_{N+1,2}(t_1 + h, t_1)$ can be written as

$$\bar{U}_{N+1,2}(t_1 + h, t_1) = \mathfrak{L}\bar{U}_2(t_1 + h, t_1)\mathfrak{L}.$$

Lemma 5.5.2. If the operator $\bar{U}_2(t_1 + h, t_1)$ is defined as Eq. (5.5.18), then

$$||\bar{U}_2(t_1 + h, t_1) - U(t_1 + h, t_1)|| \leq c_3 h^3, \tag{5.5.19}$$

where c_3 is a positive constant.

Proof: For $(\phi_\delta, \omega_1^*)$, $(\phi_\delta, \omega_2^*) \in \mathscr{P}^+_{Lip} \times \mathscr{P}^+$, based on Eq. (5.5.4), It is easy to have

$$||\bar{U}_2(t_1 + h, t_1) - U(t_1 + h, t_1)|| = ||L(\phi_\delta, \omega_1^*) - L(\phi_\delta, \omega_2^*)|| = ||L_2(\omega_1^* - \omega_2^*)||,$$

where

$$\omega^* = \bar{I}_{\mathscr{P}^+}\Theta L(\phi_\delta, \omega_1^*)$$

and

$$\sigma^* = \Theta L(\phi_\delta, \omega_2^*).$$

So

$$\begin{aligned}||\bar{U}_2(t_1+h,t_1)-U(t_1+h,t_1)|| =&||L_2(\omega_1^*-\omega_2^*)||\\ =&||\int_{t_1}^{t_1+h}(\omega_1^*-\omega_2^*)(t)\mathrm{d}t|| = ||(\omega_1^*-\omega_2^*)||^+h.\end{aligned}$$

According to Eqs. (5.5.14) and (5.5.15) and the inequality (5.5.16), then the following can be obtained

$$||\bar{U}_2(t_1+h,t_1)-U(t_1+h,t_1)|| \leq c_3h^3.$$

It is worth noting that the evolution operator $\bar{U}_2(t_1+ih,t_1+(i-1)h)$, where $i=1,\cdots,\bar{N}$ and $\bar{N}:=N+\hat{n}+\triangle N+1$, must have the same properties as the operator $U(t_1+ih,t_1+(i-1)h)$ in the inequality (5.5.19). Thus, the Poincaré map can be obtained by combining all the evolution operators $U(t_1+ih,t_1+(i-1)h)$ over the entire time interval $[t_1,t_1+T]$. As a result, the convergence problem is equivalent to studying the convergence of the operator $\prod_{i=1}^{\bar{N}}\bar{U}_2(t_1+ih,t_1+(i-1)h)$ to $U(t_1,t_1+T)$.

Lemma 5.5.3. For the entire interval $[t_1,t_1+T]$ and a sufficiently small time step h, then we can obtain

$$||U(t_1+T,t_1)-\prod_{i=1}^{\bar{N}}\bar{U}_2(t_1+ih,t_1+(i-1)h)|| \leq c_4h^2, \tag{5.5.20}$$

where $i=1,2,\cdots,\bar{N}$, $\bar{N}:=N+\hat{n}+\triangle N+1$, and c_4 is a positive constant.

Proof : According to Lemma 5.5.2, there are two positive constants M_1 and M_2 such that

$$||\prod_{i=2}^{\bar{N}-1}U(t_1+ih,t_1+(i-1)h)|| \leq M_1, \tag{5.5.21}$$

and

$$||\prod_{j=1}^{\bar{N}-1}\bar{U}_2(t_1+jh,t_1+(j-1)h)|| \leq M_2. \tag{5.5.22}$$

Therefore,

$$\begin{aligned}&||U(t_1+T,t_1)-\prod_{i=1}^{\bar{N}}\bar{U}_2(t_1+ih,t_1+(i-1)h)||\\ \leq&\bar{N}\prod_{i=2}^{\bar{N}-1}U(t_1+ih,t_1+(i-1)h)\prod_{j=1}^{\bar{N}-1}\bar{U}_2(t_1+jh,t_1+(j-1)h)c_3h^3\\ \leq&\bar{N}M_1M_2c_3h^3 = \frac{T}{h}M_1M_2c_3h^3 = c_4h^2.\end{aligned}$$

It should be noted that $\bar{U}_{N+1,2}$ and $\bar{U}_2$ have the same nonzero eigenvalues, geometric and partial multiplicities and eigenvectors. This leads to the following theorem.

Theorem 5.5.4. Let $\lambda \in \mathbb{C} \setminus \{0\}$ be an isolated eigenvalue for the operator $U(t_1+T,t_1)$ with the finite algebraic multiplicity m_a and the ascent κ, and let Γ be a neighborhood of λ for the time interval $[t_1,t_1+T]$. For a sufficiently small h, $\bar{U}_{N+1,2}(t_1+T,t_1)$ has m_a eigenvalues $\lambda_{N+1,2,\imath}$, where $\imath = 1,\ldots,m_a$, and such that

$$\max_{\imath=1,\ldots,m_a} |\lambda - \lambda_{N+1,2,\imath}| \le c_6 h^{\frac{2}{\kappa}}, \tag{5.5.23}$$

where c_6 is a positive constant.

The inequality (5.5.23) holds for any interval $[t_{\bar{m}},t_{\bar{m}}+T]$. The above study can ensure that the proposed approximation method in this chapter has the expected convergence rate on the nonzero characteristic multipliers of the system (5.5.1). So this approximation for the Jacobian of the Poincaré map (5.2.4) is reliable. It is also worth noting that by adopting a high-order integration method (e.g. Runge-Kutta method) with a sufficiently small time step h, the approximated operator could be more accurate $O(h^4)$. However, this would also require higher-order corrections at the crossing and grazing events for the terms derived in Section 5.4. Without these corrections the convergence of the approximated operator cannot be guaranteed to be the same as the order of the numerical integration. Furthermore, if the system encounters a sufficiently large number of grazing events, the convergence rate will be lower than $O(h^2)$ due to these grazing events.

5.6 Calculation of the Lyapunov exponents

The dynamics of system (5.2.3) can be represented by the Poincaré map (5.2.4) as

$$Y_{\bar{m}+1,0} = P^{\bar{m}}(Y_{1,0}) = P \circ \cdots P \circ P(Y_{1,0}), \tag{5.6.1}$$

where the Jaobian matrix of $P^{\bar{m}}$ is $\prod_{i=1}^{\bar{m}} M_i$. According to Definition 5.2.1, LEs can be calculated as

$$\vartheta_i = \lim_{\bar{m}\to\infty} \frac{1}{\bar{m}} \ln|\lambda_i^{\bar{m}}|,\ i = 1,\cdots,n(N+1), \tag{5.6.2}$$

where $\lambda_i^{\bar{m}}$ is the i^{th} eigenvalues of $\prod_{i=1}^{\bar{m}} M_i$.

However, calculating LEs by using Eq. (5.6.2) will introduce an overflow problem. Specifically, some elements of the Jacobian matrix will be very large for chaotic attractors, and some of them could be very small for periodic attractors, which may cause inaccuracy.

On the other hand, calculating LEs from the Jacobian matrix directly is time-consuming as the delay dynamical system is high-dimensional. To overcome these issues , LEs can be computed according to the average exponential divergence rate between the basis orbit started from $Y_1(0)$ and its neighborhood orbit along the direction of $v_{1,0} = \frac{Y_{1,0}}{||Y_{1,0}||}$ as

$$\vartheta(Y_{1,0}, v_{1,0}) = \lim_{\bar{m}\to\infty} \frac{1}{\bar{m}} \ln \frac{||\delta Y_{\bar{m},0}||}{||\delta Y_{1,0}||}, \tag{5.6.3}$$

where $||\delta Y_{\bar{m},0}||$ is the norm of $\delta Y_{\bar{m},0}$ and $\bar{m} \in \mathbb{Z}^+$.

Next, choose $Y_{1,0} \in \mathbb{R}^{n(N+1)}$, and its related linearly independent initial perturbed vector $(\delta Y_{1,0}^1, \delta Y_{1,0}^2, \cdots, \delta Y_{1,0}^{n(N+1)})$ can be normalised as

$$(\delta v_{1,0}^1, \delta v_{1,0}^2, \cdots, \delta v_{1,0}^{n(N+1)}) = (\frac{\delta Y_{1,0}^1}{||\delta Y_{1,0}^1||}, \frac{\delta Y_{1,0}^2}{||\delta Y_{1,0}^2||}, \cdots, \frac{\delta Y_{1,0}^{n(N+1)}}{||\delta Y_{1,0}^{n(N+1)}||}). \tag{5.6.4}$$

Substituting the vector (5.6.4) to Eq. (5.6.1) obtains the second vector $(\delta Y_{2,0}^1, \delta Y_{2,0}^2, \cdots, \delta Y_{2,0}^{n(N+1)})$, and Gram-Schmidt orthonormalization [147] can be applied to normalise the second vector, which gives a new vector $(\delta v_{2,0}^1, \delta v_{2,0}^2, \cdots, \delta v_{2,0}^{n(N+1)})$. For the next iteration, the second vector will be used as the initial vector to be substituted into Eq. (5.6.1). Likewise, repeating $\bar{m}$ times for this process gives the $\bar{m}^{\text{th}}$ vector $(\delta Y_{\bar{m},0}^1, \delta Y_{\bar{m},0}^2, \cdots, \delta Y_{\bar{m},0}^{n(N+1)})$. The steps of Gram-Schmidt orthonormalization are given as follows

$$\begin{aligned}
V_{\bar{m},0}^1 &= \delta Y_{\bar{m},0}^1, \\
\delta v_{\bar{m},0}^1 &= \frac{V_{\bar{m},0}^1}{||V_{\bar{m},0}^1||}, \\
V_{\bar{m},0}^2 &= \delta Y_{\bar{m},0}^2 - < \delta Y_{\bar{m},0}^2, \delta v_{\bar{m},0}^1 > \delta v_{\bar{m},0}^1, \\
\delta v_{\bar{m},0}^2 &= \frac{V_{\bar{m},0}^2}{||V_{\bar{m},0}^2||}, \\
&\vdots \\
V_{\bar{m},0}^{n(N+1)} &= \delta Y_{\bar{m},0}^{2(N+1)} - < \delta Y_{\bar{m},0}^{2(N+1)}, \delta v_{\bar{m},0}^1 > \delta v_{\bar{m},0}^1 - \cdots \\
&\quad - < \delta Y_{\bar{m},0}^{n(N+1)}, \delta v_{m,0}^{n(N+1)-1} > \delta v_{\bar{m},0}^{n(N+1)-1},
\end{aligned}$$

$$\delta v_{\bar{m},0}^{n(N+1)} = \frac{V_{\bar{m},0}^{n(N+1)}}{||V_{\bar{m},0}^{n(N+1)}||},$$

where $||V^i_{\bar{m},0}||$ is the norm of $V^i_{\bar{m},0}$, $\langle \delta Y^i_{\bar{m},0}, \delta v^{\bar{i}}_{\bar{m},0} \rangle$ $(i,\bar{i}=1,2,\cdots,d(N+1))$ is a standard scalar product. Finally, LEs can be calculated by using

$$\vartheta_i \approx \frac{1}{\bar{m}} \ln \prod_{\rho=1}^{\bar{m}} ||V^i_\rho(0)|| = \frac{1}{\bar{m}} \sum_{\rho=1}^{\bar{m}} \ln ||V^i_\rho(0)||. \tag{5.6.5}$$

Remark. Based on the above analysis, a guideline for the implementation of the algorithm is presented as follows, and the flowchart of the algorithm is shown in Fig. 5.6.1.

Step 1: Calculate the Jacobian matrix according to the relevant trajectory at the time step after the system is stabilised by the delay feedback control;

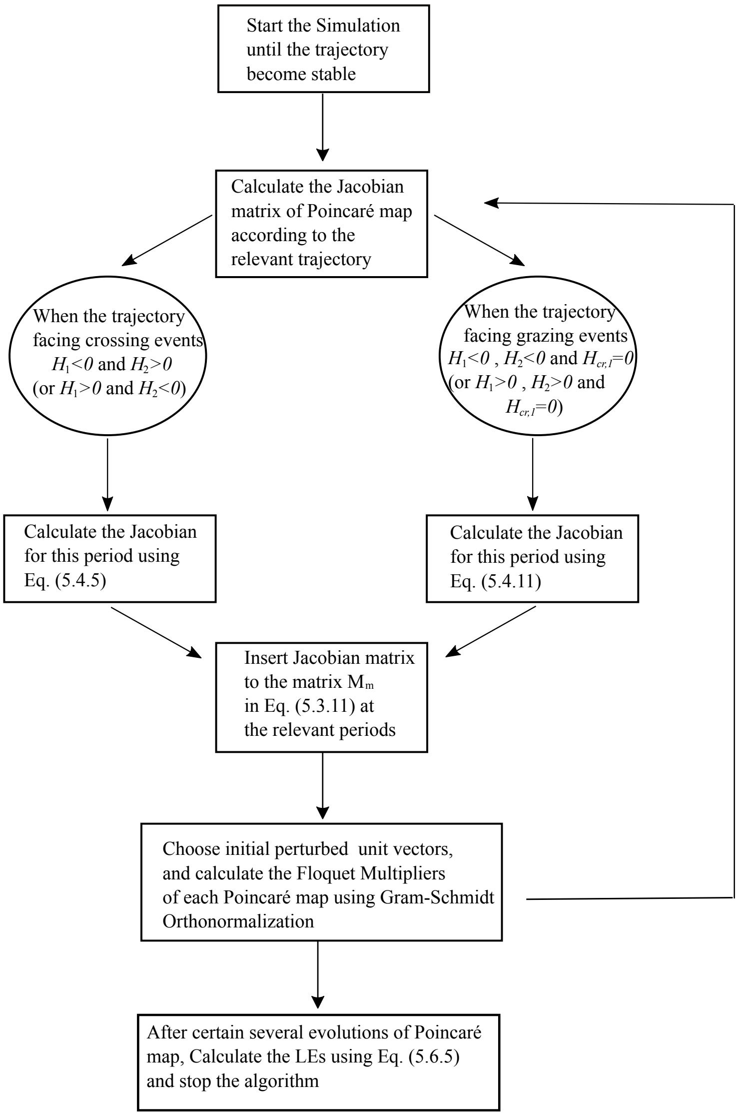

Fig. 5.6.1 Flowchart of the algorithm for calculating LEs.

Step 2: If the trajectory approaches to grazing, calculate its relevant Jacobian using Eq. (5.4.5) or Eq. (5.4.11), and then insert it to the matrix $M_{\bar{m}}$ in Eq. (5.3.11) at the grazing moment;

Step 3: Choose appropriate initial perturbed unit vectors, and calculate the Floquet Multipliers of each Poincaré map using Gram-Schmidt orthonormalization;

Step 4: Calculate the LEs using Eq. (5.6.5) after several evolutions of Poincaré map.

5.7 Numerical studies

This section will show the effectiveness of the proposed method by studying the soft impacting system with a delay feedback control presented in Fig. 3.2.1. Since the system has many coexisting attractors when grazing is encountered [1], the control objective here is to drive the system from its current attractor to a desired one. Calculating the LEs of the system allows us to monitor the stability of the delay feedback control and its effective parametric regime.

The following parameters for the impacting system are chosen,

$$\zeta = 0.01,\ e = 1.26,\ a = 0.7,\ \beta = 28 \text{ and } \omega = 0.802.$$

For these parameters a grazing event is encountered, and a chaotic and a period-5 attractors coexist as shown in Fig. 5.7.1.

5.7.1 Case $\tau_d \geq T$

Fig. 5.7.2 presents the first example of using the delay feedback control (5.2.2) for which a large delay time (i.e. $\tau_d \geq T$) was considered, and the control parameter K was varied from 0 to 1.4. As can be seen from Fig. 5.7.2(a), the largest LEs are all greater than 0 for $K \in [0, 0.04]$ and the system presents a chaotic motion as shown in Fig. 5.7.2(b). The phase trajectory of the chaotic motion for $K = 0.02$ is presented in Fig. 5.7.2(c). For $K \in (0.04, 0.055)$, the largest LEs decrease and suddenly increase to the neighbourhood of zero at $K = 0.055$ indicating a period doubling of the system. Similarly, at $K = 0.065$, such a fluctuation is observed again. Thereafter, the largest LEs decrease dramatically, and then increase gradually from $K = 0.07$. For $K \in [0.07, 1.4]$, both LEs are below zero, and the system has period-1 response which is demonstrated by Figs. 5.7.2(d) and (e).

A critical issue for computing nonsmooth dynamical systems is that the accumulated computational error from the impact boundary due to grazing event could lead to inaccurate simulation. Fig. 5.7.3 compares the computations of the impacting system for $e = 1.2609$

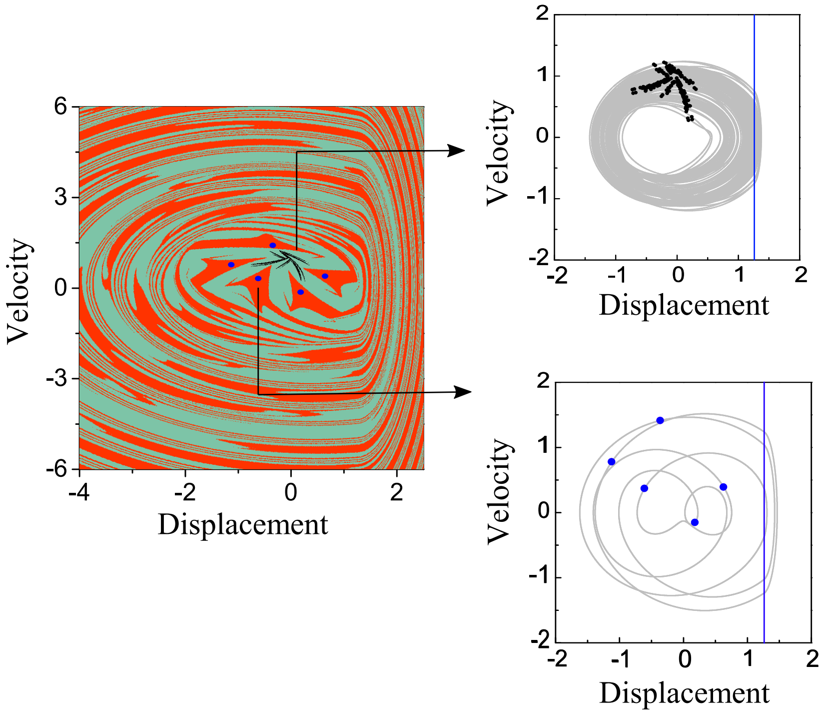

Fig. 5.7.1 Basin of attraction of the impacting system computed for $\zeta = 0.01$, $e = 1.26$, $a = 0.7$, $\beta = 28$ and $\omega = 0.802$. Black dots denote the chaotic attractor with green basin, blue dots represent the period-5 attractor with red basin, and blue lines denote the impact boundary.

controlled from a chaotic response to a period-1 response by using the delay feedback control with and without the grazing estimation algorithm. The number of impacts as a function of time without (black line) and with (orange line) the grazing estimation algorithm is presented in Fig. 5.7.3(a) which were counted from $t = 9722$, and the phase trajectories from chaotic (grey line) to period-1 (red line) response are shown in Fig. 5.7.3(b). It can be seen from the figure that the accumulated error was built up in the number of impacts, and a clear difference can be observed from $t = 10411$. The cause of such a difference can be found from Figs. 5.7.3(c) and (d), where the time histories of displacement of the impacting system are shown. As can be seen from these two figures, the system with the grazing estimation algorithm was stabilised quicker than the one without the algorithm.

5.7.2 Case $0 < \tau_d < T$

For the case of a small time delay (i.e. $0 < \tau_d < T$), the example for $\tau_d = T/2$ is shown in Fig. 5.7.4. It can be seen from the figures that the system has chaotic motion for $K \in [0, 0.007]$ and its largest LEs are all greater than zero (green line). For $K \in (0.007, 0.015]$, the system experiences transient periodic motion, and the relevant largest LEs are smaller than zero which

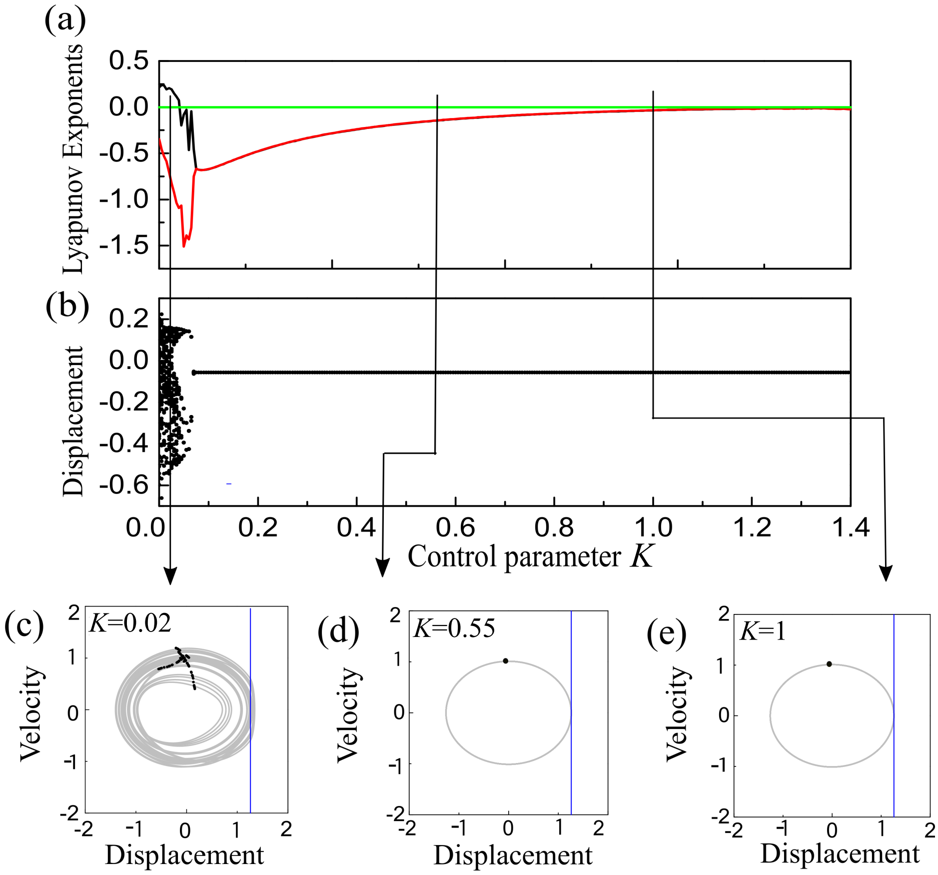

Fig. 5.7.2 (a) LEs and (b) displacement of the impacting system under the delay feedback controller as functions of the control parameter K. Black, red and green lines denote the two largest LEs and the zero line, respectively. Additional panels show the phase trajectories of the system calculated for (c) $K = 0.02$, (d) $K = 0.55$ and (e) $K = 1$. Black dots represent the Poincaré sections, and blue lines represent the impact boundary.

is consistent with the result shown in Fig. 5.7.4(b) indicating several alternations between chaotic and periodic motions. At $K = 0.016$, the system has a very narrow chaotic window and bifurcates into a non-impact period-1 response immediately lasting until $K = 0.0425$ at where another chaotic regime is encountered. For $K \in [0.0425, 0.045]$, the system has chaotic response in most of the region, but has a small window of period-3 response in $K \in [0.044, 0.04475]$. After $K = 0.045$, the non-impact period-1 response emerges again as the control parameter k increases. To compare Figs. 5.7.4(a) and (b), the evolution of the calculated LEs is consistent with system's bifurcation, which is also demonstrated by the phase trajectories presented in Figs. 5.7.4(c)-(f).

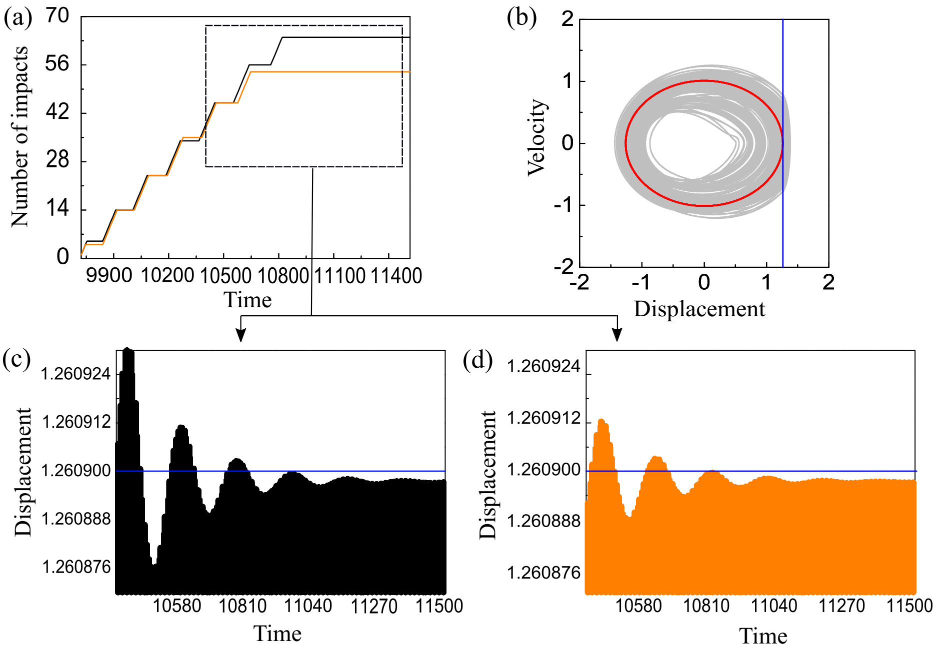

Fig. 5.7.3 (a) Number of impacts as a function of time without (black line) and with (orange line) the grazing estimation algorithm based on the discontinuous condition calculated for $\zeta = 0.01$, $e = 1.2609$, $a = 0.7$, $\beta = 28$, $\omega = 0.802$ and $K = 1.4$. (b) Phase trajectories of the impacting system controlled from chaotic (grey line) to period-1 (red line) response. Time histories of displacement of the system (c) without and (d) with the algorithm are presented, and blue lines indicate the discontinuous boundary.

5.8 Conclusion

This chapter studies a numerical method for calculating the LEs of nonsmooth delay systems by using a soft impact system under the delay feedback control with a particular focus on its near-grazing dynamics. The main feature of the proposed method is that it can provide improved accuracy for the stability analysis of periodic orbits by estimating the point of discontinuity locally along trajectories of nonsmooth DDEs with an accuracy of the same order as its integration method. In addition, the method can also be applied to the other nonsmooth dynamical systems with a delay argument, such that it can be used as a generic computational tool for stability analysis.

The main tasks were to build an effective variational equation and obtain the Jacobian for the delay soft impact system. As this system is infinite dimensional, it was approximated by finite dimensional systems, which were discretised by the modified Euler integration method at each time step. Then the DDE system was converted to a time-discrete map by constructing a Poincaré map, and its linearisation was introduced to obtain its variational equation. Then the Jacobian of the map was obtained by combining all the approximating

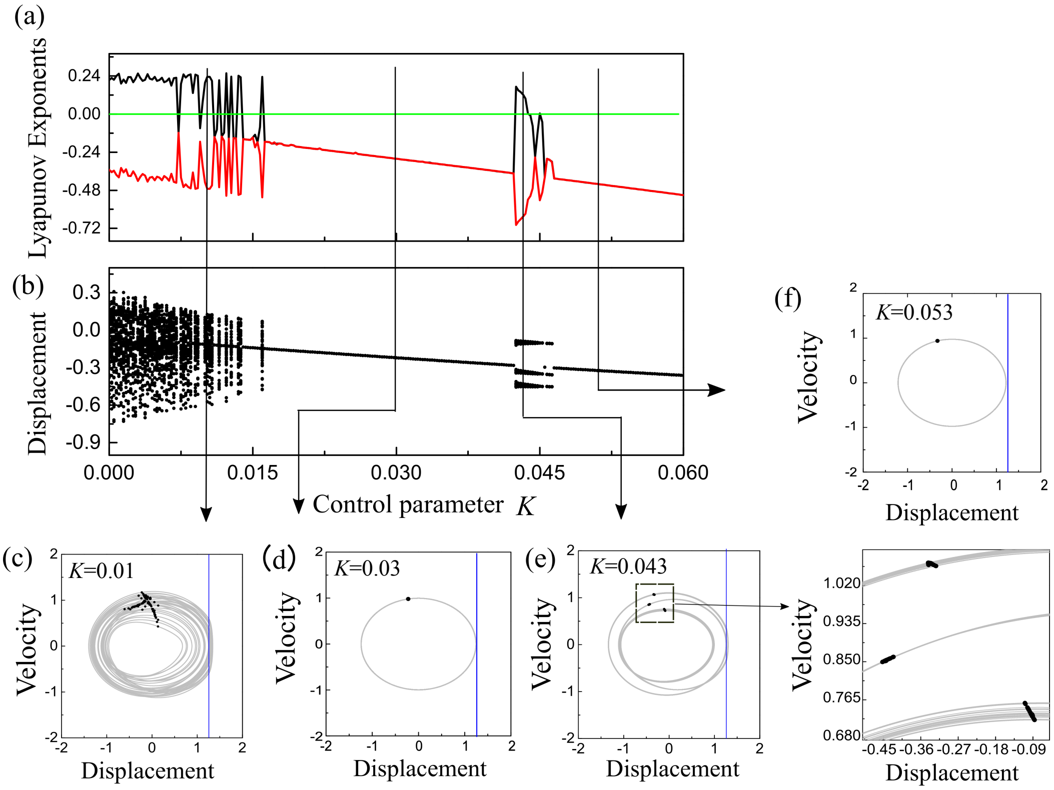

Fig. 5.7.4 (a) LEs and (b) displacement of the impacting system under the delay feedback controller as functions of the control parameter K. Black, red and green lines denote the two largest LEs and the zero line, respectively. Phase trajectories of the system calculated for (c) $K = 0.01$, (d) $K = 0.03$, (e) $K = 0.043$ and (f) $K = 0.052$ are shown. Black dots represent the Poincaré sections, and blue lines indicate the nonsmooth boundary.

systems linearised from the variational equation at each time step in one period of external excitation. In order to increase the convergence rate and improve computational accuracy, a grazing estimation algorithm was introduced. The convergence rate of eigenvalues of the Jacobian matrix was studied by using the spectral theory of the evolutionary operator. In particular, the delay soft impact system was described as an evolutionary operator with the expected convergence rate for the relevant nonzero eigenvalues of the Jacobian, therefore guaranteeing the reliability of the proposed numerical method.

The numerical studies considered two scenarios of delay time in the system, a larger ($\tau_d \geq T$) and a smaller ($0 < \tau_d < T$) delay than the period of excitation. Both cases showed that the calculated LEs were consistent with the bifurcation of the system, and the grazing estimation algorithm did improve accuracy for simulating nonsmooth dynamical systems.

Chapter 6

Control of coexisting attractors by the delay feedback control

6.1 Introduction

It is well-known that delay feedback control was originally proposed by Pyragas [19] for controlling chaos. In fact, this controller also can be used to control the multistability of dynamical systems, including nonsmooth dynamical systems. The control's aim is to achieve the switching from one of its coexisting attractors to a target attractor. If τ_d in Eq. (5.2.2) is equal to the forcing period and the system with delay feedback control shows periodic motion with period τ_d, the control effort $u(\tau)$ is zero (hence, called *non-invasive*). In addition, due to the effect from the delay feedback controller, the multistability of system can disappear, and only some attractors with the certain periods or multiple of this periods left. Thus, the delay feedback controller is a powerful tool for controlling multistability.

This chapter will present the details about how the delay feedback controller is working on controlling coexisting attractors of nonsmooth systems. The chapter is organised as follows. In Section 6.2, it presents the details on how the delay feedback controller is controlling the multistability of soft impact system and the dynamical responses of the controlled soft impact system. In Section 6.3, it shows the dynamical response of the impact system with a drift under the control from the delay feedback controller. In Section 6.4, it shows a vibro-impact capsule system can be controlled by the delay feedback controller. Some conclusions are drawn in Section 6.5.

6.2 Control of the soft impact system via the delay feedback control

6.2.1 Mathematical preparation

Because system (3.2.3) has many coexisting attractors, when the grazing occurs. In order to suppress the near-grazing multistability of the soft impact system, a delay feedback controller [67] is applied to system (3.2.3) by adding an input $u(\tau)$ as Eq. (5.2.2), and the soft impact system with a delay feedback control can be written as Eq. (5.2.1). In Eq. (5.2.2) $K \geq 0$ is the control gain, setting the coupling strength between the soft impact system output $v(\tau-\tau_d)-v(\tau)$ and the control input $u(\tau)$, and $\tau_d > 0$ is a tunable time delay (in contrast to a lag introduced by the control loop, which is assumed to be zero here). Since the purpose of this present work is to control the system to a period-1 response, the delay term τ_d is set to one period of the external excitation $\tau_d = T := 2\pi/\omega$.

Construction of the Stroboscopic map

To calculate the LEs, a Stroboscopic map needs to be constructed to obtain a discrete-time system. For the nonsmooth DDEs (5.2.1), a constant phase surface can be defined as

$$P_s^T := \{(y,\tau) \in \mathbb{R}^2 \times \mathbb{R}^+ |\ \tau = \tau_0 + kT,\ k \in \mathbb{Z}^+\}, \tag{6.2.1}$$

and the relevant continuous Stroboscopic map is

$$P_D:\ P_s^T \to P_s^T, \tag{6.2.2}$$

which is defined by the semiflow described by the nonsmooth DDE system (5.2.1). The two regions are determined by the Heaviside step function on their right-hand side of system (5.2.1). Since the system's dynamics can be described using the Stroboscopic map (6.2.2), the following discussion will use the definition of LEs for discrete-time dynamical systems.

Definition 6.2.1. [108] For any initial condition $x_0 \in P_s^T$, let $\{x_m\}_{m^*=0}^{\infty}$ be the corresponding orbit of the map P_D, and let $\lambda_0^{m^*}, \cdots, \lambda_n^{m^*}$ be the n largest in modulus eigenvalues of $D(P_D)^{m^*}(x_0)$, sorted such that $|\lambda_0^{m^*}| \geq \ldots \geq |\lambda_n^{m^*}|$. The LEs of x_0 are

$$\vartheta_i := \lim_{m^* \to \infty} \ln |\lambda_i^{m^*}|^{\frac{1}{m^*}}, i = 1, \ldots, n \tag{6.2.3}$$

whenever the limit exists for x_0 and for all $i \leq n$.

Construction of basins of attraction

Similarly, the relevant continuous Stroboscopic map of the uncontrolled system (3.2.3) can be constructed as

$$P:\ P_s^T \to P_s^T, \tag{6.2.4}$$

which is defined as a semiflow with two dimensions, or is consisted as two regions. The basin of a compact invariant subset $A \subset M$ of system (3.2.3) is defined as

$$\mathscr{B}(A) := \{y \in M : (P)^{\tau}(y) \in A, \tau \to +\infty\}, \tag{6.2.5}$$

where the manifold M is two dimensional.

According to the construction of the maps P and P_D, the basin of a compact invariant subset $A \subset M$ of system (5.2.1) can be defined as

$$\mathscr{B}_d(A) := \{y \in M : (P_D)^{\tau} \circ P(y) \in A \text{ for } \tau \to \infty\}. \tag{6.2.6}$$

Thus, by monitoring the evolution of the basin (6.2.6) through varying system parameters and comparing with the basin (6.2.5) for the system (3.2.3), multistability in the system (5.2.1) can be observed.

Construction of the Jacobian matrix

In order to construct the Jacobian matrix of the map (6.2.2), system (5.2.1) can be written as a nonlinear DDE of the form

$$q' = f(\tau, q, q(\tau - \tau_d)) \tag{6.2.7}$$

by inserting Eqs. (5.2.2) into (5.2.1). For this DDE τ is in $\mathbb{P}$, where $\mathbb{P}$ is an interval of $\mathbb{R}^+$ unbounded on the right, and $f : \mathbb{P} \times \mathbb{R}^2 \times \mathbb{R}^2 \to \mathbb{R}^2$ is a piecewise-smooth function based on the Heaviside step function. Take $N \in \mathbb{Z}^+$ sufficiently large, and define the grid points $\tau_d^i := i\frac{\tau_d}{N}$, $i = 0, \ldots, N$, and $\bar{y}_i(t) := q(t - \tau_d^i)$ for all $t \geq 0$, $i = 0, \ldots, N$, where $\tau_d := T$. The DDE (6.2.7) can be approximated as a $2(N+1)$-dimensional piecewise-smooth discretised system, as studied in [116]. Thus, in detail, for any time interval $[\tau_{\bar{m}}, \tau_{\bar{m}} + \tau_d]$, where $\tau_{\bar{m}} = \tau_1 + (\bar{m} - 1)T$, $\tau_1 = \tau_0$ and $\bar{m} \in \mathbb{Z}^+$, the solution of DDE (6.2.7) can be approximated by N steps of size $h = \frac{\tau_d}{N}$ by using numerical integration. The modified Euler integration formula [147] gives a single step of size as

$$\begin{aligned}\bar{y}_0(\tau_{\bar{m}}+h) =&\bar{y}_0(\tau_{\bar{m}})+\tfrac{h}{2}\Big[f(\tau_{\bar{m}},\bar{y}_0(\tau_{\bar{m}}),\bar{y}_0(\tau_{\bar{m}}-hN))\\ &+f(\tau_{\bar{m}+1},\bar{y}_0(\tau_{\bar{m}+1}),\bar{y}_0(\tau_{\bar{m}}-h(N-1)))\Big].\end{aligned} \tag{6.2.8}$$

Applying the recursion (6.2.8) $N+1$ times, the discretised the map P_D can be obtained and such that $F_P:\mathbb{R}^{2(N+1)}\to\mathbb{R}^{2(N+1)}$, mapping $Y_{\bar{m}}:=(\bar{y}_N^T(\tau_{\bar{m}}),\cdots,\bar{y}_1^T(\tau_{\bar{m}}),\bar{y}_0^T(\tau_{\bar{m}}))^T\in\mathbb{R}^{2(N+1)}$ to $Y_{\bar{m}+1}=F_P(Y_{\bar{m}})$, where $Y_{\bar{m}+1}:=(\bar{y}_N^T(\tau_{\bar{m}}+\tau_d),\cdots,\bar{y}_1^T(\tau_{\bar{m}}+\tau_d),\bar{y}_0^T(\tau_{\bar{m}}+\tau_d))^T\in\mathbb{R}^{2(N+1)}$. When an arbitrary perturbation δY is applied, the variational equation for F_P can be written as

$$\delta Y_{\bar{m}+1}=\sum_{i=1}^{N+1}\frac{\partial F_P(Y_{\bar{m}})}{\partial\bar{y}_{i-1}(\tau_{\bar{m}})}\delta y_{i-1}(\tau_{\bar{m}}), \tag{6.2.9}$$

where $\delta Y_{\bar{m}}:=(\delta y_N^T(\tau_{\bar{m}}),\cdots,\delta y_1^T(\tau_{\bar{m}}),\delta y_0^T(\tau_{\bar{m}}))^T\in\mathbb{R}^{2(N+1)}$ and $\delta y_i(\tau):=\delta y(\tau-\tau_d^i)$, $i=0,\cdots,N$. As Eq. (6.2.9) can be obtained by linearising the variational equation of the nonlinear differential equation as

$$\frac{\mathrm{d}}{\mathrm{d}\tau}\delta y_0(\tau)=\frac{\partial f(\tau,\bar{y}_0(\tau),\bar{y}_N(\tau))}{\partial y_0}\delta\bar{y}_0(\tau)+\frac{\partial f(\tau,\bar{y}_0(\tau),\bar{y}_N(\tau))}{\partial\bar{y}_N}\delta\bar{y}_N(\tau), \tag{6.2.10}$$

using the modified Euler integration formula, Eq. (6.2.10) can be disretised in the same way as Eq. (6.2.8). Iterating this process for $N+1$ times, the approximation of Jacobian matrix $J_{\bar{m}}$ of the map P_D, applied to $\delta Y_{\bar{m}}$, equals $\delta Y_{\bar{m}+1}$, such that $J_{\bar{m}}$ can be assembled through the relation

$$\delta Y_{\bar{m}+1}=J_{\bar{m}}\delta Y_{\bar{m}}.$$

Then, for an arbitrary sufficiently small $\delta>0$, through selecting an arbitrary initial separation vector (e.g. $\delta Y_1=(0,\cdots,0,0,\delta)^T$) and renormalisation, and calculating the leading LEs of the map P_D along approximate trajectory $\bar{y}_i(\tau_{\bar{m}})$ using Gram-Schmidt orthonormalisation and Eq. (6.2.3), which details have been shown in Chapter 5.

6.2.2 Numerical investigation of the soft impact system with the delay feedback controller

The numerical investigation starts with the bifurcation analysis of near-grazing dynamics of the soft impact system without the delay feedback control, as given in Eq. (3.2.3). Fig. 6.2.1 shows the bifurcation diagram of the system (3.2.3) with excitation $\omega\in[0.845,0.854]$ as the bifurcation parameter. The calculation was run for 350 cycles of external excitation, and the data for the first 300 cycles were omitted to ensure the steady state response, whereas the last

50 values of the displacement x at $\tau = \frac{2n_s\pi}{\omega}$, $n_s \in \mathbb{Z}^+$ were plotted in the bifurcation diagram for each value of the bifurcation parameter. For the range $\omega \in [0.851, 0.8512]$, the system present many coexisting attractors: one period-7, one period-4 and one period-3 orbits, shown as green, red and blue dots, respectively. The additional panels of Fig. 6.2.1 show the continuous-time trajectories of the orbits and the corresponding discrete orbits of the Stroboscopic map for $\tau_0 = 0$. At $\omega = 0.845$ (first row), the system presents a period-1 (blue) and a period-7 (green) attractors. At $\omega = 0.8510$ (second row), there are a period-3 (blue), a period-7 (green), and a period-4 (red) orbits. At $\omega = 0.8513$ (third row), the system has a period-3 (blue) and a period-7 (green) responses, which both persist throughout the entire parameter range. Please be noted that at the end of this row, it show the unstable period-1 response (red dashed line), which is the desired target for the delay feedback controller to suppress this grazing-induced complex dynamics. At $\omega = 0.8528$ (fourth row), a new period-7 response (red) can be observed coexisting with the period-3 (blue) and the period-7 (green) orbits. At $\omega = 0.8538$ (final row), only period-7 (green) and period-3 (blue) attractors are left. Basins of attraction of the soft impact system are presented in Fig. 6.2.2 computed using DYNAMICS-WIN [152] showing the evolution of all these attractors as the frequency of excitation ω varies.

Since the system has multiple attractors at $\omega = 0.8528$, the delay feedback control (5.2.2), $u(\tau) = K\left(v(\tau - \tau_d) - v(\tau)\right)$ with $\tau_d = 2\pi/\omega$ was applied to suppress this multistable regime. The period-1 orbit is stable only for control gains K in a certain range. Fig. 6.2.3 (a) shows a bifurcation diagram of the controlled soft impact system for varying the bifurcation parameter K. The calculations were run for 80 periods of the external excitation with $K = 0$ to ensure that the system (3.2.3) settles down to its steady state, and then switched the controller (5.2.2) on and kept the system (5.2.1) under a particular value of the control gain K running for 600 periods, whereas the last 80 values of oscillator's displacement x were plotted in the bifurcation diagram. Fig. 6.2.3 (b) shows the corresponding LE diagram of the controlled soft impact system by varying the control parameter K. Likewise, the calculations for the LEs were run for 80 periods of external excitation with $K = 0$ initially, followed by another 600 periods calculations with a certain value of K, where the first 200 periods were omitted to ensure the steady state response of the controlled system while the rest 400 periods were used to calculate the LEs as studied in Section 6.2.1. It can be seen from the figures that, when $K < 0.148$, the system presents multi-periodic responses. For example, when $K = 0.0015$, the system has a period-3 attractor, which is a small perturbation of the period-3 attractor in the uncontrolled system (see inset in Fig. 6.2.3(a)). For a range of K larger than 0.04, the chaotic motion can be observed, as indicated by the leading positive LEs, shown in Fig. 6.2.3(b). For $K \in [0.148, 0.42]$, the control stabilises the desired period-1

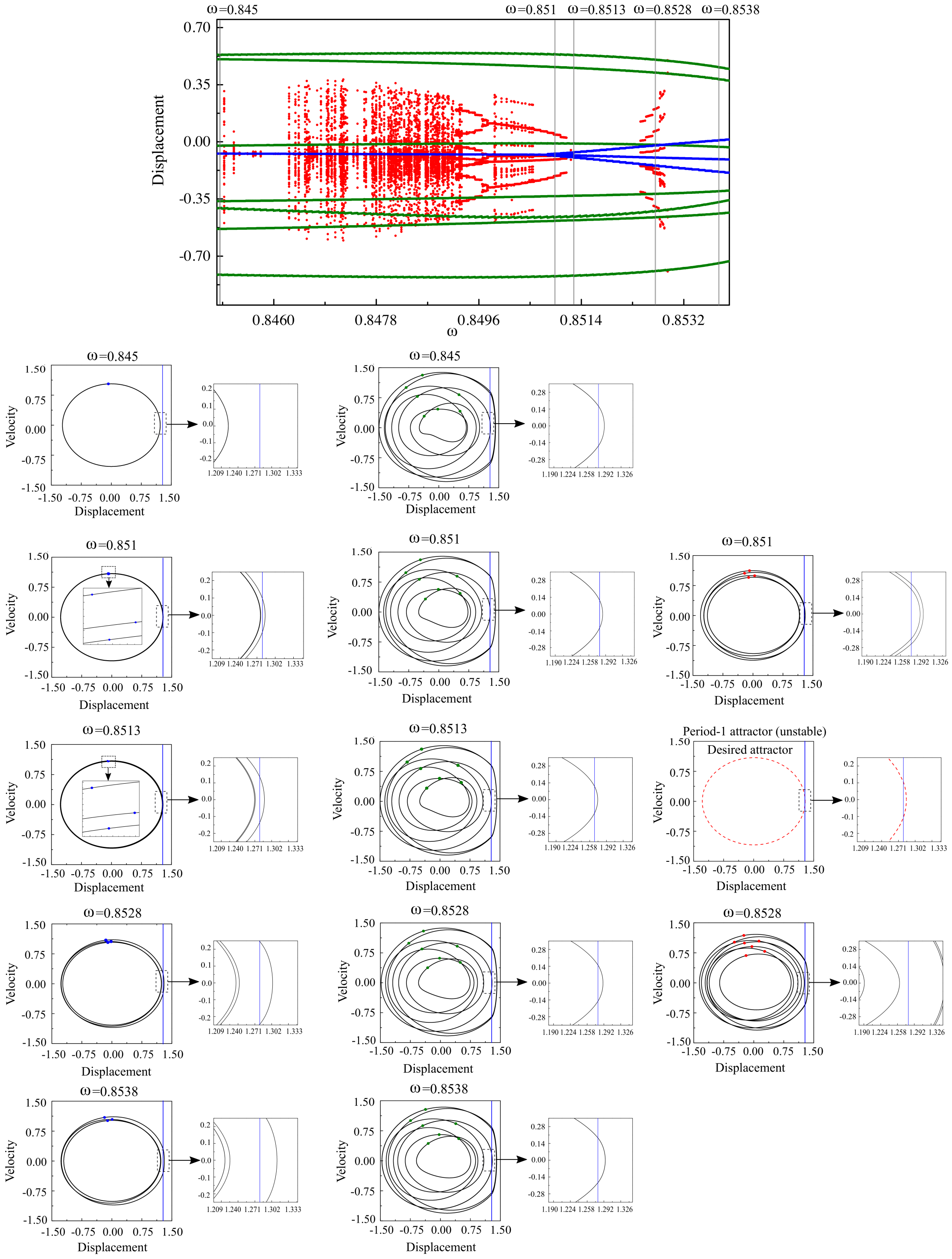

Fig. 6.2.1 Bifurcation diagram of the soft impact system computed for $\zeta = 0.01$, $e = 1.28$, $a = 0.49$, $\beta = 28$ and varying frequency of external excitation ω. The period-7, period-4 and period-3 (period-1) attractors are denoted by green, red and blue dots, respectively. Additional panels below present the corresponding periodic orbits and Poincaré sections for $\omega = 0.845$, $\omega = 0.851$, $\omega = 0.8513$, $\omega = 0.8528$ and $\omega = 0.8538$. The desired attractor for control purpose, i.e. an unstable period-1 orbit, is shown in red dashed line. The location of the impact boundary is indicated by the vertical blue lines.

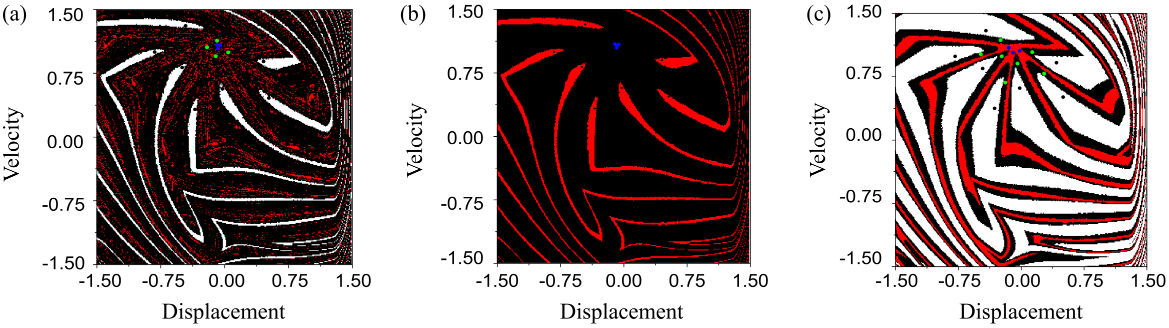

Fig. 6.2.2 Basins of attraction for frequencies ω highlighted in Fig. 6.2.1: (a) $\omega = 0.851$ with a period-3 (blue dots, black basin), a period-4 (green dots, red basin) and a period-7 attractors (black dots, white basin), (b) $\omega = 0.8513$ with a period-3 (blue dots, black basin) and a period-7 attractors (black dots, red basin), (c) $\omega = 0.8528$ with a period-3 (blue dots, red basin), a period-7 (black dots, white basin) and a new period-7 attractors (green dots, black basin). The other parameters are $\zeta = 0.01$, $e = 1.28$, $a = 0.49$ and $\beta = 28$.

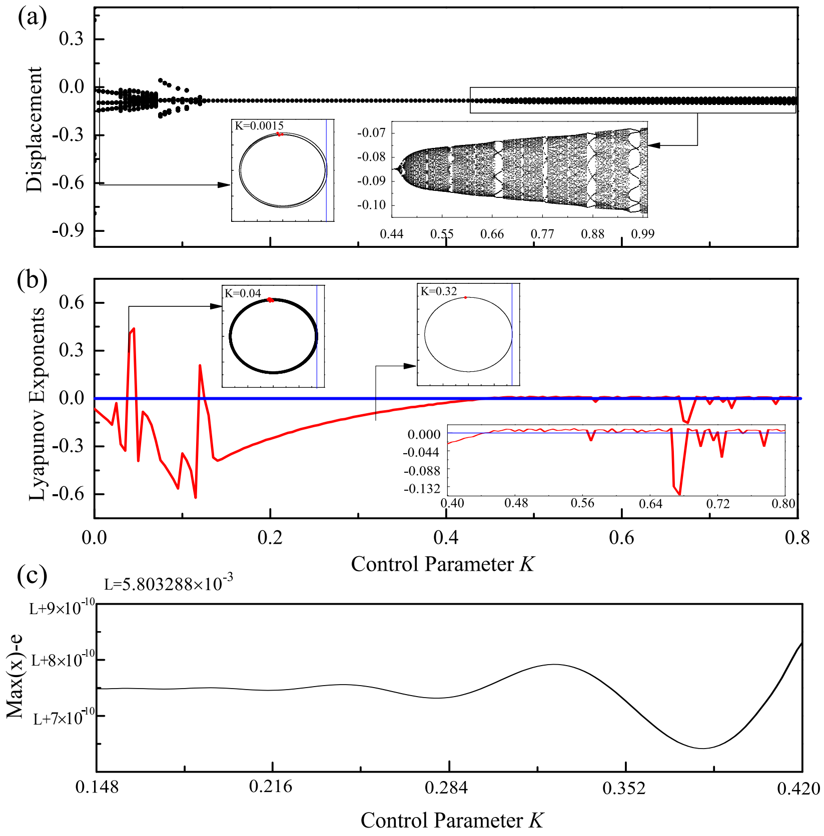

Fig. 6.2.3 (a) Bifurcation diagram and (b) the largest LEs of the soft impact system with the delay feedback control for varying the control gain K. System parameters are $\zeta = 0.01$, $e = 1.28$, $a = 0.49$, $\beta = 28$, $\omega = 0.8528$ and $\tau_d = \frac{2\pi}{\omega}$.

motion at grazing. The leading LE is smaller than 0, as expected for stable periodic motion, for $K \in [0.148, 0.42]$. For $K > 0.42$, the desired period-1 motion loses its stability via a Neimark-Sacker bifurcation and transits into chaos via torus. The chaotic motions have been shown in the periodic windows and their relevant LEs are around 0, which means that the controller is not successful on stabilising the system on period-1 motion.

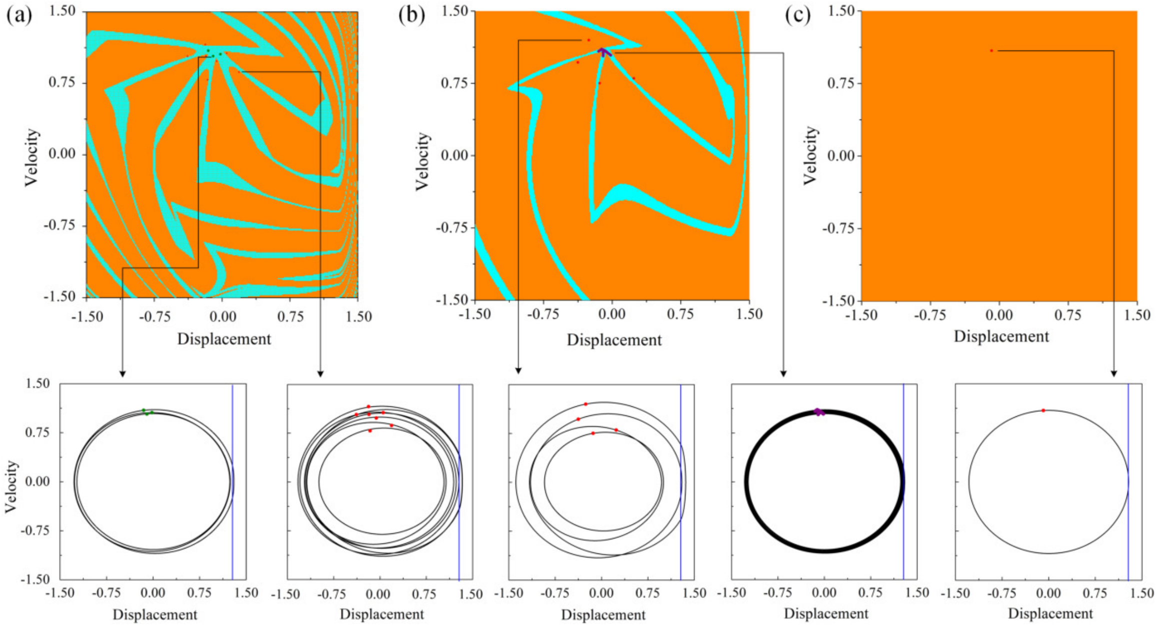

Fig. 6.2.4 Basins of attraction of the soft impact system with delay feedback control, (5.2.1)–(5.2.2), and different control gains K: (a) $K = 0.0015$ (period-3: green dots with cyan basin, period-7: red dots with orange basin), (b) $K = 0.04$ (period-4: red dots with orange basin, chaos: purple dots with cyan basin) and (c) $K = 0.32$ (period-1: red dot with orange basin). Additional panels demonstrate the phase trajectories of the soft impact system. The location of the impact boundary is denoted by the vertical blue lines. The other parameters of the system are $\zeta = 0.01$, $e = 1.28$, $a = 0.49$, $\beta = 28$ and $\omega = 0.8528$.

To demonstrate global stability of the delay feedback control strategy for suitable control gains K, the basins of attraction for various control gains K in Fig. 6.2.4 is presented. The computation procedure for these basins is given as follows: From any initial value (x_0, v_0), the trajectory of the system (3.2.3) at the moment $\tau_0 + T$ was calculated, and then was inserted into the system (5.2.1) under a certain value of the control gain K. As the trajectory converged to an attractor, this initial value was marked by a specific colour in the phase plane. As the control gain K is set to its non-zero value only for $\tau > T = \tau_d = 2\pi/\omega$, the basins of attraction are subsets of $\mathbb{R}^2$, even though the controlled system is a DDE. In Fig. 6.2.4(a), there are two coexisting attractors for $K = 0.0015$, a period-3 (green dots with cyan basin) and a period-7 (red dots with orange basin) attractors. Both attractors are small perturbations of attractors existing in the uncontrolled system. For $K = 0.04$, as shown in Fig. 6.2.4(b), the system is bistable consisting of a period-4 (red dots with orange basin) and a chaotic attractors (purple dots with cyan basin). The basin of the chaotic attractor is noticeably smaller than the basin of the period-3 attractor in Fig. 6.2.4(a). At $K = 0.32$ the system is monostable with the desired period-1 attractor only (see Fig. 6.2.4(c)).

According to the above results, when $K \in [0.148, 0.42]$, the delay feedback controller can stabilise the soft impact system on the target period-1 orbit. Fig. 6.2.5 presents the time profiles of displacement of the system and its external excitation with the control signal u as a demonstration of controlling from different coexisting attractor. As can be seen from the figure, the controller was switched on at the 81th period of the external excitation, and for all the coexisting attractors at $\omega = 0.8528$, including a period-3 and two period-7 attractors, the system was successfully driven to the desired period-1 motion at grazing with one impact per period of excitation. It is worth noting that, as the targeted period-1 attractor is very similar with the period-3 attractor as shown in Fig. 6.2.1, the switching from the period-3 to the period-1 attractor just needs a small control signal. Hence, as shown in Fig. 6.2.5(a), the displacement and the external excitation before and after the control is on are almost the same.

6.2.3 Path-following study of the delay feedback controller

In this section the periodically forced soft impact system considering the delay feedback controller introduced previously (see system (5.2.1) with (5.2.2)) will be investigated by the path-following (continuation) methods. As mentioned before, this model is a piecewise-smooth dynamical system with delay, for which no specialized software package for numerical continuation is available to the best of our knowledge. Therefore, in order to carry out a detailed path-following study of the soft impact system with delay feedback control the numerical approach proposed in Chapter 4 will be employed.

Defining systems for continuation

The numerical approach presented in Chapter 4 is based on the *chain approximation* [91] using a higher-order approximation scheme of the original DDE by introducing a finite sequence of Taylor expansions as follows. Let us consider a general DDE of the form

$$\dot{q}(t) = f(t, q(t), q(t - \tau_d)), \tag{6.2.11}$$

which defines a system of delay differential equations (DDEs) with constant delay $\tau_d > 0$, where $f : \mathbb{R} \times \mathbb{R}^n \times \mathbb{R}^n \to \mathbb{R}^n$ is a sufficiently smooth function. Now, the value of $N \in \mathbb{N}$

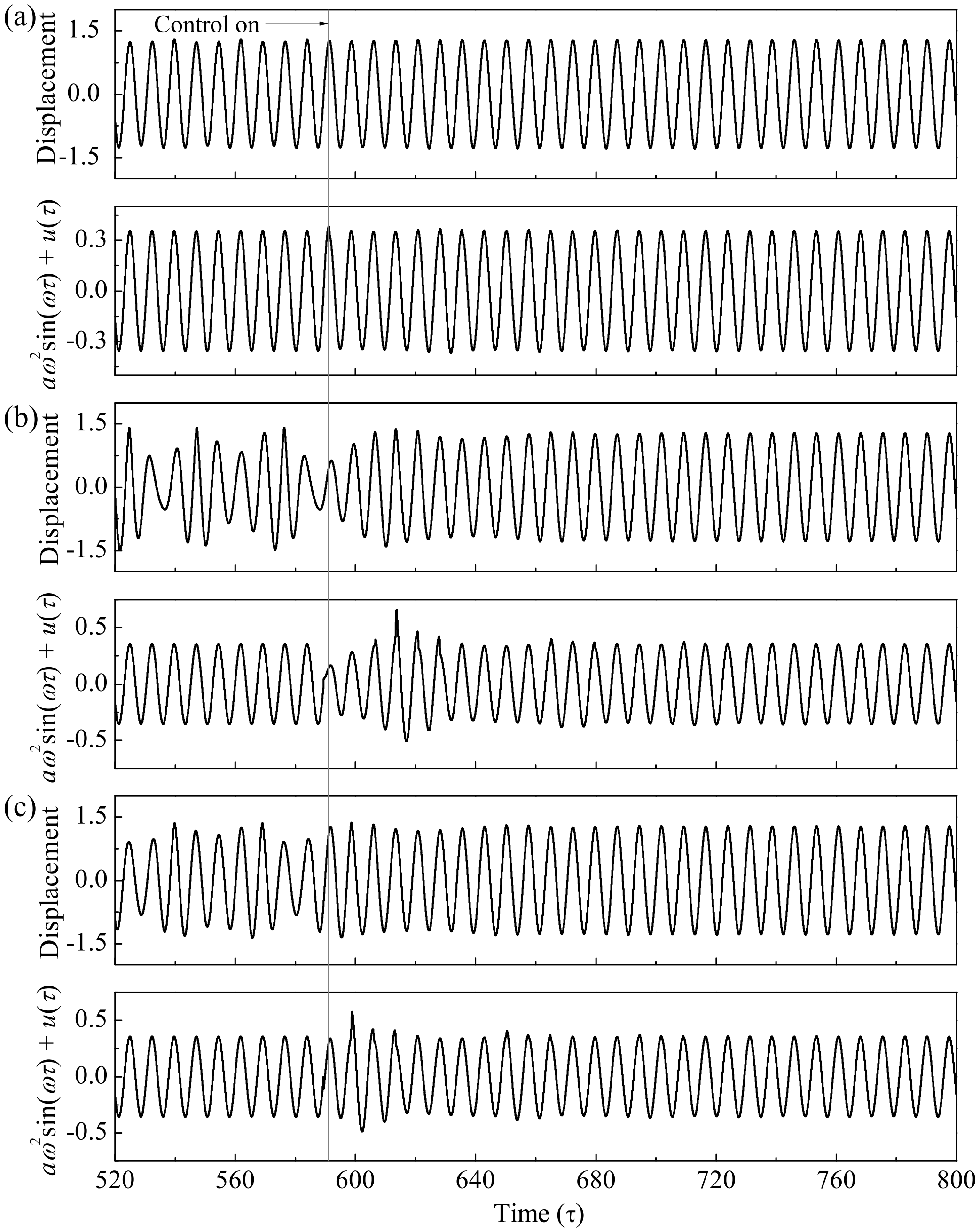

Fig. 6.2.5 Time profiles of displacement of the soft impact system and the external excitation including the control signal u. Grey line indicates the time when the delay feedback control was switched on. Before this time the gain $K = 0$ and the uncontrolled system is on its (a) period-3, (b) first period-7 and (c) second period-7 attractors. The parameters of the controlled soft impact system are $\zeta = 0.01$, $e = 1.28$, $a = 0.49$, $\beta = 28$, $\omega = 0.8528$ and $K = 0.32$.

should be sufficiently large and the grid points can be defined as $t_i := i\frac{\tau_d}{N}$, $i = 0, \dots, N$. Furthermore, define $u_i(t) := q(t - t_i)$ for all $t \geq 0$, $i = 0, \dots, N$. In this setting, we obtain via Taylor expansion to order M with

$$u_{i-1}(t) = q\left(t - \left(t_i - \frac{\tau_d}{N}\right)\right) = u_i\left(t + \frac{\tau_d}{N}\right) = \sum_{k=0}^{M} \frac{1}{k!} u_i^{(k)}(t) \left(\frac{\tau_d}{N}\right)^k + \mathscr{O}\left(\left(\frac{\tau_d}{N}\right)^{M+1}\right), \tag{6.2.12}$$

and

$$\dot{u}_0(t) = f(t, u_0(t), u_N(t)), \tag{6.2.13}$$

for all $t \geq 0$, $i = 1, \dots, N$, $M \geq 1$. After neglecting the $\mathscr{O}$-terms, from (6.2.12), a system of dN differential equations of order M can be obtained. In this way, a piecewise-smooth dynamical system of dimension n with constant delay can be approximated by a piecewise-smooth system of ODEs of dimension $n(NM+1)$ for large N, which then allows the study of the resulting model in the framework of hybrid dynamical systems [28]. Choosing order $M = 2$, the defining system for periodic orbits of a soft impact system with delay feedback control (5.2.1) can be approximated by the following piecewise-smooth system of ODEs on the interval $[0, 1]$:

$$\tilde{z}'(\tau) = f(\tilde{z}(\tau), \tilde{\phi}(\tilde{z}(\tau), \alpha), \alpha), \quad \text{where } \tilde{\phi}(\tilde{z}, \alpha) = \begin{cases} 0 & \text{if } x - e < 0 \text{ (\textit{no contact})}, \\ \beta(x - e) & \text{if } x - e \geq 0 \text{ (\textit{contact})}, \end{cases} \tag{6.2.14}$$

$$\tilde{z} := (x, r, s, u_0, \dots, u_N, w_1, \dots, w_N)^T \in \mathbb{R}^{2N+4}, \quad \alpha := (\omega, a, \beta, \zeta, e, K, \tau_d) \in \left(\mathbb{R}_0^+\right)^7$$

and

$$f(\tilde{z}, \alpha, \tilde{\phi}) := \begin{pmatrix} \tau_d u_0 \\ r + \omega\tau_d s - r\left(r^2 + s^2\right) \\ s - \omega\tau_d r - s\left(r^2 + s^2\right) \\ \tau_d\left(a\omega^2 r + K(u_N - u_0) - 2\zeta u_0 - x - \tilde{\phi}\right) \\ (w_i)_{i=1,\dots,N} \\ \left(2N^2\left(u_{i-1} - u_i - \frac{1}{N} w_i\right)\right)_{i=1,\dots,N} \end{pmatrix}. \tag{6.2.15}$$

The argument $\tilde{\phi}$ of the right-hand side f defines the *no contact* and *contact* operation modes of the soft impact system, respectively. In the approximating system (6.2.14) a time re-scaling

$\tau/\tau_d \to \tau$ was introduced such that the approximation of the history $q(\tau - t)$ for $t \in [0, \tau_d]$ by Taylor expansion (6.2.12) is always over the unit interval, regardless the value of the delay τ_d. Furthermore, in the approximating system (6.2.14) we have that $u_0(\tau) = v(\tau)$ and

$$u_i(\tau) \approx v(\tau - \tau_i), \quad \text{for all} \quad \tau \in [0,1], \quad \tau_i = \frac{i}{N}, \quad i = 1, \dots, N. \tag{6.2.16}$$

The approximation of the history of q by u_i on the evenly spaced grid of τ_i on $[0,1]$ with order $M = 2$ is a special case of the pseudospectral approximation of DDEs by ODEs, as used for bifurcation analysis in MATCONT by [153]. The spectral approximation from [153] has no advantage over the low-order approximation (6.2.16) for this problem, because the history segment is only differentiable once with Lipschitz continuous derivative, whenever the contact threshold $x = e$ has been crossed during the previous time interval of length τ_d. Thus, the proposed second-order approximation has the most suitable order M.

In what follows, all numerical continuation results will be obtained from the approximating model (6.2.14) (with $N = 15$) via the continuation platform COCO [25]. Specifically, this numerical anlaysis will make use of the COCO-toolbox ‘hspo’, which implements a segment-specific discretization strategy in the framework of multisegment boundary-value problems, thus allowing the numerical continuation of periodic solutions for piecewise-smooth dynamical systems. In this way, a locus of grazing periodic orbits can be computed by introducing an extra solution segment with a terminal point satisfying the condition $x' = 0$, where the mass velocity becomes zero. Here, a grazing solution can be detected via the auxiliary boundary condition $x - e = 0$, and therefore a locus of such orbits can be obtained by freeing two parameters during the continuation process, using the COCO-command ‘coco xchg pars’. On the other hand, simulations generated via direct numerical integration will be computed for the original DDE model (5.2.1) using the MATLAB solver ‘`dde23`’, in combination with its built-in event location routines [154, 155] to detect accurately collisions with the impact boundary $x = e$.

Continuation of periodic orbits

The behavior of the soft impact system (3.2.3) (without control) will be investigated firstly, when this system presents the dynamical scenario analysed in Fig. 6.2.5. Figure 6.2.6 shows the periodic response of system (3.2.3) with respect to the excitation frequency ω, showing in the vertical axis the time the oscillating mass is in contact with the secondary spring k_2 (see Fig. 3.2.1). As can be seen in this bifurcation diagram, low values of ω produce oscillations of small amplitude, with no contact with the secondary spring. A critical point, however, is found at $\omega \approx 0.85061$, where a grazing bifurcation (labeled GR1) of limit cycles occurs.

Here, the system presents a periodic solution making tangential contact with the impact boundary $x = e$. Shortly after the GR1 point a period-doubling bifurcation (PD1) is detected for $\omega \approx 0.85113$. At this value, the period-1 solution loses stability and a family of stable period-2 solutions is born. The unstable period-1 orbit recovers stability at $\omega \approx 0.91440$, where another period-doubling bifurcation (PD2) occurs. Using direct numerical integration it is convenient to find further attractors of higher period between the period-doubling points PD1 and PD2, as can be seen in Fig. 6.2.6(b) (see also Fig. 6.2.1). Here, a (stable) period-7 solution is depicted together with the original (unstable) period-1 orbit computed at the test point $\omega = 0.8528$ (P1). The purpose of the delay feedback control is to stabilise this period-1 response, as discussed before, for the parameter window defined by the period-doubling points PD1 and PD2.

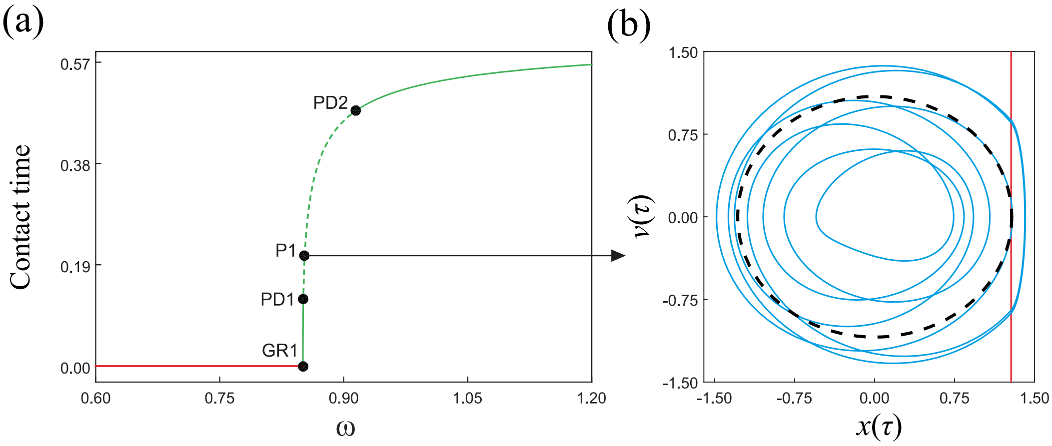

Fig. 6.2.6 (a) Continuation of period-1 solutions of the (uncontrolled) soft impact system (3.2.3) with respect to the excitation frequency ω, for the parameter values given in Fig. 6.2.1. The vertical axis presents the time the oscillating mass is in contact with the secondary spring k_2 (see Fig. 3.2.1). The labels GR1, PD1 and PD2 stand for grazing and period-doubling bifurcations detected at $\omega \approx 0.85061$, $\omega \approx 0.85113$ and $\omega \approx 0.91440$, respectively. Solid and dashed branches mark stable and unstable solutions, respectively. Furthermore, impacting solutions are represented by the green line, while non-impacting orbits correspond to the red branch (before the grazing bifurcation GR1). Panel (b) depicts a phase plot corresponding to the test point P1 ($\omega = 0.8528$), where two periodic solutions coexist, one stable (in blue, solid line) and one unstable (in black, dashed curve).

The presence of the stable more complex (period-7) response in the range between PD1 and PD2 suggests that the period-doubling bifurcations PD1 and PD2 are the boundary of a parameter region with more complex system responses in two parameters. Now these period-doubling bifurcation will be investigated by tracing them in two parameters (frequency ω and amplitude a of excitation) via two-parameter continuation. The result is presented in Fig. 6.2.7. From this figure, it presents that the bifurcation points PD1 and PD2 belong to the same branch of period-doubling bifurcations in the two-parameter plane, bounding the isola plotted in panel (a), located between the two extremes of ω on this curve at $\omega \approx 0.66708$ and $\omega \approx 0.91456$, which define the window of existence of this isola. Inside the isola the period-1 solution is unstable. The delay feedback control stabilises the period-1 response, as verified at three test points (P1, P2, P3) within the isola, where the uncontrolled response (in blue, see Fig. 6.2.7(b)–(d)) ranges from periodic to chaotic motion, while the controller in all these cases is able to stabilise the original period-1 orbit (in black).

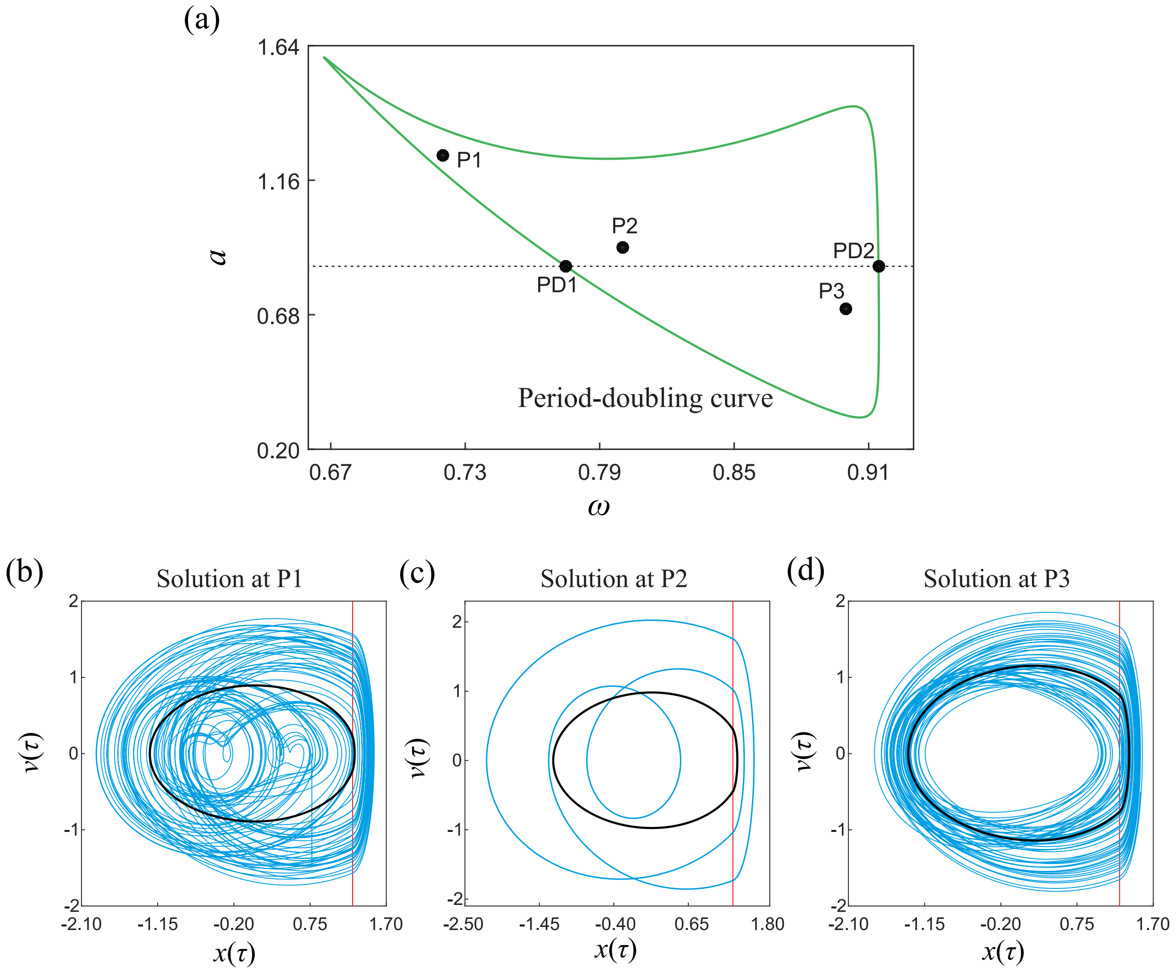

Fig. 6.2.7 (a) Two-parameter continuation of the period-doubling bifurcations found in Fig. 6.2.6, with respect to frequency ω and amplitude a of excitation. The intersection with the horizontal line $\omega = 0.8528$ defines the period-doubling points PD1 and PD2 detected before. Panels (b)–(d) display phase plots corresponding to the test points P1 ($\omega = 0.72$, $a = 1.25$), P2 ($\omega = 0.8$, $a = 0.92$) and P3 ($\omega = 0.9$, $a = 0.7$), respectively. These panels present the system response without control (in blue) and with control (in black), using the control parameters $K = 0.32$ and $\tau_d = \frac{2\pi}{\omega}$.

Next, it is necessary to investigate the periodic response of the soft impact system with delay feedback control using the approximating system (6.2.14) and the continuation platform COCO. In this way, the numerical continuation of period-1 solutions of the soft impact system with delay feedback control is shown in Fig. 6.2.8, for the range $0 < \tau_d \leq 3$, using the (unstable) period-1 orbit shown in Fig. 6.2.6(b) as starting solution. As expected, a family of unstable period-1 orbits is found for small time delay τ_d. This orbit becomes stable at $\tau_d \approx 0.47404$, where a period-doubling bifurcation is located. As the time delay grows, another bifurcation (GR2) is found at $\tau_d \approx 1.78922$, where the periodic orbit makes tangential contact with the impact boundary $x = e$. This point, therefore, defines a boundary between impacting and non-impacting motion, as can be seen from the right phase plots in Fig. 6.2.8. This numerical investigation indicates that the delay feedback controller is able to not only stabilise the desired period-1 motion but also control impacting regimes in the system.

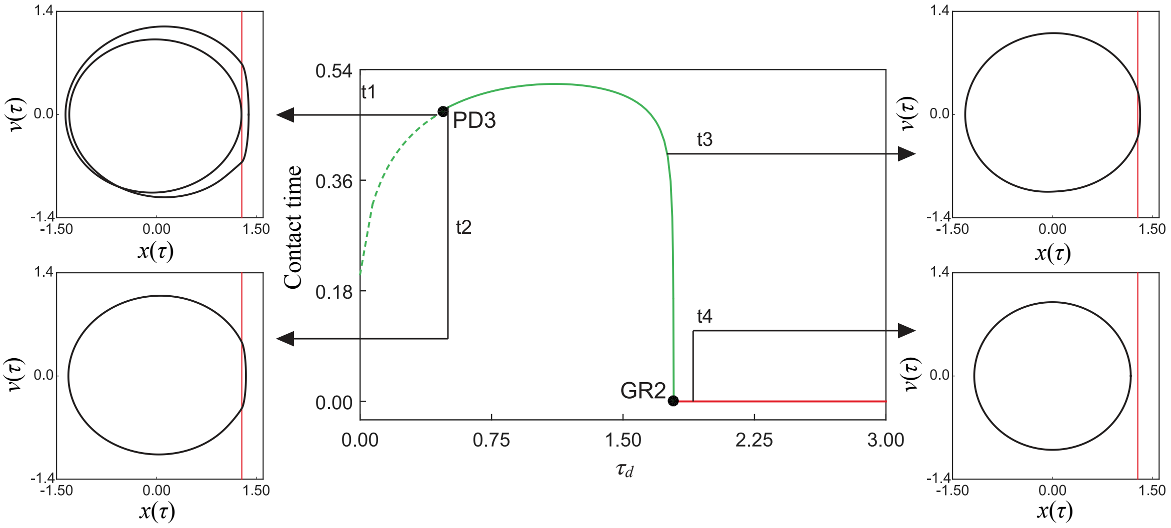

Fig. 6.2.8 Continuation of the periodic response of the controlled soft impact system (5.2.1) with respect to the control delay τ_d, for the parameter values given in Fig. 6.2.1, showing the contact time on the vertical axis. The period-doubling (PD3) and grazing (GR2) bifurcations are located at $\tau_d \approx 0.47404$ and $\tau_d \approx 1.78922$, respectively. Lateral panels present phase portraits for different values of the control delay τ_d.

Next, a two-parameter continuation with respect to the main control parameters, i.e. the time delay τ_d and the control gain K, will be carried out for the detected bifurcations above. Fig. 6.2.9 shows the resulting red and green curves that represent the two-parameter continuation of the period-doubling and grazing bifurcations found in Fig. 6.2.8. The bifurcation curves divide the two-dimensional parameter space into three regions. The first region, to the left of the period-doubling curve, corresponds to operation points for which the period-1 response is unstable in the controlled system. Crossing this line from the right produces a supercritical period-doubling bifurcation, due to which stable period-2 solutions are created, as the one computed in Fig. 6.2.9(b), for the test point P1 ($\tau_d = 0.62$, $K = 0.23$). The region between the period-doubling and grazing curves provides parameter values producing stable period-1 responses, as discussed before, see for instance the solution calculated at the test point P2 ($\tau_d = 1.3$, $K = 0.3$), shown in Fig. 6.2.9(c). The third region, located to the right of the grazing curve, defines operation points yielding period-1 non-impacting solutions, similar to the test point P3 ($\tau_d = 2.1$, $K = 0.4$), see Fig. 6.2.9(d).

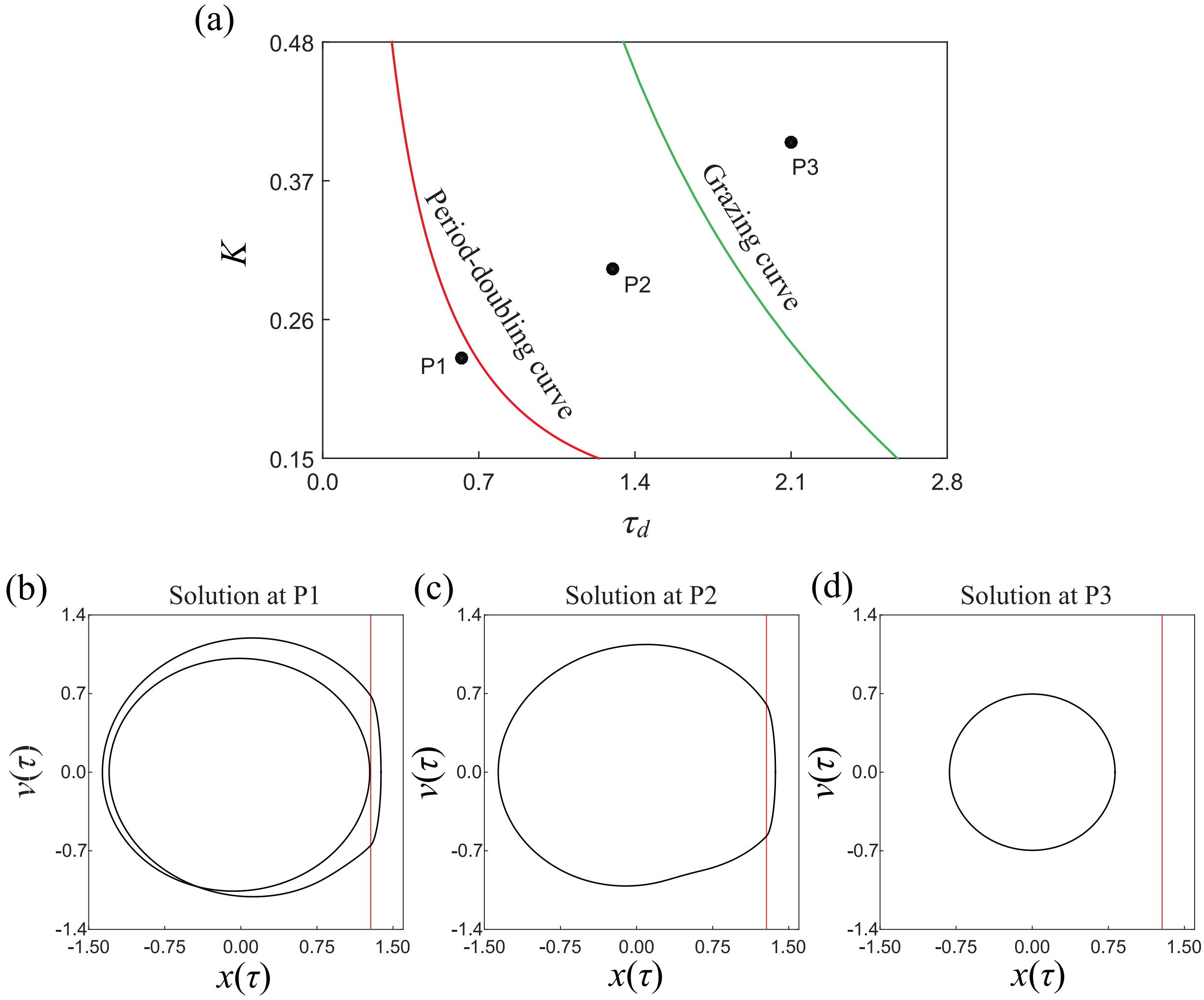

Fig. 6.2.9 (a) Two-parameter continuation of the period-doubling and grazing bifurcations found in Fig. 6.2.8, with respect to the control delay τ_d and control gain K. Panels (b)–(d) display phase plots corresponding to the test points P1 ($\tau_d = 0.62$, $K = 0.23$), P2 ($\tau_d = 1.3$, $K = 0.3$) and P3 ($\tau_d = 2.1$, $K = 0.4$), respectively.

6.3 Control of the impact system with a drift via the delay feedback control

6.3.1 Mathematical preparation

With the introducing of the delay feedback controller into the impact system with a drift, the system can be describe as

- **No contact**, i.e. $x < z + g$,

$$\begin{aligned} x' &= y, \\ y' &= acos(\omega\tau + \phi) + b + u(\tau), \\ z' &= -\frac{1}{2\xi}(z - \bar{v}), \\ \bar{v}' &= 0. \end{aligned} \tag{6.3.1}$$

- **Contact without progression**, i.e. $x \geq z + g$ and $0 < 2\xi z' + (z - \bar{v}) < 1$,

$$\begin{aligned} x' &= y, \\ y' &= -2\xi z' - (z - \bar{v}) + acos(\omega\tau + \phi) + b + u(\tau), \\ z' &= x', \\ x &= z + g, \\ \bar{v}' &= 0. \end{aligned} \tag{6.3.2}$$

- **Contact with progression**, i.e. $x \geq z + g$ and $2\xi z' + (z - \bar{v}) \geq 1$,

$$\begin{aligned} x' &= y, \\ y' &= acos(\omega\tau + \phi) + b - 1 + u(\tau), \\ z' &= x', \\ x &= z + g, \\ \bar{v}' &= z' + \frac{1}{2\xi}(z - \bar{v} - 1). \end{aligned} \tag{6.3.3}$$

where

$$u(\tau) = K\left(y(\tau - \tau_d) - y(\tau)\right), \quad \tau \geq 0, \tag{6.3.4}$$

is the delay feedback control. In Eq. (6.3.4) $K \geq 0$ is the control gain, setting the coupling strength between the velocity output $y(\tau-\tau_d)-y(\tau)$ and the control input $u(\tau)$, and $\tau_d > 0$ is a tunable time delay (in contrast to a lag introduced by the control loop, which is assumed to be zero here). Since the purpose of this present work is to control the system to a period-1 response, the delay term τ_d is set to one period of the external excitation $\tau_d = T := 2\pi/\omega$.

Since the impact system with a drift and delay feedback control described by Eq. (6.3.1), (6.3.2) and (6.3.3) is hard to analyse due to the problem of the motion unboundedness, a co-ordinates transformation $p := x - \bar{v}$ and $q := z - \bar{v}$ as show in Section 3.3 has to be adopt, so that the above system can be changed to the following form:

- **No contact**, i.e. $p < q + g$.

$$\begin{aligned} p' &= y, \\ y' &= acos(\omega\tau + \phi) + b + u(\tau), \\ q' &= -\frac{1}{2\xi}(q). \end{aligned} \tag{6.3.5}$$

- **Contact without progression**, i.e. $p \geq q + g$ and $0 < 2\xi y + q < 1$.

$$\begin{aligned} p' &= y, \\ y' &= -2\xi y - q + acos(\omega\tau + \phi) + b + u(\tau), \\ q' &= y. \end{aligned} \tag{6.3.6}$$

- **Contact with progression**, i.e. $p \geq q + g$ and $2\xi y + q \geq 1$.

$$\begin{aligned} p' &= -\frac{1}{2\xi}(q-1), \\ y' &= acos(\omega\tau + \phi) + b - 1 + u(\tau), \\ q' &= -\frac{1}{2\xi}(q-1). \end{aligned} \tag{6.3.7}$$

Through the above forms, the problem of motion unboundedness can be avoided and the LEs can be calculated. At the following discussion, the definition of Stroboscopic map and Jacobian matrix in Section 6.2.1 will be adopt to calculate the LEs for the above impact system with a drift.

6.3.2 Numerical investigation of the impact system with a drift and the delay feedback controller

The numerical investigation starts with the bifurcation analysis of the dynamics of the impact system with a drift without the delay feedback control, as given in Eq. (3.3.4), (3.3.5) and (3.3.6). In Fig. 6.3.1, it shows the relevant bifurcation diagram, where ω is used as the bifurcation parameter. The calculation was run for 330 cycles of external excitation, and the data for the first 300 cycles were omitted to ensure the steady state response, whereas the last 30 values of the velocity y were plotted in the bifurcation diagram for each value of the bifurcation parameter. It can be seen that a period-1 motion is presented during $\omega \in [0, 0.268]$. In addition, the phase portraits of the period-1 attractor at $\omega = 0.12$ and $\omega = 0.24$ are separately shown in Fig 6.3.1 (b) and (c), and the relevant trajectories at $\omega = 0.12$ and $\omega = 0.24$ are presented in Fig. 6.3.2 (a) and (b), which show that the slider bottom under the external excitation with frequency $\omega = 0.12$ is moving faster than the slider bottom under the external excitation with frequency $\omega = 0.24$. In details, the initial displacements of the mass and slider bottom under these two cases are all $\bar{v} = 0$. But the displacement of the slider bottom under the external excitation with frequency $\omega = 0.12$ at $\tau = 1600$ is $\bar{v} = 635$, which is more than twice the displacement of the slider bottom under the external excitation with frequency $\omega = 0.24$. For the range $\omega \in [0.268, 0.378]$, the system behaves period-2 motion, as shown in Fig. 6.3.1 (a). At $\omega = 0.3$, the phase portrait and trajectory of period-2 attractor is presented in Fig. 6.3.1 (d) and Fig. 6.3.2 (c). In Fig. 6.3.2 (c), it shows that there are two peaks in one period. During the process of progression, it can be discovered that the capsule is progressing from the displacement $\bar{v} = 0$ at $\tau = 0$ to the displacement $\bar{v} = 137$ at $\tau = 1600$. For the case at $\omega = 0.38$, during one period, there are 4 small peaks, and the moving distance between $\tau = 0$ and $\tau = 1600$ is the smallest, compared with the previous three cases. Finally, the slider bottom arrives around the displacement $\bar{v} = 36$, as shown in the small window of Fig. 6.3.2 (d).

Since the system presents period-2 dynamical response at $\omega = 0.3$ as shown in Fig. 6.3.2, the delay feedback control (6.3.4), $u(\tau) = K\left(y(\tau - \tau_d) - y(\tau)\right)$ with $\tau = 2\pi/\omega$ was applied to control the system to the period-1 dynamical response. The period-1 motion is stable only for control gains K in a certain range. In Fig. 6.3.3 (a), it shows a bifurcation diagram of the controlled impact system with a drift for varying the bifurcation parameter K. The calculations were run for 160 periods of the external excitation with $K = 0$ to ensure that the system described by Eq. (6.3.1), (6.3.2) and (6.3.3) settles down to its steady state, and then switched the controller (6.3.4) on and kept the system under a particular value of the control gain K running for 500 periods, whereas the last 50 values of the velocity y of the mass were plotted in the bifurcation diagram. Fig. 6.3.3 (b) shows the corresponding LE

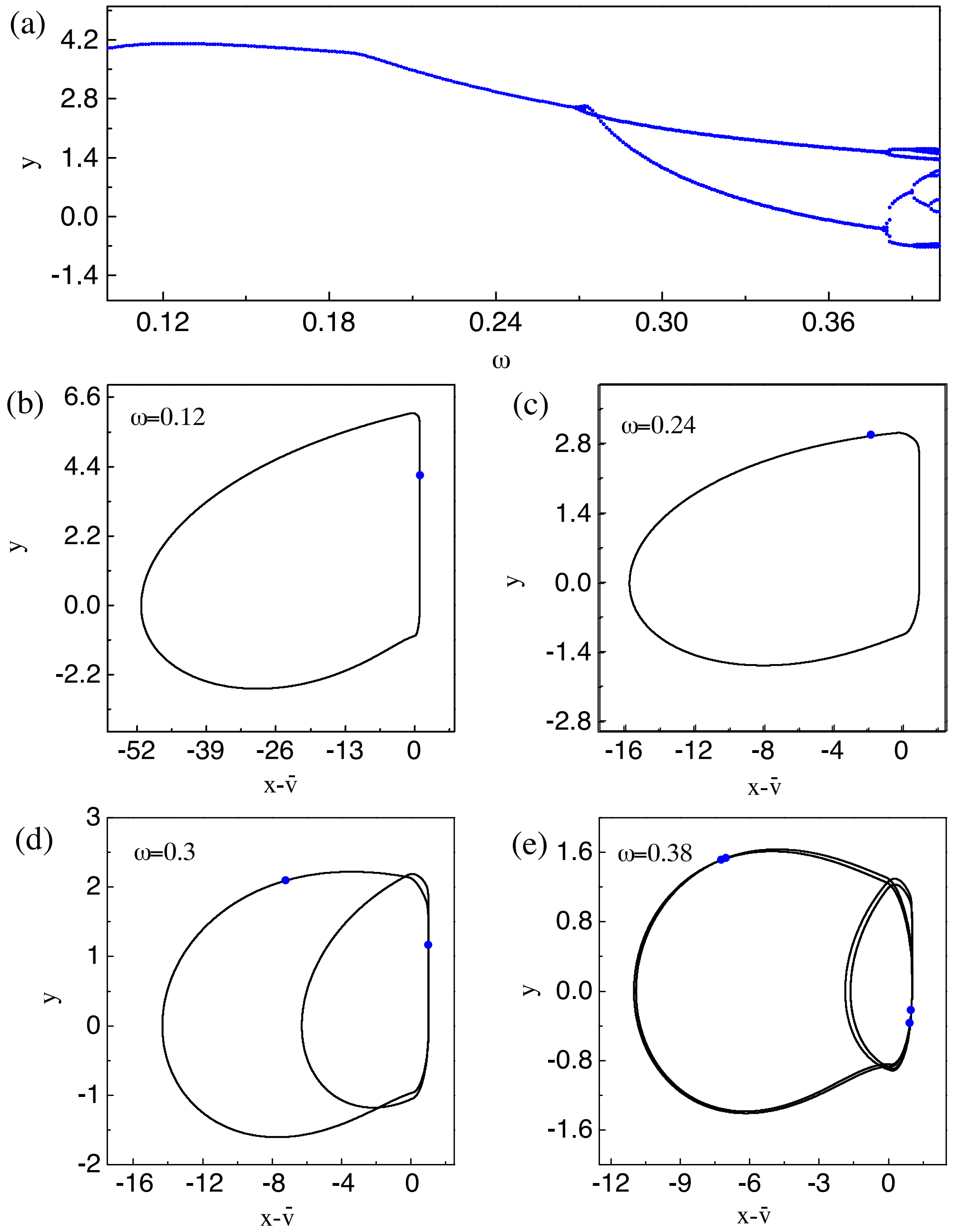

Fig. 6.3.1 (a) Bifurcation diagram of the impact system with a drift computed for $a = 0.3$, $b = 0.15$, $\xi = 0.05$, $g = 0.02$, $\phi = \frac{\pi}{2}$ and varying frequency of external excitation ω. The phase portrait of different external excitation ω: (b) $\omega = 0.12$, (c) $\omega = 0.24$, (d) $\omega = 0.3$ and (e) $\omega = 0.38$.

diagram of the controlled impact system with a drift by varying the control parameter K. Likewise, the calculations for the LEs were run for 150 periods of external excitation with $K = 0$ initially, followed by another 3000 periods calculations with a certain value of K,

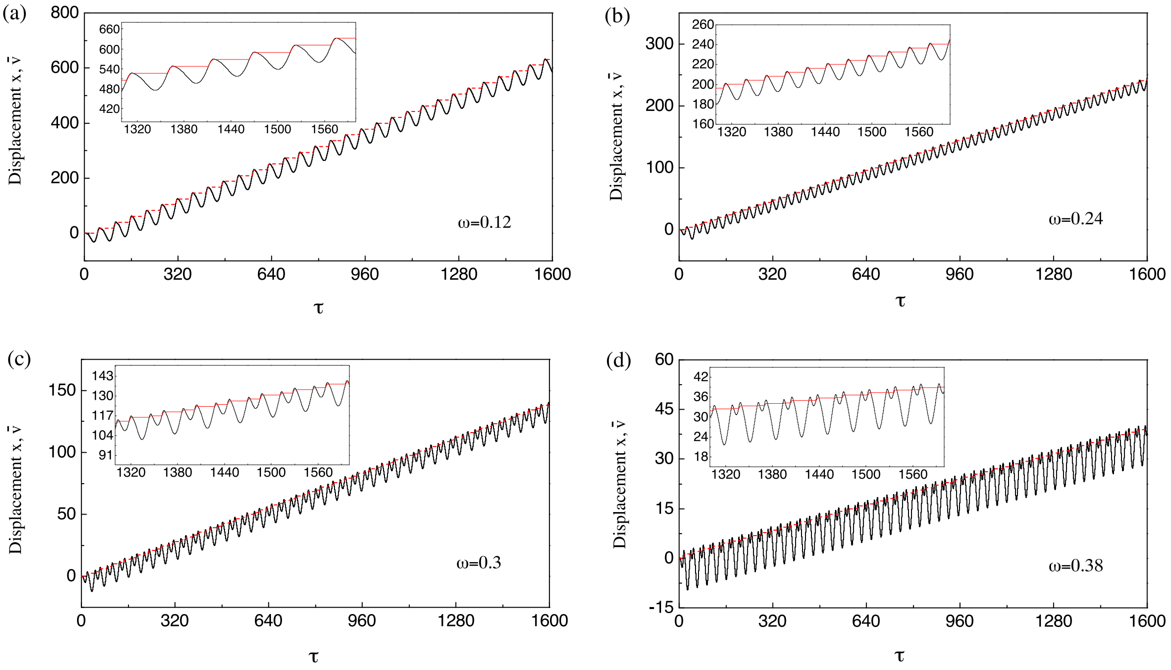

Fig. 6.3.2 Time histories of displacement of mass x (black solid curves) and slider bottom v (red dash curves) for $a = 0.3$, $b = 0.15$, $\xi = 0.05$, $g = 0.02$ and $\phi = \frac{\pi}{2}$: (a) $\omega = 0.12$, (b) $\omega = 0.24$, (c) $\omega = 0.3$ and (d) $\omega = 0.38$.

where the first 250 periods were omitted to ensure the steady state response of the controlled system while the rest periods were used to calculate the LEs. Since the period-2 and period-1 dynamical responses are described only by Eq. (6.3.6) and (6.3.7) and the performances of two variables (i.e. p and q) of these two motions are always the same, which means that the one of LEs is always around 0. It can be seen from the figures that, when $K < 0.008$, the system presents period-2 dynamical responses. For example, when $K = 0.002$, the system has a period-2 attractor as shown in the small window of Fig. 6.3.3 (a), which has a smaller area of phase portrait than the attractor at $\omega = 0.3$ and $K = 0$. For a range of K larger than 0.008, the control stabilises the desired period-1 motion. Relevantly, the period-doubling bifurcation can be discovered at $K = 0.008$ as shown in Fig. 6.3.3 (b), and the leading LE is 2.2×10^{-5}. After that, when $K > 0.008$, the leading LE is smaller than 0, as expected for stable periodic motion.

According to the above results, when $K > 0.008$, the delay feedback controller can stabilise the impact system with a drift on the target period-1 orbit. Fig. 6.3.4 presents the time profiles of displacement of mass and slider bottom, the velocity of mass and its external excitation with the control signal u as a demonstration of controlling to the period-1 motion, when $K = 0.5$. As can be seen from the figure, the controller is switched on at $\tau = 1675.512$, and the system is stable on the period-1 attractor.

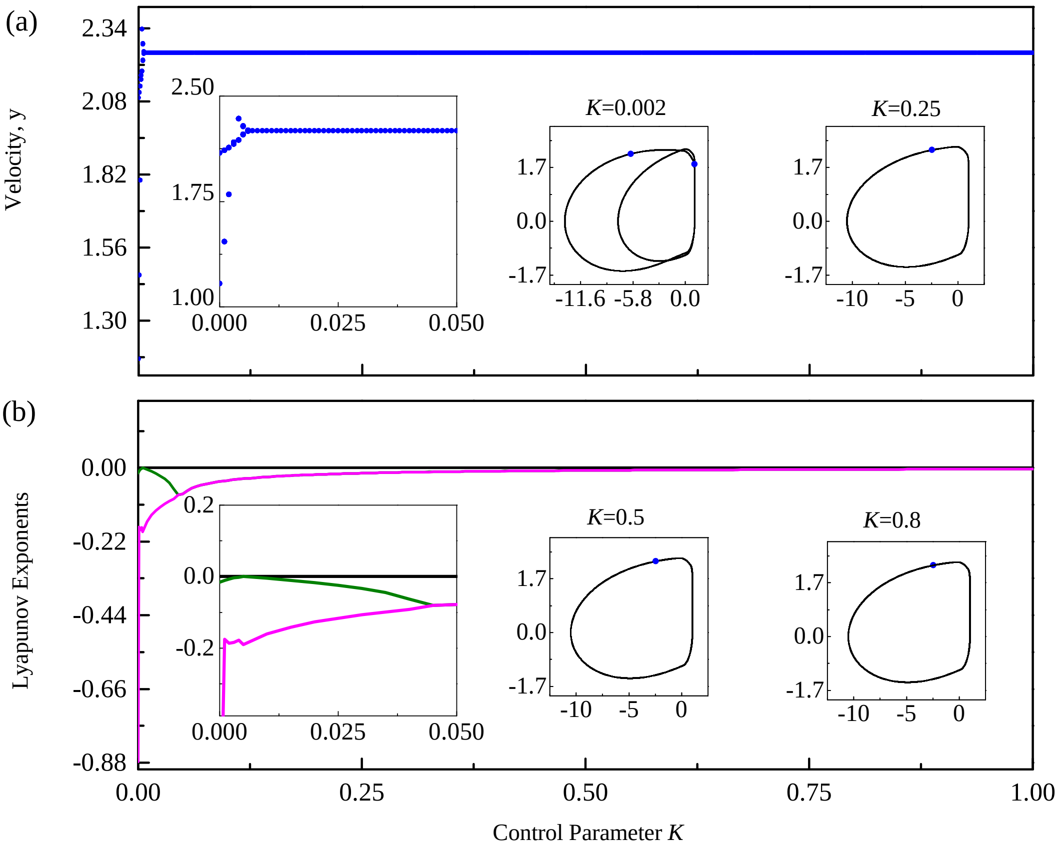

Fig. 6.3.3 (a) Bifurcation diagram and (b) LEs of impact system with a drift and the delay feedback control for varying the control gain K. System parameters are $a=0.3$, $b=0.15$, $\xi=0.05$, $g=0.02$, $\phi=\frac{\pi}{2}$, $\omega=0.3$ and $\tau_d=\frac{2\pi}{\omega}$. Black, olive and magenta lines denote the three LEs.

6.4 Control of the vibro-impact capsule system via the delay feedback control

6.4.1 Mathematical preparation

With the introducing of the delay feedback controller into the vibro-impact capsule system, the system can be described as

- **No contact with stationary capsule**, i.e. $x_1-x_2<\delta$, and $|(x_2-x_1)+2\xi(y_2-y_1)|\leq 1$. Then, the motion of the mass and capsule are:

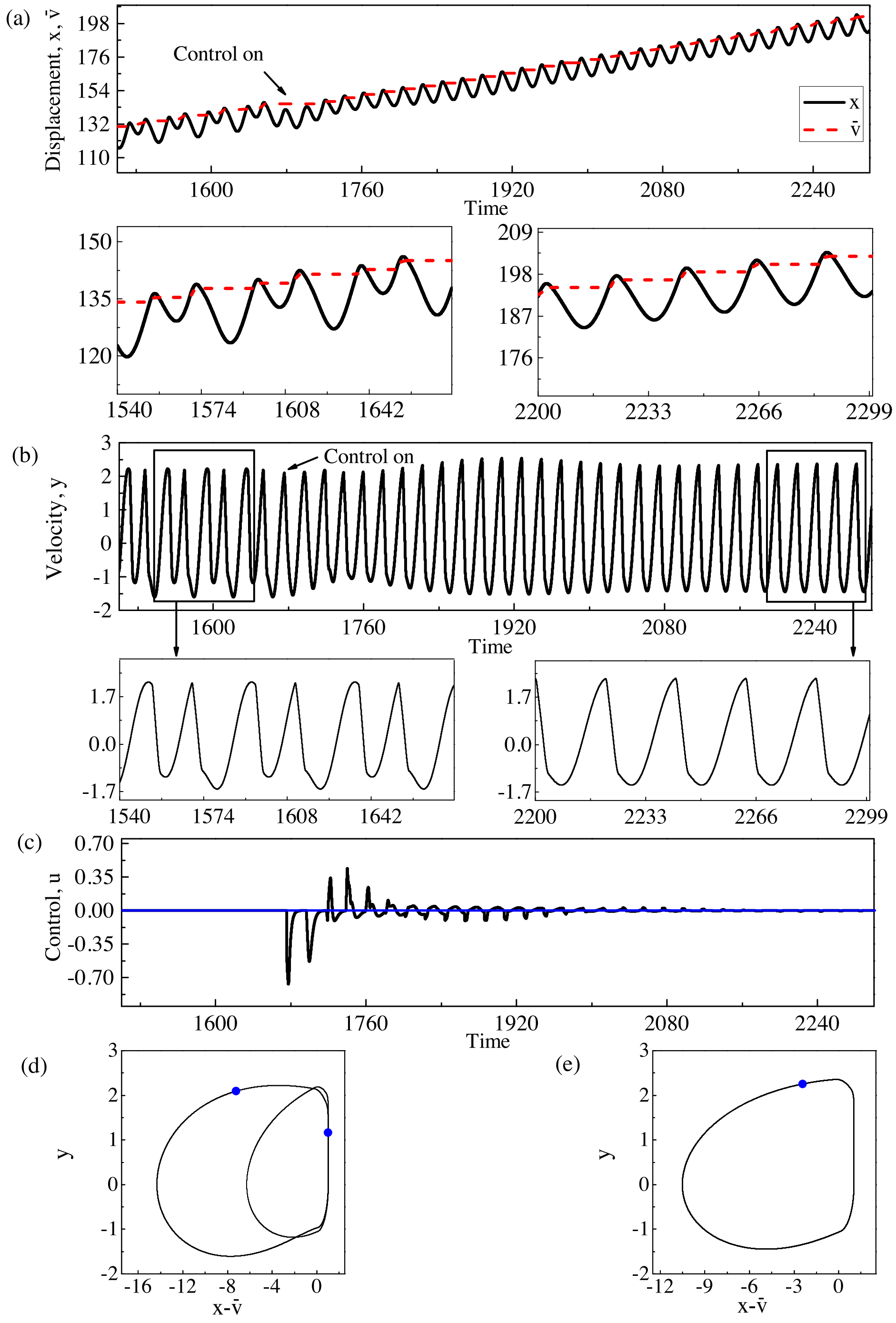

Fig. 6.3.4 (a) Time histories of displacement of mass x and slider bottom v for $a = 0.3$, $\omega = 0.3$, $b = 0.15$, $\xi = 0.05$, $g = 0.02$, $\phi = \frac{\pi}{2}$ and $K = 0.5$. (b) Time histories of the velocity of mass x. (c) Time histories of the control signal u, and blue line denotes the zero line. Panel (h) depicts the phase portrait of period-2 attractor when the controller is off. Panel (i) depicts the phase portrait of period-1 attractor when the controller is on. The black solid curves and red dash curves represent the displacement of mass x and slider bottom v.

$$\begin{aligned}
\dot{x}_1 &= y_1, \\
\dot{y}_1 &= \alpha\cos(\omega\tau) + (x_2 - x_1) + 2\xi(y_2 - y_1) + u(\tau), \\
\dot{x}_2 &= 0, \\
\dot{y}_2 &= 0, \qquad (6.4.1)
\end{aligned}$$

- **No contact with moving capsule**, i.e. $x_1 - x_2 < \delta$, and $|(x_2 - x_1) + 2\xi(y_2 - y_1)| > 1$. Then, the motion of the mass and capsule are:

$$\begin{aligned}
\dot{x}_1 &= y_1, \\
\dot{y}_1 &= \alpha\cos(\omega\tau) + (x_2 - x_1) + 2\xi(y_2 - y_1) + u(\tau), \\
\dot{x}_2 &= y_2, \\
\dot{y}_2 &= (-\operatorname{sign}(y_2) - (x_2 - x_1) - 2\xi(y_2 - y_1))/(\gamma), \qquad (6.4.2)
\end{aligned}$$

- **Contact with stationary capsule**, i.e. $x_1 - x_2 \geq \delta$, and $|(x_2 - x_1) + 2\xi(y_2 - y_1) - \beta(x_1 - x_2 - \delta)| \leq 1$. Then, the motion of the mass and capsule are:

$$\begin{aligned}
\dot{x}_1 &= y_1, \\
\dot{y}_1 &= \alpha\cos(\omega\tau) + (x_2 - x_1) + 2\xi(y_2 - y_1) - \beta(x_1 - x_2 - \delta) + u(\tau), \\
\dot{x}_2 &= 0, \\
\dot{y}_2 &= 0, \qquad (6.4.3)
\end{aligned}$$

- **Contact with moving capsule**, i.e. $x_1 - x_2 \geq \delta$, and $|(x_2 - x_1) + 2\xi(y_2 - y_1) - \beta(x_1 - x_2 - \delta)| > 1$. Then, the motion of the mass and capsule are:

$$\begin{aligned}
\dot{x}_1 &= y_1, \\
\dot{y}_1 &= \alpha\cos(\omega\tau) + (x_2 - x_1) + 2\xi(y_2 - y_1) - \beta(x_1 - x_2 - \delta) + u(\tau), \\
\dot{x}_2 &= y_2, \\
\dot{y}_2 &= [-\operatorname{sign}(y_2) - (x_2 - x_1) - 2\xi(y_2 - y_1) + \beta(x_1 - x_2 - \delta)]/\gamma, \qquad (6.4.4)
\end{aligned}$$

where

$$u(\tau) = K\left(y_1(\tau - \tau_d) - y_1(\tau)\right), \quad \tau \geq 0, \qquad (6.4.5)$$

is the delay feedback control. In Eq. (6.4.5) $K \geq 0$ is the control gain, setting the coupling strength between the velocity output $y_1(\tau - \tau_d) - y_1(\tau)$ and the control input $u(\tau)$, and $\tau_d > 0$ is a tunable time delay (in contrast to a lag introduced by the control loop, which is assumed to be zero here). Since the purpose of this present work is to control the system to a period-1 response, the delay term τ_d is set to one period of the external excitation $\tau_d = T := 2\pi/\omega$.

Since the vibro-impact capsule system with the delay feedback control described as Eq. (6.4.1), (6.4.2), (6.4.3) and (6.4.4) is hard to analyse due to the problem of the motion unboundedness, a co-ordinates transformation $\upsilon := x_1 - x_2$ and $\kappa := y_1 - y_2$ as shown in Section 3.4 has to be adopt, so that the above system can be changed to the following form:

- **No contact with stationary capsule**, i.e. $\upsilon < \delta$, and $|\upsilon + 2\xi\kappa| \leq 1$.

$$\begin{aligned}
\dot{\upsilon} &= y_1, \\
\dot{\kappa} &= \alpha\cos(\omega\tau) - \upsilon - 2\xi\kappa + u(\tau), \\
\dot{y}_1 &= \alpha\cos(\omega\tau) - \upsilon - 2\xi\kappa + u(\tau), \\
\dot{y}_2 &= 0.
\end{aligned} \tag{6.4.6}$$

- **No contact with moving capsule**, i.e. $\upsilon < \delta$, and $|\upsilon + 2\xi\kappa| > 1$.

$$\begin{aligned}
\dot{\upsilon} &= \kappa, \\
\dot{\kappa} &= \alpha\cos(\omega\tau) - \upsilon - 2\xi\kappa - (-\operatorname{sign}(y_2) + \upsilon + 2\xi\kappa)/(\gamma) + u(\tau), \\
\dot{y}_1 &= \alpha\cos(\omega\tau) - \upsilon - 2\xi\kappa + u(\tau), \\
\dot{y}_2 &= (-\operatorname{sign}(y_2) - (x_2 - x_1) - 2\xi(y_2 - y_1))/(\gamma).
\end{aligned} \tag{6.4.7}$$

- **Contact with stationary capsule**, i.e. $\upsilon \geq \delta$, and $|\upsilon + 2\xi\kappa - \beta(\upsilon - \delta)| \leq 1$.

$$\begin{aligned}
\dot{\upsilon} &= y_1, \\
\dot{\kappa} &= \alpha\cos(\omega\tau) - \upsilon - 2\xi\kappa - \beta(\upsilon - \delta) + u(\tau), \\
\dot{y}_1 &= \alpha\cos(\omega\tau) - \upsilon - 2\xi\kappa - \beta(\upsilon - \delta) + u(\tau), \\
\dot{y}_2 &= 0.
\end{aligned} \tag{6.4.8}$$

- **Contact with moving capsule**, i.e. $\upsilon \geq \delta$, and $|\upsilon + 2\xi\kappa - \beta(\upsilon - \delta)| > 1$.

$$
\begin{aligned}
\dot{\upsilon} &= \kappa, \\
\dot{\kappa} &= \alpha \cos(\omega\tau) - \upsilon - 2\xi\kappa - \beta(\upsilon-\delta) \\
&\quad - [-\operatorname{sign}(y_2) + \upsilon + 2\xi\kappa + \beta(\upsilon-\delta)]/\gamma + u(\tau), \\
\dot{y}_1 &= \alpha \cos(\omega\tau) - \upsilon - 2\xi\kappa - \beta(\upsilon-\delta) + u(\tau), \\
\dot{y}_2 &= [-\operatorname{sign}(y_2) + \upsilon + 2\xi\kappa + \beta(\upsilon-\delta)]/\gamma. \qquad (6.4.9)
\end{aligned}
$$

Through the above forms, the problem caused by motion unboundedness can be avoided and the LEs can be calculated. At the following discussion, the definition of Stroboscopic map and Jacobian matrix in Section 6.2.1 will be adopt to calculate the LEs for the above vibro-impact system.

6.4.2 Numerical investigation of the vibro-impact capsule system with the delay feedback controller

The numerical study starts with bifurcation analysis of the dynamics of the vibro-impact capsule system without the delay feedback control, as given in Eq. (3.4.10), (3.4.11), (3.4.12) and (3.4.13). In Fig. 6.4.1, it shows the relevant bifurcation diagram, where ω is used as the bifurcation parameter. 330 cycles of external excitation were run to obtain the bifurcation diagram. Among 330 cycles, the first 300 cycles were omitted to ensure the steady state response, and the last 30 values of the velocity y were plotted in the bifurcation diagram for each value of the bifurcation parameter. During the simulation, when the velocity is smaller than 10^{-3} and greater than -10^{-3}, this velocity can be treated as a small enough value. In addition, the initial condition for the all simulations is $x_1 = 0$, $x_2 = 0$, $y_1 = 0$ and $y_2 = 0$. It can be seen that a period-1 motion is presented during $\omega \in [2, 2.32]$. The phase portraits of the period-1 attractor at $\omega = 2.2$ is shown in Fig 6.4.1 (b), and the relevant trajectory is presented in Fig. 6.4.2 (a), which show that the capsule under the external excitation with frequency $\omega = 2.2$ is moving very slowly. Finally, the capsule arrives at 0.164 at $\tau = 395$. For the range $\omega \in [2.32, 2.71]$ as shown in Fig. 6.4.1, the system witnesses period-doubling twice at $\omega = 2.332$ and $\omega = 2.592$. When $\omega = 2.44$ and $\omega = 2.62$, the system present two different motions with different periods. At $\omega = 2,44$, the system behaves the period-2 motion in Fig. 6.4.1 (c), and at $\omega = 2.62$ a period-4 motion is presented as shown in Fig. 6.4.1 (d). As shown in Fig. 6.4.2 (b) and (c), the capsule does not have obvious moving, and their displacements are around 0. At $\omega = 3.175$, the system presents a period-2 motion in Fig. 6.4.1 (e). Compared with other motions, the capsule at $\omega = 3.175$ witnesses an obvious moving, which starts from $x_2 = 0$ at $\tau = 0$ and arrives at $x_2 = 11.34$ at $\tau = 395$, as shown in Fig. 6.4.2 (d).

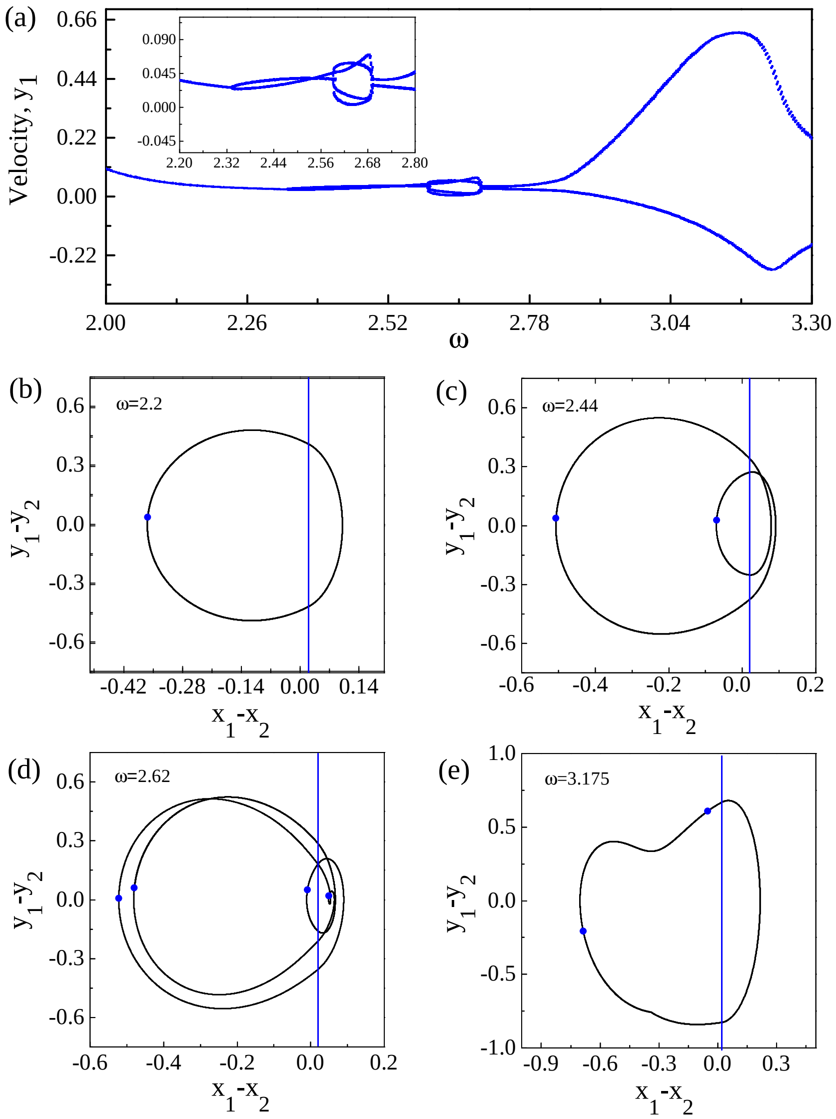

Fig. 6.4.1 (a) Bifurcation diagram of the capsule computed for $\alpha = 0.6$, $\delta = 0.02$, $\xi = 0.05$, $\beta = 12$, $\gamma = 3$ and varying frequency of external excitation ω. The phase portrait of different external excitation ω: (b) $\omega = 2.2$, (c) $\omega = 2.44$, (d) $\omega = 2.62$ and (e) $\omega = 3.175$. The locations of the impact surface are shown by blue lines and Poincareé sections are marked by blue dots.

Since the system presents period-2 dynamical response at $\omega = 3.175$ as shown in Fig. 6.4.2, the delay feedback control (6.4.5), $u(\tau) = K\left(y_1(\tau - \tau_d) - y_1(\tau)\right)$ with $\tau = 2\pi/\omega$ was applied to control the system to the period-1 dynamical response. In fact, there is an effective

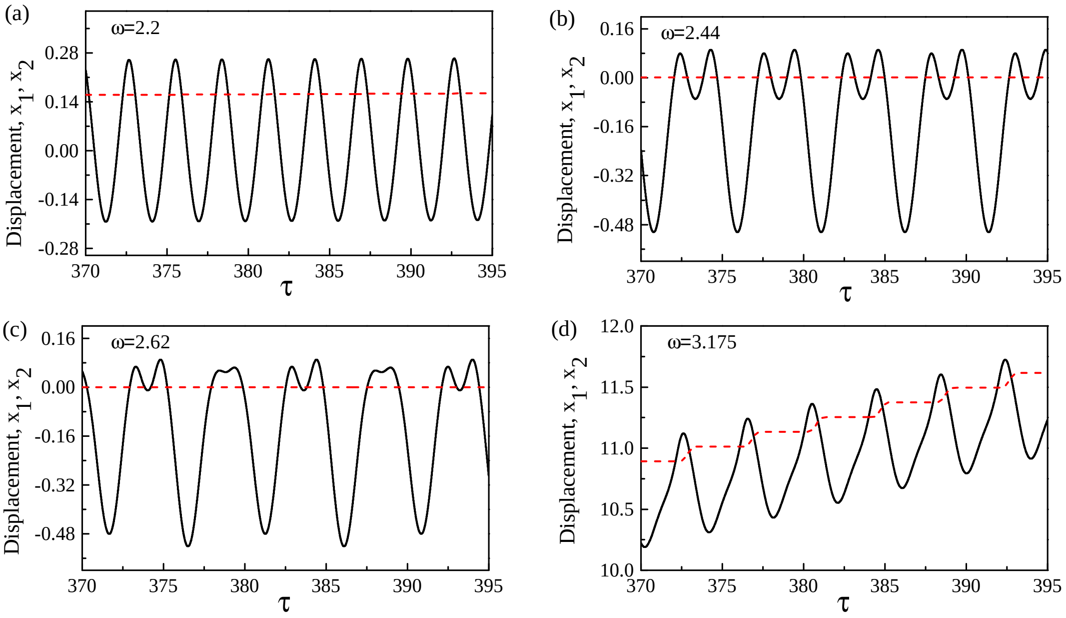

Fig. 6.4.2 Time histories of displacement of mass (black solid curves) and capsule (red dash curves) for $\alpha = 0.6$, $\delta = 0.02$, $\xi = 0.05$, $\beta = 12$ and $\gamma = 3$: (a) $\omega = 2.2$, (b) $\omega = 2.44$, (c) $\omega = 2.62$ and (d) $\omega = 3.175$.

interval of control gains K to stable the system on the period-1 motion. In Fig. 6.4.3 (a), it shows a bifurcation diagram of the controlled vibro-impact capsule system for varying the bifurcation parameter K. The calculation were run for 160 periods of the external excitation with $K = 0$ to ensure that the system described by Eq. (6.4.6), (6.4.7), (6.4.8) and (6.4.9) settles down to its steady state, and then switched the controller (6.4.5) on and kept the system under a particular value of the control gain K running for 500 periods, whereas the last 50 values of the velocity y_1 of the mass were plotted in the bifurcation diagram. Fig. 6.4.3 (b) shows the corresponding LE diagram of the controlled vibro-impact capsule system by varying the control parameter K. The calculations for the LEs were run for 150 periods of external excitation with $K = 0$ initially, followed by another 3000 periods calculations with a certain value of K, where the first 250 periods were omitted to ensure the steady state response of the controlled system while the rest periods were used to calculate the LEs. Since after $K = 0.18$ the capsule does not move any more after the system becomes stable, the period-2 and period-1 dynamical responses in Fig. 6.4.3 after $K = 0.18$ are described only by Eq. (6.4.6) and (6.4.8), which means that the two of LEs are always around 0. It can be seen from the figures that, when $K < 0.707$, the system presents period-2 dynamical responses. For example, when $K = 0.1$, the system has a period-2 attractor as shown in the small window of Fig. 6.4.3 (a), which has a smaller area of phase portrait than the attractor at $\omega = 3.175$ and $K = 0$. When $K = 0.45$, the system presents a period-2 motion with a smaller area than the attractor at $K = 0.1$. It should be pointed out that when $K = 0.707$, the system witnesses a period-doubling bifurcation, and the leading LE is -4.94×10^{-4}, which is very close to 0. In addition, the system presents period-1 motion at $K \in [0.707, 1.5]$, and the leading LE is less than 0.

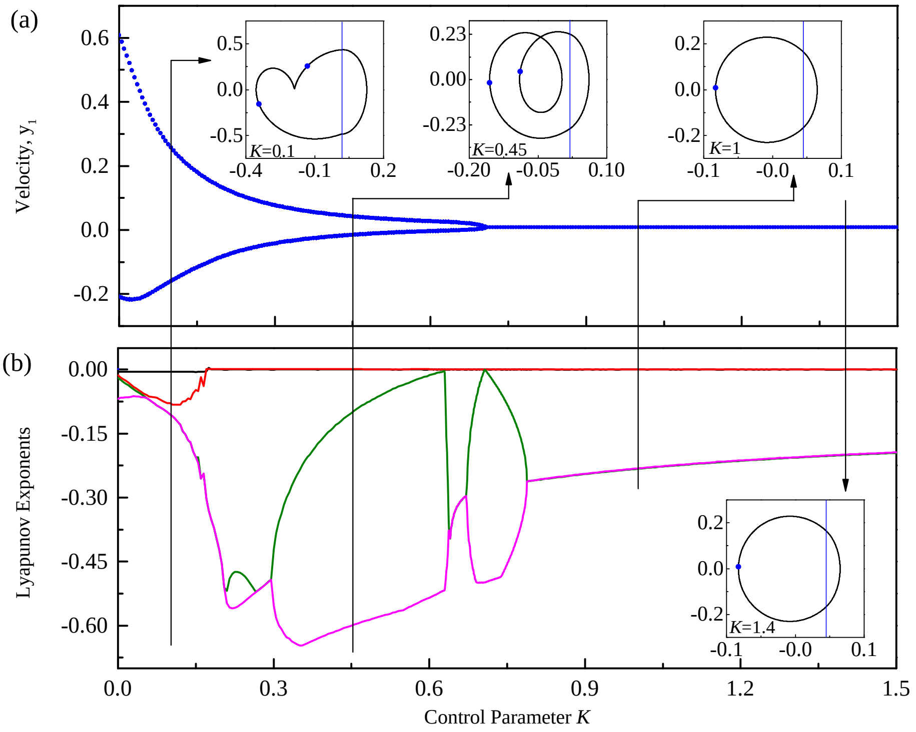

Fig. 6.4.3 (a) Bifurcation diagram and (b) LEs of capsule system with the delay feedback control for varying the control gain K. System parameters are $\alpha = 0.6$, $\delta = 0.02$, $\xi = 0.05$, $\beta = 12$, $\gamma = 3$, $\omega = 3.175$ and $\tau_d = \frac{2\pi}{\omega}$. Black, red, olive and magenta lines denote the four LEs.

According to the above results, when $K > 0.707$, the delay feedback controller can stabilise the vibro-impact capsule system on the target period-1 orbit. In Fig. 6.4.4, it presents the time profiles of displacement of mass and capsule, velocity of the mass, velocity of the capsule and its external excitation with the control signal u as a demonstration of controlling to the period-1 motion, when $K = 1$. As can be seen from the figure, the controller is switched on at $\tau = 158.197$, and the relative motion between the inner mass and the capsule is stable on the period-1 attractor. The capsule is stop and inner mass presents a period-1 motion.

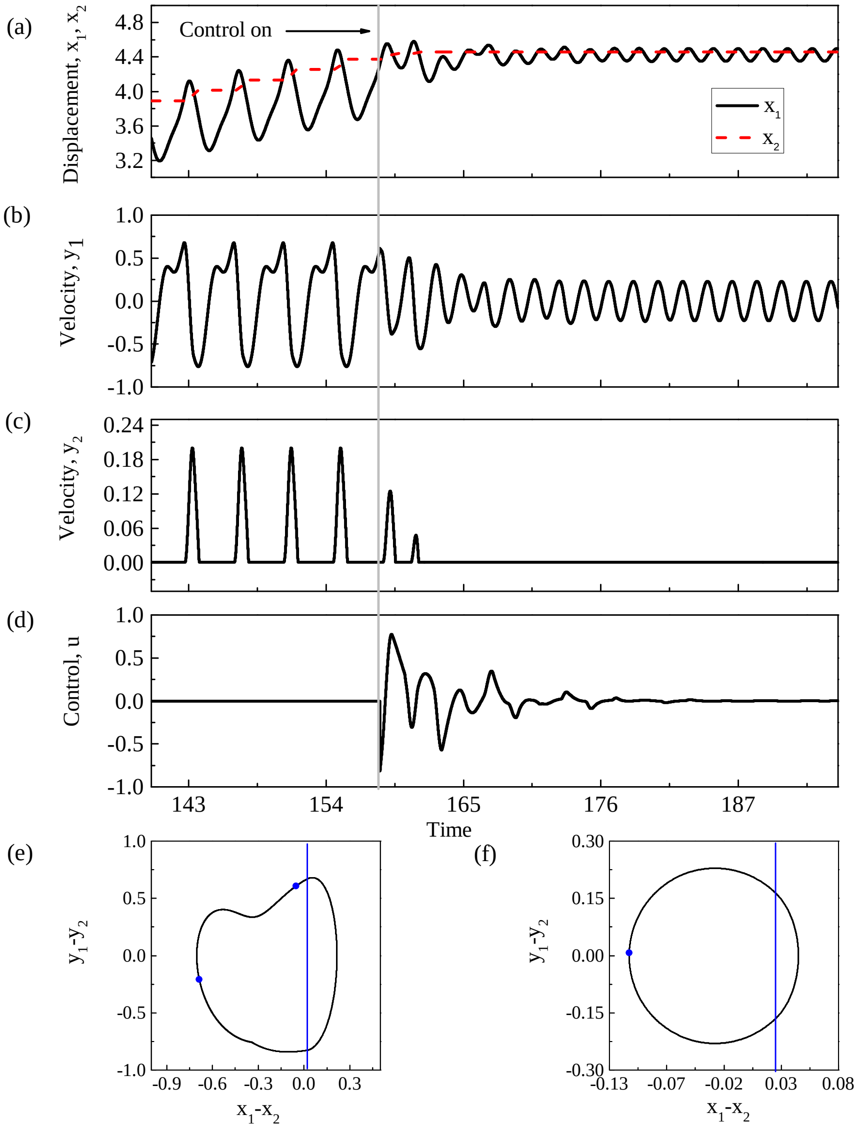

Fig. 6.4.4 (a) Time histories of displacement of mass x_1 and capsule x_2 for $\alpha = 0.6$, $\delta = 0.02$, $\xi = 0.05$, $\beta = 12$, $\gamma = 3$, $\omega = 3.175$ and $\tau_d = \frac{2\pi}{\omega}$ and $K = 1$. The black solid curves and red dash curves represent the displacement of mass x_1 and capsule x_2. (b) Time histories of the velocity y_1 of mass. (c) Time histories of the velocity y_2 of mass. (d) Time histories of the control signal u. Panel (e) depicts the phase portrait of period-2 attractor when the controller is off. Panel (f) depicts the phase portrait of period-1 attractor when the controller is on.

6.5 Conclusion

This chapter studies the dynamical performance of three different impact systems with a periodical force by a delay feedback controller. The control aims to switch the system from undesired coexisting attractors to a desired period-1 response, so that some complex dynamical phenomenons can be avoided, such as the coexisting attractors and chaotic motions. Compared with the other control methods, such as the linear gain control and the Lai's method [21], the advantage of the delay feedback control is that it does not need to have the complete information of the desired attractor, while only the periods of the target attractor is required. However, the delay feedback control has some disadvantages. For example, the delay feedback control is hard to achieve the control from an undesired attractor to a coexisting one with multiple periods of the undesired attractor. In addition, after introducing this control, the controlled system becomes a infinite-dimensional system, which can result in a significant increase of the computation time.

- In the first part, for the soft impact system, a scenario with grazing-induced multistability with coexisting period-3, period-4 and period-7 attractors was investigated. Basins of attraction reveal the complex dynamics of the system during grazing events. It was found that, through fixing $\tau_d = 2\pi/\omega$ in the delay feedback control, the system can be controlled to a globally stable period-1 motion with grazing and one impact per period of excitation, when its control parameter is $K \in [0.148, 0.42]$. As the control gain parameter increases ($K > 0.42$) the control destabilises the period-1 motion through a Neimark-Sacker bifurcation and the system can bifurcate to chaos via torus. In addition, the continuation techniques for nonsmooth dynamical systems were used for identifying the parameter window defined by two period-doubling points at where the desired (unstable) period-1 exists. The results show that the control is able to not only stabilise the desired period-1 motion but also control impacting regimes in the system.

- In the second part, for the impact system with a drift, the bifurcation analysis was studied, and the dynamical performance under different frequencies was revealed. Through introducing the delay feedback control and fixing $\tau_d = 2\pi/\omega$ in the delay feedback control, the relative motion between the mass and slider bottom can be controlled to the period-1 motion from the period-2 motion, when its control parameter is $K \in [0.008, 1]$.

- In the third part, for the vibro-impact capsule system, the bifurcation analysis and the simulations reveal the complex dynamics of the system under the complex discontinuous conditions. This relative motion between mass and capsule can be controlled to the period-1 motion from the period-2 motion, through introducing the delay feedback control with $\tau_d = 2\pi/\omega$, when its control parameter is $K \in [0.707, 1.5]$.

6.6 Practical implementation of the delay feedback control

From the previous numerical results, the efficiency of the delay feedback control on the control of coexisting attractors was validated. In practice, the delayed feedback control can be implemented by using a proper actuator. Based on the feedback from the historical time series of the velocity, the control signal can be generated and applied together with the external excitation of the system. However, when the delay feedback control is applied to the system, the system's states may witness a significant change due to the control signal. Therefore, some constrains are needed for the controller (e.g., input saturation) to satisfy the experimental setup for safety issues. On the other hand, the introduction of control constrains may lead to a longer duration of stabilisation. Although there are some limitations, the delay feedback control is still easy to be implemented, and is effective to control the coexisting attractors.

Chapter 7

Control of coexisting attractors via the linear and non-linear control strategies

7.1 Introduction

This chapter presents a new control method to achieve the control of coexisting attractors for a class of non-autonomous dynamical systems. The central idea is through introducing a control to a system parameter, which can be used to switch between coexisting attractors, to generate a continuous path from the original undesired stable attractor to a desired one, according to the information from the desired attractor. Special attention is given to the process of which the value of the system parameter varies continuously from its original value, and then returns continuously to the original value after the controlled trajectory of the undesired attractor falls into the neighbourhood of the desired attractor, during switching between coexisting attractors.

The chapter is split into sections in the following way: In Section 7.2, it presents the concepts of the control method and details on how this control method is working on controlling coexisting attractors of the soft impact system. In Section 7.3, it shows the performance of this method on controlling coexisting attractors of the impact system with a drift. In Section 7.4, the control of coexisting attractors in a vibro-impact capsule system is studied, via the varying parameter control method. In Section 7.5, this control method is adopted to duffing oscillator. Finally, some conclusions are drawn in Section 7.6.

7.2 Control of the soft impact system

7.2.1 Design of the feedback control strategies

The following periodically forced systems with a single control input is considered

$$\begin{aligned} \dot{Y}_{\mathrm{u}}(\tau) &= F(\tau, Y_{\mathrm{u}}(\tau), u(\tau)), \\ Y_{\mathrm{u}}(\tau_0) &= Y_{\mathrm{u},0}, \end{aligned} \tag{7.2.1}$$

where the input $u(\tau)$ is a scalar function of time, and $\dot{Y}$ denotes differentiation with respect to time τ. Assuming that the uncontrolled system, (7.2.1) with $u(\tau) = 0$, has an attractor $Y_{\mathrm{d}}(\cdot)$ (where the subscript in Y_{d} stands for "desired"), but that the initial condition $Y_{\mathrm{u},0}$ is away from $Y_{\mathrm{d}}(0)$, and possibly outside the basin of attraction of $Y_{\mathrm{d}}(\cdot)$. Also assuming that this "desired" attractor $Y_d(\cdot)$ is (internally) stable in the sense that it has no positive Lyapunov exponents. It should be pointed out that the typical scenario is that $Y_{\mathrm{u},0}$ is on one of the other ("undesirable") attractors of the uncontrolled system.

Soft impact system

In this section, the soft impact system shown in Fig. 3.2.1 will be used as an example to study the proposed control method. Soft impacts occur in mechanical systems when an object hits an obstacle with a negligible mass but with a non-negligible stiffness, see e.g. [39, 15, 156, 9, 157]. As can be seen from Fig. 3.2.1, it is assumed that the discontinuity boundary is fixed at $x = e$, with $e > 0$ being the nondimensional gap. The equations of motion of the oscillator are in form (7.2.1), where $Y(\tau) := (x(\tau), v(\tau))^T$. Three different cases will be considered. Defining for scalar $\tilde{u}$

$$F_{\mathrm{gen}}(Y, \tilde{u}, u_e) := \begin{bmatrix} 0 & I \\ -I - \beta H(x-e) & -2\zeta \end{bmatrix} Y + \begin{bmatrix} 0 \\ \beta(e+u_e)H(x-e-u_e) + \tilde{u} \end{bmatrix}, \tag{7.2.2}$$

the three cases for control input are

$$F_{\mathrm{lin}}(\tau, Y, u) := F_{\mathrm{gen}}(Y, a\omega^2 \sin(\omega\tau) + u, 0), \tag{7.2.3}$$

$$F_a(\tau, Y, u) := F_{\mathrm{frc}}(Y, (a+u)\omega^2 \sin(\omega\tau), 0), \tag{7.2.4}$$

$$F_e(\tau, Y, u) := F_{\mathrm{frc}}(Y, a\omega^2 \sin(\omega\tau), u). \tag{7.2.5}$$

The first case, F_{lin} has linear control input and the second case, F_a, has parametric control input, varying the forcing amplitude, while the third case adjusts the gap e. The function

$H(\cdot)$ stands for the Heaviside step function. In the right-hand side F_{frc}, defined in (7.2.2), the variables (including time) and parameters of the system are nondimensionalised, as shown in Section 3.2.

The right-hand side given in Eq. (7.2.2) is a typical non-autonomous dynamical system with the one-sided elastic constraint considered as the nonsmooth property that can lead to complex phenomena, such as the grazing bifurcation [44, 46], the coexistence of multistable attractors [158, 54] and the chaotic motions [156]. Here, a situation that system (7.2.1) with $u(\tau) = 0$ has many coexisting attractors within some specific ranges of the system parameters was considered. In particular, among the coexisting attractors, Y_{d} denotes a desired stable attractor with non-positive Lyapunov exponents exists. Usually, this $Y_{\mathrm{d}}(\cdot)$ is a stable periodic orbit. For Y_{d}, small changes in system parameters do not affect the response of the system significantly, such that the attractor Y_{d} will persist.

Distance-reducing control

Let us introduce the following definition.

Definition 7.2.1. For a dynamical system $\dot{Y}(\tau) = F(\tau, Y(\tau), 0)$, $Y_{\mathrm{u}}(\tau_0) = Y_{\mathrm{u},0}$ (so, of type (7.2.1) with $u = 0$) with two stable coexisting attractors $Y_{\mathrm{c}}(\cdot)$ and $Y_{\mathrm{d}}(\cdot)$, if there exists a continuous control $u(\tau)$ such that system (7.2.1) with this control $u(\cdot)$ and $Y_{\mathrm{u},0} = Y_{\mathrm{c}}(\tau_0)$ satisfies $Y_{\mathrm{u}}(\tau) - Y_{\mathrm{d}}(\tau) \to 0$ for $\tau \to \infty$, it is said that Y_{c} is controllable to Y_{d} (by u). If $Y_{\mathrm{u}}(\tau^*) = Y_{\mathrm{d}}(\tau^*)$ for some finite time τ^*, it is said that Y_{c} is controllable to Y_{d} in finite time.

Since $Y_{\mathrm{d}}(\cdot)$ is an attractor for $u(\tau) = 0$, the system will follow $Y_{\mathrm{d}}(\tau)$ for $\tau > \tau^*$, if $u(\tau) = 0$ for $\tau > \tau^*$ after controlling to Y_d in finite time τ^*. Let us assume that system (7.2.1) is controllable, and there exists a control input $u(\cdot)$ that can be used for controlling its multistability.

Define the difference between the desired and the current states as

$$\begin{aligned} d(\tau) &:= Y_{\mathrm{d}}(\tau) - Y_{\mathrm{u}}(\tau), \quad \text{such that} \\ \Delta(\tau) &:= \langle d(\tau), d(\tau) \rangle \geq 0 \end{aligned}$$

is the distance at time τ from the desired attractor Y_{d}, where $\langle \cdot, \cdot \rangle$ is the inner product of two vectors. Then, a simple feedback control strategy will be investigated to reduce this distance Δ over time, such that $[\mathrm{d}/\mathrm{d}\tau]\Delta(\tau) < 0$. Requiring that $u(\tau)$ has permissible values between $-M_1$ and M_1, i.e. $u \in [-M_1.M_1]$, and Lipschitz constant M_2, where $M_{1,2} \in \mathbb{R}^+$, u at every time $\tau \geq \tau_0$ can be adjusted according to

$$\dot{u}(\tau) = M_2 \operatorname{sign}\left[-\frac{\partial}{\partial u}\frac{\mathrm{d}}{\mathrm{d}\tau}\Delta(\tau)\right] H(M_1+u)H(M_1-u), \tag{7.2.6}$$

starting from $u(\tau_0) = 0$, for as long as $\Delta(\tau) > \varepsilon$ with some tolerance $\varepsilon \ll 1$. In Eq. (7.2.6), $H(M_1-u)H(M_1+u)$ is the indicator function for the interval $[-M_1, M_1]$ (recall that H is the Heaviside function). The term $[\mathrm{d}/\mathrm{d}\tau]\Delta(\tau)$ is a function of $(\tau, Y_\mathrm{u}(\tau), Y_\mathrm{d}(\tau), u(\tau))$, making the derivative with respect to u non-zero:

$$\frac{\partial}{\partial u}\left[\frac{\mathrm{d}}{\mathrm{d}\tau}\Delta\right](\tau, Y_\mathrm{u}, Y_\mathrm{d}, u) = 2\langle Y_\mathrm{d} - Y_\mathrm{u}, \partial_u F(\tau, Y_\mathrm{u}, u)\rangle. \tag{7.2.7}$$

In the practical algorithms described in Section 7.2.1 and 7.2.1, Eq. (7.2.6) will be applied only when $[\mathrm{d}/\mathrm{d}\tau]\Delta(\tau) > 0$, otherwise, $\dot{u}(\tau) = 0$.

Implementation with finite sampling step — linear case

Let us assume the sampling time step, $h > 0$, such that $\tau_i = \tau_0 + ih$. If the control input u enters the right-hand side linearly with a constant coefficient vector b, such that $F(\tau, Y, u) = F(\tau, Y) + bu$ (as in example F_lin given in (7.2.2), where $b = (0, 1)^\mathrm{T}$), the notation in the definition (7.2.6) of the control u and the resulting expression (7.2.7) simplifies. Thus, Algorithm 1 can be formulated separately for this common case. In the formulation of Algorithm 1 with the sampling step h, the control input $u(\tau)$ is of type "zero-order hold". That is, $u(\tau)$ is a constant u_i on the sampling interval $[\tau_i, \tau_{i+1}]$, and the Lipschitz constant M_2 applies to changes per time step: $|u_{i+1} - u_i| \leq hM_2$.

After introducing the algorithm, the following main theorem can be obtained.

Theorem 7.2.1. Let the dynamical system $\dot{Y}(\tau) = F(\tau, Y) + (\mathbf{0}, u(\tau))^\mathrm{T}$ with $u = 0$ have two stable coexisting attractors Y_c and Y_d, and let $M_{1,2}$ be bounded intervals in $\mathbb{R}$. We assume that there exists a time $\tau^* > \tau_0$, such that for all sufficiently small sampling steps h the control U and trajectory Y_u obtained by Algorithm 1 with bounds $M_{1,2}$ satisfy

$$\begin{aligned}\Big|\langle d(\tau_0), d(\tau_0)\rangle + \sum_{i=0}^{n^*}\Big[&2\langle d(\tau_i), F(\tau_i, Y_\mathrm{d}(\tau_i)) - F(\tau_i, Y_\mathrm{u}(\tau_i)) - U(\tau_i)\rangle h - \langle d(\tau_i), \dot{U}(\tau_i)\rangle h^2 \\ &+ \langle F(\tau_i, Y_\mathrm{d}(\tau_i)) - F(\tau_i, Y_\mathrm{u}(\tau_i)) - U(\tau_i), F(\tau_i, Y_\mathrm{d}(\tau_i)) - F(\tau_i, Y_\mathrm{u}(\tau_i)) - U(\tau_i)\rangle h^2\Big]\Big| \leq c_1 h^2\end{aligned} \tag{7.2.8}$$

(here $d(\tau)=Y_{\mathrm{d}}(\tau)-Y_{\mathrm{u}}(\tau)$ and the τ_i are from the interval partition $[\tau_0,\tau^*)=\bigcup_{i=0}^{n^*}[\tau_{\mathrm{i}},\tau_{i+1})$ with $\tau_{i+1}=\tau_{\mathrm{i}}+h$ for $i=0,\dots,n^*$). Then these two stable attractors are controllable by this external controller.

Proof. Assume that there exists a sufficiently small $h>0$, the interval $[\tau_0,\tau^*]=\bigcup_{i=0}^{n^*}[\tau_i,\tau_{i+1}]$, where $\tau_{i+1}=\tau_i+h$ and $i=1,\cdots,n^*$. For $\tau\in[\tau_i,\tau_i+h]$, the distance vector can be defined as $d(\tau):=Y_{\mathrm{d}}(\tau_0)+\int_{\tau_0}^{\tau}F(\tau_{\mathrm{s}},Y_{\mathrm{d}}(\tau_{\mathrm{s}}))\mathrm{d}\tau_{\mathrm{s}}-Y_c(\tau_0)-\int_{\tau_0}^{\tau}(F(\tau_{\mathrm{s}},Y_u(\tau_{\mathrm{s}}))+U(\tau_{\mathrm{s}}))\mathrm{d}\tau_{\mathrm{s}}$.Thus,

$$\begin{aligned}\langle d(\tau),d(\tau)\rangle =&\langle Y_{\mathrm{d}}(\tau_{\mathrm{i}})+\int_{\tau_{\mathrm{i}}}^{\tau}F(\tau_{\mathrm{s}},Y_{\mathrm{d}}(\tau_{\mathrm{s}}))\mathrm{d}\tau_{\mathrm{s}}-Y_{\mathrm{u}}(\tau_{\mathrm{i}})-\int_{\tau_{\mathrm{i}}}^{\tau}(F(\tau_{\mathrm{s}},Y_{\mathrm{u}}(\tau_{\mathrm{s}}))+U(\tau_{\mathrm{s}}))\mathrm{d}\tau_{\mathrm{s}},\\ &Y_{\mathrm{d}}(\tau_{\mathrm{i}})+\int_{\tau_{\mathrm{i}}}^{\tau}F(\tau_{\mathrm{s}},Y_{\mathrm{d}}(\tau_{\mathrm{s}}))\mathrm{d}\tau_{\mathrm{s}}-Y_{\mathrm{u}}(\tau_{\mathrm{i}})-\int_{\tau_{\mathrm{i}}}^{\tau}(F(\tau_{\mathrm{s}},Y_{\mathrm{u}}(\tau_{\mathrm{s}}))+U(\tau_{\mathrm{s}}))\mathrm{d}\tau_{\mathrm{s}}\rangle,\end{aligned}$$

where $Y_{\mathrm{u}}(\tau_{\mathrm{i}}):=Y_c(\tau_0)+\int_{\tau_0}^{\tau_{\mathrm{i}}}(F(\tau_{\mathrm{s}},Y_{\mathrm{u}}(\tau_{\mathrm{s}}))+U(\tau_{\mathrm{s}}))\mathrm{d}\tau_{\mathrm{s}}$. Since $U(\tau)=U(\tau_{\mathrm{i}})+\dot{U}(\tau_{\mathrm{i}})(\tau-\tau_{\mathrm{i}})$, where $\tau\in[\tau_{\mathrm{i}},\tau_{\mathrm{i}}+h]$, and Eq. (7.2.7), it gives

$$\begin{aligned}\langle d(\tau),d(\tau)\rangle =&\langle Y_{\mathrm{d}}(\tau_{\mathrm{i}})-Y_{\mathrm{u}}(\tau_{\mathrm{i}})+\int_{\tau_{\mathrm{i}}}^{\tau}(F(\tau_{\mathrm{s}},Y_{\mathrm{d}}(\tau_{\mathrm{s}}))-F(\tau_{\mathrm{s}},Y_{\mathrm{u}}(\tau_{\mathrm{s}}))-U(\tau_{\mathrm{s}}))\mathrm{d}\tau_{\mathrm{s}},\\ &Y_{\mathrm{d}}(\tau_{\mathrm{i}})-Y_{\mathrm{u}}(\tau_{\mathrm{i}})+\int_{\tau_{\mathrm{i}}}^{\tau}(F(\tau_{\mathrm{s}},Y_{\mathrm{d}}(\tau_{\mathrm{s}}))-F(\tau_{\mathrm{s}},Y_{\mathrm{u}}(\tau_{\mathrm{s}}))-U(\tau_{\mathrm{s}}))\mathrm{d}\tau_{\mathrm{s}}\rangle\\ =&\langle d(\tau_{\mathrm{i}}),d(\tau_{\mathrm{i}})\rangle+2\langle d(\tau_{\mathrm{i}}),\int_{\tau_{\mathrm{i}}}^{\tau}(F(\tau_{\mathrm{s}},Y_{\mathrm{d}}(\tau_{\mathrm{s}}))-F(\tau_{\mathrm{s}},Y_{\mathrm{u}}(\tau_{\mathrm{s}}))-U(\tau_{\mathrm{i}}))\mathrm{d}\tau_{\mathrm{s}}\rangle\\ &-2\langle d(\tau_{\mathrm{i}}),\int_{\tau_{\mathrm{i}}}^{\tau}\dot{U}(\tau_{\mathrm{i}})(\tau_{\mathrm{s}}-\tau_{\mathrm{i}})\mathrm{d}\tau_{\mathrm{s}}\rangle+\langle\int_{\tau_{\mathrm{i}}}^{\tau}(F(\tau_{\mathrm{s}},Y_{\mathrm{d}}(\tau_{\mathrm{s}}))-F(\tau_{\mathrm{s}},Y_{\mathrm{u}}(\tau_{\mathrm{s}}))\\ &-U(\tau_{\mathrm{i}}))\mathrm{d}\tau_{\mathrm{s}},\int_{\tau_{\mathrm{i}}}^{\tau}(F(\tau_{\mathrm{s}},Y_{\mathrm{d}}(\tau_{\mathrm{s}}))-F(\tau_{\mathrm{s}},Y_{\mathrm{u}}(\tau_{\mathrm{s}}))-U(\tau_{\mathrm{i}}))\mathrm{d}\tau_{\mathrm{s}}\rangle\\ &-2\langle\int_{\tau_{\mathrm{i}}}^{\tau}(F(\tau_{\mathrm{s}},Y_{\mathrm{d}}(\tau_{\mathrm{s}}))-F(\tau_{\mathrm{s}},Y_{\mathrm{u}}(\tau_{\mathrm{s}}))-U(\tau_{\mathrm{i}}))\mathrm{d}\tau_{\mathrm{s}},\int_{\tau_{\mathrm{i}}}^{\tau}\dot{U}(\tau_{\mathrm{i}})(\tau_{\mathrm{s}}-\tau_{\mathrm{i}})\mathrm{d}\tau_{\mathrm{s}}\rangle\\ &+\langle\int_{\tau_{\mathrm{i}}}^{\tau}\dot{U}(\tau_{\mathrm{i}})(\tau_{\mathrm{s}}-\tau_{\mathrm{i}})\mathrm{d}\tau_{\mathrm{s}},\int_{\tau_{\mathrm{i}}}^{\tau}\dot{U}(\tau_{\mathrm{i}})(\tau_{\mathrm{s}}-\tau_{\mathrm{i}})\mathrm{d}\tau_{\mathrm{s}}\rangle.\end{aligned}$$

When $\tau=\tau_{i+1}$, it can obtain that,

$$\begin{aligned}&\langle d(\tau_{i+1}),d(\tau_{i+1})\rangle-\langle d(\tau_{\mathrm{i}}),d(\tau_{\mathrm{i}})\rangle\\ =&2\langle d(\tau_{\mathrm{i}}),F(\tau_{\mathrm{i}},Y_{\mathrm{d}}(\tau_{\mathrm{i}}))-F(\tau_{\mathrm{i}},Y_{\mathrm{u}}(\tau_{\mathrm{i}}))-U(\tau_{\mathrm{i}})\rangle h-\langle d(\tau_{\mathrm{i}}),\dot{U}(\tau_{\mathrm{i}})\rangle h^2\\ &+\langle F(\tau_{\mathrm{i}},Y_{\mathrm{d}}(\tau_{\mathrm{i}}))-F(\tau_{\mathrm{i}},Y_{\mathrm{u}}(\tau_{\mathrm{i}}))-U(\tau_{\mathrm{i}}),F(\tau_{\mathrm{i}},Y_{\mathrm{d}}(\tau_{\mathrm{i}}))-F(\tau_{\mathrm{i}},Y_{\mathrm{u}}(\tau_{\mathrm{i}}))-U(\tau_{\mathrm{i}})\rangle h^2\\ &-\langle F(\tau_{\mathrm{i}},Y_{\mathrm{d}}(\tau_{\mathrm{i}}))-F(\tau_{\mathrm{i}},Y_{\mathrm{u}}(\tau_{\mathrm{i}}))-U(\tau_{\mathrm{i}}),\dot{U}(\tau_{\mathrm{i}})\rangle h^3+\tfrac{1}{4}\langle\dot{U}(\tau_{\mathrm{i}}),\dot{U}(\tau_{\mathrm{i}})\rangle h^4\\ =&2\langle d(\tau_{\mathrm{i}}),F(\tau_{\mathrm{i}},Y_{\mathrm{d}}(\tau_{\mathrm{i}}))-F(\tau_{\mathrm{i}},Y_{\mathrm{u}}(\tau_{\mathrm{i}}))-U(\tau_{\mathrm{i}})\rangle h-\langle d(\tau_{\mathrm{i}}),\dot{U}(\tau_{\mathrm{i}})\rangle h^2\\ &+\langle F(\tau_{\mathrm{i}},Y_{\mathrm{d}}(\tau_{\mathrm{i}}))-F(\tau_{\mathrm{i}},Y_{\mathrm{u}}(\tau_{\mathrm{i}}))-U(\tau_{\mathrm{i}}),F(\tau_{\mathrm{i}},Y_{\mathrm{d}}(\tau_{\mathrm{i}}))-F(\tau_{\mathrm{i}},Y_{\mathrm{u}}(\tau_{\mathrm{i}}))-U(\tau_{\mathrm{i}})\rangle h^2+O(h^3).\end{aligned}$$

If $\langle d(\tau_{i+1}), d(\tau_{i+1})\rangle - \langle d(\tau_{\mathrm{i}}), d(\tau_{\mathrm{i}})\rangle$ is not positive, the inequality (7.2.9) in **Step 2** is obtained. By repeating n^* times, then

$$\begin{aligned}
&\langle d(\tau_{n^*}), d(\tau_{n^*})\rangle - \langle d(\tau_0), d(\tau_0)\rangle\\
=&\sum_{i=0}^{n^*-1}\Big[\langle d(\tau_{i+1}), d(\tau_{i+1})\rangle - \langle d(\tau_{\mathrm{i}}), d(\tau_{\mathrm{i}})\rangle\Big]\\
=&\sum_{i=0}^{n^*}\Big[2\langle d(\tau_{\mathrm{i}}), F(\tau_{\mathrm{i}}, Y_{\mathrm{d}}(\tau_{\mathrm{i}})) - F(\tau_{\mathrm{i}}, Y_{\mathrm{u}}(\tau_{\mathrm{i}})) - U(\tau_{\mathrm{i}})\rangle h - \langle d(\tau_{\mathrm{i}}), \dot{U}(\tau_{\mathrm{i}})\rangle h^2\\
&+\langle F(\tau_{\mathrm{i}}, Y_{\mathrm{d}}(\tau_{\mathrm{i}})) - F(\tau_{\mathrm{i}}, Y_{\mathrm{u}}(\tau_{\mathrm{i}})) - U(\tau_{\mathrm{i}}), F(\tau_{\mathrm{i}}, Y_{\mathrm{d}}(\tau_{\mathrm{i}})) - F(\tau_{\mathrm{i}}, Y_{\mathrm{u}}(\tau_{\mathrm{i}})) - U(\tau_{\mathrm{i}})\rangle h^2\Big] + O(h^2)
\end{aligned}$$

Hence, $\langle d(\tau_{n^*}), d(\tau_{n^*})\rangle \leq c_1 h^2$ indicating that the controlled trajectory is within the neighborhood of the desired attractor. □

Algorithm 1 Linear control

```
  Step 0:
  Choose $M_1$ and $M_2$, where $M_1$ is the boundary of $|u(\tau)|$, $M_2$ is the boundary of $|\dot{u}(\tau)|$, and
  $\dot{u}(\tau) := \frac{\mathrm{d}u(\tau)}{\mathrm{d}\tau}$. Take the initial control $u(\tau_0) = 0 \in M_1$, and set the iteration index $i = 0$ and
  the time step $h$. Below we denote $U(\tau) = bu(\tau)$.
  while the termination criterion $\langle d(\tau_{\mathrm{i}}), d(\tau_{\mathrm{i}})\rangle \leq \varepsilon$ is not satisfied, do
    Step 1: Compute the range of $\dot{u}(\tau_{\mathrm{i}})$ that satisfies the following criterion

      $\langle d(\tau_{\mathrm{i}}), \dot{U}(\tau_{\mathrm{i}})\rangle h \geq 2\langle d(\tau_{\mathrm{i}}), F(\tau_{\mathrm{i}}, Y_{\mathrm{d}}(\tau_{\mathrm{i}})) - F(\tau_{\mathrm{i}}, Y_{\mathrm{u}}(\tau_{\mathrm{i}})) - U(\tau_{\mathrm{i}})\rangle$        (7.2.9)
          $+ \langle F(\tau_{\mathrm{i}}, Y_{\mathrm{d}}(\tau_{\mathrm{i}})) - F(\tau_{\mathrm{i}}, Y_{\mathrm{u}}(\tau_{\mathrm{i}})) - U(\tau_{\mathrm{i}}), F(\tau_{\mathrm{i}}, Y_{\mathrm{d}}(\tau_{\mathrm{i}}))$
          $- F(\tau_{\mathrm{i}}, Y_{\mathrm{u}}(\tau_{\mathrm{i}})) - U(\tau_{\mathrm{i}})\rangle h,$

    calling this range the feasible range for $\dot{u}(\tau_i)$.
    Step 2: If this feasible range is greater than $M_2$ and ensure that $u_{i+1}$ satisfies $M_1$, take
    the minimum value of $|\dot{u}(\tau_{\mathrm{i}})|$ and go to Step 3. Otherwise, choose the value $\dot{u}(\tau_{\mathrm{i}})$ such
    that both $M_1$ and $M_2$ are satisfied and is the closest to the feasible range of $\dot{u}(\tau_{\mathrm{i}})$, and go
    to Step 3. (NB. Use $\dot{u}(\tau_{\mathrm{i}}) = 0$ if $d(\tau_{\mathrm{i}})$ decreases at $\tau_{\mathrm{i}}$.)
    Step 3:
    Use $u_{i+1} = u_i + \dot{u}(\tau_{\mathrm{i}})h$ for input $u$ in Eq. (7.2.1) for $\tau > \tau_i$. Increase $i$ by 1 and return to
    Step 1.
  end while
```

According to **Theorem 7.2.1**, the following lemma can be obtained.

Lemma 7.2.2. For any two of stable coexisting attractors of system (7.2.2), if the control sequence $\{u_i\}$, $i = 1, \cdots, n^*$ generated by Algorithm 1 satisfies $u(\tau_0) = 0$, $u(\tau) \in M_1$, $\dot{u}(\tau) \in$

M_2, where $M_{1,2}$ are the bounded intervals of $\mathbb{R}$, inequality (7.2.8) and $|u(\tau^*)| \leq c_1 h$, then these two stable attractors are controllable by this external control sequence.

Implementation with finite sampling step — nonlinear case

By adjusting the accessible parameter of non-autonomous dynamical systems, such as the amplitude of excitation, system energy is altered, so the dynamical property of the system can be controlled (see e.g. [66, 21, 72]). In this part, the control method in in Algorithm 1 will be applied to an accessible system parameter to achieve the switching between two stable coexisting attractors. The detailed algorithm of the new control method (Algorithm 2) is given as below, and the following theorem is introduced.

Theorem 7.2.3. Let the dynamical system $\dot{Y}(\tau) = F(\tau, Y, u_p(\tau))$ with $u_p = 0$ have two stable coexisting attractors Y_c and Y_d, and let $M_{p,\kappa}$, $\kappa = 1,2$ be bounded intervals in $\mathbb{R}$. We assume that there exists a time $\tau^* > \tau_0$, such that for all sufficiently small sampling steps h the control u_p and trajectory Y_u obtained by Algorithm 2 with bounds $M_{p,\kappa}$ satisfy

$$\begin{aligned}
&\Big|\langle d_\mathrm{p}(\tau_0), d_\mathrm{p}(\tau_0)\rangle + \sum_{i=0}^{n^*}\Big[2\langle d_\mathrm{p}(\tau_\mathrm{i}), F(\tau_\mathrm{i}, Y_\mathrm{d}(\tau_\mathrm{i})) - F(\tau_\mathrm{i}, Y_\mathrm{u}(\tau_\mathrm{i}), u_\mathrm{p}(\tau_\mathrm{i}))\rangle h \\
&- \langle d_\mathrm{p}(\tau_\mathrm{i}), \frac{\mathrm{D}F(\tau_\mathrm{i}, Y_\mathrm{u}(\tau_\mathrm{i}), u_\mathrm{p}(\tau_\mathrm{i}))}{\mathrm{D}\tau}\rangle h^2 + \langle F(\tau_\mathrm{i}, Y_\mathrm{d}(\tau_\mathrm{i})) - F(\tau_\mathrm{i}, Y_\mathrm{u}(\tau_\mathrm{i}), u_\mathrm{p}(\tau_\mathrm{i})), F(\tau_\mathrm{i}, Y_\mathrm{d}(\tau_\mathrm{i})) \\
&- F(\tau_\mathrm{i}, Y_\mathrm{u}(\tau_\mathrm{i}), u_\mathrm{p}(\tau_\mathrm{i}))\rangle h^2 - \langle d_\mathrm{p}(\tau_\mathrm{i}), \frac{\mathrm{D}F(\tau_\mathrm{i}, Y_\mathrm{u}(\tau_\mathrm{i}), u_\mathrm{p}(\tau_\mathrm{i}))}{\mathrm{D}Y}\rangle h^2 \\
&- \langle d_\mathrm{p}(\tau_\mathrm{i}), \frac{\mathrm{D}F(\tau_\mathrm{i}, Y_\mathrm{u}(\tau_\mathrm{i}), u_\mathrm{p}(\tau_\mathrm{i}))}{\mathrm{D}u_\mathrm{p}}\dot{u}_\mathrm{p}(\tau_\mathrm{i})\rangle h^2\Big]\Big| \leq c_2 h^2, \qquad (7.2.10)
\end{aligned}$$

(here $d(\tau) = Y_\mathrm{d}(\tau) - Y_\mathrm{u}(\tau)$ and the τ_i are from the interval partition $[\tau_0, \tau^*) = \bigcup_{i=0}^{n^*}[\tau_\mathrm{i}, \tau_{i+1})$ with $\tau_{i+1} = \tau_\mathrm{i} + h$ for $i = 0, \ldots, n^*$). Then these two stable attractors are controllable by this external controller.

Proof. Assume that there exists a sufficiently small $h > 0$, the interval $[\tau_0, \tau^*] = \bigcup_{i=0}^{n^*}[\tau_\mathrm{i}, \tau_\mathrm{i+1}]$, where $\tau_\mathrm{i+1} = \tau_\mathrm{i} + h$, $i = 1, \cdots, n^*$. For $\tau \in [\tau_\mathrm{i}, \tau_\mathrm{i} + h]$, the distance vector can be defined as

$$d_\mathrm{p}(\tau) := Y_\mathrm{d}(\tau_0) + \int_{\tau_0}^{\tau} F(\tau_\mathrm{s}, Y_\mathrm{d}(\tau_\mathrm{s}))\mathrm{d}\tau_\mathrm{s} - Y_\mathrm{c}(\tau_0) - \int_{\tau_0}^{\tau} F(\tau_\mathrm{s}, Y_\mathrm{u}(\tau_\mathrm{s}), u_\mathrm{p}(\tau_\mathrm{s}))\mathrm{d}\tau_\mathrm{s}.$$

Next, we consider the Taylor expansion of $F(\tau, Y_\mathrm{u}(\tau), u_\mathrm{p}(\tau))$ within the time interval as

$$
\begin{aligned}
&\langle d_{\mathrm{p}}(\tau_{i+1}), d_{\mathrm{p}}(\tau_{i+1})\rangle \\
&= \langle Y_{\mathrm{d}}(\tau_{\mathrm{i}}) - Y_{\mathrm{u}}(\tau_{\mathrm{i}}) + \int_{\tau_{\mathrm{i}}}^{\tau_{\mathrm{i}+1}} (F(\tau_{\mathrm{s}}, Y_{\mathrm{d}}(\tau_{\mathrm{s}})) - F(\tau_{\mathrm{i}}, Y_{\mathrm{u}}(\tau_{\mathrm{i}}), u_{\mathrm{p}}(\tau_{\mathrm{i}})) - \frac{\mathrm{D}F(\tau_{\mathrm{i}}, Y_{\mathrm{u}}(\tau_{\mathrm{i}}), u_{\mathrm{p}}(\tau_{\mathrm{i}}))}{\mathrm{D}\tau}(\tau_{\mathrm{s}} \\
&\quad - \tau_{\mathrm{i}}) - \frac{\mathrm{D}F(\tau_{\mathrm{i}}, Y_{\mathrm{u}}(\tau_{\mathrm{i}}), u_{\mathrm{p}}(\tau_{\mathrm{i}}))}{\mathrm{D}Y}\dot{Y}_{\mathrm{u}}(\tau_{\mathrm{i}})(\tau_{\mathrm{s}} - \tau_{\mathrm{i}}) - \frac{\mathrm{D}F(\tau_{\mathrm{i}}, Y_{\mathrm{u}}(\tau_{\mathrm{i}}), u_{\mathrm{p}}(\tau_{\mathrm{i}}))}{\mathrm{D}u_{\mathrm{p}}}\dot{u}_{\mathrm{p}}(\tau_{\mathrm{i}})(\tau_{\mathrm{s}} - \tau_{\mathrm{i}}))\mathrm{d}\tau_{\mathrm{s}}, \\
&\quad Y_{\mathrm{d}}(\tau_{\mathrm{i}}) - Y_{\mathrm{u}}(\tau_{\mathrm{i}}) + \int_{\tau_{\mathrm{i}}}^{\tau_{\mathrm{i}+1}} (F(\tau_{\mathrm{s}}, Y_{\mathrm{d}}(\tau_{\mathrm{s}})) - F(\tau_{\mathrm{i}}, Y_{\mathrm{u}}(\tau_{\mathrm{i}}), u_{\mathrm{p}}(\tau_{\mathrm{i}})) - \frac{\mathrm{D}F(\tau_{\mathrm{i}}, Y_{\mathrm{u}}(\tau_{\mathrm{i}}), u_{\mathrm{p}}(\tau_{\mathrm{i}}))}{\mathrm{D}\tau}(\tau_{\mathrm{s}} \\
&\quad - \tau_{\mathrm{i}}) - \frac{\mathrm{D}F(\tau_{\mathrm{i}}, Y_{\mathrm{u}}(\tau_{\mathrm{i}}), u_{\mathrm{p}}(\tau_{\mathrm{i}}))}{\mathrm{D}Y}\dot{Y}_{\mathrm{u}}(\tau_{\mathrm{i}})(\tau_{\mathrm{s}} - \tau_{\mathrm{i}}) - \frac{\mathrm{D}F(\tau_{\mathrm{i}}, Y_{\mathrm{u}}(\tau_{\mathrm{i}}), u_{\mathrm{p}}(\tau_{\mathrm{i}}))}{\mathrm{D}u_{\mathrm{p}}}\dot{u}_{\mathrm{p}}(\tau_{\mathrm{i}})(\tau_{\mathrm{s}} - \tau_{\mathrm{i}}))\mathrm{d}\tau_{\mathrm{s}}\rangle.
\end{aligned}
$$

By following the same procedure in **Theorem 7.2.1**, this theorem can be proved. □

Algorithm 2 Nonlinear control

```
Step 0: Choose $M_{\mathrm{p},1}$ and $M_{\mathrm{p},2}$, which are the boundaries of $u_{\mathrm{p}}(\tau)$ and $\dot{u}_{\mathrm{p}}(\tau)$, respectively. Take the initial control $u_{\mathrm{p}}(\tau_0) = 0 \in M_{\mathrm{p},1}$, and set the iteration $i := 0$ and the time step $h$.
while the termination criterion $\langle d_{\mathrm{p}}(\tau_{\mathrm{i}}), d_{\mathrm{p}}(\tau_{\mathrm{i}})\rangle \leq \varepsilon$ is not satisfied, do
    Step 1: Compute the feasible range of $\dot{u}_{\mathrm{p}}(\tau_{\mathrm{i}})$ to satisfy the following criterion
        $\langle d_{\mathrm{p}}(\tau_{\mathrm{i}}), \frac{\mathrm{D}F(\tau_{\mathrm{i}}, Y_{\mathrm{u}}(\tau_{\mathrm{i}}), u_{\mathrm{p}}(\tau_{\mathrm{i}}))}{\mathrm{D}u_{\mathrm{p}}}\rangle \dot{u}_{\mathrm{p}}(\tau_{\mathrm{i}})h$
        $\geq 2\langle d_{\mathrm{p}}(\tau_{\mathrm{i}}), F(\tau_{\mathrm{i}}, Y_{\mathrm{d}}(\tau_{\mathrm{i}})) - F(\tau_{\mathrm{i}}, Y_{\mathrm{u}}(\tau_{\mathrm{i}}), u_{\mathrm{p}}(\tau_{\mathrm{i}}))\rangle - \langle d_{\mathrm{p}}(\tau_{\mathrm{i}}), \frac{\mathrm{D}F(\tau_{\mathrm{i}}, Y_{\mathrm{u}}(\tau_{\mathrm{i}}), u_{\mathrm{p}}(\tau_{\mathrm{i}}))}{\mathrm{D}\tau}\rangle h$
        $+ \langle F(\tau_{\mathrm{i}}, Y_{\mathrm{d}}(\tau_{\mathrm{i}})) - F(\tau_{\mathrm{i}}, Y_{\mathrm{u}}(\tau_{\mathrm{i}}), u_{\mathrm{p}}(\tau_{\mathrm{i}})), F(\tau_{\mathrm{i}}, Y_{\mathrm{d}}(\tau_{\mathrm{i}})) - F(\tau_{\mathrm{i}}, Y_{\mathrm{u}}(\tau_{\mathrm{i}}), u_{\mathrm{p}}(\tau_{\mathrm{i}}))\rangle h$
        $- \langle d_{\mathrm{p}}(\tau_{\mathrm{i}}), \frac{\mathrm{D}F(\tau_{\mathrm{i}}, Y_{\mathrm{u}}(\tau_{\mathrm{i}}), u_{\mathrm{p}}(\tau_{\mathrm{i}}))}{\mathrm{D}Y}\rangle h,$    (7.2.11)
    Step 2: If this range is greater than $M_2$ and ensure that $u_{\mathrm{p,i}}$ satisfied $M_{\mathrm{p},1}$, take the minimum value of $|\dot{u}_{\mathrm{p}}(\tau_{\mathrm{i}})|$ and go to Step 3. Otherwise, choose the value $\dot{u}_{\mathrm{p}}(\tau_{\mathrm{i}})$ such that both $M_{\mathrm{p},1}$ and $M_{\mathrm{p},2}$ are satisfied and is closest to the feasible range of $\dot{u}_{\mathrm{p}}(\tau_{\mathrm{i}})$. Then go to Step 3.
    Step 3: Use $u_{\mathrm{p,i+1}} = u_{\mathrm{p,i}} + \dot{u}_{\mathrm{p}}(\tau_{\mathrm{i}})h$ for Eq. (7.2.1) for $\tau > \tau_i$. Increment $i$ by 1 and return to Step 1.
end while
```

According to **Theorem 7.2.3**, the following lemma can be obtained.

Lemma 7.2.4. For any two of stable coexisting attractors of system (7.2.2), if the control sequence $\{u_{\mathrm{p,i}}\}$, $i = 1, \cdots, n^*$ generated by Algorithm 2 satisfies $u_{\mathrm{p}}(\tau_0) = 0$, $u_{\mathrm{p}}(\tau) \in M_{\mathrm{p},1}$, $\dot{u}_{\mathrm{p}}(\tau) \in M_{\mathrm{p},2}$, where $M_{\mathrm{p},1}$ and $M_{\mathrm{p},2}$ are the bounded intervals of $\mathbb{R}$, inequality condition

(7.2.10) and $|u_p(\tau^*)| \leq c_2 h$, then these two stable attractors are controllable by varying the system parameter p.

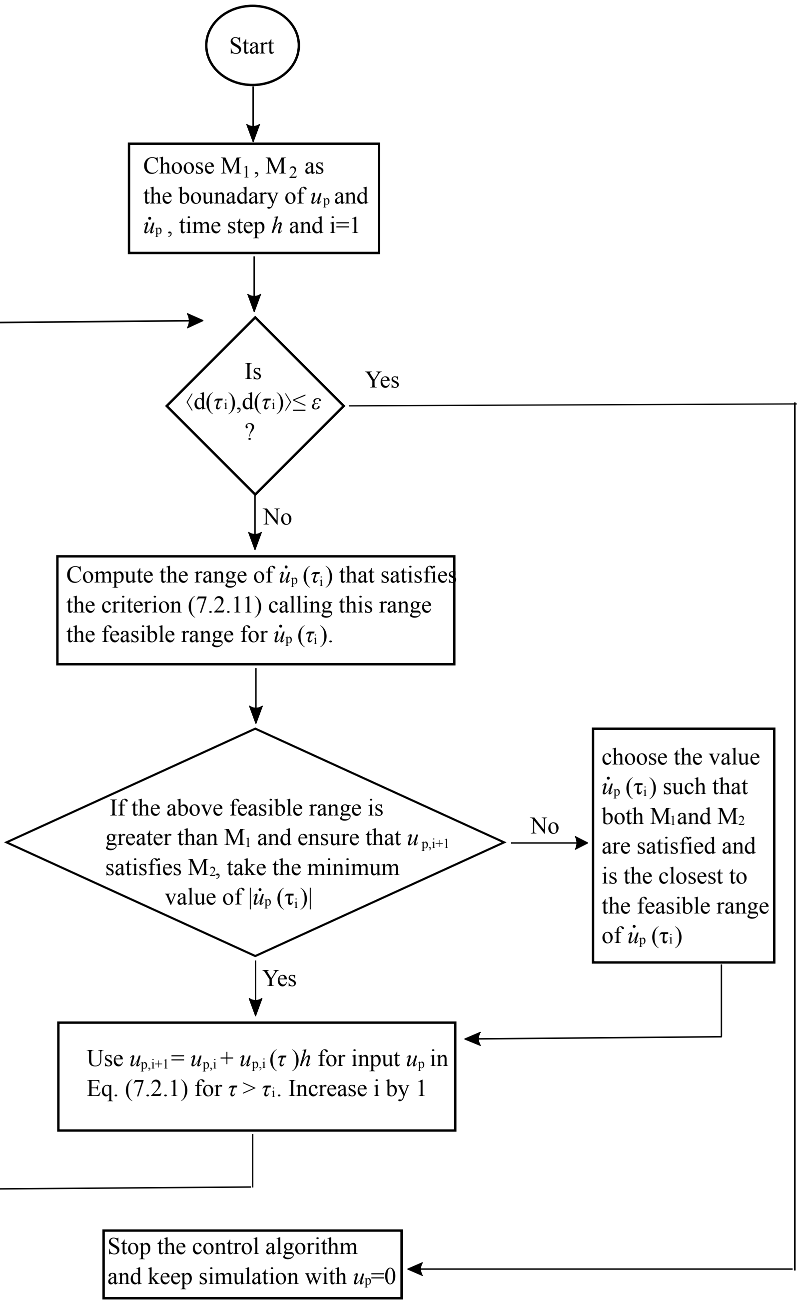

Fig. 7.2.1 Flowchart of the nonlinear control algorithm

The flowchart to implement the nonlinear control strategy is presented in Fig. 7.2.1. This flowchart is also applicable to the linear control strategy.

7.2.2 Numerical investigation

This section will show the effectiveness of the proposed control methods by using the soft impact system shown in Fig. 3.2.1, which is a typical nonsmooth dynamical system exhibiting many coexisting attractors at its near-grazing dynamics [54]. The following parameters were used for which two stable attractors, a period-2 and a period-5 responses, coexist as shown in Fig. 7.2.2.

$$\zeta = 0.01,\ e = 1.26,\ a = 0.7,\ \beta = 28 \text{ and } \omega = 0.85.$$

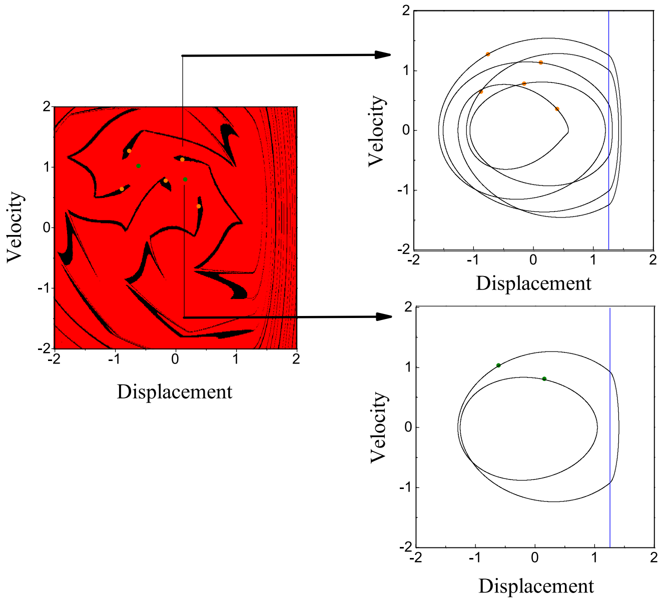

Fig. 7.2.2 Basins of attraction of the soft impact system computed for $\zeta = 0.01$, $e = 1.26$, $a = 0.7$, $\beta = 28$ and $\omega = 0.85$. Orange dots denote the period-5 attractor with black basin, and green dots represent the period-2 attractor with red basin. The right panels present the trajectories of the period-5 and the period-2 attractors on the phase plane, where blue lines indicate the impact boundary.

Linear control

Firstly, the dynamical response of the soft impact system of type (7.2.2) with right-hand side F_{lin} given in (7.2.3) is presented in Fig. 7.2.3 at where the original period-5 attractor was switched to the period-2 attractor by using the external control strategy. The time step of the simulations was fixed at $h = 0.002$, and the control strategy was implemented at $\tau = 591.358$. As can be seen from Figs. 7.2.3(b) and (c), the period-5 response experienced a transition and was settled down to the period-2 response around $\tau = 637$. Fig. 7.2.3(d) shows the transition by grey line on the phase plane and indicates the steady-state response by red line.

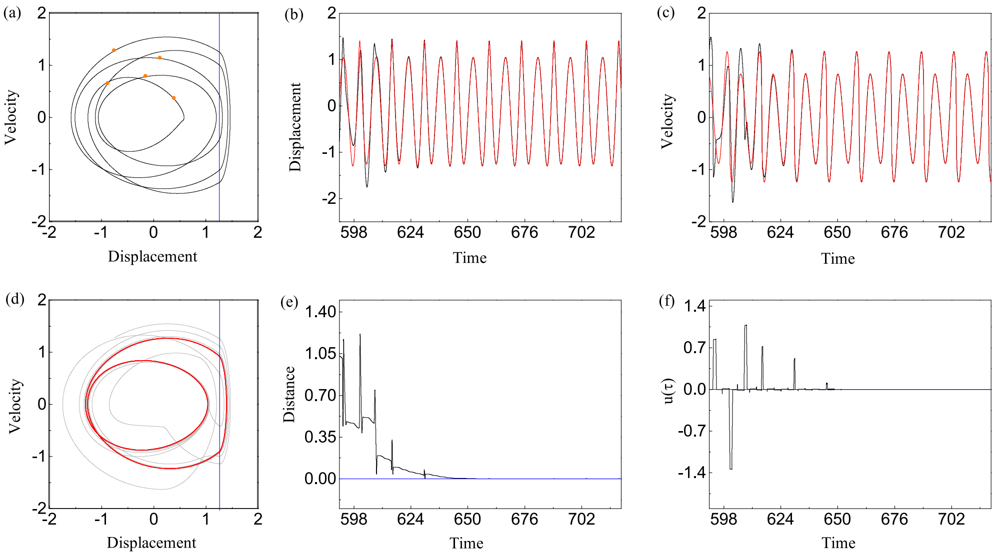

Fig. 7.2.3 (a) The period-5 response on the phase plane with the Poincaré sections denoted by orange dots. (b) Time histories of the desired (red line) and the current (black line) displacements of the system under the external control strategy (Algorithm 1) with $M_1 = 5$ and $M_2 = 3$. (c) Time histories of the desired (red line) and the current (black line) velocities of the system. (d) Trajectory of the system on the phase plane under the external control strategy, where grey and red lines represent the transient and the steady-state responses, respectively. (e) Time history of the distance between the desired and the controlled trajectories in 2-norm. (f) Time history of the control sequence generated by the external control strategy. Blue lines in (a) and (d) indicate the impact boundary, while the blue lines in (e) and (f) mark the zero reference. The result was computed for $\zeta = 0.01$, $e = 1.26$, $a = 0.7$, $\beta = 28$ and $\omega = 0.85$.

Figs. 7.2.3(e) and (f) also demonstrate the effectiveness of the control where the distance between the present and the desired attractors was reduced once the control sequence was applied. It can be seen that the overall trend of the distance was decreased, and according to the simulation, it was about 0.026 at $\tau = 637$ and was about nil after $\tau = 650$. In addition, it can be seen from Fig. 7.2.3(f) that, during the control process, no control was applied when the distance between the two trajectories was decreasing. Then a continuous increase in the control signal to 0.832 at $\tau = 593.01$ and a continuous decrease to 0 at $\tau = 594.65$ were recorded. Thereafter, the control experienced intermittent control actions, and the amplitudes of the control actions decreased as the two trajectories were closer. Finally, the control was turned off when the control target was achieved.

Fig. 7.2.4 shows the control result from the period-2 to the period-5 attractor by using the external control strategy. According to the simulation, the control was switched on at $\tau = 591.358$, and the distance between the two trajectories was decreased to 0.01 at

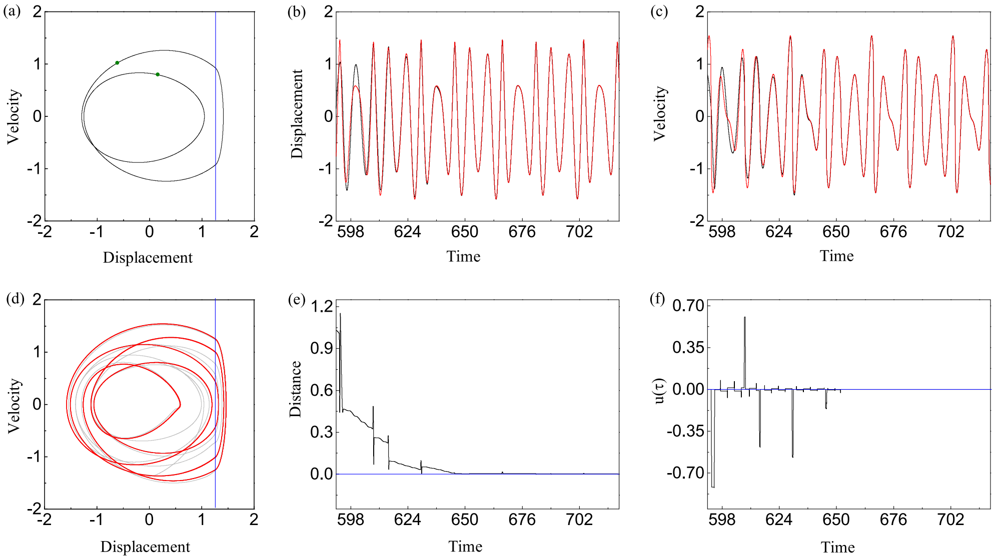

Fig. 7.2.4 (a) The period-2 response on the phase plane with the Poincaré sections denoted by green dots. (b) Time histories of the desired (red line) and the current (black line) displacements of the system under the external control strategy (Algorithm 1) with $M_1 = 5$ and $M_2 = 3$. (c) Time histories of the desired (red line) and the current (black line) velocities of the system. (d) Trajectory of the system on the phase plane under the external control strategy, where grey and red lines represent the transient and the steady-state responses, respectively. (e) Time history of the distance between the desired and the controlled trajectories in 2-norm. (f) Time history of the control sequence generated by the external control strategy. Blue lines in (a) and (d) indicate the impact boundary, while the blue lines in (e) and (f) mark the zero reference. The result was computed for $\zeta = 0.01$, $e = 1.26$, $a = 0.7$, $\beta = 28$ and $\omega = 0.85$.

$\tau = 643.5$. The control signal became zero gradually when the distance was sufficiently small at $\tau = 651.9$.

Nonlinear control

In this part, the effectiveness of the nonlinear control strategy (Algorithm 2) by varying the amplitude of excitation a and the gap e, as given in (7.2.4) and (7.2.5) will be verified. Again, the control target here is to switch the response of system (7.2.1) with right-hand side (7.2.4) between the period-5 and period-2 attractors by varying its amplitude of excitation.

Fig. 7.2.5 shows the control of the soft impact system from the period-5 attractor to the period-2 attractor by varying its amplitude of excitation a. Based on the calculation, when the nonlinear control strategy was applied at $\tau = 591.358$, the controlled trajectory of the system experienced a transition as observed in Figs. 7.2.5(b), (c) and (d). As can be seen from Fig. 7.2.5(e), the distance between the desired and the controlled trajectories in 2-norm was decreased indicating the controlled trajectory approached to the desired one,

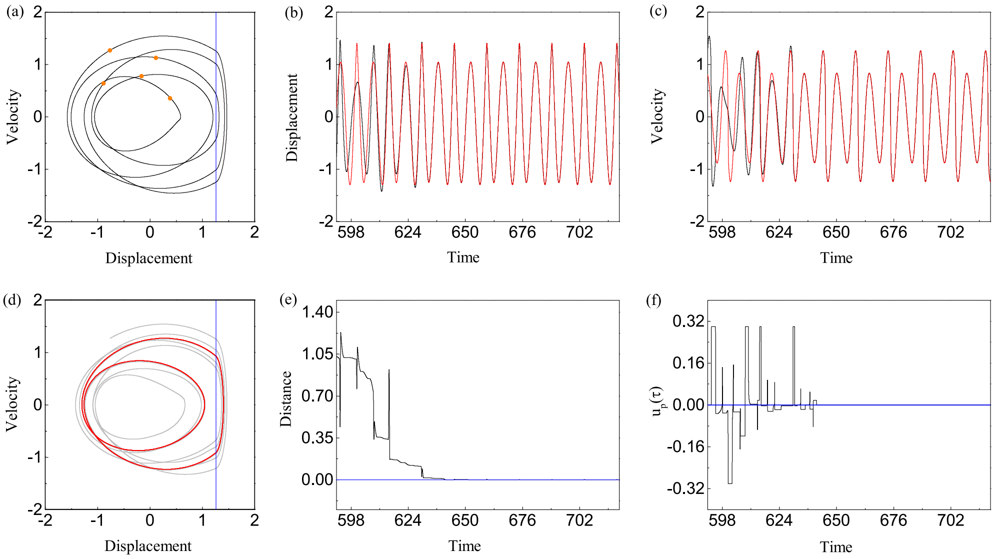

Fig. 7.2.5 (a) The period-5 response on the phase plane with the Poincaré sections denoted by orange dots. (b) Time histories of the desired (red line) and the current (black line) displacements of the system under the nonlinear control strategy (Algorithm 2) by varying the amplitude of excitation with $M_{a,1} = 0.3$ and $M_{a,2} = 5$. (c) Time histories of the desired (red line) and the current (black line) velocities of the system. (d) Trajectory of the system on the phase plane under the nonlinear control strategy, where grey and red lines represent the transient and the steady-state responses, respectively. (e) Time history of the distance between the desired and the controlled trajectories in 2-norm. (f) Time history of the control sequence generated by the nonlinear control strategy. Blue lines in (a) and (d) indicate the impact boundary, while the blue lines in (e) and (f) mark the zero reference. The result was computed for $\zeta = 0.01$, $e = 1.26$, $a = 0.7$, $\beta = 28$ and $\omega = 0.85$.

and this distance was reduced to 0.001 at $\tau \approx 640.64$. Fig. 7.2.5(f) presents the time history of the control signal $u_p(\tau)$ that initiated from $\tau = 591.358$ and terminated at $\tau = 640.854$. Thereafter, $u_p(\tau) = 0$, and the amplitude of excitation was back to its original value, $a = 0.7$.

The control from the period-2 attractor to the period-5 attractor by varying the amplitude of excitation a is presented in Fig. 7.2.6. The control strategy was applied at $\tau = 591.358$, but the distance between the two trajectories was not decreased continuously. Therefore, compared to the external control strategy, it took a longer time for the system to settle down to the period-5 attractor. According to the simulation, the control was switched off at $\tau = 689.1$ when the distance was reduced to 0.001.

When applying the control input $u_p(\tau)$ to the gap e, as given in (7.2.5), the control aims again to switch the response of the soft impact system (7.2.1) with right-hand side $F_e(\tau, Y, u_p)$ given in (7.2.5), between the period-5 and period-2 attractors by varying its gap e.

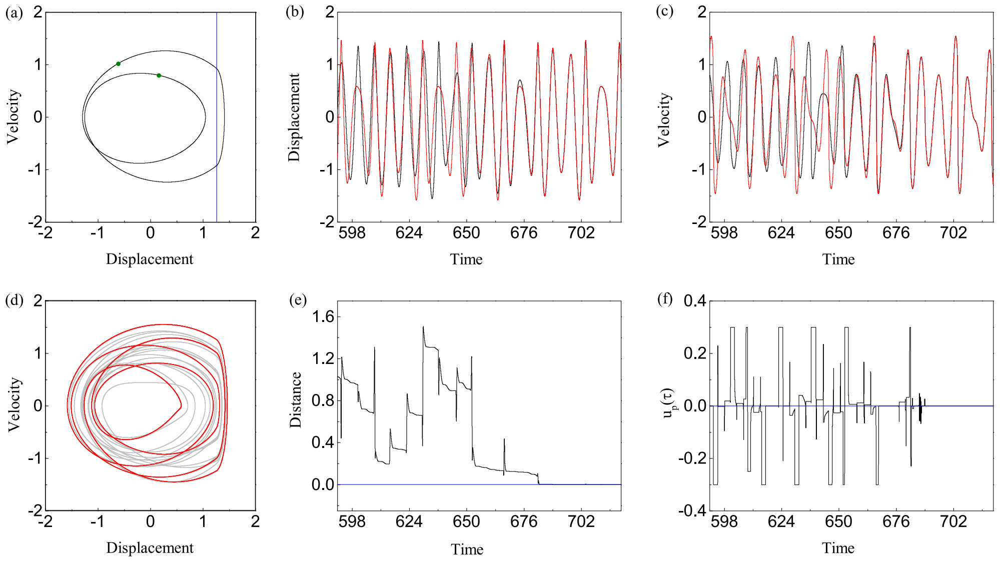

Fig. 7.2.6 (a) The period-2 response on the phase plane with the Poincaré sections denoted by green dots. (b) Time histories of the desired (red line) and the current (black line) displacements of the system under the nonlinear control strategy (Algorithm 2) by varying the amplitude of excitation with $M_{a,1} = 0.3$ and $M_{a,2} = 5$. (c) Time histories of the desired (red line) and the current (black line) velocities of the system. (d) Trajectory of the system on the phase plane under the nonlinear control strategy, where grey and red lines represent the transient and the steady-state responses, respectively. (e) Time history of the distance between the desired and the controlled trajectories in 2-norm. (f) Time history of the control sequence generated by the nonlinear control strategy. Blue lines in (a) and (d) indicate the impact boundary, while the blue lines in (e) and (f) mark the zero reference. The result was computed for $\zeta = 0.01$, $e = 1.26$, $a = 0.7$, $\beta = 28$ and $\omega = 0.85$.

Fig. 7.2.7 presents the control result from the period-5 to the period-2 attractor by varying system's gap e. The control strategy was applied at $\tau = 591.358$ and was switched off at $\tau = 659.6$. During the control period, the trajectory of the system experienced a transition, and the distance between the controlled and the desired trajectories was decreased from 1.03 to 0.001. Within the same time duration, the control signal $u_p(\tau)$ reached a maximum value $u_p(\tau) = 0.21$ and decreased to -0.02 at $\tau = 630.326$. Thereafter, the control signal did not change significantly and reduced to nil gradually after $\tau = 659.49$.

To demonstrate the switching from the period-2 to the period-5 attractor by varying system's gap, Fig. 7.2.8 presents the control result. Based on the calculation, the control strategy was applied at $\tau = 591.358$, and the distance between the two trajectories was reduced from 1.03 to 0.001 at $\tau = 703.794$. Thereafter, the control signal $u_p(\tau)$ decreased to nil, and the control target was achieved. Compared to the control result shown in Fig. 7.2.7,

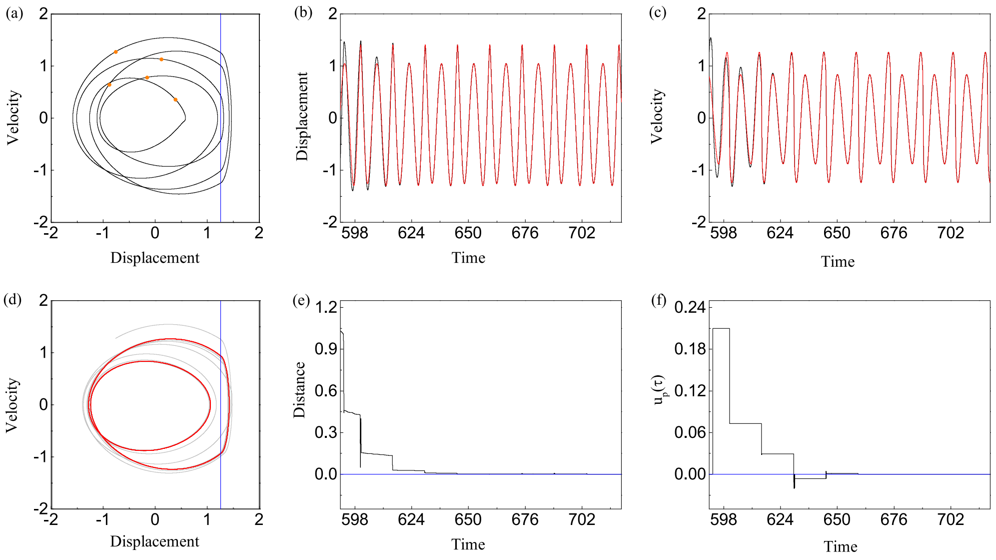

Fig. 7.2.7 (a) The period-5 response on the phase plane with the Poincaré sections denoted by orange dots. (b) Time histories of the desired (red line) and the current (black line) displacements of the system under the nonlinear control strategy (Algorithm 2) by varying system's gap with $M_{e,1} = 0.3$ and $M_{e,2} = 5$. (c) Time histories of the desired (red line) and the current (black line) velocities of the system. (d) Trajectory of the system on the phase plane under the nonlinear control strategy, where grey and red lines represent the transient and the steady-state responses, respectively. (e) Time history of the distance between the desired and the controlled trajectories in 2-norm. (f) Time history of the control sequence generated by the nonlinear control strategy. Blue lines in (a) and (d) indicate the impact boundary, while the blue lines in (e) and (f) mark the zero reference. The result was computed for $\zeta = 0.01$, $e = 1.26$, $a = 0.7$, $\beta = 28$ and $\omega = 0.85$.

the transition from the period-2 to the period-5 attractor took a longer time and had a more complex transient response, which was due to the complexity of the period-5 response.

Bifurcation analysis of the coexisting attractors

In this section how the control parameters (excitation amplitude a and mass-spring gap e) will affect the period-2 and period-5 coexisting attractors studied in the previous section will be studied in detail. For this purpose the path-following methods for piecewise-smooth dynamical systems, using the continuation platform COCO [25], will be employed. The precise COCO-implementation for the soft impact system (7.2.2) can be found in a previous publication by the authors [1], which will be adopted in the present work.

As can be seen from the previous section, in order to apply the proposed control mechanism it is essential to identify parameter regimes where the considered period-2 and period-5 attractors maintain both their stability properties and orbit structure. For this purpose a one-

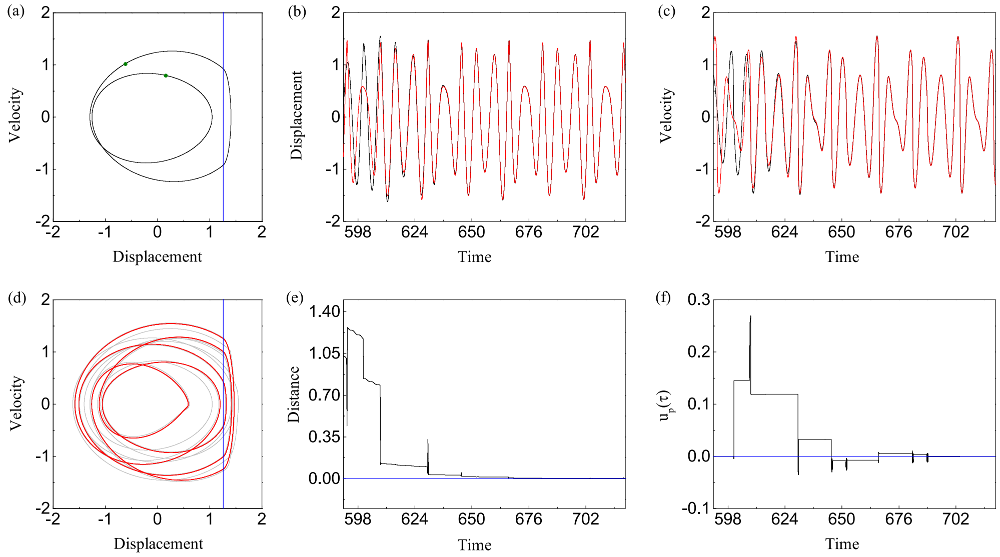

Fig. 7.2.8 (a) The period-2 response on the phase plane with the Poincaré sections denoted by green dots. (b) Time histories of the desired (red line) and the current (black line) displacements of the system under the nonlinear control strategy (Algorithm 2) by varying system's gap with $M_{e,1} = 0.3$ and $M_{e,2} = 5$. (c) Time histories of the desired (red line) and the current (black line) velocities of the system. (d) Trajectory of the system on the phase plane under the nonlinear control strategy, where grey and red lines represent the transient and the steady-state responses, respectively. (e) Time history of the distance between the desired and the controlled trajectories in 2-norm. (f) Time history of the control sequence generated by the nonlinear control strategy. Blue lines in (a) and (d) indicate the impact boundary, while the blue lines in (e) and (f) mark the zero reference. The result was computed for $\zeta = 0.01$, $e = 1.26$, $a = 0.7$, $\beta = 28$ and $\omega = 0.85$.

parameter continuation of the underlying attractors with respect to the excitation amplitude a will be carried out, through using the *contact time* as solution measure, i.e. the time the impacting mass stays in contact with the secondary spring per orbital period.

The result of the process described above is depicted in Fig. 7.2.9, which shows yellow and green curves corresponding to the numerical continuation of the period-2 and period-5 attractors detected in Fig. 7.2.2, respectively. In both cases, the parameter window where the corresponding periodic solutions remain stable and maintain their orbit structure is determined by period-doubling and grazing bifurcations of limit cycles. Specifically, the period-2 solution traced along the yellow branch loses stability when the excitation amplitude decreases below $a \approx 0.63111$, where the solution undergoes a period-doubling bifurcation (PD1). Here, the original period-2 orbit (with one impact per orbital period) becomes unstable and a family of period-4 orbits is born, see for instance the test solution plotted in Fig. 7.2.9(f), right after the bifurcation occurs. On the other hand, when the parameter a

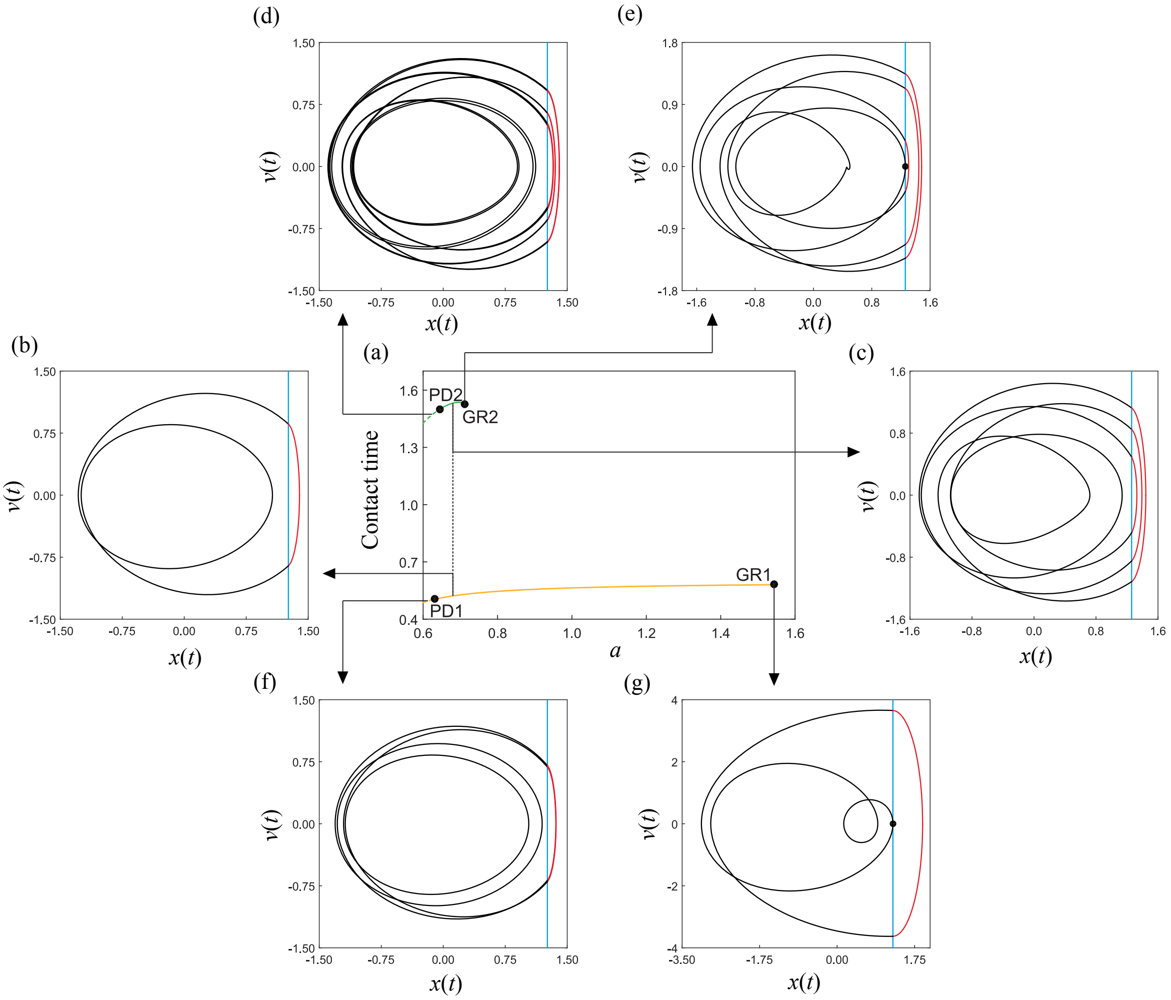

Fig. 7.2.9 (a) One-parameter continuation of the coexisting attractors shown in panels (b) (yellow branch) and (c) (green branch) with respect to the excitation amplitude a, computed for the parameter values $\zeta = 0.01$, $e = 1.26$, $a = 0.68$, $\beta = 28$ and $\omega = 0.85$ of the soft impact system (7.2.2). The vertical axis shows the *contact time*, the time the impacting mass stays in contact with the secondary spring per orbital period. Branches of stable and unstable periodic orbits are depicted with solid and dashed lines, respectively. The points labeled GR1 ($a \approx 1.54462$), GR2 ($a \approx 0.71258$) and PD1 ($a \approx 0.63111$), PD2 ($a \approx 0.64564$) denote grazing and period-doubling bifurcations of limit cycles. Panels (g) and (e) depict periodic solutions corresponding to the grazing bifurcations points GR1 and GR2, respectively. Here, a dot marks a grazing contact with the impact boundary $x = e$ (vertical blue line). Panel (f) presents a period-4 attractor computed for $a = 0.63$, while panel (d) depicts a period-10 solution calculated at $a = 0.645$, originated by the period-doubling bifurcations PD1 and PD2, respectively.

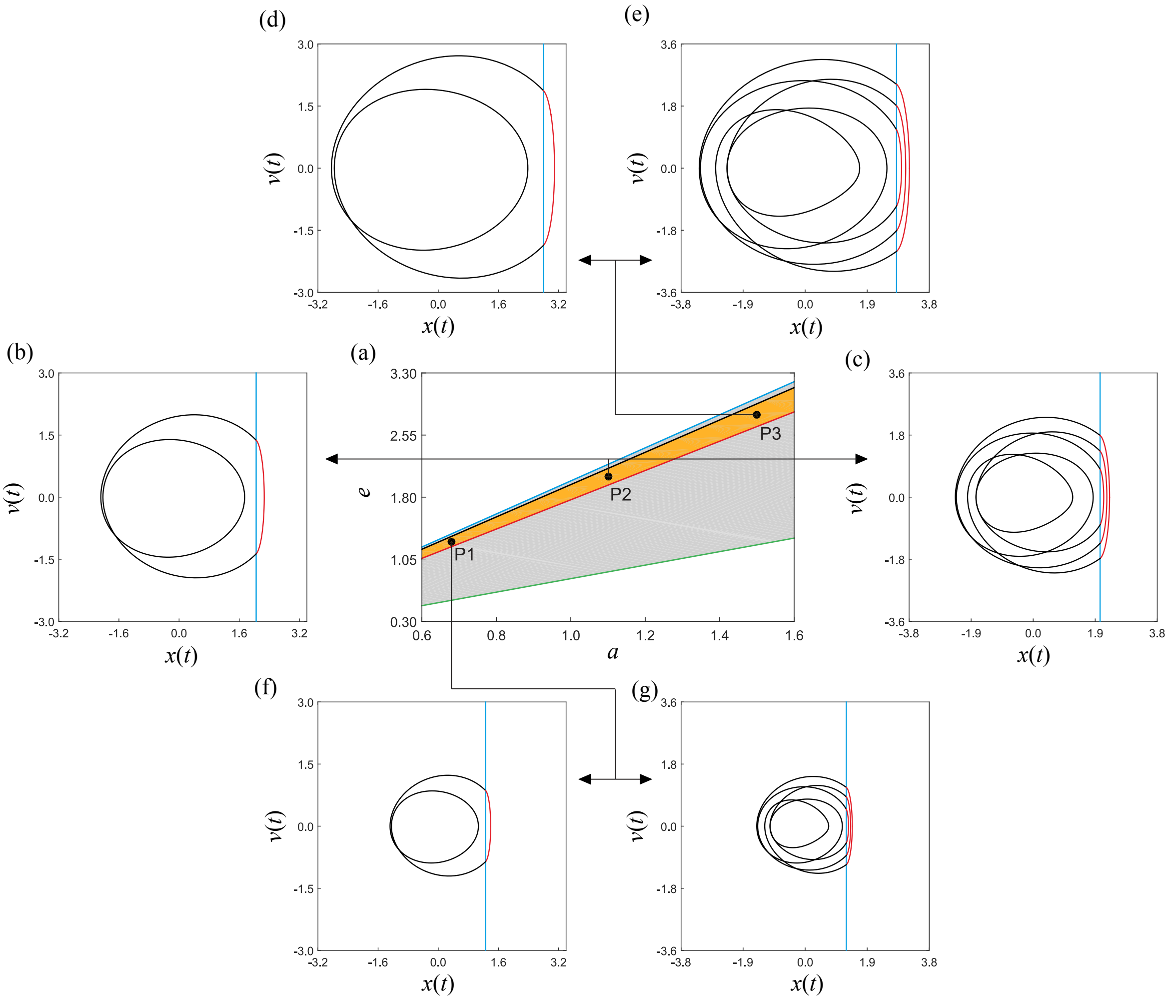

Fig. 7.2.10 (a) Two-parameter continuation of the bifurcation points PD1 (blue curve), GR1 (green curve), PD2 (black curve) and GR2 (red curve) found in Fig. 7.2.9(a), with respect to the excitation amplitude a and mass-spring gap e. The grey area represents the parameter region in which the stable period-2 solution of the type shown in panel (b) exists. The yellow region corresponds to the coexistence of the latter solution type with the stable period-5 orbit type presented in panel (c). Panels (f)-(g), (b)-(c) and (d)-(e) represent pairs of coexisting attractors computed at the test points P1 ($a = 0.68$, $e = 1.26$), P2 ($a = 1.1$, $e = 2.05$) and P3 ($a = 1.5$, $e = 2.8$).

increases, a grazing bifurcation is found at $a \approx 1.54462$, where the solution makes tangential contact with the impact boundary $x = e$, see Fig. 7.2.9(g). After this point, a small window of period-2 solutions with two impacts per orbital period exists, and they lose stability via a fold bifurcation at $a \approx 1.54486$ (not shown in the diagram). An analogous scenario is found for the period-5 attractor (with three impacts per orbital period) depicted in Fig. 7.2.9(c). As before, the window of stability (and orbit structure preservation) for this solution is determined by the period-doubling bifurcation PD2 ($a \approx 0.64564$) and the grazing point GR2 ($a \approx 0.71258$), which results in a significantly smaller window than the one obtained for the period-2 attractor.

With the results of the one-parameter continuation it is necessary to determine a parameter region in the a-e plane where the considered period-2 and period-5 attractors maintain both their stability properties and orbit structure. To this end, a two-parameter continuation of the codimension-one bifurcations detected above will be performed. Fig. 7.2.10(a) shows the locus of the period-doubling points PD1 (blue curve), PD2 (black curve) and grazing bifurcations GR1 (green curve), GR2 (red curve) encountered in Fig. 7.2.9(a). In this figure, two regions are highlighted, in grey and yellow colors. The grey area represents the parameter region in which the stable period-2 solution (with one impact per orbital period, see panel (b)) exists. The yellow region corresponds to the coexistence of the latter solution with the stable period-5 orbit (with three impacts per orbital period, see panel (c)). Furthermore, several test points have been selected in order to illustrate the validity of the highlighted yellow area in the a-e plane. Specifically, pairs of coexisting attractors have been computed at the test points P1 ($a = 0.68$, $e = 1.26$), P2 ($a = 1.1$, $e = 2.05$) and P3 ($a = 1.5$, $e = 2.8$), see panels (b)–(g) in Fig. 7.2.10. In this way, the yellow area can be used as a reference for the applicability of the proposed control scheme, so as to guarantee that the parametric perturbations do not bring the system to a regime where either of the considered attractors lose stability or the intended orbit structure.

7.3 Control of the impact system with a drift

7.3.1 Mathematical description and preparation

In this part, the control of coexisting attractors of an impact system with a drift described by Eq. (3.3.7), (3.3.8) and (3.3.9) will be considered. As shown in [4], this system has a phenomenon of coexisting attractors. It is an ideal model to test the effectiveness of the varying parameter control method. Hence, at the following numerical discussion, the concepts and strategy in Section 7.2.1 will be adopt to achieve the control from one attractor to other coexisting attractors for the impact system with a drift.

The equations of motion of the impact system with a drift are in form (7.2.1), where $Y(\tau) := (p(\tau), y(\tau), q(\tau))^T$. Two different cases will be considered. Defining for scalar $\tilde{u}$

- **No contact**, i.e. $p < q + g$,

$$F_{\text{gen, dr}}(Y(\tau),\tilde{u}) := \begin{bmatrix} 0 & 1 & 0 \\ 0 & 0 & 0 \\ 0 & 0 & -\frac{1}{2\xi} \end{bmatrix} Y(\tau) + \begin{bmatrix} 0 \\ \tilde{u}+b \\ 0 \end{bmatrix},$$

- **Contact without progression**, i.e. $p \geq q+g$ and $0 < 2\xi y + q < 1$,

$$F_{\text{gen, dr}}(Y(\tau),\tilde{u}) := \begin{bmatrix} 0 & 1 & 0 \\ 0 & -2\xi & -1 \\ 0 & 1 & 0 \end{bmatrix} Y(\tau) + \begin{bmatrix} 0 \\ \tilde{u}+b \\ 0 \end{bmatrix},$$

- **Contact with progression**, i.e. $p \geq q+g$ and $2\xi y' + q \geq 1$.

$$F_{\text{gen, dr}}(Y(\tau),\tilde{u}) := \begin{bmatrix} 0 & 0 & -\frac{1}{2\xi} \\ 0 & 0 & 0 \\ 0 & 0 & -\frac{1}{2\xi} \end{bmatrix} Y(\tau) + \begin{bmatrix} \frac{1}{2\xi} \\ \tilde{u}+b-1 \\ \frac{1}{2\xi} \end{bmatrix},$$

the two cases for control input are

$$F_{\text{lin, dr}}(\tau,Y,u) := F_{\text{gen, dr}}(Y, a\cos(\omega\tau+\phi)+u), \tag{7.3.1}$$

$$F_{a,\text{ dr}}(\tau,Y,u) := F_{\text{gen, dr}}(Y, (a+u)\cos(\omega\tau+\phi)). \tag{7.3.2}$$

The first case, $F_{\text{lin, dr}}$ has linear control input and the second case, $F_{a,\text{ dr}}$, has parametric control input, varying the forcing amplitude. The details of the algorithm for the above systems are illustrated in Section 7.2.1.

7.3.2 Numerical investigation

In this section, the impact system with a drift shown in Fig. 3.3.1 will be used for studying the effectiveness of the proposed method. This system will choose the following parameters

$$a = 0.3,\ b = 0.1,\ \xi = 0.1,\ \omega = 1.4,\ g = 0.02,\ \phi = \frac{\pi}{2}.$$

For these parameters, the impact system with a drift coexists one stable and one chaotic attractor. One is the period-4 attractor, and another is the chaotic attractor, as shown in Fig. 7.3.1. The control target at following discussions is to achieve the switching from the chaotic attractor to the period-4 attractor through introducing the information of the desired attractor as a target. Specifically, in the first part, a linear control input will be introduced into the system described by Eq. (3.3.7), (3.3.8) and (3.3.9) to achieve the control target. In addition, in the second part, since the amplitude a is the parameter, which can control the velocity conveniently, a parametric control input will be introduced into the amplitude to achieve the control target.

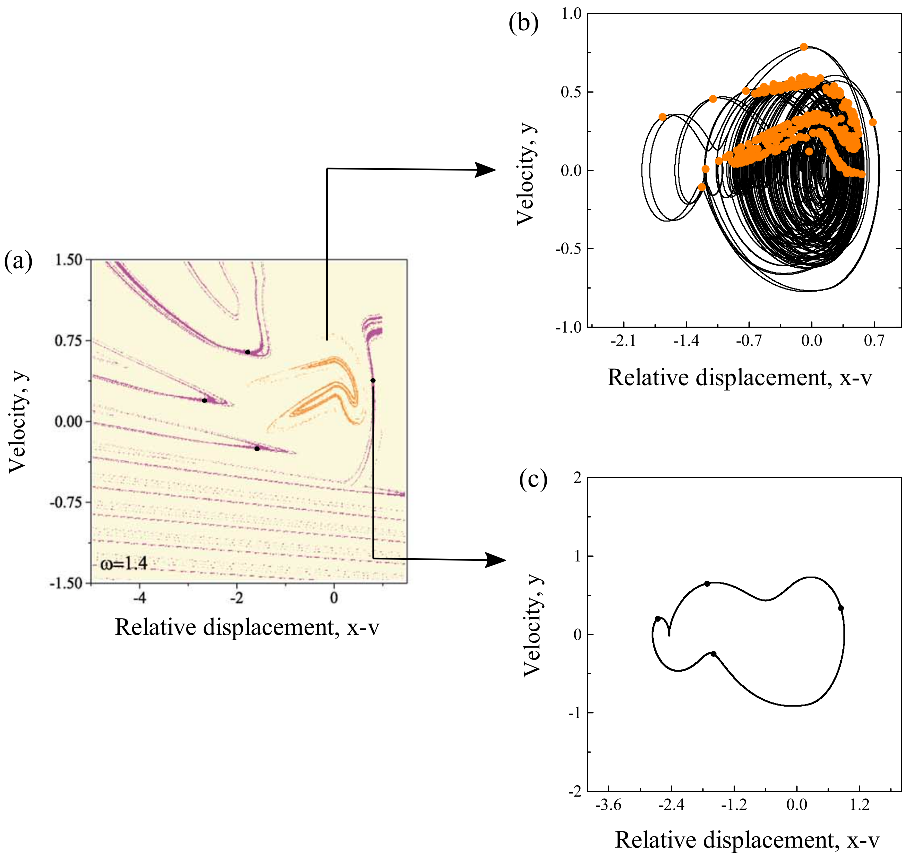

Fig. 7.3.1 Basin of attraction of the impact system with a drift computed for $a = 0.3$, $b = 0.1$, $\xi = 0.1$, $\omega = 1.4$, $g = 0.02$ and $\phi = \frac{\pi}{2}$ [4]. Orange dots denote the chaotic attractor with yellow basin and black dots represent the period-4 attractor with purple basin.

Linear control

At this part, how the linear control input affects the dynamical behavior of the impact system with a drift will be investigated. In Fig. 7.3.2, it shows the original chaotic attractor is switched to the period-4 attractor by an external control input. The time step of the simulations was fixed as $h = 0.001$ and the control ends when the distance between this two attractors is 0.005. At time $\tau = 2692.8$ the control strategy was implemented and the chaotic

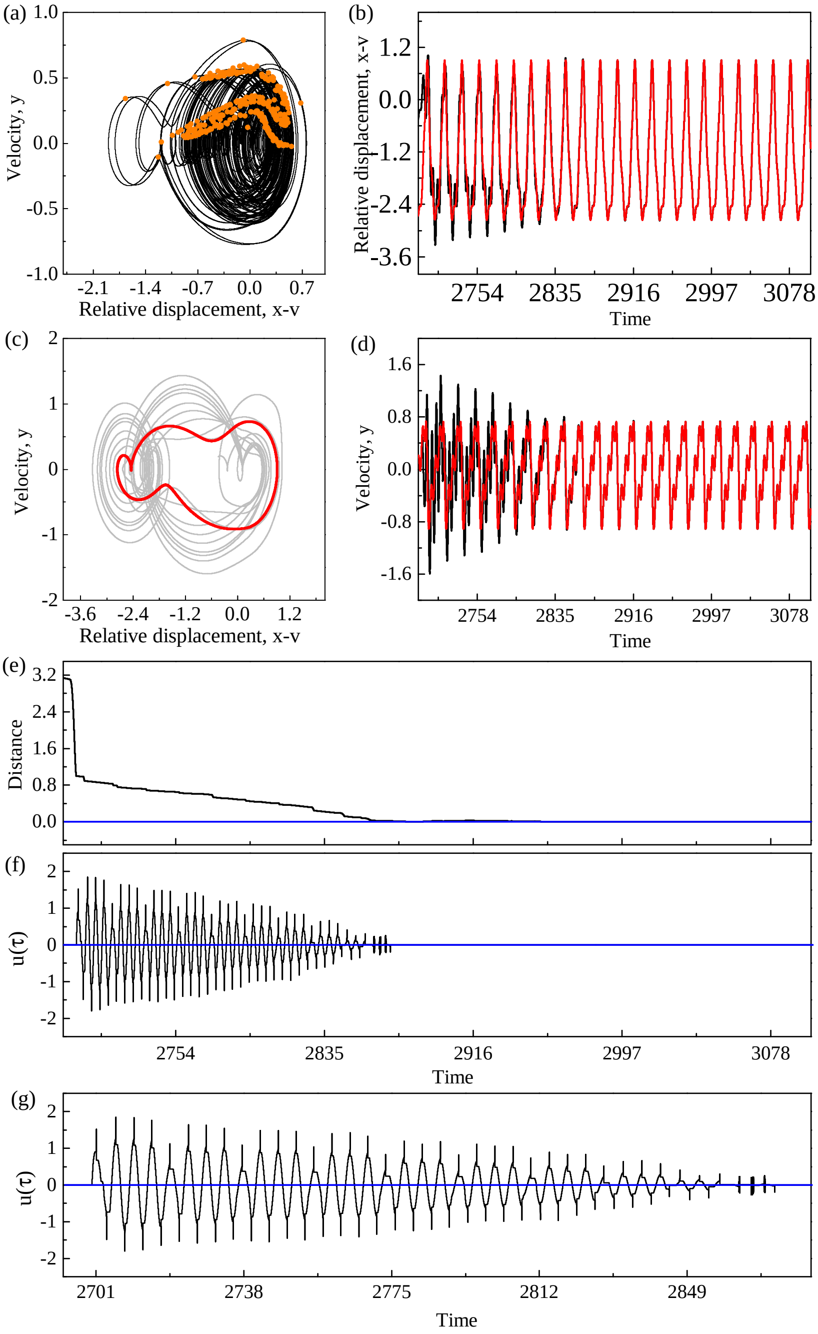

Fig. 7.3.2 (a) The chaotic attractor on the phase plane with the Poincaré sections denoted by orange dots. (b) Time history of the response relative displacement with control on, under $M_1 = 5$ and $M_2 = 150$. (c) Trajectory of the system on the phase plane under the linear control strategy, where grey and red lines represent the transient and the steady-state responses, respectively. (d) Time histories of the desired (red line) and the current (black line) velocities of the system. (e) Time history of the distance between the desired and controlled trajectory, and the distance is based on 2-Norm. (f) Time history of the control sequence generated by the linear control strategy. (g) Time history of the control sequence in the small time range. While, the blue lines in (e), (f) and (g) mark the zero reference. The result was computed for $a = 0.3$, $b = 0.1$, $\xi = 0.1$, $\omega = 1.4$, $g = 0.02$ and $\phi = \frac{\pi}{2}$.

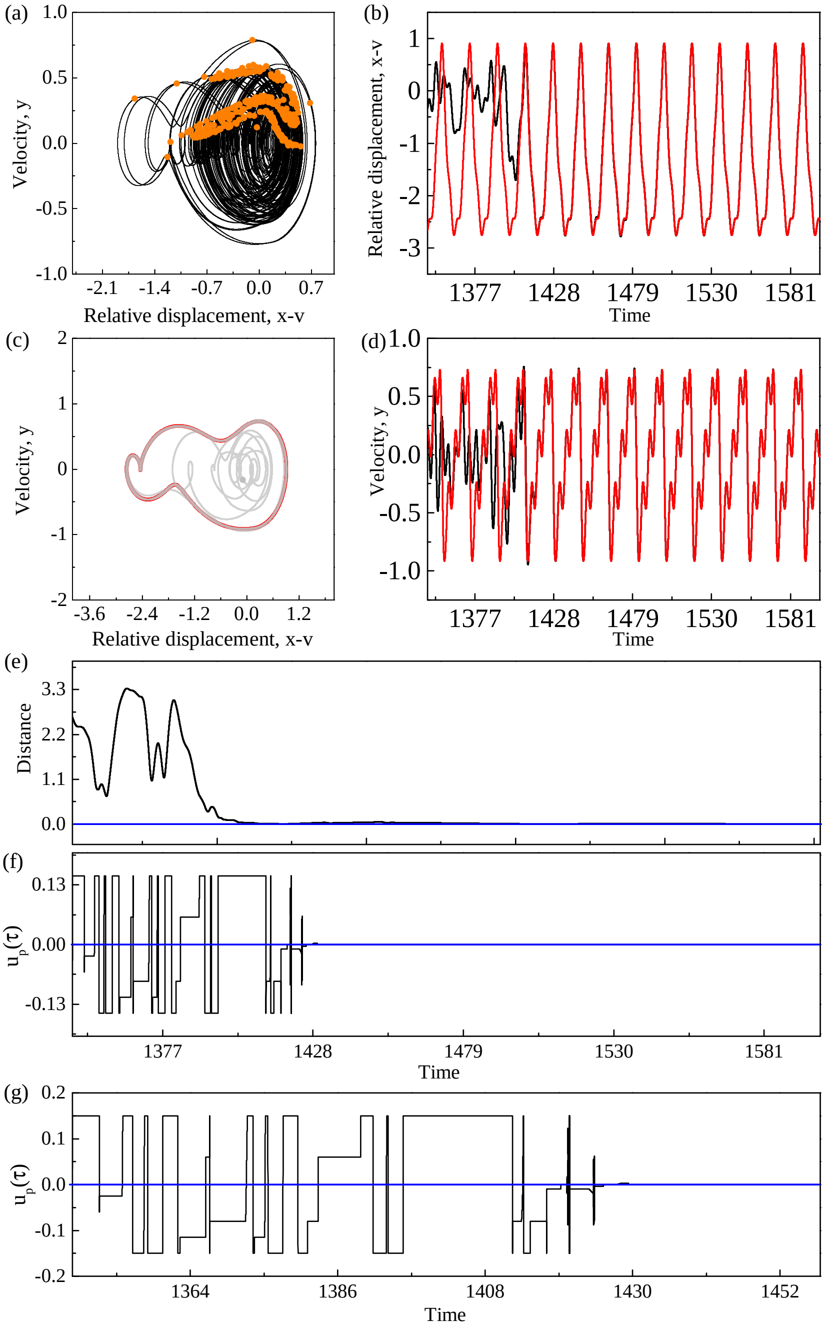

Fig. 7.3.3 (a) The chaotic attractor on the phase plane with the Poincaré sections denoted by orange dots. (b) Time history of the response relative displacement with control on, under $M_{a,1} = 0.15$ and $M_{a,2} = 35$. (c) Trajectory of the system on the phase plane under the nonlinear control strategy, where grey and red lines represent the transient and the steady-state responses, respectively. (d) Time histories of the desired (red line) and the current (black line) velocities of the system. (e) Time history of the distance between the desired and controlled trajectory, and the distance is based on 2-Norm. (f) Time history of the control sequence generated by the nonlinear control strategy. (g) Time history of the control signal in the small time range While, the blue lines in (e), (f) and (g) mark the zero reference. The result was computed for $a = 0.3$, $b = 0.1$, $\xi = 0.1$, $\omega = 1.4$, $g = 0.02$ and $\phi = \frac{\pi}{2}$.

attractor witnesses a transition and finally be stable on the period-4 attractor, as shown in Fig. 7.3.2 (b), (c) and (d). In details, from Fig.7.3.2 (b) and (c), the displacement and velocity of the controlled trajectory are very closed to the target trajectory (red line) of period-2 attractor around $\tau = 2884.98$. A similar result can be discovered from Fig.7.3.2 (e), which shows the distance between two attractors was around 0.005 at $\tau = 2884.98$. Meanwhile, the relevant control signal tends to 0. After $\tau = 2884.98$, the control is turned off, since the distance between two attractors was reduced to 0.005. Finally, the controlled trajectory can be stable on the period-4 attractor spontaneously.

Nonlinear control

Here, varying amplitude to achieve the switching from chaotic attractor to period-4 attractor will be considered. As shown in Fig. 7.3.3, the nonlinear control strategy is implemented at time $\tau = 1346.397$. The control signal increases very fast from 0 at $\tau = 1346.397$ to 0.15 at $\tau = 1346.403$ in Fig. 7.3.3 (f) and (g). With varying of the amplitude based on the nonlinear control strategy, the chaotic attractor witnesses a transition as showin in Fig. 7.3.3 (b), (c) and (d). In details, in Fig. 7.3.3 (b) and (d), the relative displacement $x - v$ and velocity y of the controlled attractor are very close to the relative displacement $x - v$ and velocity y of desired attractor around $\tau = 1429.397$, and the distance between these two trajectories is 0.005 at this moment in Fig. 7.3.3 (e). After that moment, the control becomes 0 and the amplitude returns to its original value in Fig. 7.3.3 (f) and (g). Meanwhile, the controlled attractor is stable on the desired period-4 attractor.

7.4 Control of the vibro-impact capsule system

7.4.1 Mathematical description and preparation

In this part, the following discussion will consider controlling coexisting attractors of a vibro-impact capsule system, which is described by Eq. (3.4.14), (3.4.15), (3.4.16) and (3.4.17). As shown in [3], many coexisting attractors in this vibro-impact system under the Coulomb friction were discovered. Hence, through studying this case, it can prove the effectiveness of the concept of varying parameter control method. At the following numerical discussion, the similar concepts and strategy in Section 7.2.1 will be adopt to achieve the control from one attractor to other coexisting attractors for the vibro-impact capsule system.

The equations of motion of the vibro-impact capsule system are in form (7.2.1), where $Y(\tau) := (\upsilon(\tau), \kappa(\tau), y_1(\tau), y_2(\tau))^T$. Two different cases will be considered. Defining for scalar $\tilde{u}$

- **No contact with stationary capsule**, i.e. $\upsilon < \delta$, and $|\upsilon + 2\xi\kappa| \leq 1$.

$$F_{\text{gen, cap}}(Y(\tau),\tilde{u}) := \begin{bmatrix} 0 & 0 & 1 & 0 \\ -1 & -2\xi & 0 & 0 \\ -1 & -2\xi & 0 & 0 \\ 0 & 0 & 0 & 0 \end{bmatrix} Y(\tau) + \begin{bmatrix} 0 \\ \tilde{u} \\ \tilde{u} \\ 0 \end{bmatrix},$$

- **No contact with moving capsule**, i.e. $\upsilon < \delta$, and $|\upsilon + 2\xi\kappa| > 1$.

$$F_{\text{gen, cap}}(Y(\tau),\tilde{u}) := \begin{bmatrix} 0 & 1 & 0 & 0 \\ -1-\frac{1}{\gamma} & -2\xi-\frac{2\xi}{\gamma} & 0 & 0 \\ -1 & -2\xi & 0 & 0 \\ \frac{1}{\gamma} & \frac{2\xi}{\gamma} & 0 & 0 \end{bmatrix} Y(\tau) + \begin{bmatrix} 0 \\ \tilde{u}+\frac{\text{sign}(y_2)}{\gamma} \\ \tilde{u} \\ -\frac{\text{sign}(y_2)}{\gamma} \end{bmatrix},$$

- **Contact with stationary capsule**, i.e. $\upsilon \geq \delta$, and $|\upsilon + 2\xi\kappa - \beta(\upsilon - \delta)| \leq 1$.

$$F_{\text{gen, cap}}(Y(\tau),\tilde{u}) := \begin{bmatrix} 0 & 0 & 1 & 0 \\ -1-\beta & -2\xi & 0 & 0 \\ -1-\beta & -2\xi & 0 & 0 \\ 0 & 0 & 0 & 0 \end{bmatrix} Y(\tau) + \begin{bmatrix} 0 \\ \tilde{u}+\beta\delta \\ \tilde{u}+\beta\delta \\ 0 \end{bmatrix},$$

- **Contact with moving capsule**, i.e. $\upsilon \geq \delta$, and $|\upsilon + 2\xi\kappa - \beta(\upsilon - \delta)| > 1$.

$$F_{\text{gen, cap}}(Y(\tau),\tilde{u}) := \begin{bmatrix} 0 & 1 & 0 & 0 \\ -1-\beta-\frac{1+\beta}{\gamma} & -2\xi-\frac{2\xi}{\gamma} & 0 & 0 \\ -1-\beta & -2\xi & 0 & 0 \\ \frac{1+\beta}{\gamma} & \frac{2\xi}{\gamma} & 0 & 0 \end{bmatrix} Y(\tau) + \begin{bmatrix} 0 \\ \tilde{u}+\frac{\text{sign}(y_2)}{\gamma} \\ \tilde{u} \\ -\frac{\text{sign}(y_2)}{\gamma} \end{bmatrix},$$

the two cases for control input are

$$F_{\text{lin, cap}}(\tau,Y,u) := F_{\text{gen, cap}}(Y, a\cos(\omega\tau+\phi)+u), \tag{7.4.1}$$

$$F_{a,\text{ cap}}(\tau,Y,u) := F_{\text{gen, cap}}(Y, (a+u)\cos(\omega\tau+\phi)). \tag{7.4.2}$$

The first case, $F_{\text{lin, cap}}$ has linear control input and the second case, $F_{a,\text{ cap}}$, has parametric control input, varying the forcing amplitude. The details of the algorithm for the above systems are illustrated in Section 7.2.1.

7.4.2 Numerical investigation

Here, the simulations will be presented to verify the effectiveness of the proposed method by studying the vibro-impact capsule system in Fig. 3.4.1. The following parameters are chosen for the system,

$$\alpha = 1.6,\ b = 0.1,\ \omega = 0.95,\ \xi = 0.01,\ \delta = 0.02,\ \beta = 15,\ \gamma = 5.$$

For these parameters, the vibro-impact system coexists two stable attractors. One is the period-3 attractor, and another is the period-1 attractor, as shown in Fig. 7.4.1. The control target at following discussions is to achieve the switching between this two coexisting stable attractors. Specifically, in the first part, a linear control input will be introduced into the system described by Eq. (3.4.14), (3.4.15), (3.4.16) and (3.4.17) to achieve the control target. In addition, in the second part, a parametric control input will be introduced into the amplitude to achieve the control target.

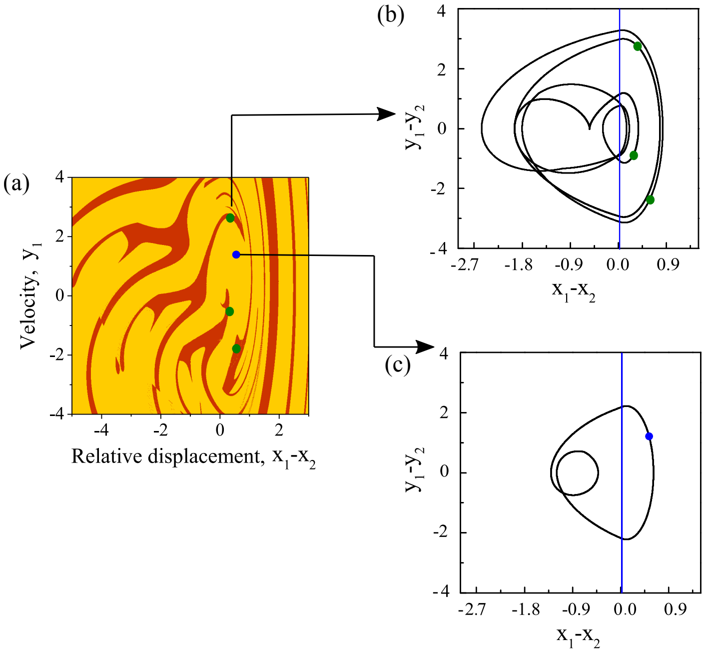

Fig. 7.4.1 Basin of attraction of the vibro-impact capsule system computed for $\alpha = 1.6$, $\omega = 0.95$, $\xi = 0.01$, $\delta = 0.02$, $\beta = 15$ and $\gamma = 5$ [3]. Oliver dots denote the period-3 attractor with red basin and blue dot represent the period-1 attractor with yellow basin.

Linear control

Here, how the linear control strategy achieves the switching between the period-3 and period-1 attractor will be studied numerically. In Fig. 7.4.2, the period-1attractor is controlled to period-3 attractor. The transition from period-1 to period-3 attractor is shown in Fig. 7.4.2 (b), (c) and (d). During the transition, the relevant distance between these two trajectories decreases from 2.8785 at $\tau = 661.388$ to 0.005 at $\tau = 678.578$. In the process, the control signal reaches the highest value $u(\tau) = 1.77$ at $\tau = 662.842$ and the lowest value $u(\tau) = -0.995$ during $\tau \in [663.396, 663.88]$. Then, the control signal returns back to 0 after $\tau = 678.578$. Finally, the controlled trajectory converges to the period-3 attractor. In addition, for the case of which the period-3 attractor is switched to the period-1 attractor in Fig. 7.4.3, the linear control strategy begins at the same time as above, and reduces the distance between two trajectories to 0.005 at $\tau = 675.877$, shown in Fig. 7.4.3(e). After that moment, the control signal $u_p(\tau)$ tends to 0, and the control target is successfully achieved. Thus, these two stable attractors can be switched by the control generated from the linear control strategy.

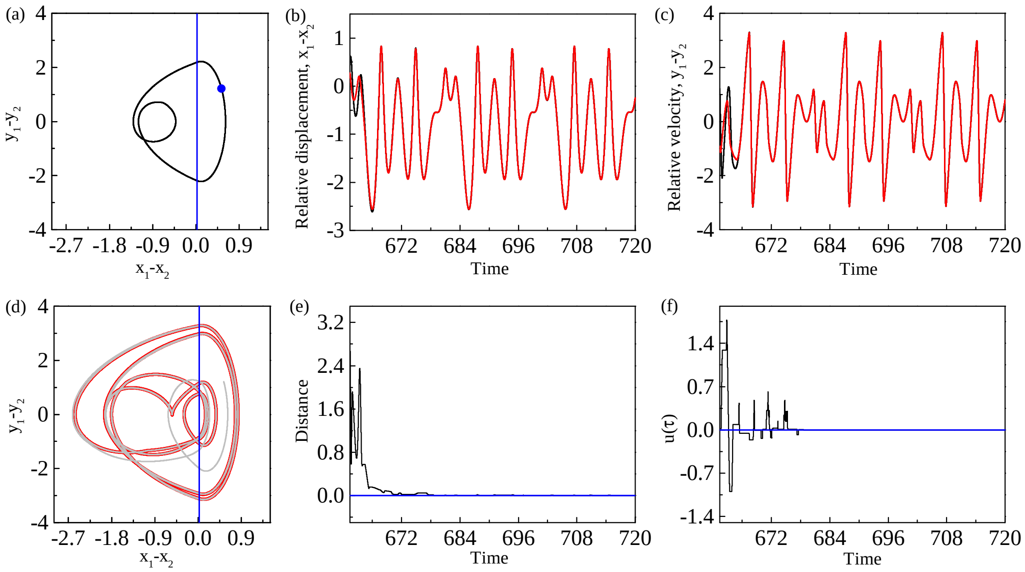

Fig. 7.4.2 (a) The period-1 response on the phase plane with the Poincaré sections denoted by a blue dot. (b) Time histories of the desired (red line) and the current (black line) displacements of the system under the linear control strategy (Algorithm 1) with $M_1 = 5$ and $M_2 = 5$.. (c) Time histories of the desired (red line) and the current (black line) velocities of the system. (d) Trajectory of the system on the phase plane under the linear control strategy, where grey and red lines represent the transient and the steady-state responses, respectively. (e) Time history of the distance between the desired and the controlled trajectories in 2-norm. (f) Time history of the control sequence generated by the linear control strategy. Blue lines in (a) and (d) indicate the impact boundary, while the blue lines in (e) and (f) mark the zero reference. The result was computed for $\alpha = 1.6$, $\omega = 0.95$, $\xi = 0.01$, $\delta = 0.02$, $\beta = 15$ and $\gamma = 5$.

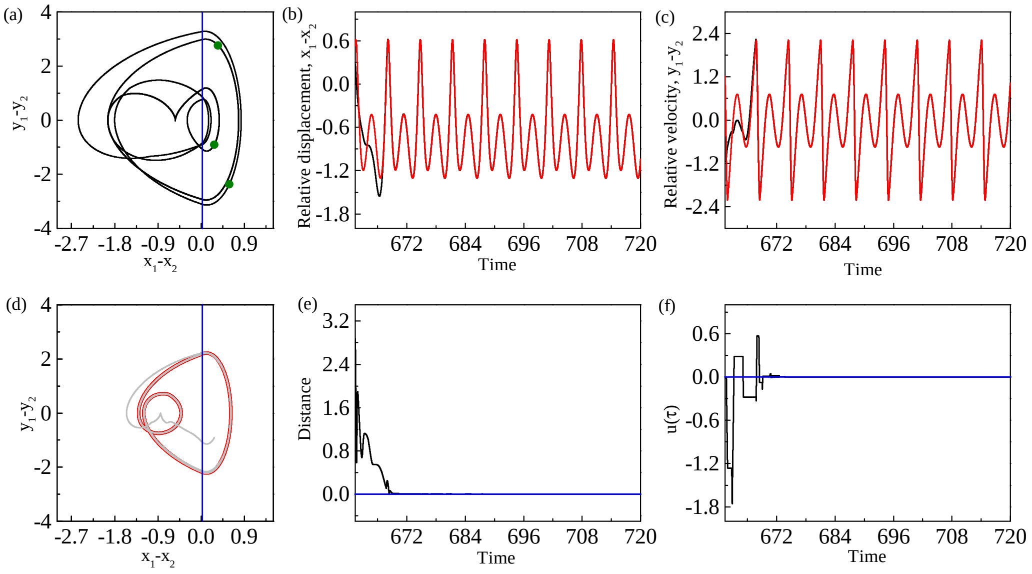

Fig. 7.4.3 (a) The period-3 response on the phase plane with the Poincaré sections denoted by oliver dots. (b) Time histories of the desired (red line) and the current (black line) displacements of the system under the linear control strategy (Algorithm 1) with $M_1 = 5$ and $M_2 = 5$. (c) Time histories of the desired (red line) and the current (black line) velocities of the system. (d) Trajectory of the system on the phase plane under the linear control strategy, where grey and red lines represent the transient and the steady-state responses, respectively. (e) Time history of the distance between the desired and the controlled trajectories in 2-norm. (f) Time history of the control sequence generated by the linear control strategy. Blue lines in (a) and (d) indicate the impact boundary, while the blue lines in (e) and (f) mark the zero reference. The result was computed for $\alpha = 1.6$, $\omega = 0.95$, $\xi = 0.01$, $\delta = 0.02$, $\beta = 15$ and $\gamma = 5$.

Nonlinear control

A case on the switching between the period-3 and period-1 attractor by the nonlinear control strategy will be studied at this part. In Fig. 7.4.4, the period-1attractor is controlled to period-3 attractor. The transition from period-1 to period-3 attractor is shown in Fig. 7.4.4 (b), (c) and (d). During the transition, the relevant distance between these two trajectories decreases from 2.8785 at $\tau = 661.388$ to 0.005 at $\tau = 688.016$. In the process, the control signal reaches the highest value $u_p(\tau) = 0.3$ and the lowest value $u(\tau) = -0.3$ at many times. Then, the control signal returns back to 0 after $\tau = 688.016$. Finally, the controlled trajectory converges to the period-3 attractor. In addition, for the case of which the period-3 attractor is switched to the period-1 attractor in Fig. 7.4.5, the nonlinear control strategy begins at the same time as above, and reduces the distance between two trajectories to 0.005 at $\tau = 674.298$, shown in Fig. 7.4.5(e). After that moment, the control signal $u_p(\tau)$ tends to 0, and the control target is successfully achieved. Thus, the nonlinear control strategy successfully calculates the value of $u_p(\tau)$ to achieve the switching between the period-1 attractor and the period-3 attractor.

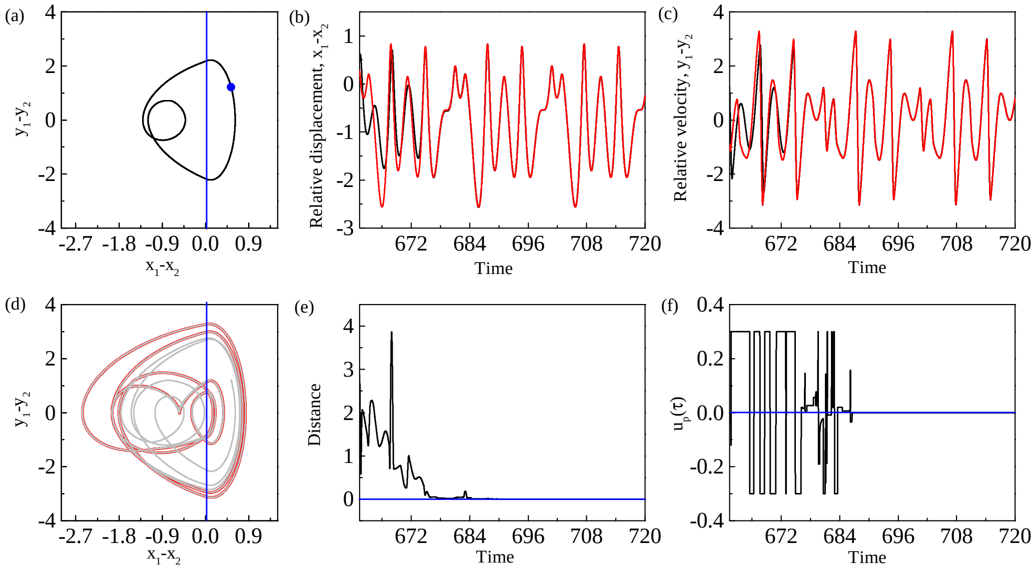

Fig. 7.4.4 (a) The period-1 response on the phase plane with the Poincaré sections denoted by a blue dot. (b) Time histories of the desired (red line) and the current (black line) displacements of the system under the nonlinear control strategy (Algorithm 2) with $M_{a,1} = 0.3$ and $M_{a,2} = 10$. (c) Time histories of the desired (red line) and the current (black line) velocities of the system. (d) Trajectory of the system on the phase plane under the nonlinear control strategy, where grey and red lines represent the transient and the steady-state responses, respectively. (e) Time history of the distance between the desired and the controlled trajectories in 2-norm. (f) Time history of the control sequence generated by the nonlinear control strategy. Blue lines in (a) and (d) indicate the impact boundary, while the blue lines in (e) and (f) mark the zero reference. The result was computed for $\alpha = 1.6$, $\omega = 0.95$, $\xi = 0.01$, $\delta = 0.02$, $\beta = 15$ and $\gamma = 5$.

7.5 Control of the Duffing system

7.5.1 Mathematical description and preparation

In this section, the Duffing oscillator representing smooth dynamical systems is employed to test the versatility of the proposed control method. The Duffing system, which is known to

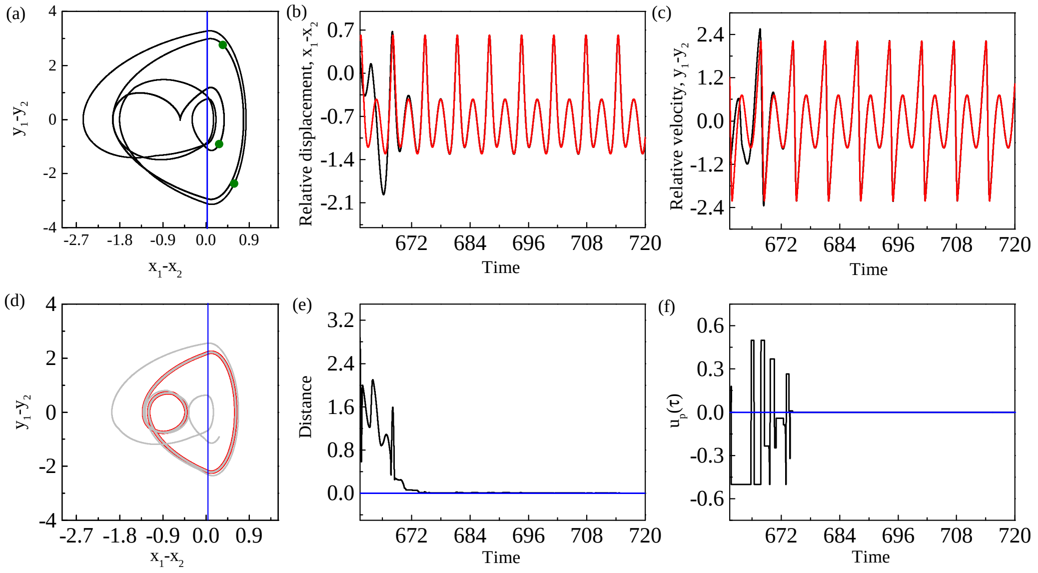

Fig. 7.4.5 (a) The period-3 response on the phase plane with the Poincaré sections denoted by oliver dots. (b) Time histories of the desired (red line) and the current (black line) displacements of the system under the nonlinear control strategy (Algorithm 2) with $M_{a,1} = 0.5$ and $M_{a,2} = 15$. (c) Time histories of the desired (red line) and the current (black line) velocities of the system. (d) Trajectory of the system on the phase plane under the nonlinear control strategy, where grey and red lines represent the transient and the steady-state responses, respectively. (e) Time history of the distance between the desired and the controlled trajectories in 2-norm. (f) Time history of the control sequence generated by the nonlinear control strategy. Blue lines in (a) and (d) indicate the impact boundary, while the blue lines in (e) and (f) mark the zero reference. The result was computed for $\alpha = 1.6$, $\omega = 0.95$, $\xi = 0.01$, $\delta = 0.02$, $\beta = 15$ and $\gamma = 5$.

have many coexisting attractors without control, can be described by

$$\begin{aligned} \dot{Y}(\tau) &= F_{\mathrm{du}}(\tau, Y(\tau), u_{\mathrm{p}}(\tau)), \\ Y_0 &= Y(\tau_0), \end{aligned} \tag{7.5.1}$$

where $Y(\tau) := (x(\tau), v(\tau))^T$, and

$$F_{\mathrm{du}}(\tau, Y, u_{\mathrm{p}}) := \begin{bmatrix} 0 \\ \Gamma\sin(\omega\tau) \end{bmatrix} + \begin{bmatrix} 0 & 1 \\ 1 & -p_1 \end{bmatrix} Y + Y^T(\tau) \begin{bmatrix} 1 \\ 0 \end{bmatrix} Y^T \begin{bmatrix} 1 \\ 0 \end{bmatrix} \begin{bmatrix} 0 & 0 \\ -(p_2 + u_{\mathrm{p}}) & 0 \end{bmatrix} Y.$$

The following parameters: $\Gamma = 1.9$, $\omega = 1.2$, $p_1 = 0.9$ and $p_2 = 1$ were considered in this study. At these parameter values, the system without control ($u_{\mathrm{p}} = 0$) has two coexisting attractors, depicted in Fig. 7.5.1, which are a period-1 small and a large amplitude attractors with their Poincaré sections denoted by black and violet dots, respectively.

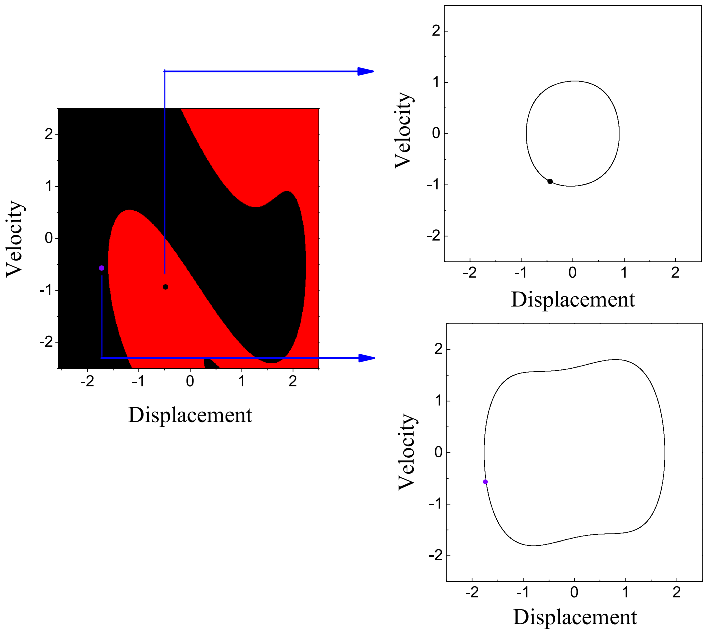

Fig. 7.5.1 Basins of attraction of the Duffing system computed for $\Gamma = 1.9$, $\omega = 1.2$, $p_1 = 0.9$ and $p_2 = 1$. Black dot denotes the period-1 small amplitude attractor with red basin, and violate dot represents the period-1 large amplitude attractor with black basin. The right panels present the trajectories of the two period-1 attractors on the phase plane.

7.5.2 Numerical investigation

Nonlinear control

The control aims for system (7.5.1) to switch the two stable attractors shown in Fig. 7.5.1 by varying the stiffness of the nonlinear spring p_2. The control result for the switching from the large to the small amplitude attractor is shown in Fig. 7.5.2, where the control strategy was applied to the original attractor at $\tau = 418.879$, and the controlled trajectory experienced a transition until $\tau = 439$. During this time the 2-norm distance between the control and the desired trajectories was reduced from 1.338 to 0.001. The control signal reached the maximum $u_\mathrm{p}(\tau) = 0.3$ and the minimum $u_\mathrm{p}(\tau) = -0.3$ for several times before it was switched off.

The control from the small to the large amplitude attractor is presented in Fig. 7.5.3, where the control strategy is switched on at $\tau = 418.879$ and is switched off at $\tau = 440.246$ when the distance between the two trajectories is decreased to 0.001. Compared to the case in Fig. 7.5.2, the transition from the small to the large amplitude attractor took a longer time.

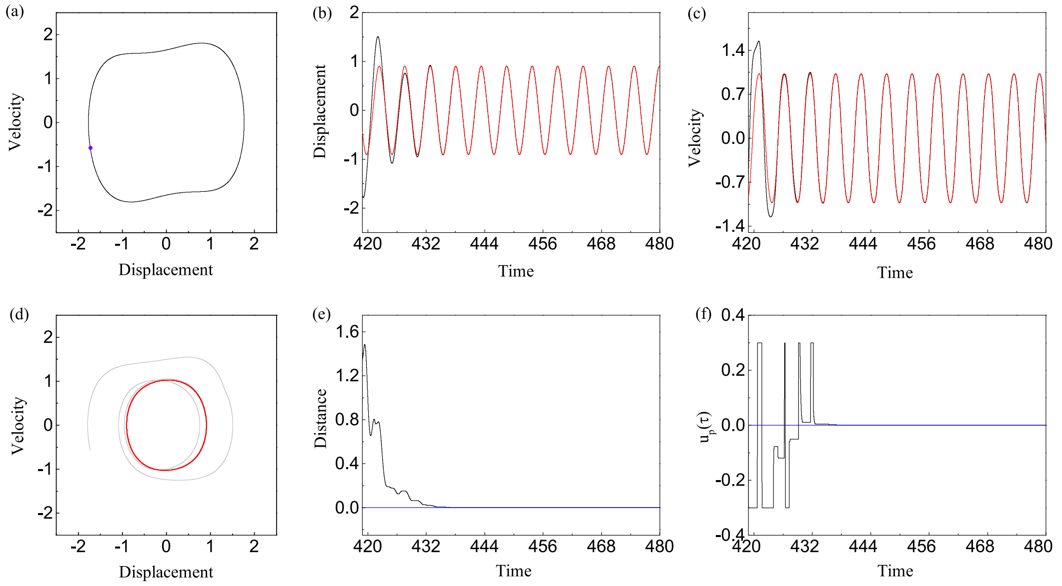

Fig. 7.5.2 (a) The large amplitude period-1 response on the phase plane with the Poincaré section denoted by violate dot. (b) Time histories of the desired (red line) and the current (black line) displacements of the system under the nonlinear control strategy (Algorithm 2) by varying the stiffness of the nonlinear spring with $M_{\mathrm{p}_2,1} = 0.3$ and $M_{\mathrm{p}_2,2} = 10$. (c) Time histories of the desired (red line) and the current (black line) velocities of the system. (d) Trajectory of the system on the phase plane under the nonlinear control strategy, where grey and red lines represent the transient and the steady-state responses, respectively. (e) Time history of the distance between the desired and the controlled trajectories in 2-norm. (f) Time history of the control sequence generated by the nonlinear control strategy. Blue lines in (a) and (d) indicate the impact boundary, while the blue lines in (e) and (f) mark the zero reference. The result was computed for $\Gamma = 1.9$, $\omega = 1.2$, $p_1 = 0.9$ and $p_2 = 1$.

Bifurcation analysis of the coexisting attractors

Analogous to Section 7.2.2, in this section the main concern will be to study in detail the effect of the control parameters p_1, p_2 on the small- and high-amplitude oscillations of the Duffing system (7.5.1), see Fig. 7.5.1. To this end, the path-following methods for limit cycles, implemented via the continuation platform COCO [25] will be employed, along with its routines for bifurcation detection and two-parameter continuation of codimension-1 bifurcations.

The starting point for this study is the high-amplitude periodic solution shown in Fig. 7.5.4(c), computed for $p_1 = 0.8$. Panel (a) presents the result of the numerical continuation of this orbit with respect to the control parameter p_1. In this diagram, changes of stability are detected, which are marked with solid (for stable solutions) and dashed (unstable solutions) lines. The window of stability of the the high-amplitude orbit is bounded from above by the

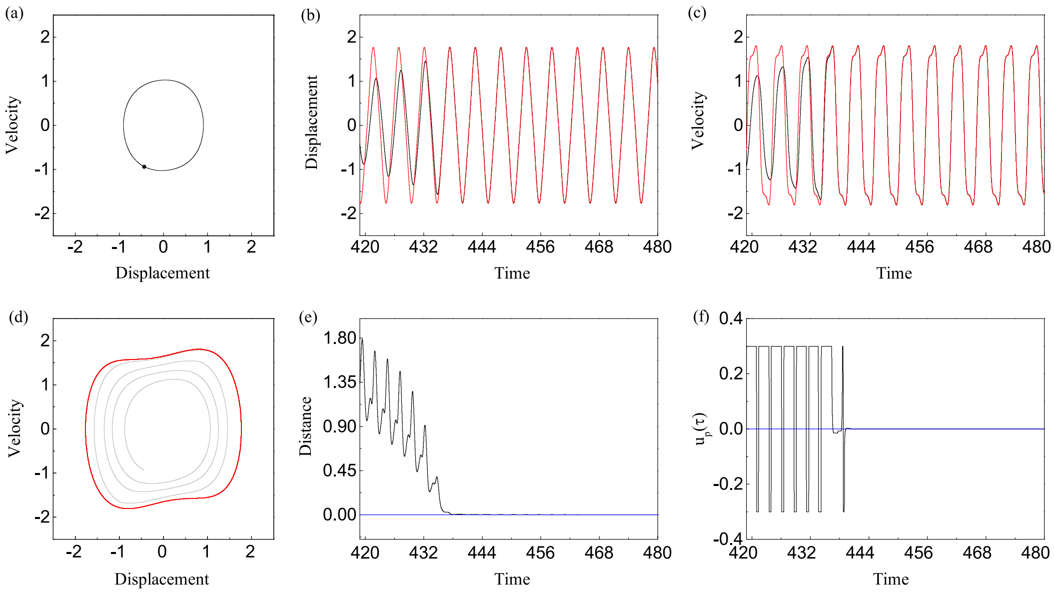

Fig. 7.5.3 (a) The small amplitude period-1 response on the phase plane with the Poincaré section denoted by black dot. (b) Time histories of the desired (red line) and the current (black line) displacements of the system under the nonlinear control strategy (Algorithm 2) by varying the stiffness of the nonlinear spring with $M_{\mathrm{p}_2,1} = 0.3$ and $M_{\mathrm{p}_2,2} = 10$. (c) Time histories of the desired (red line) and the current (black line) velocities of the system. (d) Trajectory of the system on the phase plane under the nonlinear control strategy, where grey and red lines represent the transient and the steady-state responses, respectively. (e) Time history of the distance between the desired and the controlled trajectories in 2-norm. (f) Time history of the control sequence generated by the nonlinear control strategy. Blue lines in (a) and (d) indicate the impact boundary, while the blue lines in (e) and (f) mark the zero reference. The result was computed for $\Gamma = 1.9$, $\omega = 1.2$, $p_1 = 0.9$ and $p_2 = 1$.

fold bifurcation F2 ($p_1 \approx 0.90352$). At this point, a branch of unstable periodic solutions is born, which finishes at the fold point F1 ($p_1 \approx 0.69494$). Here, a family of stable oscillations emerges, corresponding to small-amplitude periodic orbits as can be seen at the test point P2, see Fig. 7.5.4(b). Consequently, the bifurcation points F1 and F2 defines a parameter window where both attractors coexist.

Next, a two-parameter continuation of the fold points detected above will be carried out, in order to determine a region in the p_1-p_2 plane where the small- and high-amplitude attractors of the Duffing system coexist. The result of this numerical process is presented in Fig. 7.5.4(d), where the red curve stands for a locus of fold bifurcations of limit cycles. In this picture, the yellow area enclosed by the fold curve represents the parameter regime where small- and high-amplitude oscillations coexist. The intersections of the horizontal dashed line ($p_2 = 1$) with the bifurcation diagram correspond to the fold bifurcations F1 and F2 found in Fig. 7.5.4(a). Furthermore, the numerical computations reveal the presence of a

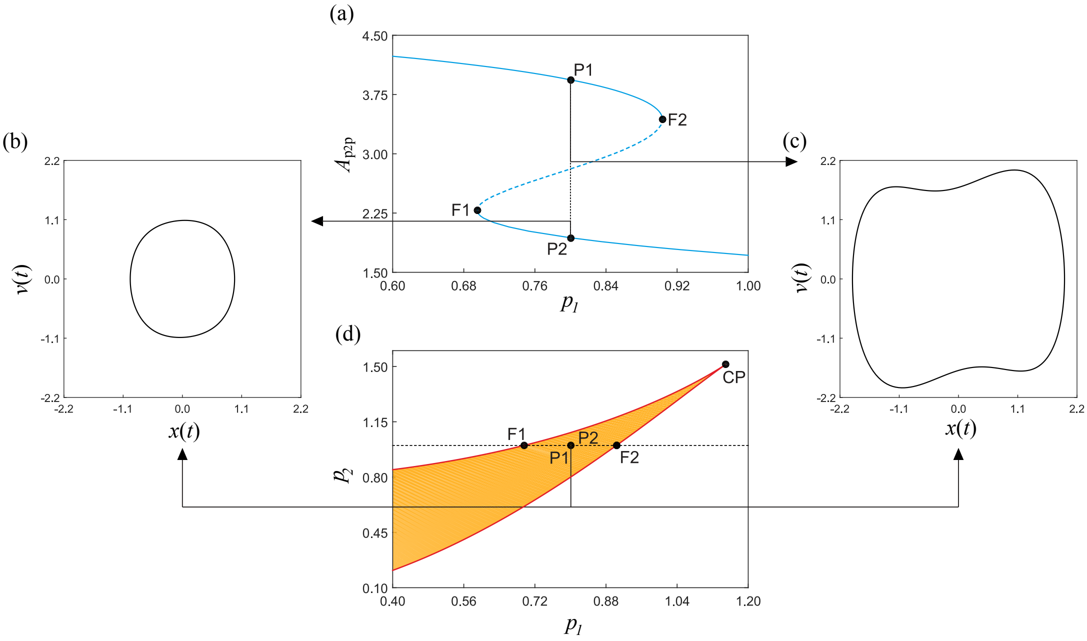

Fig. 7.5.4 (a) One-parameter continuation of the periodic response of the Duffing oscillator (7.5.1) with respect to p_1, computed for the parameter values $\Gamma = 1.9$, $\omega = 1.2$ and $p_2 = 1$. The vertical axis shows the peak-to-peak amplitude A_{p2p} of the x-component. Branches of stable and unstable periodic orbits are depicted with solid and dashed lines, respectively. The points labeled F1 ($p_1 \approx 0.69494$) and F2 ($p_1 \approx 0.90352$) stand for fold bifurcations of limit cycles. Panels (b) and (c) depict stable coexisting solutions computed at the test points P1 and P2 ($p_1 = 0.8$), respectively, shown in panel (a). (d) Two-parameter continuation of the fold points found in panel (a), with respect to p_1 and p_2. Here, the label CP represents a cusp bifurcation ($p_1 \approx 1.14902$, $p_2 \approx 1.51194$). The intersections of the horizontal dashed line ($p_2 = 1$) with the bifurcation diagram correspond to the fold bifurcations F1 and F2 shown in panel (a). The yellow area represents the parameter region in which the stable periodic solutions of the type shown in panels (b) and (c) coexist.

codimension-2 point $(p_1, p_2) \approx (1.14902, 1.51194)$ (CP), where two branches of fold points (those corresponding to F1 and F2) join together via a cusp singularity. In this way, it is possible to determine boundaries in the considered parameter region for the application of the control mechanism proposed in this work.

7.6 Conclusion

This chapter studied a control method for switching stable coexisting attractors of non-autonomous smooth and nonsmooth dynamical systems. The control aim was to control an undesired coexisting attractor to a desired one by modulating a system parameter without affecting the original property of the system. To examine the proposed control concept, the above cases were controlled by two control strategies with finite sampling step, namely the linear and nonlinear control strategies, where one was implemented through the external control input and the other one was applied via a system parameter. Then, some simple dynamical systems were used for verifying the effectiveness of this method. In details, for the soft impact system with two coexisting attractors, the varying parameter control method can achieve the switching from one of coexisting attractors to another without introducing a significant change into system's states suddenly. For the impact system with a drift, the chaotic attractor can be controlled to the coexisting period-4 attractor by this method. Similarly, for the vibro-impact capsule system, this method also can be effective on the control of coexisting attractors. Finally, a duffing system also was used for verifying the effectiveness of this method. Therefore, this new control method presented a great performance on the control of coexisting attractors without having a significant changes on system's states suddenly. The basic concept and idea of this method could be adopted to study the control of coexisting attractors for other types of dynamical systems.

7.7 Practical implementation of the proposed control strategies

From the previous numerical results, the efficiency of the proposed control methods on the control of coexisting attractors was validated. From the practical aspect, the implementation of the linear control strategy is similar with the delay feedback control studied in Chapter 6, and the varying rate of the controller can be constrained to satisfy the strict requirement, e.g., ensuring the state of the system does not experience a drastic change. But under this condition, the controlled system will undoubtedly need to spend a longer time for stabilisation. Compared with the linear control strategy, the nonlinear control strategy by varying the amplitude of the external excitation is easy to be implemented in the above systems, since it just needs to satisfy the continuous varying trend of amplitude based on Algorithm 2. For example, in the experimental environment of the soft impact system, the amplitude of the external excitation is one of the accessible control parameters, which is easy to be ajusted. In order to have more control options, the nonlinear control strategy by varying the gap is also possible to be implemented in the experiment. For this scenario, an electric motor for moving the right spring in Fig. 3.2.1 can be used to control the gap constantly based on Algorithm 2. Furthermore, similar implementation can be applied to more complex experimental platforms, such as the impact system with a drift and the vibro-impact capsule system.

Chapter 8

Conclusion and future work

8.1 Conclusion

This thesis studies the control of coexisting attractors in nonsmooth dynamical systems with the consideration of time delay by using different control and computational method for analysing their near-grazing dynamics. The main works in this thesis are presented in the following.

Chapter 4 focused on developing a numerical approach for the numerical continuation of periodic solutions of nonsmooth dynamical systems with delay. The numerical approach is based on the well-known technique of approximating delay differential equations via large systems of ODEs. This second-order approximation of the original DDE was developed by considering a finite sequence of Taylor expansions. In this way, a piecewise-smooth dynamical system with (constant) delay can be approximated by a piecewise- smooth system of ODEs of large dimension, which then allows the study of the resulting model in the framework of hybrid dynamical systems. Then, a numerical bifurcation analysis can be carried out via continuation methods, using existing numerical packages, such as COCO. The effectiveness of the proposed scheme was tested on a well-known and widely studied the soft impact system driven by a delay feedback controller.

Chapter 5 studied a numerical method to calculate the LEs of delay nonsmooth systems by using a soft impact system under the delay feedback control with a particular focus on its near-grazing dynamics. Specifically, in order to develop this algorithm with high accuracy, a grazing estimation algorithm was developed to estimate the impact time near grazing locally along trajectories of nonsmooth DDEs. In addition, as the delay impact system is infinite dimensional, it was approximated by finite dimensional systems, which were discretised by the modified Euler integration method at each time step. Then the DDE system was expressed as a time-discrete map by constructing a Poincaré map, and the variational equation was obtained from linearising the DDE system. Then the Jacobian of the map can be obtained through combining all the Jacobian from the variational equation at each time step in one period of external excitation. With the introducing of the grazing estimation algorithm, the accurate Jacobian of the map can be obtained. Through the above steps, the improvement of accuracy of the algorithm for calculating LEs was observed from the the convergence rate of eigenvalues of the Jacobian matrix, which was studied by using the spectral theory of the evolutionary operator.

Chapter 6 presented a numerical study of controlling coexisting attractors in the periodically forced nosmooth dynamcial systems by using delay feedback control. The control achieved the aim of switching the systems from undesired coexisting attractors to a desired period-1 response, and then suppressing complex dynamics of these nonsmooth dynamical systems, such as the coexisting attractors and chaotic motions. This orbit was used as the desired attractor for the system with the delay feedback control. It was found that the delay feedback control is effective, and the nonsmooth dynamical systems can be driven to a globally stable period-1 motion. In the numerical analysis, the feasible conditions of the delay feedback control on different nonsmooth dynamical systems were given. In addition, how the control effect dynamics of nonsmooth dynamical systems was analysed numerically.

Chapter 7 focused on addressing the continuous switching between two of coexisting stable attractors by varying a system parameter without affecting their original dynamics. In order to achieve this, a continuous control method was proposed to control the coexisting attractors of non-autonomous smooth and nonsmooth dynamical systems. This feedback control method was applied to the controlled system continuously until its trajectory is sufficiently close to the desired one. Two control strategies, the so-called linear and nonlinear control strategies, were developed based on this concept. Specifically, the former is implemented through an external control input and the latter is applied via a system parameter. The advantage of the nonlinear control strategy is that it depends only on the original properties of system parameter and does not rely on any external input. To examine the proposed control concept, two control strategies were implemented to control the nonsmooth dynamical systems. Specifically, for the soft impact system, a multistable scenario of the impact system, where a period-5 and a period-2 attractors coexist, was studied. For the impact system with a drift, a scenario, where a period-4 and chaotic attractors coexist, was studied. Then, a scenario of the vibro-impact capsule system, where a period-3 and period-1 attractors coexist, was studied. Following that, the nonlinear control strategy was implemented to the Duffing oscillator for switching a period-1 small and a period-1 large amplitude attractors. All simulations showed that both control strategies were effective for switching the stable coexisting attractors in the nonsmooth dynamical systems.

8.2 Future work

Overall, this thesis presented some new methods and analyses on studying the control of coexisting attractors in nonsmooth dynamical systems, which address the issues related to the multistability in nonsmooth dynamical systems. These works can be expanded to study the coexisting attractors in other nonlinear dynamical systems, such as the network systems [72, 73] and the stochastic dynamical systems [22, 159]. Following the work of this thesis, in the short-term future, the numerical bifurcation analysis of the impact system with a drift and vibro-impact capsule system with delay feedback control will be carried out via continuation methods to fully understand the dynamics of the controlled nonsmooth systems.

In the long-term future, some unclear and unsolved problems will be studied. First of all, according to the results in Chapter 7, there is a case that the capsule is stop and while the inner mass presents a period-1 motion under the effect from the time-delayed feedback controller. Obviously, the motion of capsule driven by inner mass may present different motions compared with the motion of inner mass. Hence, the relationship between the motion of the inner mass and the capsule is necessary to be studied. This relationship can be explored further through the numerical and theoretical analysis in the future. Secondly, in this thesis, some control methods are introduced to achieve the control of coexisting attractors in nonsmooth dynamical systems. The control target is only to achieve the switch from the undesired attractors to the desired one and does not consider complex targets, such as the energy-saving or time-saving switch among the coexisting attractors. Thus, the future work will adopt the optimal control theory to study the control of coexisting attractors in nonsmooth dynamical systems under some constraint conditions. Thirdly, since multistability is also important property for many dynamical systems appearing in many other applications, such as cancer diseases, epilepsy, climate change and power grid, it will be meaningful to consider the control of coexisting attractors appearing in the above applications and give the analysis of the dynamical properties of the controlled systems. Besides that, since the methods in the thesis present good performance and are validated theoretically and numerically, the future task will focus on validating these methods through experiments.

References

[1] Y. Liu and J. Páez Chávez, “Controlling coexisting attractors of an impacting system via linear augmentation,” *Physica D: Nonlinear Phenomena*, vol. 348, pp. 1–11, 2017.

[2] E. Pavlovskaia, M. Wiercigroch, and C. Grebogi, “Modeling of an impact system with a drift,” *Physical Review E*, vol. 64, no. 5, p. 056224, 2001.

[3] Y. Liu, E. Pavlovskaia, M. Wiercigroch, and Z. Peng, “Forward and backward motion control of a vibro-impact capsule system,” *International Journal of Non-Linear Mechanics*, vol. 70, pp. 30–46, 2015.

[4] E. Pavlovskaia and M. Wiercigroch, “Analytical drift reconstruction for visco-elastic impact oscillators operating in periodic and chaotic regimes,” *Chaos, Solitons & Fractals*, vol. 19, no. 1, pp. 151–161, 2004.

[5] B. Guo, Y. Liu, R. Birler, and S. Prasad, “Self-propelled capsule endoscopy for small-bowel examination: Proof-of-concept and model verification,” *International Journal of Mechanical Sciences*, vol. 174, p. 105506, 2020.

[6] Y. Liu, E. Pavlovskaia, and M. Wiercigroch, “Experimental verification of the vibro-impact capsule model,” *Nonlinear Dynamics*, vol. 83, no. 1-2, pp. 1029–1041, 2016.

[7] J. Páez Chávez and M. Wiercigroch, “Bifurcation analysis of periodic orbits of a non-smooth Jeffcott rotor model,” *Communications in Nonlinear Science and Numerical Simulation*, vol. 18, no. 9, pp. 2571–2580, 2013.

[8] K. Mora, A. R. Champneys, A. D. Shaw, and M. I. Friswell, “Explanation of the onset of bouncing cycles in isotropic rotor dynamics; a grazing bifurcation analysis,” *Proceedings of the Royal Society A*, vol. 476, no. 2237, p. 20190549, 2020.

[9] L. Serdukova, R. Kuske, and D. Yurchenko, “Post-grazing dynamics of a vibro-impacting energy generator,” *Journal of Sound and Vibration*, vol. 492, p. 115811, 2021.

[10] S. Lahriri, I. F. Santos, H. I. Weber, and H. Hartmann, “On the nonlinear dynamics of two types of backup bearings-theoretical and experimental aspects,” *Journal of engineering for gas turbines and power*, vol. 134, no. 11, 2012.

[11] Y. Yan, J. Xu, and M. Wiercigroch, “Basins of attraction of the bistable region of time-delayed cutting dynamics,” *Physical Review E*, vol. 96, no. 3, p. 032205, 2017.

[12] E. Pavlovskaia, D. C. Hendry, and M. Wiercigroch, “Modelling of high frequency vibro-impact drilling,” *International Journal of Mechanical Sciences*, vol. 91, pp. 110–119, 2015.

[13] M. Kapitaniak, V. Vaziri Hamaneh, J. Páez Chávez, K. Nandakumar, and M. Wiercigroch, “Unveiling complexity of drill-string vibrations: experiments and modelling,” *International Journal of Mechanical Science*, vol. 101-102, pp. 324–337, 2015.

[14] Y. Liu, J. Páez Chávez, D. S. Rulston, and S. Walker, “Numerical and experimental studies of stick-slip oscillations in drill-strings,” *Nonlinear Dynamics*, vol. 90, pp. 2959–2978, 2017.

[15] S. L. De Souza, I. L. Caldas, R. L. Viana, and J. M. Balthazar, “Control and chaos for vibro-impact and non-ideal oscillators,” *Journal of theoretical and applied mechanics*, vol. 46, no. 3, pp. 641–664, 2008.

[16] Y. Liu, J. Páez Chávez, E. Pavlovskaia, and M. Wiercigroch, “Analysis and control of the dynamical response of a higher order drifting oscillator,” *Proceedings of the Royal Society A: Mathematical, Physical and Engineering Sciences*, vol. 474, no. 2210, p. 20170500, 2018.

[17] M. Liao, Y. Liu, J. Páez Chávez, A. Chong, and M. Wiercigroch, “Dynamics of vibro-impact drilling with linear and nonlinear rock models,” *International Journal of Mechanical Sciences*, vol. 146-147, pp. 200–210, 2018.

[18] B. E. Martínez-Zerega, A. N. Pisarchik, and L. Tsimring, “Using periodic modulation to control coexisting attractors induced by delayed feedback,” *Physics Letters A*, vol. 318, no. 1-2, pp. 102–111, 2003.

[19] K. Pyragas, “Continuous control of chaos by self-controlling feedback,” *Physics letters A*, vol. 170, no. 6, pp. 421–428, 1992.

[20] Y. Jiang, “Trajectory selection in multistable systems using periodic drivings,” *Physics Letters A*, vol. 264, no. 1, pp. 22–29, 1999.

[21] Y.-C. Lai, “Driving trajectories to a desirable attractor by using small control,” *Physics Letters A*, vol. 221, no. 6, pp. 375–383, 1996.

[22] A. N. Pisarchik and U. Feudel, “Control of multistability,” *Physics Reports*, vol. 540, no. 4, pp. 167–218, 2014.

[23] A. N. Pisarchik and B. K. Goswami, “Annihilation of one of the coexisting attractors in a bistable system,” *Physical review letters*, vol. 84, no. 7, p. 1423, 2000.

[24] B. Goswami and A. N. Pisarchik, “Controlling multistability by small periodic perturbation,” *International Journal of Bifurcation and Chaos*, vol. 18, no. 06, pp. 1645–1673, 2008.

[25] H. Dankowicz and F. Schilder, *Recipes for continuation*. Computational Science and Engineering, Philadelphia: SIAM, 2013.

[26] W. Weckesser, “VFGEN: a code generation tool,” *JNAIAM J. Numer. Anal. Indust. Appl. Math*, vol. 3, pp. 151–165, 2008.

[27] D. A. Barton, “Stability calculations for piecewise-smooth delay equations,” *International Journal of Bifurcation and Chaos*, vol. 19, no. 02, pp. 639–650, 2009.

[28] H. Dankowicz and P. Thota, “TC-HAT: A novel toolbox for the continuation of periodic trajectories in hybrid dynamical systems,” *SIAM Journal on Applied Dynamical Systems*, vol. 7, no. 4, pp. 283–322, 2008.

[29] B. Brogliato, *Nonsmooth mechanics*. Springer, 1999.

[30] B. Brogliato, *Impacts in mechanical systems: analysis and modelling*, vol. 551. Springer Science & Business Media, 2000.

[31] M. Kunze, *Non-smooth dynamical systems*, vol. 1744. Springer Science & Business Media, 2000.

[32] J. Ing, E. Pavlovskaia, M. Wiercigroch, and S. Banerjee, “Experimental study of impact oscillator with one-sided elastic constraint,” *Philosophical Transactions of the Royal Society A: Mathematical, Physical and Engineering Sciences*, vol. 366, no. 1866, pp. 679–705, 2008.

[33] K. Popp and P. Stelter, “Stick-slip vibrations and chaos,” *Philosophical Transactions: Physical Sciences and Engineering*, pp. 89–105, 1990.

[34] S. Banerjee and G. C. Verghese, *Nonlinear phenomena in power electronics: Bifurcations, chaos, control, and applications*. Wiley-IEEE Press, 2001.

[35] M. di Bernardo, F. Garefalo, L. Glielmo, and F. Vasca, “Switchings, bifurcations, and chaos in dc/dc converters,” *IEEE Transactions on Circuits and Systems I: Fundamental Theory and Applications*, vol. 45, no. 2, pp. 133–141, 1998.

[36] M. D. Bernardo, K. H. Johansson, and F. Vasca, “Self-oscillations and sliding in relay feedback systems: Symmetry and bifurcations,” *International Journal of Bifurcation and chaos*, vol. 11, no. 04, pp. 1121–1140, 2001.

[37] A. J. van der Schaft and J. M. Schumacher, “Modelling and analysis of hybrid dynamical systems,” in *Advances in the control of nonlinear systems*, pp. 195–224, Springer, 2001.

[38] W. Chin, E. Ott, H. E. Nusse, and C. Grebogi, “Grazing bifurcations in impact oscillators,” *Physical Review E*, vol. 50, no. 6, p. 4427, 1994.

[39] M. Bernardo, C. Budd, A. R. Champneys, and P. Kowalczyk, *Piecewise-smooth dynamical systems: theory and applications*, vol. 163. Springer Science & Business Media, 2008.

[40] J. Páez Chávez, V. V. Hamaneh, and M. Wiercigroch, “Modelling and experimental verification of an asymmetric Jeffcott rotor with radial clearance,” *Journal of Sound and Vibration*, vol. 334, pp. 86–97, 2015.

[41] B. Blazejczyk-Okolewska, K. Czolczynski, and T. Kapitaniak, “Hard versus soft impacts in oscillatory systems modeling,” *Commun. Nonlinear Sci. Numer. Simulat.*, vol. 15, pp. 1358–1367, 2010.

[42] J. Thompson and R. Ghaffari, “Chaos after period-doubling bifurcations in the resonance of an impact oscillator,” *Physics Letters A*, vol. 91, no. 1, pp. 5–8, 1982.

[43] A. Muszynska and P. Goldman, “Chaotic responses of unbalanced rotor/bearing/stator systems with looseness or rubs,” *Chaos, Solitons & Fractals*, vol. 5, no. 9, pp. 1683–1704, 1995.

[44] S. Yin, J. Ji, and G. Wen, “Complex near-grazing dynamics in impact oscillators,” *International Journal of Mechanical Sciences*, vol. 156, pp. 106–122, 2019.

[45] S. Yin, J. Ji, S. Deng, and G. Wen, “Degenerate grazing bifurcations in a three-degree-of-freedom impact oscillator,” *Nonlinear Dynamics*, vol. 97, no. 1, pp. 525–539, 2019.

[46] S. Yin, G. Wen, J. Ji, and H. Xu, “Novel two-parameter dynamics of impact oscillators near degenerate grazing points,” *International Journal of Non-Linear Mechanics*, vol. 120, p. 103403, 2020.

[47] C. Budd and F. Dux, “Intermittency in impact oscillators close to resonance,” *Nonlinearity*, vol. 7, no. 4, p. 1191, 1994.

[48] A. B. Nordmark, “Existence of periodic orbits in grazing bifurcations of impacting mechanical oscillators,” *Nonlinearity*, vol. 14, no. 6, p. 1517, 2001.

[49] A. B. Nordmark, “Non-periodic motion caused by grazing incidence in an impact oscillator,” *Journal of Sound and Vibration*, vol. 145, no. 2, pp. 279–297, 1991.

[50] E. Pavlovskaia, J. Ing, M. Wiercigroch, and S. Banerjee, “Complex dynamics of bilinear oscillator close to grazing,” *International Journal of Bifurcation and Chaos*, vol. 20, no. 11, pp. 3801–3817, 2010.

[51] H. Lamba and C. Budd, “Scaling of Lyapunov exponents at nonsmooth bifurcations,” *Physical Review E*, vol. 50, no. 1, p. 84, 1994.

[52] S. Foale and S. Bishop, “Bifurcations in impact oscillations,” *Nonlinear Dynamics*, vol. 6, no. 3, pp. 285–299, 1994.

[53] H. Dankowicz and X. Zhao, “Local analysis of co-dimension-one and co-dimension-two grazing bifurcations in impact microactuators,” *Physica D: Nonlinear Phenomena*, vol. 202, no. 3-4, pp. 238–257, 2005.

[54] J. Ing, E. Pavlovskaia, M. Wiercigroch, and S. Banerjee, “Bifurcation analysis of an impact oscillator with a one-sided elastic constraint near grazing,” *Physica D: Nonlinear Phenomena*, vol. 239, no. 6, pp. 312–321, 2010.

[55] Y. Liu, J. Páez Chávez, B. Guo, and R. Birler, “Bifurcation analysis of a vibro-impact experimental rig with two-sided constraint,” *Meccanica*, pp. 1–17, 2020.

[56] F. Arecchi and F. Lisi, “Hopping mechanism generating 1 f noise in nonlinear systems,” *Physical Review Letters*, vol. 49, no. 2, p. 94, 1982.

[57] M. Beasley, D. D’Humieres, and B. Huberman, “Comment on" hopping mechanism generating 1 f noise in nonlinear systems",” *Physical Review Letters*, vol. 50, no. 17, p. 1328, 1983.

[58] F. Arecchi, R. Meucci, G. Puccioni, and J. Tredicce, “Experimental evidence of subharmonic bifurcations, multistability, and turbulence in a q-switched gas laser,” *Physical Review Letters*, vol. 49, no. 17, p. 1217, 1982.

[59] J. Foss, A. Longtin, B. Mensour, and J. Milton, “Multistability and delayed recurrent loops,” *Physical Review Letters*, vol. 76, no. 4, p. 708, 1996.

[60] S. Huang, “Genetic and non-genetic instability in tumor progression: link between the fitness landscape and the epigenetic landscape of cancer cells,” *Cancer and Metastasis Reviews*, vol. 32, no. 3, pp. 423–448, 2013.

[61] G. M. Süel, J. Garcia-Ojalvo, L. M. Liberman, and M. B. Elowitz, “An excitable gene regulatory circuit induces transient cellular differentiation,” *Nature*, vol. 440, no. 7083, pp. 545–550, 2006.

[62] S. Huang, G. Eichler, Y. Bar-Yam, and D. E. Ingber, “Cell fates as high-dimensional attractor states of a complex gene regulatory network,” *Physical review letters*, vol. 94, no. 12, p. 128701, 2005.

[63] G. Yao, C. Tan, M. West, J. R. Nevins, and L. You, “Origin of bistability underlying mammalian cell cycle entry,” *Molecular systems biology*, vol. 7, no. 1, p. 485, 2011.

[64] D. Battogtokh and J. J. Tyson, “Bifurcation analysis of a model of the budding yeast cell cycle,” *Chaos: An Interdisciplinary Journal of Nonlinear Science*, vol. 14, no. 3, pp. 653–661, 2004.

[65] Y. Liu and J. P. Chávez, “Controlling multistability in a vibro-impact capsule system,” *Nonlinear Dynamics*, vol. 88, no. 2, pp. 1289–1304, 2017.

[66] E. Ott, C. Grebogi, and J. A. Yorke, “Controlling chaos,” *Physical review letters*, vol. 64, no. 11, p. 1196, 1990.

[67] K. Pyragas and A. Tamaševičius, “Experimental control of chaos by delayed self-controlling feedback,” *Physics Letters A*, vol. 180, no. 1-2, pp. 99–102, 1993.

[68] V. Pyragas and K. Pyragas, “Act-and-wait time-delayed feedback control of nonautonomous systems,” *Physical Review E*, vol. 94, no. 1, p. 012201, 2016.

[69] K. Yamasue, K. Kobayashi, H. Yamada, K. Matsushige, and T. Hikihara, “Controlling chaos in dynamic-mode atomic force microscope,” *Physics Letters A*, vol. 373, no. 35, pp. 3140–3144, 2009.

[70] F. Arecchi, R. Badii, and A. Politi, “Generalized multistability and noise-induced jumps in a nonlinear dynamical system,” *Physical Review A*, vol. 32, no. 1, p. 402, 1985.

[71] Y. Liu, M. Wiercigroch, J. Ing, and E. Pavlovskaia, “Intermittent control of coexisting attractors,” *Philosophical Transactions of the Royal Society A: Mathematical, Physical and Engineering Sciences*, vol. 371, no. 1993, p. 20120428, 2013.

[72] L. Wang, R. Su, Z. Huang, X. Wang, W. Wang, C. Grebogi, and Y. Lai, “A geometrical approach to control and controllability of nonlinear dynamical networks,” *Nature communications*, vol. 7, no. 1, pp. 1–11, 2016.

[73] S. P. Cornelius, W. L. Kath, and A. E. Motter, “Realistic control of network dynamics,” *Nature communications*, vol. 4, no. 1, pp. 1–9, 2013.

[74] J. Páez Chávez, E. Pavlovskaia, and M. Wiercigroch, “Bifurcation analysis of a piecewise-linear impact oscillator with drift,” *Nonlinear Dynamics*, vol. 77, no. 1-2, pp. 213–227, 2014.

[75] S. L. de Souza and I. L. Caldas, “Controlling chaotic orbits in mechanical systems with impacts,” *Chaos, Solitons & Fractals*, vol. 19, no. 1, pp. 171–178, 2004.

[76] S. L. de Souza, I. L. Caldas, and R. L. Viana, “Damping control law for a chaotic impact oscillator,” *Chaos, Solitons & Fractals*, vol. 32, no. 2, pp. 745–750, 2007.

[77] H. Dankowicz and J. Jerrelind, “Control of near-grazing dynamics in impact oscillators,” *Proceedings of the Royal Society A: Mathematical, Physical and Engineering Sciences*, vol. 461, no. 2063, pp. 3365–3380, 2005.

[78] H. Dankowicz and F. Svahn, “On the stabilizability of near-grazing dynamics in impact oscillators,” *International Journal of Robust and Nonlinear Control: IFAC-Affiliated Journal*, vol. 17, no. 15, pp. 1405–1429, 2007.

[79] X. Zhao and H. Dankowicz, “Unfolding degenerate grazing dynamics in impact actuators,” *Nonlinearity*, vol. 19, no. 2, p. 399, 2005.

[80] D. W. Veldman, R. H. Fey, and H. Zwart, “Impulsive steering between coexisting stable periodic solutions with an application to vibrating plates,” *Journal of computational and nonlinear dynamics*, vol. 12, no. 1, 2017.

[81] G. Stépán and T. Insperger, “Stability of time-periodic and delayed systems?a route to act-and-wait control,” *Annual Reviews in control*, vol. 30, no. 2, pp. 159–168, 2006.

[82] S. Beregi, D. Takacs, and G. Stepan, “Bifurcation analysis of wheel shimmy with non-smooth effects and time delay in the tyre–ground contact,” *Nonlinear Dynamics*, pp. 1–18, 2019.

[83] T. Zhang, X. Meng, and Y. Song, “The dynamics of a high-dimensional delayed pest management model with impulsive pesticide input and harvesting prey at different fixed moments,” *Nonlinear Dynamics*, vol. 64, no. 1-2, pp. 1–12, 2011.

[84] A. R. Carvalho and C. M. Pinto, “New developments on aids-related cancers: The role of the delay and treatment options,” *Mathematical Methods in the Applied Sciences*, vol. 41, no. 18, pp. 8915–8928, 2018.

[85] V. Pyragas and K. Pyragas, “State-dependent act-and-wait time-delayed feedback control algorithm,” *Communications in Nonlinear Science and Numerical Simulation*, vol. 73, pp. 338–350, 2019.

[86] L. Davis, “Modifications of the optimal velocity traffic model to include delay due to driver reaction time,” *Physica A: Statistical Mechanics and its Applications*, vol. 319, pp. 557–567, 2003.

[87] L. E. Kollár, G. Stépán, and J. Turi, “Dynamics of delayed piecewise linear systems,” in *Electronic Journal of Differential Equations: Fifth Mississippi State Conference on Differential Equations and Computational Simulations*, vol. 10, pp. 163–185, Texas State University, 2003.

[88] V. Kapila, W. M. Haddad, and A. Grivas, “Stabilization of linear systems with simultaneous state, actuation, and measurement delays,” *International Journal of Control*, vol. 72, no. 18, pp. 1619–1629, 1999.

[89] J. Nilsson, B. Bernhardsson, and B. Wittenmark, “Stochastic analysis and control of real-time systems with random time delays,” *Automatica*, vol. 34, no. 1, pp. 57–64, 1998.

[90] J. D. Farmer, “Chaotic attractors of an infinite-dimensional dynamical system,” *Physica D: Nonlinear Phenomena*, vol. 4, no. 3, pp. 366–393, 1982.

[91] I. M. Repin, “On the approximate replacement of systems with lag by ordinary dynamical systems,” *J. Appl. Math. Mech.*, vol. 29, no. 2, pp. 254–264, 1965.

[92] I. Györi and J. Turi, “Uniform approximation of a nonlinear delay equation on infinite intervals,” *Nonlinear Analysis: Theory, Methods & Applications*, vol. 17, no. 1, pp. 21–29, 1991.

[93] J. A. S. Westdal and W. Lehn, “Time optimal control of linear systems with delay,” *International Journal of Control*, vol. 11, no. 4, pp. 599–610, 1970.

[94] R. A. Hess, “Optimal control approximations for time delay systems.,” *AIAA Journal*, vol. 10, no. 11, pp. 1536–1538, 1972.

[95] H. Banks, “Approximation of nonlinear functional differential equation control systems,” *Journal of Optimization Theory and Applications*, vol. 29, no. 3, pp. 383–408, 1979.

[96] G. Lipták, K. M. Hangos, and G. Szederkényi, “Approximation of delayed chemical reaction networks,” *Reaction Kinetics, Mechanisms and Catalysis*, vol. 123, no. 2, pp. 403–419, 2018.

[97] K. Engelborghs, T. Luzyanina, and D. Roose, “Numerical bifurcation analysis of delay differential equations using dde-biftool,” *ACM Transactions on Mathematical Software (TOMS)*, vol. 28, no. 1, pp. 1–21, 2002.

[98] J. Sieber, K. Engelborghs, T. Luzyanina, G. Samaey, and D. Roose, “DDE-BIFTOOL Manual-Bifurcation analysis of delay differential equations,” *arXiv preprint arXiv:1406.7144*, 2014.

[99] R. Szalai, G. Stépán, and S. John Hogan, "Continuation of bifurcations in periodic delay-differential equations using characteristic matrices," *SIAM Journal on Scientific Computing*, vol. 28, no. 4, pp. 1301–1317, 2006.

[100] R. Szalai, ""Knut: A continuation and bifurcation software for delay-differential equations." available at http://rs1909.github.io/knut.," 2017.

[101] S. Doole and S. Hogan, "A piece wise linear suspension bridge model: nonlinear dynamics and orbit continuation," *Dynamics and stability of systems*, vol. 11, no. 1, pp. 19–47, 1996.

[102] E. Fossas and G. Olivar, "Study of chaos in the buck converter," *IEEE Transactions on Circuits and Systems I: Fundamental Theory and Applications*, vol. 43, no. 1, pp. 13–25, 1996.

[103] P. Piiroinen, *Recurrent dynamics of nonsmooth systems with application to human gait*. PhD thesis, Mekanik, 2002.

[104] F. Dercole and Y. A. Kuznetsov, "SlideCont: An Auto97 driver for bifurcation analysis of Filippov systems," *ACM Transactions on Mathematical Software (TOMS)*, vol. 31, no. 1, pp. 95–119, 2005.

[105] D. A. Barton, B. Krauskopf, and R. E. Wilson, "Explicit periodic solutions in a model of a relay controller with delay and forcing," *Nonlinearity*, vol. 18, no. 6, p. 2637, 2005.

[106] D. A. Barton, B. Krauskopf, and R. E. Wilson, "Periodic solutions and their bifurcations in a non-smooth second-order delay differential equation," *Dynamical Systems*, vol. 21, no. 3, pp. 289–311, 2006.

[107] K. Mainzer and L. Chua, *The universe as automaton: From simplicity and symmetry to complexity*, vol. 1. Springer Science & Business Media, 2011.

[108] T. S. Parker and L. Chua, *Practical numerical algorithms for chaotic systems*. Springer Science & Business Media, 2012.

[109] G. Benettin, L. Galgani, A. Giorgilli, and J.-M. Strelcyn, "Lyapunov characteristic exponents for smooth dynamical systems and for hamiltonian systems; a method for computing all of them. part 1: Theory," *Meccanica*, vol. 15, no. 1, pp. 9–20, 1980.

[110] A. Wolf, J. B. Swift, H. L. Swinney, and J. A. Vastano, "Determining Lyapunov exponents from a time series," *Physica D: Nonlinear Phenomena*, vol. 16, no. 3, pp. 285–317, 1985.

[111] L. Dieci, R. D. Russell, and E. S. Van Vleck, "On the compuation of Lyapunov exponents for continuous dynamical systems," *SIAM journal on numerical analysis*, vol. 34, no. 1, pp. 402–423, 1997.

[112] A. Stefanski, "Estimation of the largest Lyapunov exponent in systems with impacts," *Chaos, Solitons & Fractals*, vol. 11, no. 15, pp. 2443–2451, 2000.

[113] P. C. Müller, "Calculation of Lyapunov exponents for dynamic systems with discontinuities," *Chaos, Solitons & Fractals*, vol. 5, no. 9, pp. 1671–1681, 1995.

[114] C. Dellago, H. A. Posch, and W. G. Hoover, "Lyapunov instability in a system of hard disks in equilibrium and nonequilibrium steady states," *Physical Review E*, vol. 53, no. 2, p. 1485, 1996.

[115] L. Jin, Q.-S. Lu, and E. Twizell, "A method for calculating the spectrum of Lyapunov exponents by local maps in non-smooth impact-vibrating systems," *Journal of sound and Vibration*, vol. 298, no. 4-5, pp. 1019–1033, 2006.

[116] I. M. Repin, "On the approximate replacement of systems with lag by ordinary dynamical systems," *Journal of Applied Mathematics and Mechanics*, vol. 29, no. 2, pp. 254–264, 1965.

[117] D. Breda, "Solution operator approximations for characteristic roots of delay differential equations," *Applied Numerical Mathematics*, vol. 56, no. 3-4, pp. 305–317, 2006.

[118] D. Breda, S. Maset, and R. Vermiglio, "Pseudospectral differencing methods for characteristic roots of delay differential equations," *SIAM Journal on Scientific Computing*, vol. 27, no. 2, pp. 482–495, 2005.

[119] D. Breda, S. Maset, and R. Vermiglio, "Approximation of eigenvalues of evolution operators for linear retarded functional differential equations," *SIAM Journal on Numerical Analysis*, vol. 50, no. 3, pp. 1456–1483, 2012.

[120] E. Pavlovskaia, M. Wiercigroch, and C. Grebogi, "Two-dimensional map for impact oscillator with drift," *Physical Review E*, vol. 70, no. 3, p. 036201, 2004.

[121] E. L. Allgower and K. Georg, *Introduction to numerical continuation methods*, vol. 45. SIAM, 2003.

[122] E. J. Doedel, A. R. Champneys, T. F. Fairgrieve, Y. A. Kuznetsov, B. Sandstede, X. Wang, *et al.*, "Auto97," *Continuation and bifurcation software for ordinary differential equations*, 1998.

[123] Y. A. Kuznetsov and V. Levitin, "CONTENT: A multiplatform environment for analyzing dynamical systems," 1997.

[124] D. A. Barton, "Stability calculations for piecewise-smooth delay equations," *International Journal of Bifurcation and Chaos*, vol. 19, no. 02, pp. 639–650, 2009.

[125] S. Guo and J. Wu, *Bifurcation theory of functional differential equations*, vol. 38. Springer, 2013.

[126] O. Diekmann, S. A. van Gils, S. V. Lunel, and H.-O. Walther, "Delay equations, volume 110 of applied mathematical sciences," 1995.

[127] M. Lakshmanan and D. V. Senthilkumar, *Dynamics of nonlinear time-delay systems*. Springer Science & Business Media, 2011.

[128] J. K. Hale and S. M. V. Lunel, *Introduction to functional differential equations*, vol. 99. Springer Science & Business Media, 2013.

[129] Y. Kuang, *Delay differential equations*. University of California Press, 2012.

[130] L. E. Elsgolts and S. B. Norkin, *Introduction to the theory and application of differential equations with deviating arguments*. Elsevier, 1973.

[131] H. Banks, “Delay systems in biological models: approximation techniques,” in *Nonlinear systems and applications*, pp. 21–38, Elsevier, 1977.

[132] A. Stefanski, A. Dabrowski, and T. Kapitaniak, “Evaluation of the largest Lyapunov exponent in dynamical systems with time delay,” *Chaos, Solitons & Fractals*, vol. 23, no. 5, pp. 1651–1659, 2005.

[133] T. Kapitaniak, “Chaotic behaviour of anharmonic oscillators with time delay,” *Journal of the Physical Society of Japan*, vol. 56, no. 6, pp. 1951–1954, 1987.

[134] N. Krasovskii, “The approximation of a problem of analytic design of controls in a system with time-lag,” *Journal of Applied Mathematics and Mechanics*, vol. 28, no. 4, pp. 876–885, 1964.

[135] B. Krasznai, I. Győri, and M. Pituk, “The modified chain method for a class of delay differential equations arising in neural networks,” *Mathematical and Computer Modelling*, vol. 51, no. 5-6, pp. 452–460, 2010.

[136] G. V. Demidenko and V. A. Likhoshvai, “On differential equations with retarded argument,” *Siberian Mathematical Journal*, vol. 46, no. 3, pp. 417–430, 2005.

[137] M. Gomoyunov and A. Plaksin, “Finite-dimensional approximations of neutral-type conflict-controlled systems,” *IFAC-PapersOnLine*, vol. 50, no. 1, pp. 5109–5114, 2017.

[138] M. Benchohra, J. Henderson, and S. Ntouyas, *Impulsive differential equations and inclusions*, vol. 2. Hindawi Publishing Corporation New York, 2006.

[139] B. Krauskopf, H. M. Osinga, and J. Galán-Vioque, *Numerical continuation methods for dynamical systems*. Springer, 2007.

[140] E. Hairer, S. P. Nørsett, and G. Wanner, *Solving Ordinary Differential Equations I*. New York: Springer-Verlag, second ed., 1993.

[141] L. Shampine and S. Thompson, “Event location for ordinary differential equations,” *Computers & Mathematics with Applications*, vol. 39, no. 5-6, pp. 43–54, 2000.

[142] L. F. Shampine and S. Thompson, “Solving ddes in matlab,” *Applied Numerical Mathematics*, vol. 37, no. 4, pp. 441–458, 2001.

[143] P. Saucez, W. Schiesser, *et al.*, *Adaptive method of lines*. CRC Press, 2001.

[144] R. J. LeVeque, *Finite difference methods for ordinary and partial differential equations: steady-state and time-dependent problems*. SIAM, 2007.

[145] S. Banerjee, J. Ing, E. Pavlovskaia, M. Wiercigroch, and R. K. Reddy, "Invisible grazings and dangerous bifurcations in impacting systems: the problem of narrow-band chaos," *Physical Review E*, vol. 79, no. 3, p. 037201, 2009.

[146] N. Krasovskii, "On the analytic construction of an optimal control in a system with time lags," *Journal of Applied Mathematics and Mechanics*, vol. 26, no. 1, pp. 50–67, 1962.

[147] J. Stoer and R. Bulirsch, *Introduction to numerical analysis*, vol. 12. Springer Science & Business Media, 2013.

[148] H. Jiang and M. Wiercigroch, "Geometrical insight into non-smooth bifurcations of a soft impact oscillator," *IMA Journal of Applied Mathematics*, vol. 81, no. 4, pp. 662–678, 2016.

[149] F. Chatelin, "Convergence of approximation methods to compute eigenelements of linear operations," *SIAM Journal on Numerical Analysis*, vol. 10, no. 5, pp. 939–948, 1973.

[150] F. Chatelin, *Spectral approximation of linear operators*. SIAM, 2011.

[151] A. Varma and T. Mills, "On the summability of lagrange interpolation," *Journal of Approximation Theory*, vol. 9, no. 4, pp. 349–356, 1973.

[152] H. E. Nusse and J. A. Yorke, *Dynamics: Numerical Explorations (Applied Mathematical Sciences)*, vol. 101. Springer-Verlag, 1997.

[153] D. Breda, O. Diekmann, M. Gyllenberg, F. Scarabel, and R. Vermiglio, "Pseudospectral discretization of nonlinear delay equations: new prospects for numerical bifurcation analysis," *SIAM Journal on applied dynamical systems*, vol. 15, no. 1, pp. 1–23, 2016.

[154] L. F. Shampine and S. Thompson, "Event location for ordinary differential equations," *Comput. Math. Appl.*, vol. 39, no. 5-6, pp. 43–54, 2000.

[155] L. F. Shampine and S. Thompson, "Solving DDEs in MATLAB," *Appl. Numer. Math.*, vol. 37, no. 4, pp. 441–458, 2001.

[156] M. Lazarek, P. Brzeski, W. Solecki, and P. Perlikowski, "Detection and classification of solutions for systems interacting by soft impacts with sample-based method," *International Journal of Bifurcation and Chaos*, vol. 30, no. 06, p. 2050079, 2020.

[157] O. Makarenkov and J. S. Lamb, "Dynamics and bifurcations of nonsmooth systems: A survey," *Physica D: Nonlinear Phenomena*, vol. 241, no. 22, pp. 1826–1844, 2012.

[158] J. Ing, E. Pavlovskaia, M. Wiercigroch, and S. Banerjee, "Experimental study of impact oscillator with one-sided elastic constraint," *Philosophical Transactions of the Royal Society A: Mathematical, Physical and Engineering Sciences*, vol. 366, no. 1866, pp. 679–705, 2007.

[159] L. Ryashko, "Sensitivity analysis of the noise-induced oscillatory multistability in higgins model of glycolysis," *Chaos: An Interdisciplinary Journal of Nonlinear Science*, vol. 28, no. 3, p. 033602, 2018.